Universidade Federal da Paraíba

Centro de Tecnologia

PROGRAMA DE PÓS-GRADUAÇÃO EM ENGENHARIA CIVIL E AMBIENTAL

MESTRADO

ANALYSIS OF PATTERNS, DRIVERS, AND TRENDS OF SURFACE URBAN HEAT ISLANDS (SUHIS) IN BRAZIL

by

Eduardo Gonçalves Patriota

Dissertação de Mestrado apresentada à Universidade Federal da Paraíba para obtenção do grau de Mestre

João Pessoa – Paraíba **Março de 2024**

Universidade Federal da Paraíba

Centro de Tecnologia

PROGRAMA DE PÓS-GRADUAÇÃO EM ENGENHARIA CIVIL E AMBIENTAL

MESTRADO

ANALYSIS OF PATTERNS, DRIVERS, AND TRENDS OF SURFACE URBAN HEAT ISLANDS (SUHIS) IN BRAZIL

Dissertação submetida ao Programa de Pós-Graduação em Engenharia Civil e Ambiental da Universidade Federal da Paraíba, como parte dos requisitos para a obtenção do título de Mestre.

Eduardo Gonçalves Patriota

Orientador: Prof. Dr. Victor Hugo Rabelo Coelho

Coorientador: Prof. Dr. Guillaume Francis Bertrand

João Pessoa – Paraíba **Março de 2024**

Catalogação na publicação
Seção de Catalogação e Classificação

P314a Patriota, Eduardo Gonçalves.
Analysis of patterns, drivers, and trends of surface urban heat islands (SUHIS) in Brazil / Eduardo Gonçalves Patriota. - João Pessoa, 2024.
152 f. : il.

Orientação: Victor Hugo Rabelo Coelho.
Coorientação: Guillaume Francis Bertrand.
Dissertação (Mestrado) - UFPB/CT.

1. Conforto térmico. 2. Sensoriamento remoto. 3. Balanço de energia da superfície. 4. Evapotranspiração. 5. Cidades sustentáveis. I. Coelho, Victor Hugo Rabelo. II. Bertrand, Guillaume Francis. III. Título.

UFPB/BC CDU 628.87(043)

Elaborado por Larissa Silva Oliveira de Mesquita - CRB-15/746

PPGECAM
Programa de Pós-Graduação
Engenharia Civil e Ambiental
UFPB Universidade Federal da Paraíba
Mestrado e Doutorado

ANALYSIS OF PATTERNS, FACTORS AND TRENDS OF SURFACE URBAN HEAT ISLANDS (SUHIS) IN BRAZIL

EDUARDO GONÇALVES PATRIOTA
Dissertação aprovada em 06 de março de 2024.
Período Letivo: 2023.2

Documento assinado digitalmente
gov.br VICTOR HUGO RABELO COELHO
Data: 07/03/2024 08:47:03-0300
Verifique em https://validar.iti.gov.br

Prof. Dr. Victor Hugo Rabelo Coelho – UFPB
Orientador

Documento assinado digitalmente
gov.br GUILLAUME FRANCIS BERTRAND
Data: 07/03/2024 09:53:24-0300
Verifique em https://validar.iti.gov.br

Prof. Dr. Guillaume Francis Bertrand – UFPB
Coorientador

Documento assinado digitalmente
gov.br SOLANGE MARIA LEDER
Data: 07/03/2024 12:32:33-0300
Verifique em https://validar.iti.gov.br

Profa. Dra. Solange Maria Leder – UFPB
Examinadora Interna

Documento assinado digitalmente
gov.br IANA ALEXANDRA ALVES RUFINO
Data: 07/03/2024 11:05:59-0300
Verifique em https://validar.iti.gov.br

Profa. Dra. Iana Alexandra Alves Rufino – UFCG
Examinadora Externa

João Pessoa/PB
2024

Dedico aos que estiveram comigo nessa jornada e contribuíram direta ou indiretamente para a concepção deste trabalho.

AGRADECIMENTOS

Gostaria de agradecer primeiramente aos meus familiares, em especial a minha mãe, Maria José, que vencem a distância e se fazem presentes em todas as etapas da minha vida pessoal e profissional, me apoiando, me incentivando a melhorar cada vez mais, tornando possível a execução deste trabalho.

Ao meu namorado Albert, que esteve presente desde o processo de seleção para o meu ingresso no curso e que todos os dias me ensina o conceito de pesquisador dedicado e com pensamento crítico diante dos desafios da pós-graduação. Sua presença e contribuição foi e é essencial para que eu continue a enxergar que é possível realizar meus sonhos.

Ao meu orientador Prof. Dr. Victor Hugo Rabelo Coelho, que tive o prazer de conhecer logo no início do mestrado e que contribuiu imensamente para execução desse trabalho. Obrigado pela maravilhosa orientação, conselhos, ajuda e disponibilidade. Que nossa colaboração siga rendendo muitos trabalhos e resultados.

Aos professores Dr. Guillaume Francis Bertrand e Dr. Cristiano das Neves Almeida, o primeiro por todo apoio no processo de coorientação e concepção deste trabalho, e o segundo por todos os ensinamentos passados desde as disciplinas até a colaboração ativa nas reuniões do grupo de pesquisa. Muito obrigado pela contribuição de cada um de vocês e que nossa cooperação enquanto grupo de pesquisa cresça cada vez mais.

Gostaria de agradecer também à Prof.ª Dr.ª Solange Maria Leder (PPGECAM-UFPB) e à Prof.ª Dr.ª Iana Alexandra Alves Rufino (PPGECA-UFCG), por estarem disponíveis para participação e contribuição como avaliadoras interna e externa, respectivamente. Agradeço imensamente pelas suas importantes considerações.

Aos meus amigos e colegas de laboratório (LARHENA-UFPB) Lindemberg Vidal, Filipe Lemos, Abner Lins, e em especial, Cinthia Maria, que contribuiu com a concepção do modelo de ET e com quem construí uma amizade e parceria que levarei para vida. Agradeço a cada um de vocês por compartilharem comigo das risadas e aflições dessa jornada que é a pós-graduação.

Agradeço à Universidade Federal da Paraíba (UFPB) pela possibilidade de execução desta pesquisa, bem como à Fundação de Apoio à Pesquisa do Estado da Paraíba (FAPESQ-PB) pelo apoio financeiro.

Por fim, agradeço a todos que corroboraram para a concepção final deste curso de Mestrado e me acompanharam até aqui, meu muitíssimo obrigado!

RESUMO

A expansão de áreas urbanas ocorre pela alteração de superfícies naturais, trazendo efeitos ambientais como modificações no balanço de energia da superfície e a formação das ilhas de calor urbano de superfície (SUHIs). A variação espaço-temporal das intensidades de SUHIs (SUHIIs) e sua relação com parâmetros biofísicos de superfície em regiões metropolitanas (RMs) brasileiras precisam ser mais exploradas, especialmente considerando a evolução mensal e anual contínua da urbanização. Este estudo tem como objetivo fornecer informações de base sobre a influência da urbanização na expansão das SUHIs e na variabilidade de parâmetros biofísicos em vinte e uma principais RMs brasileiras de 2003 a 2022. Foram utilizados dados de temperatura da superfície (LST) dos sensores MODIS (MOD11A2 e MYD11A2) para quantificar continuamente SUHIIs diurnas e noturnas. Reflectância espectral do MODIS (MOD09Q1, MYD09Q1, MOD09A1 e MYD09A1) e dados de reanálise (GLDAS 2.1 e ERA5-Land) foram usados para acessar a variabilidade do Índice de Vegetação Aprimorado-2 (EVI2), albedo de superfície (α), crescimento de áreas urbanas (UAs), radiação líquida de superfície (Rn) e evapotranspiração real (ET) com resolução espacial de 250 m. O teste de tendência de Mann-Kendall foi aplicado para todas as variáveis, e suas relações com o LST foram investigadas por meio da correlação de Pearson (r), coeficiente de determinação (R^2) e Eficiência de Kling-Gupta (KGE). Os resultados mostram que as SUHIIs foram 60% (1,64 ºC) maiores durante o dia, com tendências de crescimento significativas ao longo do período estudado e variações sazonais mensais mais pronunciadas em RMs de latitudes mais elevadas que possuem zonas climáticas subtropicais. As UAs mostraram ser mais influentes sobre a LST durante o dia, com a associação da LST com EVI2 e α desempenhando um papel fundamental na regulação do clima urbano. Os resultados também demonstraram que o aumento da ET mitiga potencialmente a LST, especialmente durante o dia. Rn influenciou mais a LST noturno, levando a uma maior disponibilidade de calor sensível durante esse período. Os resultados deste estudo proporcionam uma compreensão detalhada dos fatores que influenciam a dinâmica espaço-temporal das ICUs nas maiores RMs do Brasil, contribuindo com insights valiosos para o planejamento urbano e estratégias de mitigação climática.

PALAVRAS-CHAVE: sensoriamento remoto, balanço de energia da superfície, evapotranspiração, cidades sustentáveis, conforto térmico.

ABSTRACT

The expansion of urban areas occurs by changing natural surfaces, bringing environmental effects like modifications in the surface energy balance and the formation of surface urban heat islands (SUHIs). The spatial-temporal variation of SUHIs intensities (SUHIIs) and their relationship with surface biophysical parameters in Brazilian metropolitan regions (MRs) need to be better explored, especially taking into consideration the continuous monthly and annual evolution of urbanisation. This study aims then to provide baseline information on the influence of urbanisation in the expansion of SUHIs and the variability of biophysical parameters in twenty-one major Brazilian MRs from 2003 to 2022. We used land surface temperature (LST) data from MODIS (MOD11A2 and MYD11A2) sensors to continuously quantify the daytime and nighttime SUHIIs. Spectral reflectance from MODIS (MOD09Q1, MYD09Q1, MOD09A1, and MYD09A1) and reanalysis data (GLDAS 2.1 and ERA5-Land) were used to access the variability of Enhanced Vegetation Index-2 (EVI2), surface albedo (α), urban areas (UAs) growth, surface net radiation (Rn), and actual evapotranspiration (ET) at 250-m spatial resolution. The Mann-Kendall trend test was applied for all variables, and their relationships with LST were investigated through Pearson correlation (r), determination coefficient (R^2) and Kling-Gupta Efficiency (KGE). The results show that the SUHIs were 60% (1.64 ºC) higher during the daytime, with significant growth trends along the studied period and more pronounced monthly seasonal variations in higher latitudes MRs holding subtropical climate zones. The UAs showed to be more influential on LST during daytime, with the association of LST with EVI2 and α playing a fundamental role in regulating the urban climate. The results also demonstrated that increasing ET potentially mitigates LST, especially during the daytime. Rn highest influenced the nighttime LST, leading to a higher availability of sensible heat during this period. The results found from this study provide a nuanced understanding of the factors influencing the spatiotemporal dynamics of SUHIIs in the largest MRs of Brazil, contributing valuable insights for urban planning and climate mitigation strategies.

KEYWORDS: remote sensing, surface energy balance, evapotranspiration, sustainable cities, thermal comfort.

LIST OF FIGURES

LIST OF TABLES

LIST OF ABBREVIATIONS AND ACRONYMS

AUHIs	Atmospheric Urban Heat Islands
BU	Built-Up Index
C_p	Specific Heat Capacity of Air at Constant Pressure
e_a	Actual Water Vapour Pressure
ERA5	Fifth Generation of the European Centre for Medium-Range Weather Forecasts (ECMWF) Atmospheric Reanalysis of the Global Climate
e_{sat}	Saturated Water Vapour Pressure
ET	Actual Evapotranspiration
EVI2	Enhanced Vegetation Index 2
G	Soil Heat Flux
GEE	Google Earth Engine
GLDAS	Global Land Data Assimilation System
H	Sensible Heat Flux
IBGE	Brazilian Institute of Geography and Statistics
KGE	Kling-Gupta Efficiency
LAI	Leaf Area Index
LE	Latent Heat Flux
LST	Land Surface Temperature
LULC	Land Use and Land Cover
LW	Longwave
MODIS	Moderate Resolution Imaging Spectroradiometer
NDBI	Normalized Difference Built-Up Index
NDVI	Normalized Difference Vegetation Index
NIR	Near-Infrared
OLI	Operational Land Imager
r	Pearson's correlation coefficient
R^2	Determination Coefficient
r_a	Aerodynamic Resistance
RED	Red

Rn	Surface Net Radiation
r_s	Surface Resistance
S	Mann-Kendall Statistic
SAVI	Soil-Adjusted Vegetation Index
SEB	Surface Energy Balance
SUHIs	Surface Urban Heat Islands
SW	Shortwave
SWIR	Shortwave Infrared
T_a	In-situ air temperature
TM	Thematic Mapper
UAs	Urban Areas
UHIs	Urban Heat Islands
Var(S)	Variance of Mann-Kendall Statistic (S)
Z	Standard Normal Statistic
α	Surface Albedo
γ	Psychometric Constant
ρ	Air Density

TABLE OF CONTENTS

1 INTRODUCTION

The growth of the world population and the intense migration from rural to urban areas during the last decades has been driving the expansion of metropolises, especially in developing regions (e.g. sub-Saharan Africa, Eastern Asia, Western Asia, Latin America, and the Caribbean) (Arshad et al., 2022; United Nations, 2018; Zhang et al., 2022). Around 56% of the global population lives in urban environments (United Nations, 2018), with estimations that by the middle of the 21st century, this proportion will reach close to 70% (Hosseini et al., 2016). Specifically in Latin America, Brazil has experienced significant urbanisation over the last decades, driven by population growth, rural-urban migration, and economic development, with twenty-one metropolitan regions holding more than 1 million inhabitants, according to the last demographic census in 2022 (IBGE, 2022). Between 2010 and 2022, the Brazilian urban population reached a level of 124.1 million inhabitants, corresponding to 61% of the country's population (IBGE, 2022).

In this context of rapid growth, urbanisation may occur in an uncontrolled manner, bringing environmental changes like deforestation, land cover changes, and soil sealing (Carrillo-Niquete et al., 2022; Sfîca et al., 2023; Xiao and Weng, 2007). These modifications on natural surfaces can bring serious environmental effects (Gong et al., 2020), including changes in the surface energy balance (Grimm et al., 2008), intensification of flooding events (Berland et al., 2017), increase in air pollution (Piracha et al., 2022), and formation of urban heat islands (UHIs) (Venter et al., 2021). Therefore, urban planning alternatives based on assessments must be considered to minimise such effects.

The UHIs occur when the city experiences higher temperatures than the surrounding areas due to the amplification of thermal intensity in the urban environment because of human activities (Li et al., 2022; Oke, 1987; Santamouris et al., 2017). This mechanism, first observed in London in the early 1800s (Howard, 1833), can lead to temperatures that exceed human physiological tolerance levels (Raymond et al., 2020). UHIs also affect air circulation, leading to the concentration of pollutants, directly contributing to the emergence of air quality-related diseases (Di bernardino, et al. 2021).

Assessing environmental indicators that act as UHI's triggering factors requires detecting land surface property changes caused by land use and land cover (LULC) change and controlling environmental processes at different time scales (Carrillo-Niquete et al., 2022).

From a thermodynamic point of view, UHI development corresponds to an alteration of the surface energy balance, which plays a key role in regulating the exchange of energy between the Earth's surface and the atmosphere (Christopherson and Birkeland., 2017). This energy balance depends on biophysical parameters, such as vegetation greenness, surface albedo, net radiation of the land surface, and evapotranspiration. The reduction of green areas tends to decrease the latent heat fluxes (i.e. associated with the evapotranspiration processes) while increasing the sensible heat fluxes (i.e. rising air and soil temperatures) (Christopherson and Birkeland, 2017), contributing to the warming of the urban surface and to the development of the so-called surface urban heat islands (SUHIs) that affects in turn the atmosphere (Chen et al., 2022).

There are different techniques for quantifying and assessing the SUHIs. These techniques can be divided into two main groups: (i) field measurements and (ii) orbital measurements from remote sensing techniques by selecting shortwave and thermal bands (Mohamed et al., 2017). On the one hand, field measurements (e.g. fixed stations or mobile devices) are essential for defining the actual conditions on the ground (Hu et al., 2016). However, this approach is punctual and only representative of small areas, hardly integrating the spatial heterogeneity of the processes in urban areas. Such an approach requires the presence of many sensors in the cities and their surroundings, high financial resources, specialised labour, many materials, and time-consuming implementation. On the other hand, the quantification of such information through orbital remote sensing data may provide spatialized information, provided that the temporal resolution, although not as high as ground-based techniques, may be relevant for long-term trending analyses. Consistently, this latter has been widely used in various studies worldwide (e.g. Arshad et al., 2022; Chakraborty and Lee, 2019; Clinton and Gong, 2013; Dewan et al., 2021; Gao et al., 2022; Lai et al., 2021; Li et al., 2023; Maimaitiyiming et al., 2014; Moazzam et al., 2022; Peng et al., 2012; Peng et al., 2018; Quan et al., 2014; Si et al., 2022; Zhou et al., 2014), including Brazil (Correia Filho, 2019; Flores et al., 2016; Monteiro et al., 2021; Nascimento et al., 2022; Peres et al., 2018; Portela et al., 2020; Santos et al., 2017; Silva et al., 2018). These studies were carried out from local to global scales to demonstrate the relationship between SUHIs intensities (SUHIIs) and a range of environmental parameters. Table 1 provides a focused tabular literature review of some of the most relevant studies in urban areas around the world and Brazil, with their respective methodologies and main results.

Table 1 - Summary of relevant literature on SUHII estimation using remotely sensed data around the world in relation to the proposed study. Note that recent studies have assessed only the relationship between SUHII and triggering factors, ignoring the possible influence of that on some biophysical parameters, like net radiation and evapotranspiration

Study	Remotely sensed data/methods used	Location/period	Main results
1. Peng et al. (2012)	SUHII measured from the MODIS LST MYD11A2 (Aqua).	419 global big cities/2003-2008.	Daytime and nighttime SUHII; Correlation with driven factors (albedo, vegetation and nighttime light).
2. Clinton and Gong (2013)	SUHII measured from the MODIS LST MOD11A2 (Terra) and MYD11A2 (Aqua); EVI and NDVI from MOD13A2; and Land cover from MOD12Q1.	Global cities without specification/2010.	Daytime and nighttime SUHII; Correlation with EVI/NDVI and urban area.
3. Maimaitiyiming et al. (2014)	LST and green spaces from Landsat 5 ™.	Aksu City, Northwestern China/ One image in August 2011.	Correlation between LST and spatial configuration of vegetation.
4. Flores et al. (2016)	SUHII measured of the LST from MOD11A2 (Terra); land use and land cover (LULC) from MCD12C1; and NDVI/EVI from MOD13C2.	São Paulo and Rio de Janeiro, Brazil/2001-2014.	Daytime and nighttime SUHII using two methods and their relationship with the factors.
5. Dos Santos et al. (2017)	Landsat 5 to quantify LST, NDVI, and NDBI.	City of Vila Velha, Brazil/2008-2011.	Mapping of green and build-up areas and their relationship with LST.
6. Peres et al. (2018)	Landsat 5(TM), 7(ETM+) and 8(OLI) to estimate LST.	Rio de Janeiro, Brazil/1984-2015.	Investigation ofincreasing LST.
7. Silva et. al. (2018)	LULC and LST from Landsat 5 (TM) and 8 (OLI); and Air temperature and relative humidity from the National Institute of Meteorology (INMET).	City of Paço do Lumiar, Brazil/1988,1999, 2010, and 2014.	Temporal and spatial variability of LULC/LST and their correlation with air temperature and humidity.

8. Chakraborty and Lee (2019)	SUHII measured from the MODIS LST MOD11A2 and MYD11A2; and Land use and land cover classification (LULC) from MCD12Q1.	9500 global cities/2001-2017.	Variability and seasonality of daytime and nighttime SUHII.
9. Correia Filho et al. (2019)	Images from Landsat 5 (TM) and 8 (OLI) to estimate LST, NDVI, and NDBI.	Maceió, Brazil/1987, 1998, 2003, and 2017.	Correlation between NDVI, NDBI, and LST.
10. Khamchiangta and Dhakal (2020)	LULC, LST, and NDVI from Landsat 5 and 7 images.	Bangkok, Thailand/1991, 1997, 2005, and 2016.	Time series analysis of LULC and NDVI related with SUHII.
11. Portela et al. (2020)	LULC, NDVI. and LST from Landsat 5 (TM) and 8 (OLI).	São José dos Campos, Brazil/2010-2016	Time series analysis of LST, LULC, and NDVI; Correlations between NDVI, NDBI, and LST.
12. Dewan et al. (2021)	SUHII measured from the MODIS LST MOD11A2; LULC from MCD12Q1, and EVI, NDWI, BCI, and albedo. from MODIS reflectance.	Five large cities in Bangladesh/2000-2019.	Time series analysis of SUHII, with identification of driven factors and trends.
13. Monteiro et al. (2021)	SUHII calculated with LST from MOD11A2 (Terra), NDVI from MOD13A2, and surface albedo from MCD43A3.	21 cities in Brazil/2000-2016.	Relationship between SUHII, NDVI, and albedo, with analysis of SUHII.
14. Arshad et al. (2022)	LST, NDVI, and NDBI measured with images from Landsat 5 (TM), 7 (ETM+/TIRS), and 8 (OLI). LST time series with MOD11A2.	Lahore District, Punjab, Pakistan/2001-2020.	Times series analysis of LST and its relationship with NDVI and NDBI.
15. De Souza e Silva et al. (2022)	LULC and LST estimated from Landsat 5 (TM) and 8 (OLI) images; Air temperature and relative humidity from weather stations.	João Pessoa, Brazil/1991, 2006, 2010, and 2018.	Analysis of thermal comfort and relationship between LST and LULC.
16. Moazzam et al. (2022)	LST and LULC classification with Landsat 5 (TM), 7 (ETM+) and 8 (OLI) images.	Jeju Island, Republic of Korea/2002, 2011, and 2021.	Relationship between LULC changes and increasing LST.

17. Nascimento et al. (2022)	LULC and LST estimated from Landsat 8 (OLI), and air temperature from 29 weather stations.	São Paulo, Brazil/2019 and 2021.	Comparison between LST and air temperature correlated with LULC.
18. Li et al. (2023)	LST from Landsat 5, 7, and 8 images and LST from MOD11A2.	511 major cities worldwide/1985-2020.	Trend analysis of SUHII and its relationship with NDVI, impervious area, rainfall, and elevation.
19. This study	Daytime and nighttime SUHIIs measured from MODIS LST (MOD11A2/MYD11A2) and driven factors (i.e. EVI2, surface albedo, ET, Rn, and BU index) estimated by MODIS reflectance products and reanalysis data (ERA5-Land and GLDAS).	21 major metropolitan regions in Brazil/2003-2022	Time-series and trend analyses of daytime and nighttime SUHII and their relationships with net radiation, vegetation greenness, ET, impervious surfaces, and surface albedo.

All studies listed in Table 1 advanced in the characterisation of the relationship between the urbanisation process and some variables, mainly the correlation between SUHII, LST, and vegetation indexes. For instance, Li et al. (2023) analysed the inter-annual trends of daytime SUHII in 511 cities worldwide, of which 13 were in Brazil, using annual averages based on reconstructed thermal images of the Landsat series between 1985 and 2020. They examined the annual relationship between SUHII, vegetation index, rainfall, and elevation, whose products were resampled to a spatial resolution of 1 km. Monteiro et al. (2021) further analysed the relationship between land surface temperature, surface albedo, and NDVI in 21 metropolitan regions of Brazil during the dry season (minimising cloud contamination) from 2000 to 2016. Additionally, Monteiro et al. (2021) used the MODIS-based products MCD43A3 (a daily product with 500 m spatial resolution, recently decommissioned) and MOD13A1 (a 16-day product with 1 km spatial resolution) to analyse the influences of LST in the surface albedo and NDVI, respectively, which can be coarse spatial resolutions for some smaller urban areas.

These studies carried out worldwide and in Brazil mainly focused on the spatiotemporal analysis of LST or SUHII and its relationship with LULC and some biophysical parameters (mainly vegetation indexes). It appears that the LULC changes can affect many other biophysical parameters. For instance, the increase of impervious areas and, consequently, the

decrease of vegetated areas, can reduce the surface albedo and the LST, reducing the surface net radiation available and the latent heat fluxes associated with the actual evapotranspiration processes (Vujovic et al., 2021). This reduction of actual evapotranspiration can increase the sensible heat flux, warming the atmosphere and land surface in urban areas.

However, the studies focusing on multiple urban areas of Brazil did not consider the intra- and inter-annual variabilities of SUHIIs and their relationship with biophysical parameters, including surface net radiation and actual evapotranspiration at a reasonable timescale (e.g. monthly). Therefore, this study intends to provide baseline information on the influence of urbanisation in the expansion of SUHIs and the variability of biophysical parameters in the urban Brazilian context, which is representative of many situations encountered throughout the Global South featuring tropical climates. To do so, the specific objectives of this study are: (i) to investigate the impacts of the urbanisation process on the formation of SUHIs in the major metropolitan regions of Brazil over the past 20 years, considering both intra-annual and inter-annual scales; and (ii) to assess variations of the controlling surface biophysical parameters at a monthly timescale, including LST, surface albedo, vegetation index, net radiation, and actual evapotranspiration, over the last two decades, in response to the urbanisation process.

2 THEORICAL REFERENCE

2.1 The urban climate

Urban climate generally differs from those of nearby nonurban areas, with urban areas regularly reaching temperatures as much as 6ºC hotter than surrounding suburban and rural areas and the surface energy characteristics of urban areas are like those of desert locations, mainly because vegetation is lacking in both environments (Christopherson and Birkeland, 2017).

Defined as the complex interaction between natural and anthropogenic elements that affect atmospheric conditions in urban environments, the urban climate has been the subject of study in various fields, including meteorology, climatology, and urban geography. The increasing urbanization and global climate changes have expanded the significance of this research field, aiming to comprehend the climate characteristics in urban areas. According to Oke (1987), urban climate is shaped by a combination of factors such as urban layout, building geometry, pavement surfaces, vegetation, and anthropogenic heat release.

Research related to the study of urban climate began in the 17th century, a period during which the air pollution levels in cities and the climatic changes caused by the pace of industrialization were being assessed. The inception of this research field dates to 1661, with John Evelyn's study "Fumifugium" (1661) on the urban climate of London, motivated by a high concentration of pollutants in the air. As early as 1833, after the 2nd Industrial Revolution, Luke Howard (1833) described a significant portion of urban climatic elements, including temperature and precipitation, through his study "The Climate of London" thereby conducting the initial comparisons of these variables between the urban zone and neighbouring areas.

Local climate changes mainly arise due to modifications in land use and land cover, and these changes can be exemplified by alterations in precipitation patterns, decreased relative humidity, increased energy consumption, and intensified urban temperatures (Arshad et al., 2022). An important environmental risk of urbanization is the formation of urban heat islands (UHIs) in which the increase in impermeable surfaces (Makiranta and Hiltunen, 2019) and the gradual loss of vegetation (Shojanoori and Shafri, 2016) modify the surface energy properties.

2.2 Urban heat islands (UHIs)

In this situation, both maximum and minimum temperatures (on average) are higher within the cities when compared to the nearby rural settings (Christopherson and Birkeland, 2017). Urbanization has led to rising air and surface temperatures in built-up areas, causing seasonal heat stress and increasing heat-related mortality in most global cities, especially with the formation of UHIs (Trenberth and Fasullo, 2012; Scherer et al., 2013; Nwakaire et al., 2020). Its formation is highly associated with the heat-absorbing properties of the built environment and thermal effects of anthropogenic heat sources (Stone & Rodgers, 2001; Kim et al., 2022).

UHIs modulate local climate (Landsberg, 1981; Roth, 2007), however they can also significantly influence both local and regional climates (Kalnay and Cai, 2003). Amorim (2010) says that temperature differences lead to differences in pressure, as at local scale of climate, higher temperatures result in lower pressures, and consequently, cooler air from the surroundings moves towards the warmer areas. During this process, if there are sources of air pollution, theses pollutants are carried to warmer location, potentially resulting in health issues for people (Amorim, 2010).

On the other hand, green areas can remain cooler due to the role of trees in providing shade and dissipating energy through evapotranspiration and vegetated areas are gaining more support to become part of the solution through the structures of natured based solutions and urban green infrastructure (Nature Based Solutions Handbook, 2019; Augusto et al., 2020).

According to Dewan et al. (2021), two major types of UHIs are distinguished: a) the atmospheric urban heat island (AUHI), and b) the surface urban heat island (SUHI). The type of UHI is based on the height above the ground at which the phenomenon is observed and measured (Oke, 1982). In-situ air temperature (Tair or Ta) records are typically used to examine AUHI, and land surface temperature (LST) data is used to reveal the spatiotemporal pattern of SUHI (Figure 1).

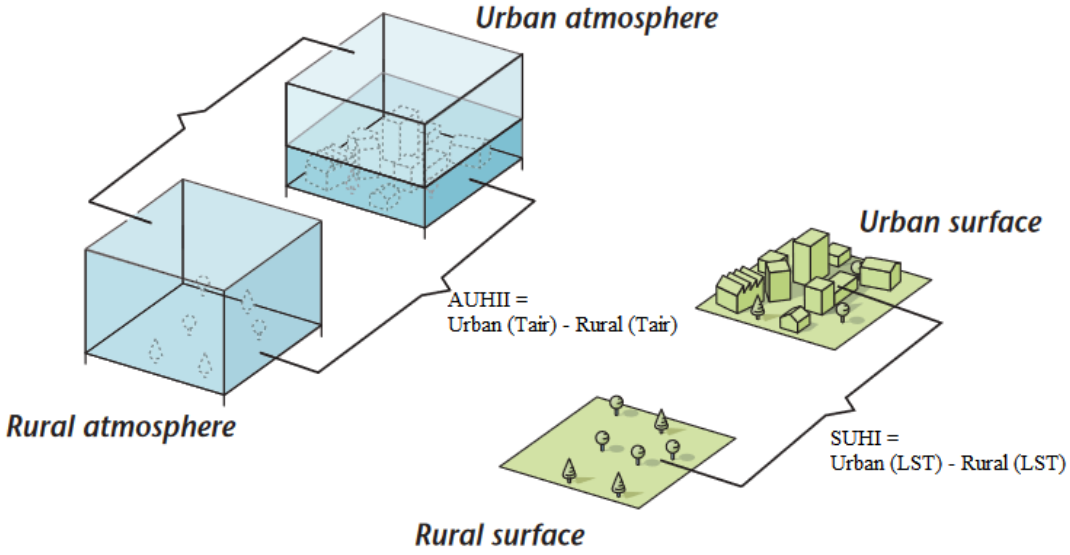

Figure 1 - Temperature differences forming the two principal types of intensity of UHIs: atmospheric urban heat island intensity (AUHII) and surface urban heat island intensity (SUHII). Adapted from Oke et al., (2017).

In-situ observations, either by fixed weather stations or mobile traversing, are valuable in defining actual ground conditions (Hu et al., 2016), however a change in location/instrumentation, as well as inadequate coverage, can complicate their use (Wang et al., 2007). To overcome these possible issues, land surface temperature (LST) data from airborne and earth observing satellites is commonly employed in UHI studies.

2.3 The remote sensing applications to SUHIs studies

Remote sensing can be understood as a set of activities that enables the acquisition of information from objects comprising the Earth's surface without the need for direct contact with them (Liu, 2015). These activities involve the detection, acquisition, and analysis (interpretation and extraction of information) of electromagnetic radiation emitted or reflected by terrestrial objects and recorded by remote sensors. According to Liu (2015), the quantity and quality of electromagnetic energy reflected and emitted by terrestrial objects result from interactions between electromagnetic energy and these objects. These interactions are determined by the physical, chemical, and biological properties of these objects and can be identified in remote sensor images and data. It allows for quantifying the spectral energy reflected and/or emitted by them, thus evaluating their key characteristics. Therefore, remote sensors are indispensable

tools for conducting inventories, mapping, and monitoring of natural resources. Characterization and monitoring of natural resources with the aid of remote sensing are often carried out by obtaining vegetation indices such as the Normalised Difference Vegetation Index (NDVI) (Rouse et al., 1973), Soil-Adjusted Vegetation Index (SAVI) (Huete, 1988), Enhanced Vegetation Index 2 (EVI2) (Jiang et al., 2008; Zhang, 2015), and Leaf Area Index (LAI) (Miller, 1997). In turn, evolutionary patterns of land use and land cover can be quantified with the help of indices such as the NDBI (Zha et al., 2003) and even classifications of land cover types and land use, as employed with Landsat data in the study by Souza et al. (2020).

The sensors on satellites also effectively provide surface temperature values from local to global scales (Moazzam et al. 2022) and can serve as a tool in characterizing the SUHIs. Several sensors provide global scale surface temperature data that are accessible for research, such as the Thermal Infrared Sensor 2 (TIRS-2) on the Landsat series, the Advanced Very High-Resolution Radiometer (AVHRR), and the Moderate Resolution Imaging Spectroradiometer (MODIS) aboard the Terra and Aqua platforms.

Satellite remotely sensed data helped to identify driving factors and spatial-temporal land-use changes of cities which includes urbanisation and economic growth along with policy guidelines and environmental measures (Samal and Gedam, 2015; Yang et al., 2019). Moazzam et al. (2022) demonstrated through a land use and land cover classification that the highest temperature in Jeju Island (Republic of Korea) was observed for the urban class. However, the forest cover and water body had the lowest temperature in the island. Similar results were detected in the study of Arshad et al. (2022) that showed that large green spaces exhibit 1 to 4ºC lower land surface temperature (LST) compared to their surrounding built-up land in a metropolitan city of Pakistan. Khamchiangta and Dhakal (2020) and Dewan et al. (2021) emphasized that the changing trends of LST tends to be increasing while the vegetation tends to be declining. Peng et al. (2012) attested that the daytime surface urban heat island intensity (SUHII) was higher that nighttime in 419 global cities and that the driven factors of SUHII differed according to the climate zone of the cities. The same result was observed for Si et al. (2022) with the use of 1711 cities around the world, during 2003-2019. Chakraborty and Lee (2019) found that the variability of SUHII is higher in equatorial zones and lower in arid zones and L. Li et al. (2023) discovered that the impacts of urbanization on SUHIs trends are larger in humid climates that characterized by dense vegetation and high precipitation.

Some studies carried out in Brazil have also applied remote sensing data to analyse the relationship between SUHIs and different land use and land cover types, vegetation presence, and urban areas (Flores R. et al., 2016; Santos et al., 2017; Peres et al., 2018; Silva et al., 2018; Correia Filho, 2019; Portela et al., 2020; Nascimento et al., 2022; De Souza e Silva et al., 2022), and surface albedo (Monteiro et al., 2021). Among these studies, Santos et al. (2017) found a positive correlation between LST and NDBI for the city of Vila Velha, Espírito Santo. Furthermore, on a local scale, Flores R. et al. (2016), Filho et al. (2019) and Portela et al. (2020) highlighted that the replacement of green areas, quantified by the NDVI, by residential and commercial areas contributed to the growth of SUHII in their respective studied cities. Only the study by Monteiro et al. (2021) was conducted on a national scale, encompassing different cities, and revealed substantial differences between daytime and nighttime SUHIIs.

The vast majority of these studies have utilized these techniques in Geographic Information System (GIS) platforms, which are still commonly used and require considerable computational demand for processing such data, as they often involve extensive files and images that occupy a large computational memory. To address such issues, these techniques can be easily adopted in the Google Earth Engine (GEE) geospatial analysis platform, which provides access to a vast amount of remote sensing, climate, and other data exclusively in the cloud, thus eliminating the need for a greater computational demand from the user's machine, with planetary-scale analysis capabilities. Scientists, researchers, and developers use GEE to detect changes, map trends, and quantify differences on the Earth's surface.

These geospatial approaches have shown a strong potential for rapid monitoring of urban expansion and devising effective policies to mitigate its environmental impacts and ensure sustainable urban development. But to understand the formation of SUHIs and mitigate its effects, it is also important to have insights about the surface energy balance dynamics.

2.4 Simplified surface energy budget (Rn and α)

The surface energy balance (SEB) is the fundamental starting point to understand and predict surface microclimates. The SEB is affected by the specific characteristics of Earth’s surface, such as the presence or absence of vegetation and local topography (Christopherson and Birkeland, 2017; Chrysoulakis et al., 2018). The surface in any given location that receives and loses shortwave (SW) and longwave energy (LW) and that balance between incoming

(downwelling) and outgoing (upwelling) these two types of radiation at the surface is defined as net radiation (Rn) (Ferreira et al., 2020) and can be represented by the Equation 1 and illustrated by the Figure 2:

$$Rn = +SW_{insolation} \downarrow - SW_{reflection} \uparrow + LW_{infrared} \downarrow - LW_{infrared} \uparrow \quad (1)$$

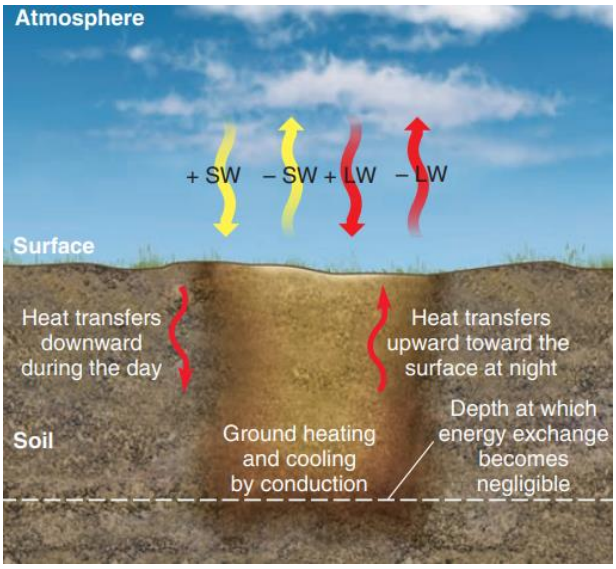

Figure 2 - Idealized input and output of energy at the surface within a column of soil (SW = shortwave, LW = longwave) (Christopherson and Birkeland, 2017).

Heat is transferred by conduction through the soil, predominantly downward during the day and toward the surface at night (Figure 2). This part of the energy is represented by the ground heating and cooling flux (G). On the other hand, energy moving from the atmosphere into the surface is reported as a positive value (gain), and energy moving outward from the surface, through sensible (H) and latent heat (LE) transfers, is reported as a negative value (loss) in the surface account. LE is the energy that is stored in water vapor as water evaporates. Water absorbs large quantities of this LE as it changes state to water vapor, thereby removing this heat energy from the surface. Conversely, this heat energy releases to the environment when water vapor changes state back to a liquid. And H is the heat transferred back and forth between air and surface in turbulent eddies through convection and conduction within materials.

According to Oke et al. (2017) the ratio of the two turbulent heat flux densities H / LE, known as the Bowen ratio (β), is significant to a surface climate. If $\beta > 1$ it indicates that the surface or system channels more heat into sensible form, which warms the lower atmosphere

whereas and the surface, if $\beta < 1$ latent heat dominates, which keeps the surface and near-surface air cooler, whilst it adds humidity to the environment.

Energy gains include shortwave from the Sun (both diffuse and direct) and longwave that is reradiated from the atmosphere after leaving Earth. Energy losses include reflected shortwave and Earth's longwave emissions that pass through to the atmosphere and space (Christopherson and Birkeland, 2017). The amount of energy losses from shortwave depends on the coefficient of reflection of incident shortwave radiation, referred to as surface albedo (α) and its variability can induce changes in non-radiant fluxes (e.g., latent, and sensible heat) within the energy balance, as well as in the surface temperature (Chen et al., 2004).

In the urban areas, surface albedo varies with complex urban morphologies (e.g., block shapes, plan density, facade density, building height, and layout orientation) and other factors (e.g., latitude and time) (Groleau et al., 2013), and the average urban surface albedo is the lowest for a medium-density city with high-rise buildings presenting greater building height differences (Yang and Li, 2015). It seems to be an effective solution to increase urban surface albedo using reflective materials, which can offset anthropogenic heat emissions in urban areas (Yuan et al., 2015; Morini et al., 2017). Modelling experiments to calculate the UHI in Sacramento, United States, by Taha (2008) indicates that increasing surface albedo does have a significant impact on the daytime SUHI but little influence on the nocturnal SUHI. The land cover change that causes the surface albedo changes is dominated by a replacement of croplands, savannas, and grasslands with urban lands (Ouyang et al., 2022).

Figure 3 illustrates the surface energy components for a typical summer day at a midlatitude location (Christopherson and Birkeland, 2017). Daily, Rn values are positive during the daylight hours, peaking just after noon with the peak in insolation; at night, values become negative because the shortwave component ceases at sunset and the surface continues to lose longwave radiation to the atmosphere. The surface rarely reaches a zero Rn value (a perfect balance) at any one moment.

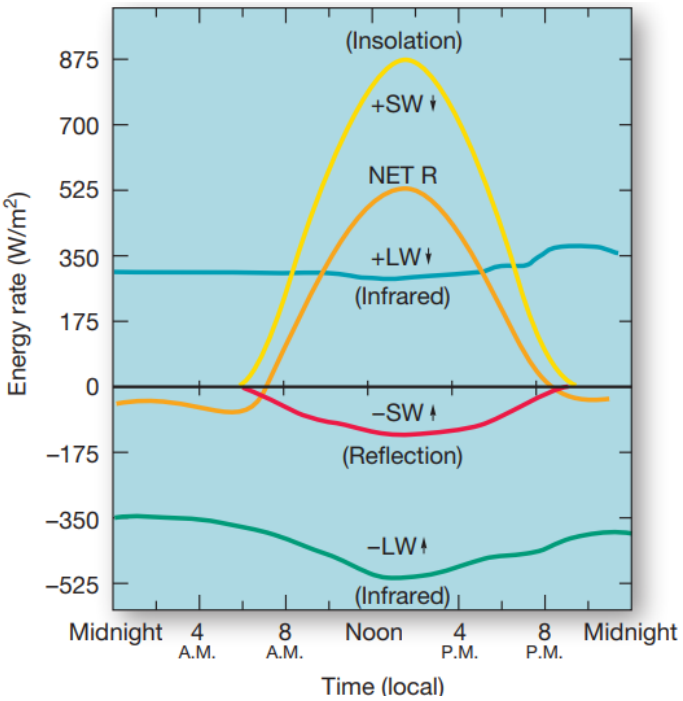

Figure 3 - Daily radiation budget on a typical summer day in Matador in southern Saskatchewan, Canada (Christopherson and Birkeland, 2015).

Satellite imagery has been widely used to determine Rn from field to regional scales, and over heterogeneous areas (Bisht et al., 2005; Allen et al., 2007; Ryu et al., 2008; Bisht and Bras, 2010; Silva et al., 2011; Silva et al., 2015). Many algorithms have been defined to quantify the downwelling shortwave radiation (Zillman, 1972; Allen et al., 2007), downwelling longwave radiation (Sugita and Brutsaert, 1993; Prata, 1996; Bastiaanssen et al., 1998; Duarte et al., 2006; Allen et al., 2007; Kruk et al., 2010; Santos et al., 2011), longwave radiation, and radiative properties (Tasumi, 2003; Muñoz-Jiménez et al., 2006; Tang and Li, 2008; Teixeira et al., 2009).

2.5 The key role of vegetation cover

In addition to the net radiation balance (Rn) and surface albedo (α), other biophysical parameters are important in analysing urban microclimate and their potential to change the SUHIs effects, including the assessment of vegetation patterns in the urban environment. Trees in urban areas can mitigate the SUHIs effect, especially locally, for example by shading surfaces and people (Figure 4).

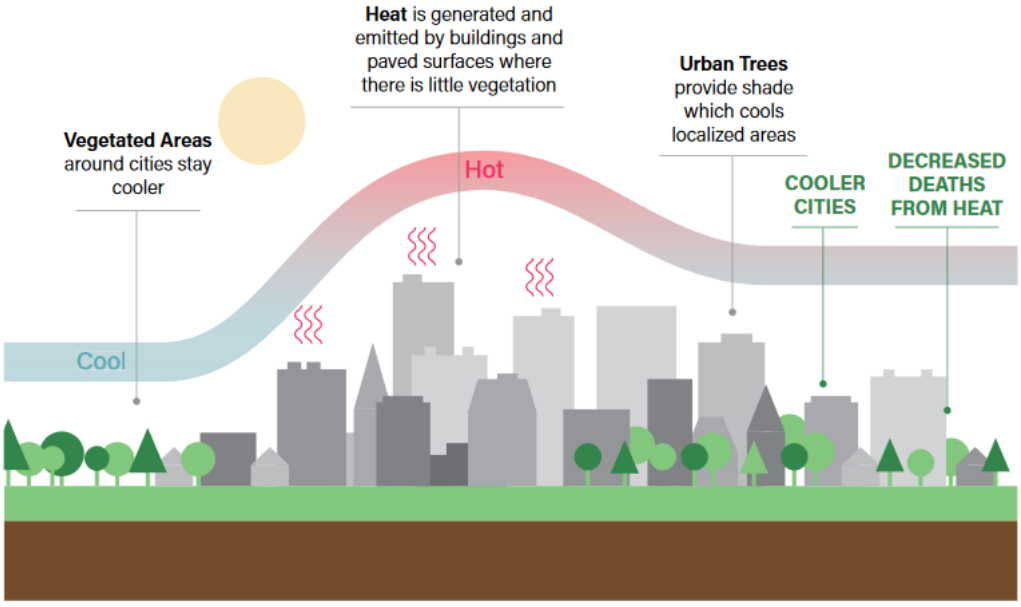

Figure 4 - The potential of vegetation in mitigating heat in the urban environment. Adapted from McDonald et al. (2015).

Shade makes heat more tolerable and can protect people from excessive sun exposure during travel, work, or leisure (Nowak and Dwyer, 2007). Trees that shade buildings can reduce surface temperatures in a wide variety of contexts (Wang et al., 2014). For example, surface temperatures were reduced by 11°C–25°C in Sacramento, California (Akbari et al., 1997); by 5°C–7°C in Akure, Nigeria (Morakinyo et al., 2013), and by 9°C in Melbourne, Australia (Berry et al., 2013).

During the day, trees may create lower air temperatures by releasing water into the air as they photosynthesize (Bowler et al., 2010; Säumel et al., 2016). As water vapor is released, it takes with it some of the ambient heat. Large trees with ample access to water may evaporate more than 100 litres of water in a single day, which dissipates about 70 kilowatt-hours (kWh) of solar energy that would otherwise remain stored in the urban environment (Fath, 2018).

Various remote-sensing studies have emphasized that key role that vegetation plays with the quantification of vegetation indexes (Santos et al., 2017; Chakraborty and Lee, 2019; Portela et al., 2020; Dewan et al., 2021). Satellite vegetation index (VI) products are commonly used in that application that aim to monitor and characterize the vegetation cover in urban environment. Some authors even state that the patterns of built-up land and vegetation have the largest impact on urban LST (Yang et al., 2017).

Gallo et al. (1993) explored the relationship between SUHIs and NDVI for the first time, which still constitutes one of the major indicators to measure the LST-vegetation relationship. Weng et al. (2004) introduced the vegetation fraction, which is an alternative indicator of vegetation to SUHI research. They found that the vegetation fraction possessed a slightly stronger relationship with LST than NDVI in urban areas. Dewan et al. (2021) characterized vegetation with Enhanced Vegetation Index (EVI) and showed a consistently negative relationship with day and nighttime SUHIs.

A good parameter to assess the spatial and temporal variability of vegetation in urban areas is crucial and Jiang et al. (2008) showed an alternative to quantify the EVI-2 without the blue band from remote satellite sensors. They developed and evaluated that index with global and local scale MODIS data, showing that EVI-2 can used to substitute the original EVI for good observations (Jiang et al., 2008).

It is important to mention that the effectiveness of vegetation in mitigating SUHIs can vary depending on factors such as vegetation density, plant types, ground cover, and other factors. Sustainable urban planning should consider the incorporation of green spaces and appropriate use of vegetation as essential strategies to mitigate the effects of SUHIs and enhance thermal comfort in cities.

2.6 The evapotranspiration process

The process of evapotranspiration (ET) can reduce both the risk of heat-related illness or death and increase the liveability of cities (Bowler et al., 2010; Mohajerani et al., 2017; Wolf et al., 2020). ET is the phenomenon by which water is converted from liquid into its vapor phase over land (Melo et al., 2021) composed by the plant transpiration and surface evaporation. It has an important role in the modulation of global climate feedback being a key driver of the Earth's carbon, energy, and water cycles at local, regional, and global scales (Tong et al., 2017; Khosa et al., 2019; Valle Júnior et al., 2020).

Quantifying ET is one of the largest research challenges in hydrology because ET is driven by a complex combination of atmospheric, vegetation, edaphic, and terrain characteristics (Wang et al., 2016; Bhattarai et al., 2017), and this complexity is also present in the urban areas. While the important role of ET in regulating the urban thermal environment is well known, the spatial characteristics of ET's cooling effect and its quantification at a regional scale are rarely studied (Wang et al., 2020). This is mainly due to the challenges of measuring

and modelling ET in urban areas with highly heterogeneous surfaces. Urban ET is a large physical process that depends on various key drivers, including air temperature, solar radiation, land cover types, building and street orientations, and radiative shade dynamics, along with landscape type, end-user aesthetical preference, and landscape affordability (Saher et al., 2021).

Current, most studies on regional-scale ET have employed remote sensing data with corresponding surface energy balance (SEB) models or the Penman–Monteith (PM) (Vahmani et al., 2014; Wang et al., 2016; Zhang et al., 2017; Zhang et al., 2018; Wang et al. 2020; Rocha et al., 2022). Wang et al. (2020) quantified the ET in urban areas of Xuzhou (China) using Landsat 8 data for the period of 2014-2018 and showed that the relationship of ET and LST was significantly negative during the warmer months of the year but during the colder months, there was no significant correlation. Their findings provide a new perspective for the improvement of urban thermal comfort, which can be applied to urban management, planning, and natural design. Rocha et al. (2022) provided a method for mapping spatially and temporally high-resolution ET for Berlin (Germany) to support actions to mitigate UHIs and severe heat waves.

These existing models have the potential to improve the estimation of urban ET, especially mapping the process and correlating with the urban expansion and the variability of LST in urban lands. The ET estimation have a great potential to address the thermal effects of urban surfaces. The substitution of natural lands and plant cover for sealed surfaces brings the reduction of the cooling effect of evaporation and plant transpiration, situation that can be evaluated with the quantification of ET.

3 STUDY AREA

This study focused on twenty-one Brazilian metropolitan regions (MRs) (Figure 5) distributed throughout different Brazilian biomes (Figure 5a): Amazon Forest (rainforest, 49% of land area), Caatinga (xeric shrubland, 10% of the land area), Cerrado (wooded savannah, 24% of land area), Atlantic Forest (several variations of forest, 13% of land area), and Pampa (grassland, 2% of the land area) (Roesch et al., 2009). The analysed MRs were: Manaus, Belém, and São Luís in Amazon; Natal, João Pessoa, Recife, Maceió, Salvador, Vitória, Belo Horizonte, Campinas, São Paulo, Rio de Janeiro, Santos, Curitiba, and Florianópolis in Atlantic Forest; Fortaleza in Caatinga; Teresina, Goiânia, and Distrito Federal in Cerrado; and Porto Alegre in Pampa. Each MR has a population of over one million inhabitants, according to the census from the Brazilian Institute of Geography and Statistics (IBGE) in 2022, with the number of inhabitants ranging from 1,249,822 (Teresina) to 20,743,587 million (São Paulo) (IBGE, 2022).

Manaus (MA), Belém (BE), and São Luís (SL) in Amazon hold tropical humid (Af), tropical monsoon (Am), and tropical with dry summer (As) climates, respectively (Alvares et al., 2013). These climate classifications in the Amazon biome are characterised by annual elevated temperatures (27ºC, on average), high air humidity (75%, on average), and abundant rainfall (2500 mm, on average). The metropoles located in the Atlantic Forest biome feature a diverse range of climates, with Natal (NA), João Pessoa (JP), Maceió (MAC), Vitória (VI), Santos (SAN), and Rio de Janeiro (RJ) holding a tropical climate with dry season in the summer (As), while Recife (RE) and Salvador (SA) possess a tropical monsoon (Am) climate. On the other hand, São Paulo (SP) and Curitiba (CU) have a subtropical climate with tempered summer (Cfb), while Belo Horizonte (BH) has a subtropical climate with dry winter and tempered summer (Cwb), and Campinas (CAM) and Florianópolis (FLO) hold a subtropical climate with hot summer (Cfa). Fortaleza (FO), in the Caatinga biome, is characterised by a tropical climate with a dry season in the summer (As). Teresina (TE), Goiânia, and Distrito Federal (DF), located in the Cerrado biome, have a tropical climate with a dry season in the winter (Aw), whose mean air temperatures remain constantly high throughout the year (i.e. higher than 35ºC). Located in the Pampa biome, Porto Alegre (PA) has a subtropical climate with a hot summer (Cfa), with a dominant presence of low mean air temperatures in the winter season, ranging from 0 to 22 ºC (Alvares et al., 2013).

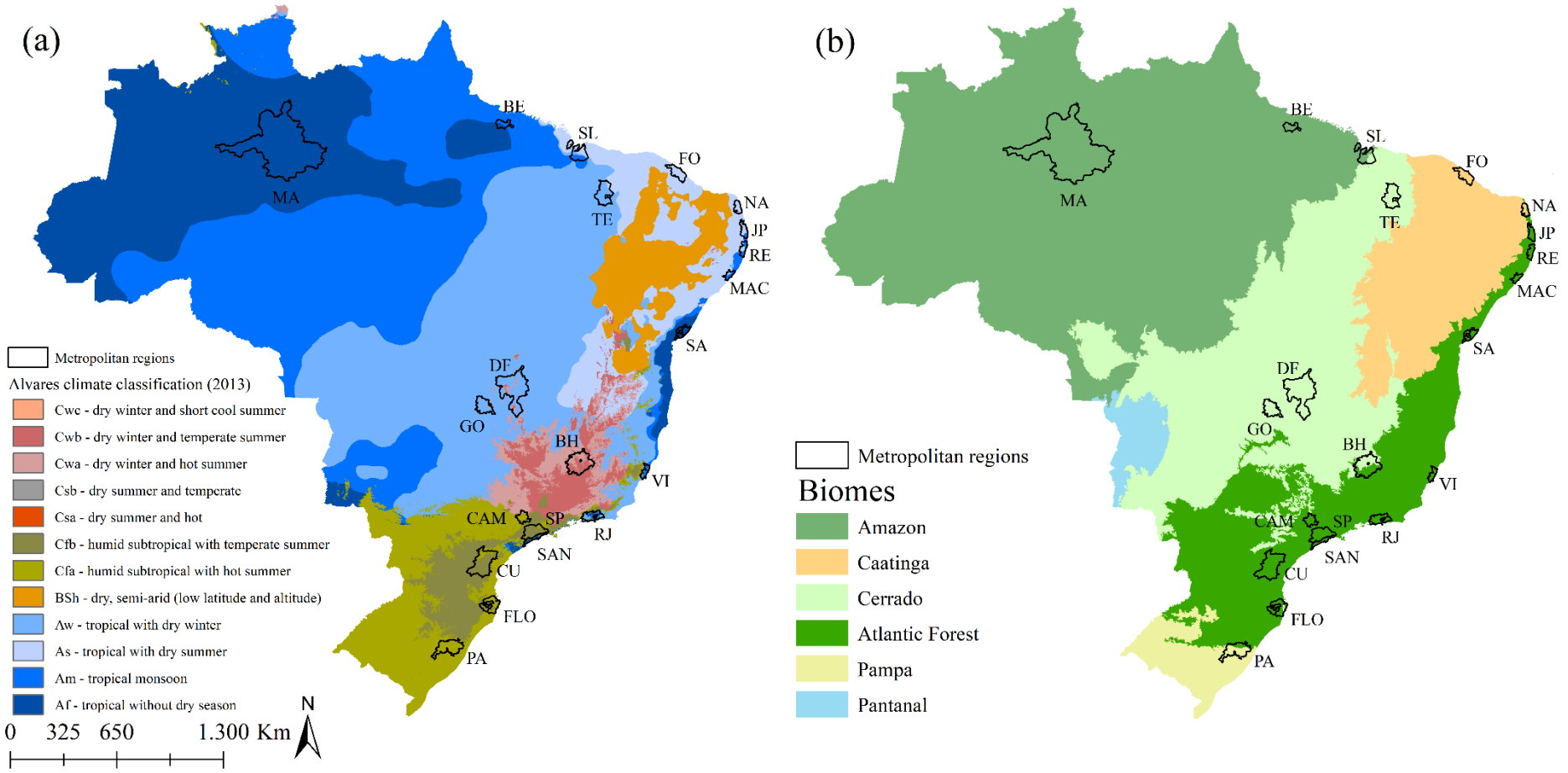

Figure 5 - Spatial distribution of the analysed metropolitan regions according to (a) the different Köppen's climate classification defined by Alvares et al. (2013) for Brazil and (b) the Brazilian biomes (IBGE, 2022).

4 MATERIAL AND METHODS

This study analysed the spatial-temporal variability of SUHIIs between 2003 and 2022. In order to investigate the impacts of the urbanisation process on the formation of SUHIs (objective i) and (ii) to assess the variations of the controlling surface biophysical parameters (objective ii), the following steps were applied (Figure 6): (a) delimitation of urban areas and their spatial-temporal variability; (b) estimation of SUHIs intensities (SUHIIs); (c) quantification of biophysical parameters; (d) analysis of temporal trends; and (e) statistical analyses of the relationship between urban areas, urban LST, and biophysical parameters. All data used in this study is summarised in Table 2 and its available on the Google Earth Engine (GEE) platform, the tool used in this research application. GEE is a geospatial analysis platform that utilizes JavaScript programming language and combines a multi-petabyte catalog of satellite imagery and geospatial datasets with planetary-scale analysis capabilities. The methodological steps are described in detail in the next items of this section.

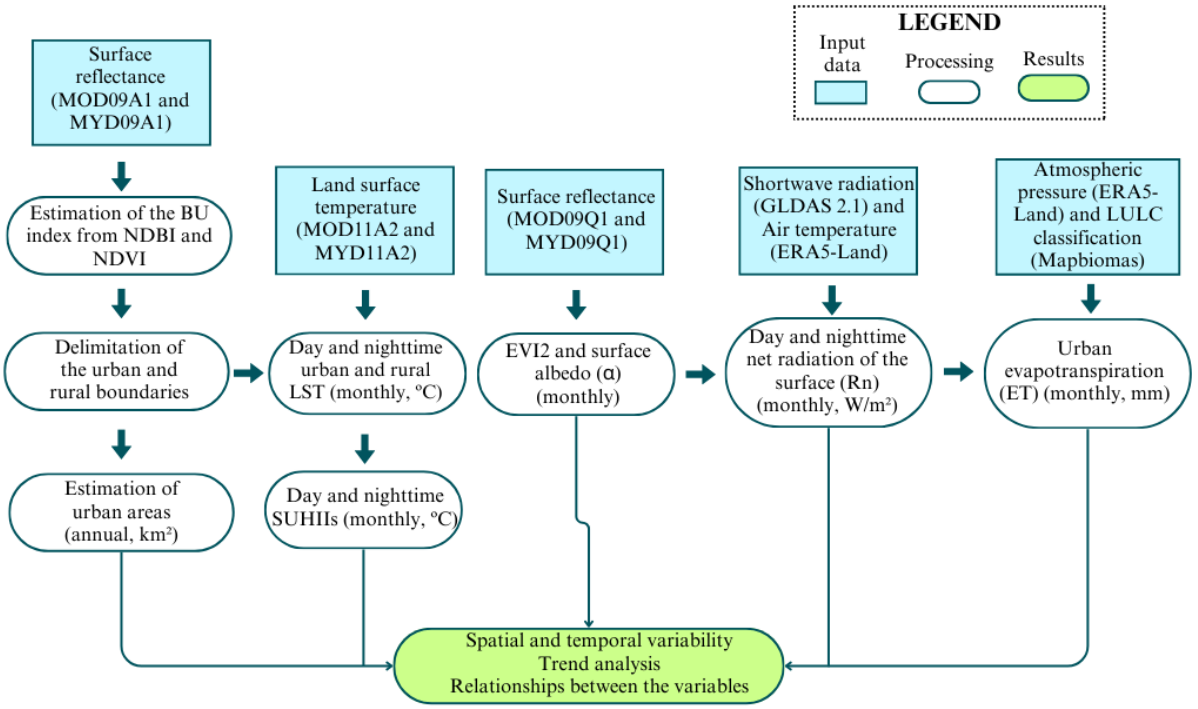

Figure 6 - Analytical techniques applied in the study. The inputs are represented for the identification products and the outputs are the variables cited.

Table 2 - Description of the datasets used in the research

Product	Bands/applied variables	Time coverage	Spatial Resolution	Temporal Resolution	Results
MOD11A2 MYD11A2	Day and nighttime land surface temperature (ºC)	2000-present	1 km	8 days	SUHIIs
MOD09Q1 MYD09Q1	RED – surface reflectance (620-670 nm); NIR – surface reflectance (841-876 nm)	2000-present	250 m	8 days	Surface albedo Vegetation index
MOD09A1 MYD09A1	SWIR - surface reflectance (1628-1652 nm)	2000-present	500 m	8 days	Urban areas
GLDAS 2.1	short-wave radiation flux (W/m²)	2000-present	27,83 km	3h	Net radiation Evapotranspiration
ERA5-Land	air temperature (ºC) surface pressure (kPa)	1981-present	11,13 km	1h	Net radiation Evapotranspiration
Mapbiomas Collection 7	LULC classification	1985-2021	30 m	Yearly	Canopy conductance and plant transpiration

4.1 Growth of urban areas (UAs)

The growth of the metropolitan regions over the last two decades was annually analysed through the use of the built-up index (BU; Zha et al., 2003), which allows distinguishing built and non-built surfaces using the NDBI (Normalised Difference Built-Up Index) and the NDVI (Normalised Difference Vegetation Index), as follows:

$$\mathrm{BU} = \mathrm{NDBI} - \mathrm{NDVI} \quad (2)$$

The NDBI (Zha et al., 2003) and NDVI (Rouse et al., 1973) were calculated by Eqs. 3 and 4, respectively:

$$\mathrm{NDBI} = \frac{\mathrm{SWIR} - \mathrm{NIR}}{\mathrm{SWIR} + \mathrm{NIR}} \quad (3)$$

$$\mathrm{NDVI} = \frac{\mathrm{NIR} - \mathrm{RED}}{\mathrm{NIR} + \mathrm{RED}} \quad (4)$$

where SWIR, NIR, and RED correspond to the surface reflectance in the shortwave infrared, near-infrared, and red wavelengths, respectively, detected by the Moderate-Resolution Imaging Spectroradiometer (MODIS) sensor on board the Terra and Aqua satellites, provided by the MOD09Q1 (NIR and RED bands), MYD09Q1 (NIR and RED bands), MOD09A1 (SWIR band), and MYD09A1 (SWIR band) products. Both MOD09Q1 and MYD09Q1 products have a spatial resolution of 250 m, while the MOD09A1 and MYD09A1 products have a spatial resolution of 500 m. For each pixel of all reflectance products used to calculate the BU, a value is selected from all the acquisitions within the 8-day composite period, mainly based on lower view angles and the absence of clouds. Overall, 3,678 images from these reflectance products were used, corresponding to all the images available in the period from 2003 to 2022. It is important to mention that the NDVI and NDBI scales range from -1 to +1. Therefore, the BU scale is virtually between -2 and 2, where only pixels with BU > -0.5 are classified as urban areas (UAs), as also defined by Zha et al. (2003).

4.2 Estimation of surface urban heat island intensities (SUHIIs)

Land surface temperature (LST) data, obtained from the thermal infrared bands of MODIS sensors, were used to analyse the temporal (monthly and annual) and spatial variability of SUHIIs during the day and nighttime. SUHII was estimated by evaluating the difference between the average temperatures of the urban and the surrounding rural areas. The BU index was used to set the boundary between urban and rural areas, using a buffer of 2 km around the urban areas to delineate the rural area boundaries for calculating the SUHIIs, similar to Li and Zha (2019), Suomi et al. (2012), Tian et al. (2021), Xian et al. (2021), and Zhou et al. (2014).

MODIS sensors onboard the Terra (data obtained at 10:30 a.m. and 10:30 p.m.) and Aqua (data obtained at 1:30 a.m. and 1:30 p.m.) platforms can provide LST from 2003. The daytime and nighttime data from MOD11 products present quality control (QC) bands indicating the reliability and conditions of measurements performed by the sensors (Wan et al., 2021). Such bands can be used to identify pixels affected by clouds and temperature errors, which consist of binary (bit) information where each bit has a specific meaning. Based on this, the LST data were filtered to use only pixels with error estimates less than or equal to 3 K, allowing a focus on areas of interest with higher reliability (Chakraborty and Lee, 2009). In the frame of this

study, 920 and 919 images of the MOD11A2 (Terra) and MYD11A2 (Aqua) products, respectively, were used, which similarly to the surface reflectance products, consist of pixels with the best observations within an 8-day period, containing LST with 1 km spatial resolutions. Similarly, to Chakraborty and Lee (2019) and Li et al. (2022), we removed from the analysis the pixels corresponding to water bodies due to their cooling capacity, which, consequently, can influence the average estimation of LST in the metropolitan regions. The selection of pixels corresponding to water bodies was based on the collection 7 of the annual land use and land cover (LULC) classifications provided by Mapbiomas, a Landsat-based project that makes available twenty-seven LULC classes at a 30-m spatial resolution for the Brazilian territory from 1985 to the present (Souza et al., 2020).

The reason for conducting the urban heat island analysis at the metropolitan region level rather than at the neighbourhood or smaller areas within cities is primarily due to the moderate spatial resolution of the MODIS Land Surface Temperature (LST) product. Additionally, the study limited itself to this product for quantifying LST because it provides greater temporal coverage, ensuring a more suitable analysis of time series data.

4.3 Variability of biophysical parameters

4.3.1 Vegetation greenness

In order to assess the vegetation greenness at the monthly and annual scales, we determined the Enhanced Vegetation Index 2 (EVI2) (Jiang et al., 2008; Zhang, 2015; Eq. 5):

$$\mathrm{EVI2} = 2.5 \text{ x } \frac{\mathrm{RED} - \mathrm{NIR}}{\mathrm{NIR} + 2.4\mathrm{RED} + 1.0} \quad (5)$$

To obtain the EVI2, 1,839 images of the MOD09Q1 and MYD09Q1 products were used, where the RED and NIR (near-infrared) bands are available. To address the shortcomings related to cloudy conditions, we carried out monthly map compositions based on the selection of pixels with the higher values of EVI2 obtained from the eight images available per month (i.e. four MOD09Q1 and four MYD09Q1), assuming that lower or negative values of EVI2 were possibly contaminated by clouds. The EVI2 scale ranged from 0 to 1, with the remaining negative values being considered water bodies and, therefore, excluded from the spatialisation.

4.3.2 Surface albedo

To estimate the monthly and annual variations of surface albedo (α), the same reflectance products used to obtain the EVI2 were utilised, according to the model proposed by Teixeira et al. (2013; 2014) (Eq. 6):

$$\alpha = a + bRED + cNIR \quad (6)$$

where a, b, and c are the regression coefficients calibrated for each Brazilian biome. These coefficients were obtained through the comparison between remote sensing and field measurements of five well-distributed flux towers across the country, located in different Brazilian biomes (Claudino et al., 2024; Table 3). Similarly, to EVI2, we carried out monthly map compositions with the 8-day images of α to also address the shortcomings related to cloudy conditions. Only the lower value of α per pixel, from the eight images available per month (i.e. four MOD09Q1 and four MYD09Q1), were considered, assuming that higher values of surface albedo resulted from cloud contamination.

Table 3 - Regression coefficients used to estimate the surface albedo (α) for each Brazilian biome and, consequently, each metropolitan region.

Brazilian biome	Metropolitan Regions	a	b	c
Atlantic Forest	Natal, João Pessoa, Recife, Maceió, Salvador, Vitória, Rio de Janeiro, Belo Horizonte, São Paulo, Santos, Campinas, Curitiba, and Florianópolis	0.156	-0.099	0.103
Amazon	Manaus, Belém, and São Luís	0.118	-0.016	0.016
Caatinga	Fortaleza	0.08	0.41	0.14
Cerrado	Teresina, Goiânia, and Distrito Federal	0.124	-0.009	0.043
Pampa	Porto Alegre	0.139	-0.125	0.192

4.3.3 Net radiation of the land surface (Rn)

Rn is the result of the balance between the incoming (positive flux) and outgoing (negative flux) short- and long-wave radiation at the Earth's surface (Ferreira et al. 2020). Rn influences other surface energy balance components (e.g. evapotranspiration, photosynthesis, and heating of air and soil). Therefore, quantifying Rn in the urban environment is significant

for the analysis because it can influence the LST variations in urban areas. The daily daytime (i.e. considered for solar radiation > 10 W/m^2 in this study; Mu et al., 2011) and nighttime Rn were computed in this study through the method proposed by Cleugh et al. (2007) (Eq. 7):

$$\mathrm{Rn} = (1 - \alpha)\mathrm{S} + \sigma(\varepsilon_a - \varepsilon_s)(273.15 + \mathrm{T_a}) \quad (7)$$

where ε_s is the surface emissivity, S the shortwave radiation reaching the surface (W/m^2) obtained from the Global Land Data Assimilation System version 2.1 (GLDAS 2.1; Rodell et al., 2004), σ (W m^{-2} K^{-4}) is Stefan-Boltzmann constant, $\mathrm{T_a}$ is the air temperature (ºC) obtained from the European Centre for Medium-Range Weather Forecasts Reanalysis version 5 (ERA5-Land; Muñoz Sabater, 2019), and ε_a is the atmospheric emissivity (Eq. 8):

$$\varepsilon_a = 1 - 0.26\exp\left(7.77 \cdot 10^{-4}\mathrm{T_a}^2\right) \quad (8)$$

ε_s was estimated using Eq. 9:

$$\varepsilon_s = 0.95 + 0.01\mathrm{LAI} \quad (9)$$

where LAI is the Leaf Area Index (Eq. 10; Miller, 1997). For pixels with LAI > 3 or NDVI < 0, ε_s were set as 0.98 and 0.99, respectively.

$$\mathrm{LAI} = -\frac{\ln\left(\frac{0{,}69 - \mathrm{SAVI}}{0{,}59}\right)}{0{,}91} \quad (10)$$

where SAVI represents the Soil-Adjusted Vegetation Index (Huete, 1988), calculated using the surface reflectance from RED and NIR bands (Eq. 11).

$$\mathrm{SAVI} = \frac{(1 + \mathrm{L})(\mathrm{RED} - \mathrm{NIR})}{(\mathrm{L} + \mathrm{RED} + \mathrm{NIR})} \quad (11)$$

where L corresponds to the soil adjustment factor, fixed as 0.2 in this study (Allen et al., 2002).

4.3.4 Actual evapotranspiration (ET)

Actual evapotranspiration (ET) corresponds to the combined process of water evaporation from surfaces and transpiration from plants (Mu et al., 2011), playing a crucial role in regulating

the LST and the energy balance in urban areas. We estimated ET based on the logic of the Penman-Monteith equation (Monteith, 1965), similar to Mu et al. (2011) to create the global MOD16 ET product made available by NASA (National Aeronautics and Space Administration). Currently, the MOD16 dataset provides global ET information at a 500 m spatial resolution and three temporal scales: 8-day, monthly, and annual.

Unlike the original MOD16 dataset, we followed the adaptations proposed by Claudino et al. (2024), which include a cloud cleaning procedure and the application of more fine-tuned LULC (Mapbiomas project) and meteorological (ERA5-Land and GLDAS 2.1) information for Brazil to provide daily ET data with 250-m spatial resolution, the so-called ESTIMET (Evaluation and Spatial-Temporal Improvement of MODIS Evapotranspiration). The cloud cleaning procedure of ESTIMET consists of the adoption of monthly compositions of biophysical parameters as input of the model, similar to the described in this study to estimate LAI, EVI2, and α. The daily ET was then calculated based on Eq. 12, assuming daily ET as the sum of daytime and nighttime components (Mu et al., 2011):

$$\lambda ET = \lambda E_{wet\,c} + \lambda E_{trans} + \lambda E_{soil} = \frac{s\,A\ + \rho\,C_p\,\frac{(e_{sat} - e_a)}{r_a}}{s + \gamma\,\left(1 + \frac{r_s}{r_a}\right)} \quad (12)$$

where λET is the latent heat flux density (W/m^2), consisting of the evaporation from the wet canopy of vegetation ($\lambda E_{wet\,c}$), plant transpiration (λE_{trans}), and soil evaporation (λE_{soil}), converted to daily ET (mm dia^{-1}) after multiplying by the conversion factor (3.53×10^{-2} mm d^{-1} W^{-1} m^2). A is the available energy determined from the daily net radiation of the land surface (Rn) in W/m^2 and calculated as Eq. 6, s is the slope (kPa $°C^{-1}$) of the curve relating saturated water vapour pressure (e_{sat}) to temperature, ρ is the air density (1.2 kg m^{-3}), C_p is the specific heat capacity of air at constant pressure (1005 J kg^{-1} $^oC^{-1}$), r_a is the aerodynamic resistance (s m^{-1}), r_s is the surface resistance (s m^{-1}), e_a is the actual water vapour pressure (kPa), e_{sat} is the saturated water vapour pressure to the temperature (kPa $^oC^{-1}$), and γ is the psychometric constant (kPa $^oC^{-1}$).

4.4 Spatiotemporal analysis and statistical metrics

The spatiotemporal patterns of the estimated variables were obtained based on their averages over 5-year periods within the historical series (i.e. 2003-2007, 2008-2012, 2013-

2017, and 2018-2022). To assess the presence of statistically significant trends in the twenty years series of data, the non-parametric Mann-Kendall test (Mann, 1945; Kendall, 1948) was applied at a significance level of 95% to all variables, and computed by Eq. 13:

$$S = \sum_{i=1}^{n-1} \sum_{j=i+1}^{n} \text{sign}(X_j - X_i), \text{sign}(X_j - X_i) = \{+1\ (X_j - X_i) > 0\ 0\ (X_j - X_i) = 0\ -1\ (X_j - X_i) < 0 \quad (13)$$

where n is the number of observations, X_i represents the observation at time i, X_j represents the observation at time j, and sign(x) is the sign function of x. The variance of S (Var(S)) and the standard normal statistic (Z) were computed from the Eq. 14 and Eq. 15, respectively:

$$\text{Var}(S) = \frac{n(n+1)(2n+5) - \sum_{i=1}^{m} ti(ti-1)(2ti+5)}{18} \quad (14)$$

$$Z = \{\frac{S-1}{\sqrt{\text{Var}(S)}}, S > 0\ 0, \quad S = 0\ \frac{S+1}{\sqrt{\text{Var}(S)}}, S < 0 \quad (15)$$

where n is the number of data, m is the number of tied groups and ti denotes the number of ties to the extent i. A tied group is a set of sample data having the same value. Positive values of Z indicated increasing trends, while negative Z values indicated decreasing trends. The corresponding p-value was also calculated to determine the statistical significance of the observed trends. Finally, the Theil-Sen slope (Sen, 1968) was used to estimate the slope of the found trends.

Historical averages of SUHII for each month of the year were obtained from the monthly time series to investigate the variability of SUHIs throughout the year in different cities, analysed according to the biome in which each MR is located. Pearson's correlation coefficient (r) (Eq. 16) was used to identify the relationship between the UA and the variability of urban LST, Rn, and ET. The same statistical parameter was used to assess the triggering factors of SUHIs, represented by the urban LST and its relationship with the analysed surface biophysical parameters (EVI2, surface albedo, Rn, and ET).

$$r = \frac{\sum (x_i - \underline{x})(y_i - \underline{y})}{\sqrt{\sum (x_i - \underline{x})^2 \sum (y_i - \underline{y})^2}} \quad (16)$$

where x_i is the value of the x variable, y_i is the value of the y variable, $\underline{x}$ is the mean of the x variable and $\underline{y}$ is the mean of the y variable. The values of r range from -1 to 1, with -1 indicating the strongest negative correlations and 1 indicating the strongest positive correlations. The reason for using urban LST instead of SUHIIs was to quantify the local problem of intensification of surface temperature within the urban boundaries, as performed by other studies (Tran et al., 2006; Zhou et al., 2020; Xian et al., 2021; Moazzam et al., 2022; Nascimento et al., 2022; Sfîcă et al., 2023).

The associations were also evaluated with the Determination Coefficient (R^2) and Kling-Gupta Efficiency (KGE) (Gupta et al., 2009) presented in Eqs. 17 and 18, respectively:

$$R^2(y, \hat{y}) = 1 - \frac{\sum_{i=1}^{n}(yi - \hat{y}i)^2}{\sum_{i=1}^{n}\left(yi - \underline{y}\right)^2} \quad (17)$$

$$KGE\,(y, \hat{y}) = 1 - \sqrt{(r-1)^2 + (\beta-1)^2 + (\delta-1)^2} \quad (18)$$

where y is the real values, $\hat{y}$ corresponds to predicted values, $\underline{y}$ represents the mean of the real values, n is the number of values, β is the ratio of quantified to predicted standard deviations and δ is the bias (i.e. the difference between the quantified and predicted means, normalised by the observed standard deviation). R^2 and KGE values vary from 0 to 1 and from -∞ to 1, respectively, whose results close to 1 represent that the modelled relationship is more explanatory. The populational data (e.g. total population and population density) from the last demographic census of IBGE in 2022 was used to evaluate the overall impact on the daytime and nighttime SUHIs.

5 RESULTS AND DISCUSSIONS

5.1 The country scale perspective: Regional contrasts of surface urban heat island intensities (SUHIIs)

The analysis of SUHIIs over the 2003-2022 period reveals that all MRs were subject to the SUHI effects, with values ranging from 0.08 ºC (JP) to 6.1 ºC (MA) in the daytime. For the nighttime, the values were between -0.24 ºC (FLO) and 2.71 ºC (MA and RE) (Figure 7). The Mann-Kendall test performed in the annual time series of daytime SUHII (Table 4) highlights the growth trends in seventeen MRs, of which nine exhibiting statistically significant growth trends, two located in Amazon (i.e. BE, and SL) and seven in Atlantic Forest (i.e. RE, JP, SA, VI, SAN, CU, and FLO; p-value < 0.05). Overall, the average value of SUHIIs during daytime was 1.64 ºC, i.e. 60% superior when compared to the nighttime estimations. This pattern of higher values during daytime was also identified by Dewan et al. (2021), Monteiro et al. (2021), and Chakraborty et al. (2019) in Bangladesh, Brazil, and the United States of America, respectively.

The analyses of daytime SUHIIs trend revealed that the highest and lowest growth rates were observed in the MRs of BE/RE (0.05 ºC/year) and MAC (0.01 ºC/year), respectively. From a nighttime perspective, SUHIIs presented positive rates in eleven MRs, of which three in the Atlantic Forest biome exhibited statistically significant trends (i.e. JP, SA, and CAM; p-value < 0.05). The highest and lowest levels of nighttime SUHII were observed in SA (0.02 ºC/year) and JP (0.01 ºC/year), respectively.

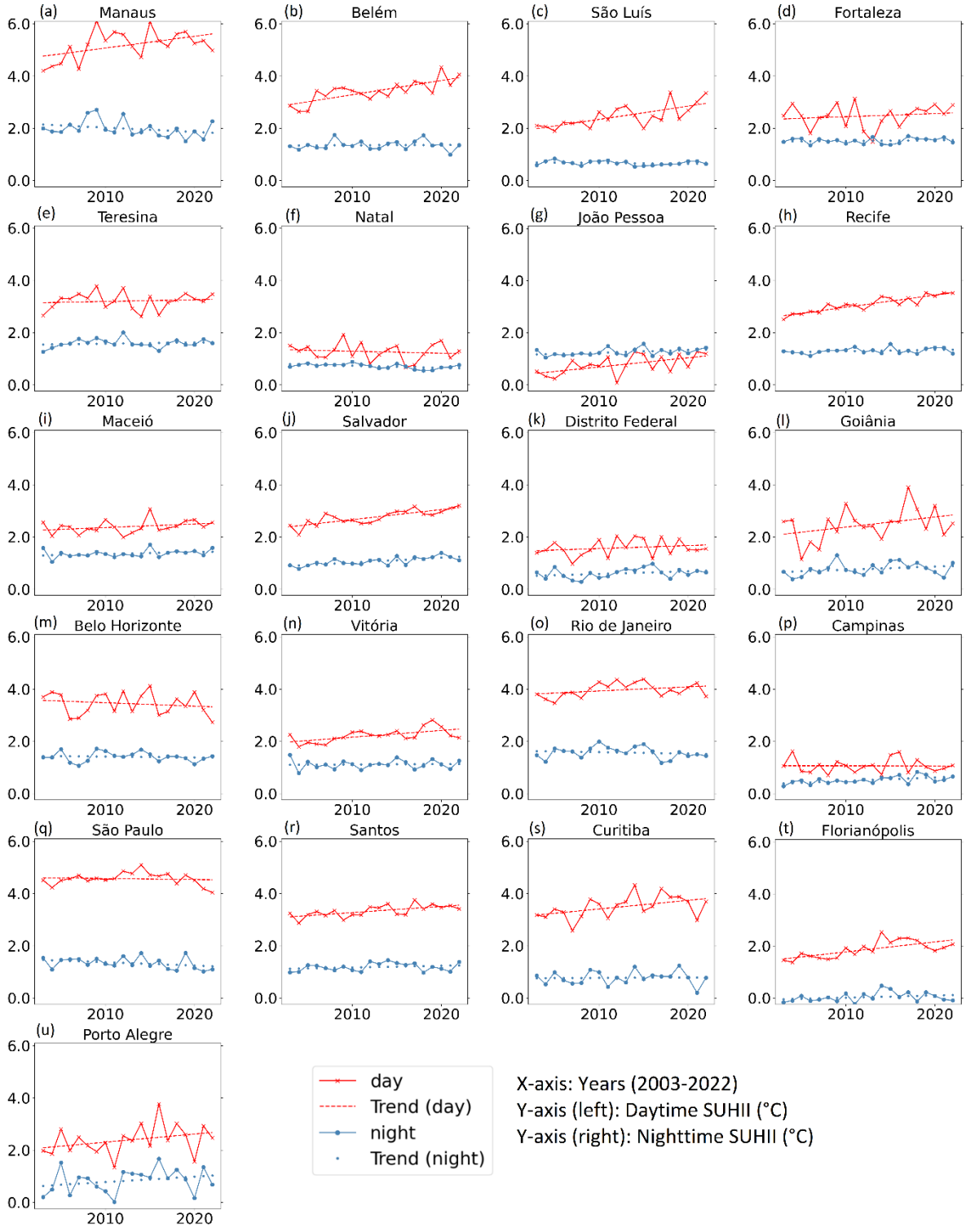

Figure 7 - Annual variability of daytime and nighttime SUHIIs and trend for MRs of (a) Manaus, (b) Belém, (c) São Luís, (d) Fortaleza, (e) Teresina, (f) Natal, (g) João Pessoa, (h) Recife, (i) Maceió, (j) Salvador, (k) Distrito Federal, (l) Goiânia, (m) Belo Horizonte, (n) Vitória, (o) Rio de Janeiro, (p) Campinas, (q) São Paulo, (r) Santos, (s) Curitiba, (t) Florianópolis, and (u) Porto Alegre.

Table 4 - Annual trends for day and nighttime SUHII, performed by the Mann-Kendall test and Sen's slope, where + (increasing trend); - (decreasing trend); and 0 (no trend).

MR	daytime SUHII			nighttime SUHII		
	Trend	p-value	Sen's slope	Trend	p-value	Sen's slope
MA	0	0,06	0,04	0	0,11	-0,02
BE	+	0,00	0,05	0	0,60	0,00
TE	0	0,63	0,01	0	0,63	0,00
RE	+	0,00	0,05	0	0,38	0,01
FO	0	0,31	0,01	0	0,72	0,00
SL	+	0,00	0,04	0	0,63	0,00
NA	0	0,72	-0,01	-	0,04	-0,01
JP	+	0,01	0,04	+	0,03	0,01
SA	+	0,00	0,04	+	0,00	0,02
MAC	0	0,14	0,01	0	0,18	0,01
VI	+	0,02	0,03	0	0,77	0,00
SAN	+	0,01	0,02	0	0,35	0,01
RJ	0	0,21	0,02	0	0,46	-0,01
SP	0	0,92	0,00	0	0,07	-0,02
CAM	0	1,00	0,00	+	0,01	0,01
BH	0	0,58	-0,01	0	0,72	0,00
CU	+	0,04	0,03	0	0,72	0,01
FLO	+	0,00	0,04	0	0,26	0,01
PA	0	0,09	0,03	0	0,42	0,03
GO	0	0,35	0,04	0	0,21	0,01
DF	0	0,35	0,01	0	0,16	0,01

Figure 8 shows the spatial distribution of the 21 Brazilian MRs, exhibiting the average daytime and nighttime SUHIIs by Brazilian biome over the twenty years. The MRs in the Amazon biome exhibited the highest historical averages for daytime SUHII (i.e. 3.69 ºC), mainly influenced by the scenario observed in MA, with an average of 5.18 ºC. The second prominent biome was the Atlantic Forest (2.62 ºC), followed by Caatinga (2.47 ºC), Cerrado (2.42 ºC), and Pampa (2.38 ºC). Two MRs presented mean daytime SUHIIs between 4 and 6 °C (i.e. MA and SP), fourteen ranging from 2 to 4 °C (i.e. BE, SL, RE, MAC, SA, VI, BH, RJ, SAN, CU, FO, TE, GO, and PA), and five between 0 and 2 °C (NA, JP, CAM, FLO, and DF) (Figure 8ac). These overall higher values for the daytime SUHIIs in the MRs located in the Amazon biome (i.e. MA, BE, and SL) may have been induced by the changes in climate, primarily represented by imbalances in precipitation and air temperature (Dubreuil et al., 2017; West et al., 2019). Such a context makes these MRs susceptible to droughts and potential fires

triggered by the deforestation process through wildfires, i.e. serving as a contributor to the formation of SUHIs (Carrillo-Quinete et al., 2022; Silva et al. 2017).

During the nighttime period, four MRs presented nighttime values between 1.5 ºC and 2 ºC (i.e. MA, RJ, FO, and TE), nine between 1 ºC and 1.5 ºC (i.e. BE, JP, RE, MAC, SA, BH, VI, SP, and SAN), seven between 0.5 ºC and 1ºC (i.e. SL, NA, CAM, CU, GO, DF, and PA), and only one between 0 ºC and 0.5 ºC (i.e. FLO). Analysing from the biome perspective, the SUHII magnitudes were observed, in descending order, in the following biomes: Caatinga (1.52 ºC), Amazon (1.33 ºC), Atlantic Forest (1.04 ºC), Cerrado (0.99 ºC), and Pampa (0.83 ºC). The higher values for nighttime SUHIIs in Caatinga may reflect the characteristic semi-arid climate of this biome (Alvares et al., 2013; Santos e Silva, 2024). This climate features elevated temperatures on natural surfaces during the day, often followed by significant drops at night (Alvares et al., 2013; Borges et al., 2020; Santos e Silva, 2024). Additionally, Caatinga is characterised by less dense vegetation, predominantly consisting of shrubs and small trees (Giulietti et al., 2004; Lima et al., 2010). Wang et al. (2021) mention that greater vegetation cover leads to increased emission of long-wave radiation back to the soil surface, resulting in reduced heat loss during nighttime (He et al., 2024). In contrast, due to its lower vegetation cover, the Caatinga biome behaves oppositely, causing lower nighttime rural LST and consequently higher SUHIIs values in this period. The semi-arid climate also contributes to the persistence of clear skies, meaning with fewer clouds, a situation that contributes to higher values of SUHIIs in the nighttime.

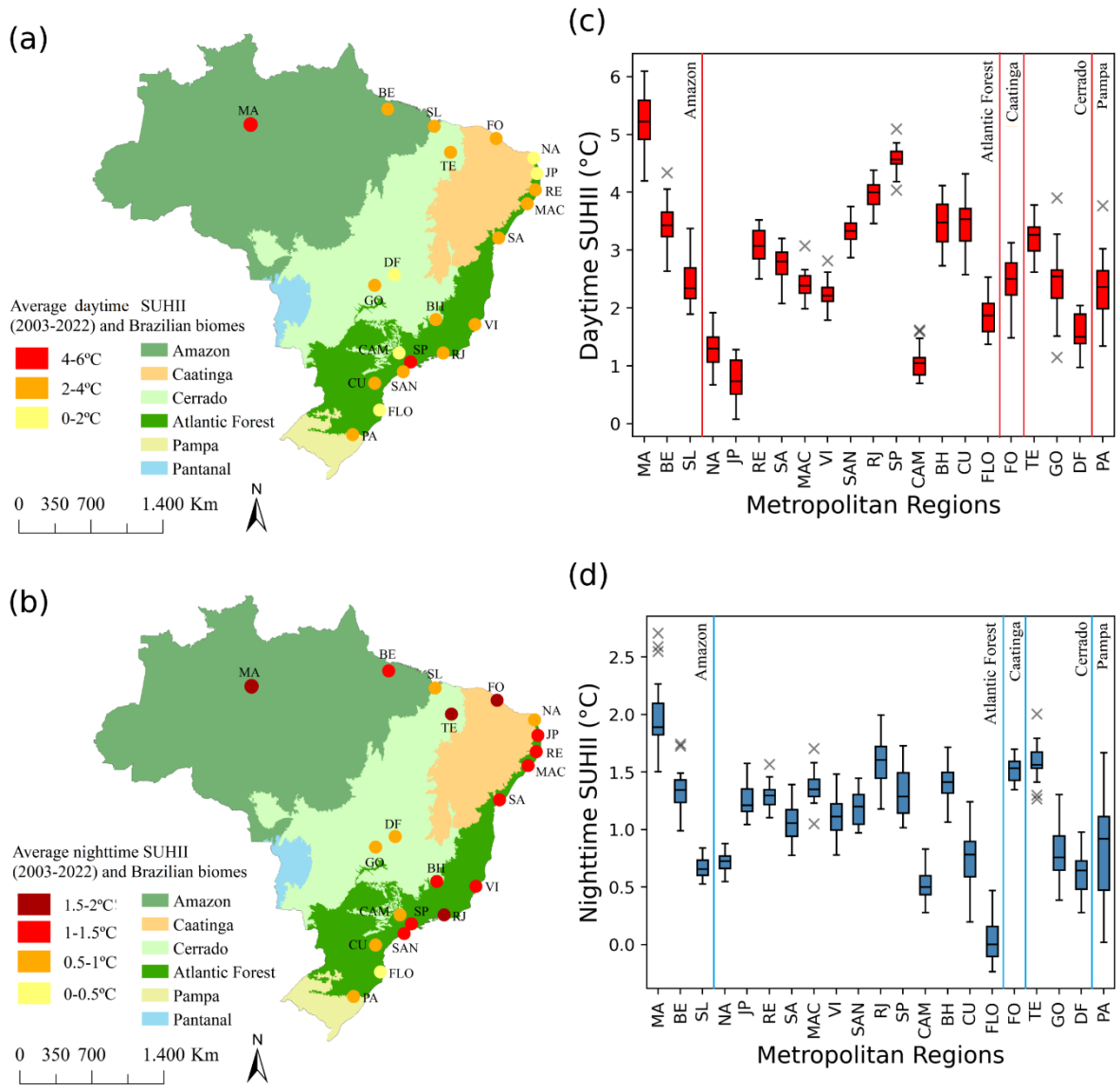

Figure 8 - Spatial distribution of the average (a) daytime and (b) nighttime SUHII, and box plots of (c) daytime and (d) nighttime SUHII for each MR.

MRs located within the Amazon and Atlantic Forest biomes tend to be more populous, presenting a faster pace of urban growth (IBGE, 2022) that contributes to increased impermeable areas and reduced vegetation cover (Carlson and Arthur, 2000; Zhou et al., 2023). In general, the population of the MRs obtained from the last demographic census (Table S1; Appendixes) showed a stronger correlation with the average daytime SUHIIs (r = 0.48) when compared to nighttime (r = 0.23). The results obtained by Tran et al. (2006) in 18 cities in Asia also showed that the influence of the population size on the daytime UHIs is greater than that on the nighttime due to the strong presence of anthropogenic heat. The daytime socio-economic

activities (e.g. vehicular traffic, industries, and building operations) are recognised as a source of imbalance for the surface energy balance by the emission of sensible heat (Chrysoulakis et al., 2016; Grimmond, 1992; Oke, 1988; Sailor et al., 2015), potentially enhancing the formation of SUHIs during daytime (Yang et al., 2015; Yang W. et al., 2017).

Nevertheless, in contrast to the studies performed by Hung et al. (2006), Kalnay and Cai (2003), Oke (1973), and Shahmohamadi et al. (2010), which identified the population density as a crucial factor in the growth of SUHIs, no such significant correlation was found when the statistical correlation was applied using the population density from the demographic census (IBGE, 2022). This suggests that, similarly to Du et al. (2016) in the Yangtze River Delta Urban Agglomeration (China) or Clinton and Gong (2013) globally, the population density is a less significant factor compared to other more local potential factors, such as vegetation loss and the expansion of urban areas. Considering that the two highest historical averages of daytime (i.e. MA and SP) and nighttime (i.e. MA and TE) SUHIIs were found in inland areas, a possible effect of continentality has been noticed, as suggested by Peng et al. (2019). These authors observed that the UHI was stronger in inland areas of China when compared to the coastal regions. Such contrast may result from a thermal regulation between land and sea in coastal cities, where other natural circulations, such as monsoons and ocean currents, may favour the limitations of UHI development by changing the energy balance of a city (Peng et al., 2019).

At the monthly scale, the temperature anomalies vary significantly according to the MRs (Figure 9). In Amazon, BE presented the highest mean monthly daytime (5.5 ºC in September) and nighttime (2.2 ºC in July) SUHIIs (Figure 9). For Caatinga, FO presented the highest values of daytime and nighttime SUHIIs in March, with 5.3 and 2.1 ºC, respectively. For the Atlantic Forest, the highest values for daytime and nighttime SUHIIs were observed in January in BH, with 7.8 and 3.2 ºC, respectively. In Cerrado, GO recorded the highest monthly averages for daytime (5.3 ºC in April) and nighttime (2.9 ºC in May) SUHIIs. The Pampa biome, represented by PA, exhibited in December the highest daytime and nighttime averages, with anomalies of 5.6 and 2.5 ºC, respectively.

These monthly variations highlight a seasonality in the daytime and nighttime SUHIIs, with some similarities in the variabilities among the MRs within the biomes. For instance, seasonalities were observed in the MRs located at higher latitudes (from -30 to -16°) in different biomes (i.e. Pampa, Atlantic Forest, and Cerrado), exhibiting higher mean values of daytime SUHII during the austral summer and spring seasons in subtropical climates zones (Shen et al.,

2023), where the magnitudes of surface warming are often larger (i.e. SP, SAN, CU, and PA). On the other hand, MRs at lower latitudes (from -13 to -1º) exhibited an absence of seasonality, as observed in Amazon (e.g. MA, BE, and SL), Atlantic Forest (e.g. NA, JP, RE, MAC), Caatinga (e.g. FO), and Cerrado (e.g. TE). These seasonal/latitudinal variabilities suggest the sensitivity of the latitudinal position of MR in the development of SUHIs (Halder et al., 2023; Miles and Eseau, 2017; Wienert and Kuttler, 2005). In a recent analysis using solar angle, Halder et al. (2023) observed that during a specific period of summer, sunlight reaches certain locations on the Earth's surface with a 90º angle, resulting in maximum insolation and, consequently, maximum surface temperature from the equatorial area to the tropics, potentializing the SUHIs effect in these areas. However, the same does not occur from the tropics to the poles, where sunlight strikes with an angle less than 90º. Based on this, the availability of sunlight varies from the Equator to the poles in locations with different latitudes, and places with the same or close latitudes receive similar amounts of sunlight throughout the year.

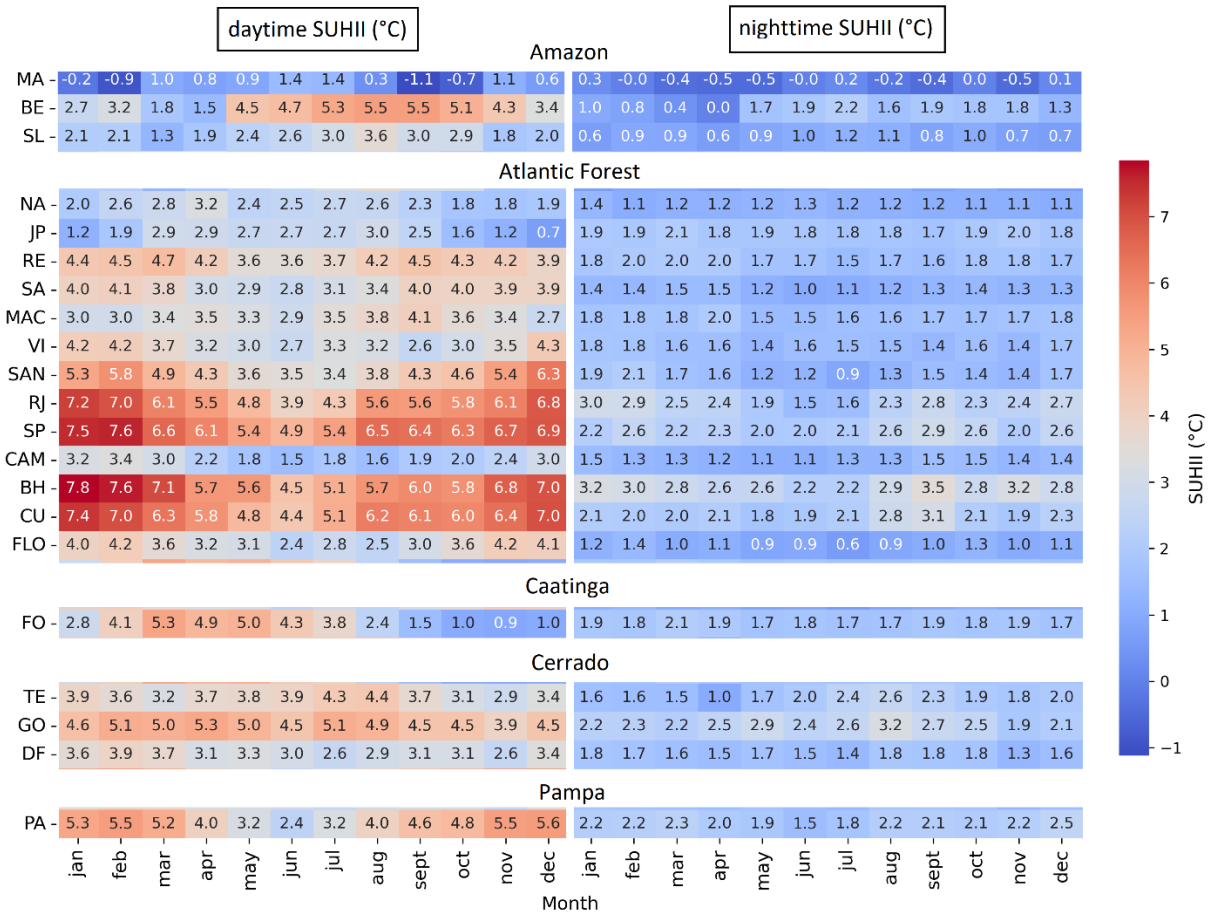

Figure 9 - Heatmap for the monthly average daytime and nighttime SUHII (ºC) for each MR, organised by the Brazilian biomes.

Overall, the monthly trends in Table 5 show that the daytime SUHII presented more months with growth trends in all Brazilian biomes. However, none of the biomes showed growth trends concentrated in specific months, demonstrating the absence of an intra-annual pattern of growth in all MRs. This situation is exemplified by Atlantic Forest, a biome that encompasses MRs at different latitudes with trends occurring in different months of the year.

Table 5 - Monthly trends for daytime and nighttime SUHIIs, performed by the Mann-Kendall test and Sen's slope, where + means an increasing trend, - indicates a decreasing trend, and 0 denotes no trend.

Biome	Month/trend																							
	Daytime SUHII													Nighttime SUHII										
	MR	Jan	Feb	Mar	Apr	May	Jun	Jul	Aug	Sep	Oct	Nov	Dec	Jan	Feb	Mar	Apr	May	Jun	Jul	Aug	Sep	Oct	Nov	Dec
Amazon	MA	0	-	0	0	0	0	0	0	0	0	0	0	0	0	0	0	0	0	0	0	-	0	0	0
	BE	0	0	0	-	0	+	+	0	0	0	0	0	0	0	0	0	0	0	0	0	0	0	0	0
	SL	0	0	0	0	0	0	0	0	+	0	0	0	0	0	0	0	0	+	0	0	0	0	0	0
Caatinga	FO	0	0	0	0	0	0	0	0	0	0	0	0	0	0	0	0	0	+	0	0	0	0	0	0
Cerrado	TE	0	0	0	+	+	0	0	0	0	0	0	0	0	0	0	0	0	0	0	0	0	0	0	0
	GO	+	0	0	0	0	0	0	0	0	0	0	0	+	0	0	0	0	0	0	0	0	0	0	0
	DF	+	0	+	0	0	0	0	0	0	0	0	0	0	0	+	0	0	0	0	0	0	0	0	0
Atlantic Forest	RE	0	0	+	0	0	+	0	0	+	+	+	+	0	0	0	0	0	0	0	0	0	0	0	0
	NA	0	0	0	0	0	0	0	0	0	0	0	0	-	0	0	0	0	0	0	0	0	0	0	0
	JP	0	0	0	0	0	+	0	0	0	0	0	0	0	0	0	+	0	0	0	0	0	0	0	0
	SA	+	0	0	0	0	0	+	0	0	0	0	0	0	0	0	0	0	0	0	0	0	0	0	0
	MAC	0	0	0	0	+	+	0	0	0	0	0	0	0	0	0	0	0	0	0	0	0	0	0	0
	VI	+	0	0	+	0	0	+	0	0	0	+	+	0	0	0	+	0	0	0	0	0	0	0	0
	SAN	0	0	0	0	0	0	0	0	0	0	0	+	0	0	0	0	0	0	-	0	0	0	0	0
	RJ	0	0	0	0	0	0	0	0	0	0	0	0	0	0	0	0	-	0	0	0	0	0	0	0
	SP	0	0	0	0	0	0	0	0	0	0	0	0	0	0	0	0	-	0	0	0	0	0	0	0
	CAM	0	0	0	0	0	0	0	0	0	0	0	0	0	0	0	0	0	0	0	0	0	0	0	0
	BH	0	0	0	0	0	0	0	0	0	0	0	0	+	0	0	0	0	0	0	0	0	0	0	0
	CU	0	0	0	0	0	0	0	0	0	+	0	0	0	0	0	0	0	0	0	0	+	0	0	0
	FLO	+	0	0	0	0	+	0	0	0	+	+	+	0	0	0	0	-	0	0	0	0	0	0	0
Pampa	PA	0	0	0	0	0	0	0	+	0	+	0	0	0	0	0	0	0	0	0	0	0	0	0	0

5.2 The urban land-use perspective: surface alteration systematically favouring temperature increase

5.2.1 Evolution of urban areas (UA) and LST

The quantification of UA by the BU index revealed an increase in the coverage rate of build-up materials (e.g. asphalt and concrete) in eighteen MRs (Table 6), with slope trends higher than 0.31 km^2/year. It is also possible to notice an intensification of the urbanisation processes in already urbanised regions of some MRs, represented by the observed fourteen increasing rates of the mean BU in the urban areas, with slope trends higher than 0.007/year, suggesting an increase in the coverage rate of the build-up materials. For instance, the spatial distribution of the BU in RE shows considerable temporal changes in the values of BU, with a clear presence of diverse alterations of the surface materials over the years highlighted by the greater intensity of red in Figure 10.

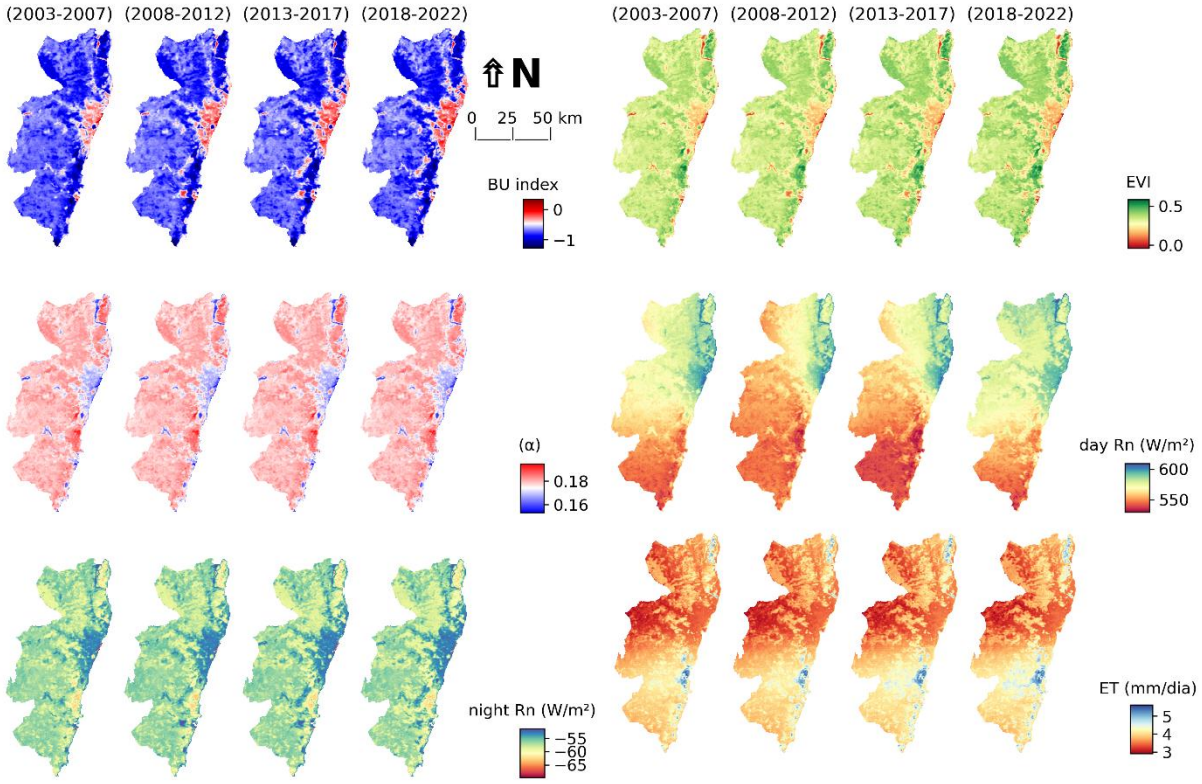

Figure 10 - 5-year average of (a-d) BU index, (e-h) EVI2, (i-l) surface albedo, (m-p) daytime Rn, (q-t) nighttime Rn, and (u-x) ET with a 250-m spatial resolution for the Recife metropolitan region (RE): (a, e, i, m, q and u) 2003-2007; (b, f, j, n, r and v) 2008-2012; (c, g, k, o, s and w) 2013-2017; and (d, h, l, p, t, and u) 2018-2022.

Table 6 also demonstrates that thirteen MRs distributed in all Brazilian biomes exhibited statistically significant trends of UA growth, with the highest and lowest rates observed in GO (3.60 km²/year; Cerrado) and SAN (0.31 km²/year; Atlantic Forest). Pampa presented the highest value of Sen's slope (2.71 km^2/year) but only PA is located at this biome. When analysing biomes with more than one MR, Amazon showed the highest value of increasing rate, with 2.02 km^2/year. Souza et al. (2020) also indicated an increase in non-natural areas of the Amazon biome, which experienced, together with Cerrado, the highest pressure on natural areas in recent years in Brazil.

The correlation between UAs and mean daytime LST was globally positive when considering all analysed MRs ($r = 0.54$, $R^2 = 0.38$, and KGE = 0.09) (Figure 11), with only SP ($r = -0.19$, $R^2 = 0.04$, and KGE = 0.02) and CU ($r = -0.14$, $R^2 = 0.02$, and KGE = 0.01) presenting negative or absence of correlation (Table S2; Appendixes). The highest positive correlations between UA and daytime LST were found in TE ($r = 0.88$, $R^2 = 0.77$, and KGE = 0.09), FO ($r = 0.84$, $R^2 = 0.71$, and KGE = 0.11), and VI ($r = 0.81$, $R^2 = 0.66$, and KGE = 0.12), with the low positive correlation observed in DF ($r = 0.25$, $R^2 = 0.06$, and KGE = 0.03). Overall, the positive correlation for nighttime was lower than for the daytime LST, with the highest coefficients noticed in TE ($r = 0.73$, $R^2 = 0.53$, and KGE = 0.13), GO ($r = 0.68$, $R^2 = 0.43$, and KGE = 0.13), and RJ ($r = 0.63$, $R^2 = 0.40$, and KGE = 0.13). This trend suggests that the fast urban expansion in Brazil, characterised by the suppression of natural areas, can be potentially linked to LST alteration, possibly reflecting the effect of surface changes.

Table 6 - Annual trends for urban areas, EVI2, surface albedo, day and nighttime Rn, and ET, performed by the Mann-Kendall test and Sen's slope, where + means an increasing trend, - indicates a decreasing trend, and 0 denotes no trend.

Biome	MR	Urban areas (km^2)			EVI2			Surface albedo (α)			daytime Rn (W/m^2)			nighttime Rn (W/m^2)			ET (mm)		
		Trend	p-value	Sen's slope	Trend	p-value	Sen's slope	Trend	p-value	Sen's slope	Trend	p-value	Sen's slope	Trend	p-value	Sen's slope	Trend	p-value	Sen's slope
Amazon	MA	+	0	2,46	-	0	0	-	0	0	-	0,03	-2,39	+	0,04	0,12	-	0	-18,1
	BE	+	0	1,94	-	0	0	-	0	0	-	0,01	-2,71	+	0,01	0,07	0	0,87	-1,1
	SL	+	0,01	1,67	-	0	0	-	0	0	0	0,5	-1,54	+	0,01	0,07	0	0,06	5,79
Atlantic Forest	RE	+	0	3,1	-	0	0	-	0	0	+	0,01	4,09	+	0	0,05	0	0,06	7,24
	NA	0	0,54	-0,1	0	0,08	0	0	0,1	0	+	0	4,38	+	0,02	0,03	+	0,01	11,36
	JP	+	0	1,21	-	0	0	-	0	0	+	0	4,29	+	0	0,05	+	0,05	6,3
	SA	+	0	1,39	-	0,04	0	-	0,01	0	0	0,46	-0,96	+	0,05	0,04	0	0,77	0,87
	MAC	0	0,14	0,32	-	0	0	-	0,01	0	0	0,26	0,76	+	0,03	0,04	+	0,03	6,23
	VI	0	0,5	0,77	0	0,58	0	0	0,29	0	0	0,97	-0,04	0	0,07	0,05	0	0,58	-1,86
	SAN	+	0	0,31	0	0,87	0	0	0,4	0	0	0,54	-0,33	0	0,14	0,04	0	0,97	-0,31
	RJ	+	0,03	2,93	-	0,05	0	-	0,03	0	0	0,58	-0,38	0	0,06	0,07	0	0,13	-6,43
	SP	0	0,54	-0,28	+	0,01	0	+	0,02	0	0	0,46	0,49	0	0,23	0,02	0	0,38	-3,44
	CAM	0	0,18	0,73	0	0,1	0	0	0,82	0	0	0,42	0,34	+	0,03	0,09	-	0	-13,2
	BH	0	0,14	1,09	-	0,01	0	-	0,02	0	0	0,21	0,72	+	0	0,08	-	0,05	-7,47
	CU	0	0,13	1,14	0	0,16	0	0	0,73	0	0	0,35	-0,85	+	0,02	0,05	0	0,14	-2,37
	FLO	+	0	0,9	-	0	0	-	0	0	-	0	-2,07	+	0	0,09	-	0,01	-4,82
Caatinga	FO	+	0,05	1,69	-	0	0	-	0	0	0	0,5	0,78	+	0	0,12	0	0,72	2,34
Cerrado	TE	+	0	1,99	-	0	0	-	0	0	0	0,13	-1,16	0	0,13	0,06	0	0,97	-0,51
	GO	+	0,01	3,6	-	0	0	-	0,03	0	0	0,7	0,12	+	0	0,09	-	0,03	-6,19
	DF	-	0	-6	+	0,01	0	+	0,04	0	0	0,23	-0,72	+	0,03	0,04	0	0,06	-5,58
Pampa	PA	+	0,01	2,71	0	0,79	0	0	0,6	0	0	0,06	-1,4	0	0,28	0,03	0	0,18	-2,66

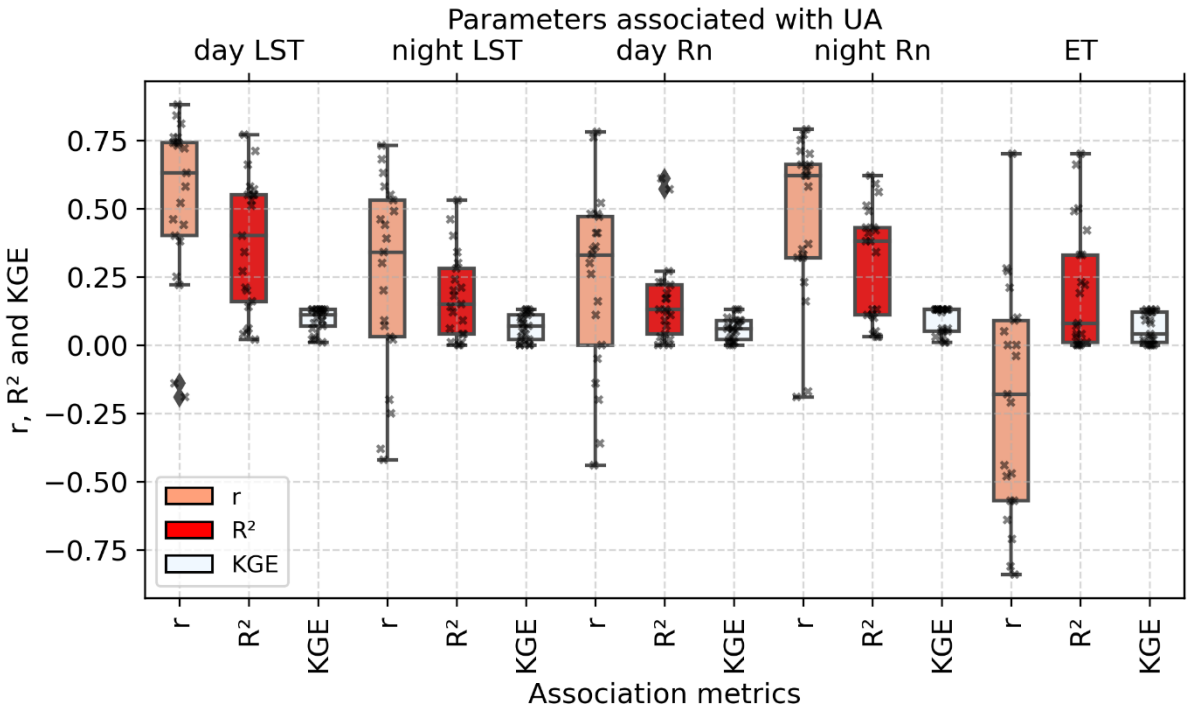

Figure 11 - Associations represented by the statistical metrics (r, R^2, and KGE) between the urban areas (UA) and the variables daytime LST, nighttime LST, daytime Rn, nighttime Rn, and ET.

5.2.2 Evolution of surface alteration proxies in urban areas: EVI2 and α

Impervious surfaces without vegetation appeared to be strong contributors to the rise of urban temperature (Dewan et al., 2021), which consequently plays an important role in further latent heat (ET) transfers, especially during the daytime (e.g. Chakraborty and Lee, 2019; Li et al., 2020; Quan et al., 2016; Peng et al., 2019; Raj et al., 2020; Xu et al., 2017; Yao et al., 2018; Zhou et al., 2014). A decrease in green areas then determines the loss of cooling potential in urban areas (Charabi and Bakhit, 2011; Ojeh et al., 2016; Shojaei et al., 2017). This loss of the cooling potential in all MRs of Brazil was also confirmed by the downward trends in EVI2 during the twenty years of analysis, with decreasing trends ranging from -0.0001 in PA to -0.0026/year in TE (Table 6). From a biome perspective, Amazon and Cerrado showed the highest mean rates of decreasing trend for EVI2 (-0.0020/year), as also observed by Souza et al. (2020), which identified the highest removal of natural surfaces in the last two decades in these two biomes. Consistently, the EVI2 showed a negative association with daytime (r = -0.37, R^2 = 0.26, and KGE = 0.08) and nighttime (r = -0.20, R^2 = 0.15, and KGE = 0.06) LST when considering the average values of all MRs. The highest and lowest negative correlations

for daytime LST were identified in TE (r = -0.82, R^2 = 0.67, and KGE = 0.12) and DF (r = -0.11, R^2 = 0.01, and KGE = 0.01), respectively. The highest and lowest negative correlations for nighttime LST were observed in GO (r = -0.68, R^2 = 0.46, and KGE = 0.13) and SAN (r = -0.03, R^2 = 0, and KGE = 0), respectively.

These results show that the impact caused by the presence of vegetation (i.e. with evaporative cooling and shadowing effects) in the intensification of urban LST predominates in the daytime period, as also observed in other studies considering multiple (e.g. Chakraborty and Lee, 2019; Clinton and Gong, 2013; Peng et al., 2012) and individual cities (e.g. Chakraborty et al., 2016; Qiao et al., 2013). Nevertheless, the findings also showed that the effectiveness of vegetation in mitigating SUHIs can vary across the Brazilian territory from biome to biome. First, both the Amazon (EVI2 vs daytime LST = -0.52; EVI2 vs nighttime LST = -0.47) and the Atlantic Forest (EVI2 vs daytime LST = -0.49; EVI2 vs nighttime LST = -0.26) biomes exhibited a negative association between the vegetation greenness and urban LST, especially during the daytime. This supports the hypothesis that the dense and tropical vegetation in these territories (Randow et al., 2004; Teixeira et al., 2020; Laipelt et al., 2021) constitutes an important tool for minimising LST during the day due to photosynthetic activity during this period. On the other hand, despite having a natural savanna vegetation characterised by grassland, sparse shrubland, and deciduous seasonal forests (Furley, 1999; Laipelt et al., 2021), the Cerrado biome showed the highest magnitudes of overall negative association between EVI2 and LST (EVI2 vs daytime LST = -0.53; EVI2 vs nighttime LST = -0.61), indicating that its less dense vegetation acts as a significant factor in decreasing LST during the night.

Additionally, the Caatinga biome (EVI2 vs daytime LST = -0.67; EVI2 vs nighttime LST = -0.39), characterised by seasonally dry forests with a predominance of shrubs and thorny trees that minimise water loss during long periods of precipitation absence (Althoff et al., 2016; Moro et al., 2016; Queiroz et al., 2017; Tavares-Damasceno et al., 2017), also showed an overall negative association between these variables, especially during the day. Finally, the Pampa, with dominant vegetation of grasslands, sparse shrubs, and tree formations (Berreta, 2001), did not exhibit associations indicating the cooling role of the local vegetation (EVI2 vs daytime LST = 0.02; EVI2 vs nighttime LST= 0.56). Therefore, the findings support the idea that sustainable urban planning should consider implementing suitable green spaces as an essential strategy to mitigate the effects of heat risk and enhance thermal comfort in cities, especially in

cities located in biomes where vegetation presents a major control of LST, as also highlighted by other studies (e.g. Dewan et al., 2021; Maimaitiyiming et al., 2014; Vulova et al., 2023).

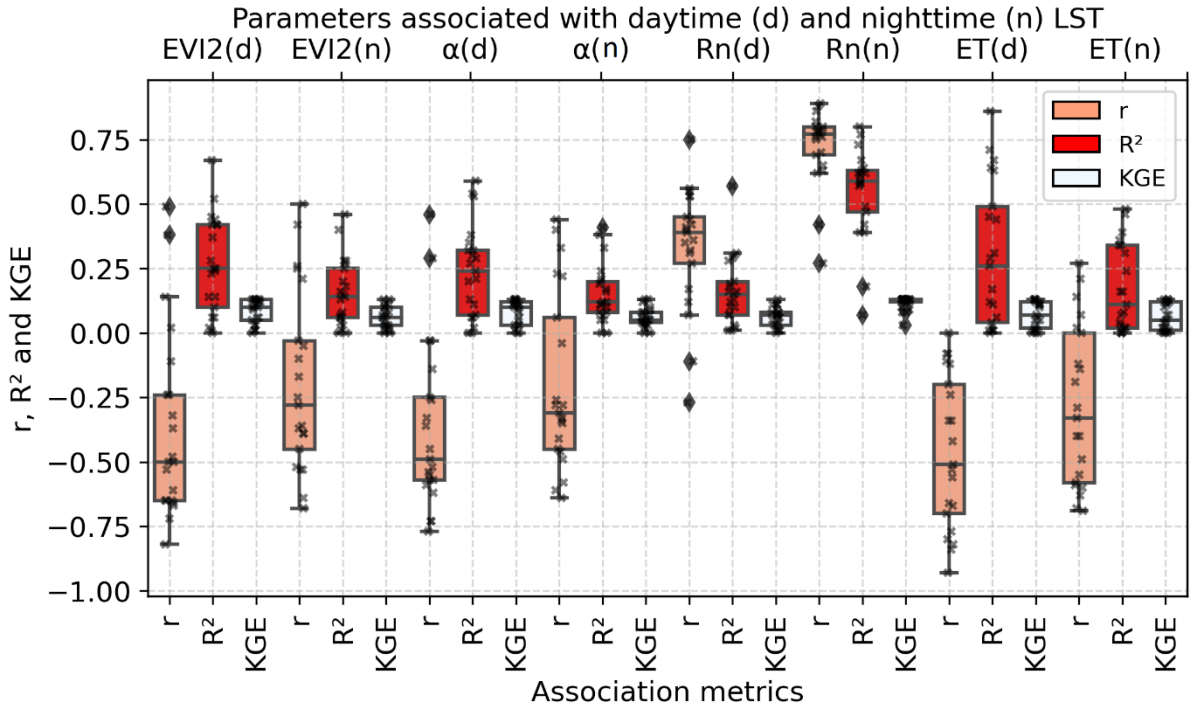

Figure 12 - Associations represented by the statistical metrics considered in the study (i.e. r, R^2, and KGE) between LST and the biophysical parameters EVI2, surface albedo, Rn, and ET.

The replacement of vegetation cover by urban canopies presupposes alterations in surface albedo (Christopherson and Birkeland, 2017; Myhre G. et al., 2013) by the replacement of forests, croplands, savannas, and grasslands with urban lands (Ouyang et al., 2022), inducing an overall decrease of the sunlight reflected by the surface (shortwave wavelengths) and an increase of emissivity (longwave wavelengths) (Zhou et al., 2014). The results obtained in this study show that thirteen MRs in Brazil presented statistically significant decreases of α (Table 6), with an overall rate of -0.0001/year. In parallel, α also presented an overall inversely proportional relationship with daytime (r = -0.37, R^2 = 0.24, and KGE = 0.08) and nighttime LST (r = -0.20, R^2 = 0.15, and KGE = 0.06) (Figure 12). Nineteen and seventeen MRs presented negative associations of α with daytime and nighttime LST, respectively, with the highest levels observed in TE during the day (r = -0.77, R2 = 0.59, and KGE = 0.13) and at night (r = -0.64, R2 = 0.41, and KGE = 0.13).

This inversely strong relationship between LST and α was also observed by Taha (2008) in Sacramento, United States, with a more significant impact on the daytime SUHII when compared to the nocturnal SUHII. This negative statistical association between α and LST confirms the role of α as a mitigating factor for the occurrence of SUHIs, especially during the daytime period (e.g. Dugord et al., 2014; Herath et al., 2021; Nwakaire et al., 2020). Not only is it necessary to preserve green areas, but adopting alternative construction materials from the usual ones is also an option for increasing α (Dugord et al., 2014). For instance, the use of reflective pavements, which have high solar reflectivity to dissipate solar radiation (Ferrari et al., 2020; Nwakaire et al., 2020), as well as permeable or water-retentive pavements that utilise the latent heat of vaporisation to lower their surface temperature (Ferrari et al., 2020), are potential strategies.

5.3 The energy balance perspective: an interplay between country-scale and urban-scale trends

5.3.1 UA and Rn

The relationship between the urban surfaces and their thermal properties was investigated by the analysis of links between the UA and the mean annual Rn (Figure 11). Overall, good correlations between UA and Rn were observed at night when considering global values for all MRs (r = 0.47, R^2 = 0.30, and KGE = 0.09), with nineteen MRs displaying positive relationships. The MRs in the Cerrado biome showed the highest association between UA and nighttime Rn, especially in TE (r = 0.79, R^2 = 0.62, and KGE = 0.13). Only SP (r = -0.17, R^2 = 0.03, and KGE = 0.01) and DF (r = -0.19, R^2 = 0.04, and KGE = 0.01) exhibited an absence of a relationship between UA and nighttime Rn. The overall correlation between UA and daytime Rn (r = 0.24, R^2 = 0.16, and KGE = 0.06) was moderated compared to nighttime Rn. JP presented a higher correlation between UA and daytime Rn (r = 0.78, R^2 = 0.61, and KGE = 0.13), with five MRs (i.e. MA, BE, FLO, CU, and SP) showing negative or lack of correlations. During the daytime, Rn showed statistically significant decreasing trends in three MRs (Table 6): FLO (-2.07 W/m^2/year; Atlantic Forest), MA (-2.39 W/m^2/year; Amazon), and BE (-2.71 W/m^2/year; Amazon) (Table 6). The increasing trends of daytime Rn was identified in NA (4.38 W/m^2/year), RE (4.09 W/m^2/year), and JP (4.29 W/m^2/year). For the nighttime Rn, an increasing trend over the time series was observed in all MRs, with fifteen exhibiting statistically significant trends (i.e. MA, BE, RE, FO, SL, NA, JP, SA, MAC, CAM, BH, CU,

FLO, GO, and DF) and the highest estimated growth rate from the Sen's slope observed in FO (0.12 W/m^2/year).

The stronger correlation between UA and nighttime Rn, as well as the observed growth trends in Rn during this period, suggest that urban characteristics related to construction materials and land use patterns exert a more pronounced influence on radiative processes during the night. This influence is particularly notable in the emission of long-wave radiation, which is stored in the ground during the day and released at night (Chen et al., 2020; Sabino et al., 2020), contributing to maintaining elevated temperatures in urban areas (Peng et al., 2020). Based on the results, Rn exhibited a highly heterogeneous variability among the MRs. As expected, the highest averages of daytime and nighttime Rn were detected in the MRs located in Amazon, Atlantic Forest (lower latitudes), and Caatinga due to the greater availability of solar radiation in low latitude regions (Figures S152 to S172; Appendixes). The spatial distributions of Rn show that the urban areas presented higher values during the daytime and nighttime (i.e. Rn > 520 W/m^2 and -55 W/m^2, respectively) (Figures S22 to S151; Appendixes).

5.3.2 LST and energy balance proxies

The relationship between LST and Rn (Figure 12) was overall directly proportional for daytime (r = 0.33, R^2 = 0.16, and KGE = 0.06) and nighttime (r = 0.72, R^2 = 0.54, and KGE = 0.12), with values of r ranging from -0.27 to 0.89. During the daytime and nighttime, the highest correlations between LST and Rn were observed in BH (r = 0.75, R^2 = 0.57, and KGE = 0.13; Atlantic Forest) and RJ (r = 0.89, R^2 = 0.80, and KGE = 0.08; Atlantic Forest), respectively.

For the nighttime, the correlations for all MRs were positive (r ranging from 0.27 to 0.89), indicating that increasing Rn is a crucial factor in heat production. The absorbed net radiation at the surface should balance outgoing fluxes and can be expressed as the sum of G (soil heat flux), H (sensible heat flux), and LE (latent heat flux) (Kato and Yamaguchi, 2005). During the daytime, soil heat is conducted into the soil due to lower underground temperatures than the surface. Stored heat in the soil is released to the atmosphere by longwave radiation overnight (Chen et al., 2020; Kato and Yamaguchi, 2005). H increases while LE decreases, warming the surface and driving heat exchange from the Earth's surface to the atmosphere, raising both air temperature and surface temperatures, a situation represented by the correlations found at night.

The replacement of vegetated surfaces with urban materials influences the amount of LE (i.e. ET) and, consequently, the values of Rn. Higher ET rates play a key role in regulating the

surface energy balance by increasing LE and reducing H, bringing cooling effects to the cities (Chrysoulakis et al., 2018). Such a relationship can be expressed by the negative associations between daytime LST and ET (r = -0.47, R^2 = 0.30, and KGE = 0.07) when considering all analysed MRs. This association highlights the strong potential of ET to mitigate the effects of thermal intensification. The highest negative association between ET and LST was observed during the daytime in CAM (r = -0.93, R^2 = 0.86, and KGE = 0.06). In the nighttime context, the strongest negative association was noticed in DF (r = -0.69, R^2 = 0.48, and KGE = 0.13). The values of ET decreased in fourteen MRs across all the biomes along the twenty years of analysis, with four exhibiting yearly statistically significant trends (p-value < 0.05): MA (-18.12 mm/year), CAM (-13.20 mm/year), FLO (-4.82 mm/year), and GO (-6.19 mm/year) (Table 6). While the intensification of daytime LST was broadly regarded as the consequence of a reduction in LE (Arnfield, 2003; Clinton and Gong, 2013; Oke, 1982; Peng et al., 2012; Voogt and Oke, 2003), during the nighttime this rising of LST may result from an increase in the heat storage in the urban zones during the day compared to surrounding areas (Clinton and Gong, 2013; Voogt and Oke, 2003).

6 CONCLUSIONS AND RECOMENDATIONS

By analysing the spatio-temporal evolution of SUHIIs over Brazil, this study aimed at providing a baseline information to better characterise the evolution of this effect over the past 20 years in twenty-one MRs of the country, considering both intra-annual and inter-annual scales and assessing variations of the controlling surface biophysical parameters at a monthly timescale in response to urbanisation. This allowed highlighting that the SUHIIs were globally amplified during the studied period, but the trends may differ in amplitude depending on the location (biomes) of the MRs as well as their local characteristics.

The continental perspective underscores the widespread presence of SUHI effects across all MRs, with significant variations in intensity observed during daytime and nighttime. At the country scale, the results therefore demonstrate that the latitudinal and demographic gradients seem to have a moderate influence in explaining the development of SUHIIs in Brazil. In contrast, the absence of a clear influence of continentality and population density suggests that more local features such as urban area size and building density, combined with a reduction of evaporative cooling and alteration of albedo (Zhao et al., 2014), may play an important role at the metropolitan scale.

The findings also reveal a concerning trend of increasing urban coverage in several metropolitan regions (MRs) of Brazil, notably the rapid growth of built-up areas in materials such as asphalt and concrete. This urban expansion is closely linked to the rise in land surface temperature (LST), particularly during the day, due to the replacement of natural areas with impermeable surfaces. Additionally, the decrease in green areas, evidenced by the decline in the vegetation index EVI2, contributes to the elevation of urban surface temperatures. The inversely proportional relationship between EVI2 and LST underscores the importance of green spaces in mitigating the effects of urban heat, especially in biomes like the Amazon and the Atlantic Forest, where dense vegetation plays a crucial role in thermal regulation.

On the other hand, the replacement of vegetative cover by urban areas also results in a decrease in surface albedo, which contributes to the increase in urban temperatures. Strategies such as the use of more reflective construction materials and the preservation of green areas are essential to mitigate the impacts of urban heat and promote a healthier and more sustainable urban environment.

The examination of energy balance dynamics at both country-scale and urban-scale levels reveals intricate interplays between urban surfaces and thermal properties, particularly regarding radiative processes and LST variations. Notably, the correlation between UAs and Rn demonstrates distinct patterns during daytime and nighttime. While a moderate correlation is observed between UA and daytime Rn, nighttime Rn exhibits a stronger association with urban surfaces, especially in regions within the Cerrado biome. The heterogeneity in Rn among the MRs underscores the influence of local factors on radiative processes, with higher Rn values detected in regions characterized by greater solar radiation availability, such as those situated in lower latitudes.

The direct proportional relationship between LST and Rn emphasizes the role of radiative fluxes in heat production, particularly evident during nighttime when higher Rn values contribute to elevated temperatures. The replacement of vegetated surfaces with urban materials alters the energy balance, affecting Rn values, with more sensible heat available (H) and less presence of latent heat flux (LE). Notably, higher rates of evapotranspiration (ET) are associated with cooling effects, highlighting the potential of ET in mitigating thermal intensification. However, the observed decreasing trends in ET across various MRs underscore the challenges posed by urbanisation to surface energy balance dynamics.

Overall, the findings underscore the complex interplay between urbanisation, radiative processes, and surface temperature variations, with implications for urban heat management strategies. These findings highlight the urgent need for urban planning policies that prioritize the conservation of green spaces and the adoption of more sustainable construction practices to address the challenges of urban warming, enhancing the urban resilience to climate change. Such mitigation policies, implemented with a prioritisation of Nature-Based Solutions (NBS) and through regulation of municipal master plans, can be the solution to the accelerated growth of SUHIs and many other environmental issues arising from the urbanisation process. Within urban settings, some examples of NBS include rain gardens, green roofs, linear and river parks, river naturalisation, and slope restoration. In a context of changing climate, interventions like these contribute to rainwater drainage and aquifer recharge; temperature regulation and reduction of urban heat; and erosion reduction and landslide prevention. In the peri-urban areas, forest restoration contributes to the quantity and quality of water reaching reservoirs, as well as reducing the risk of floods and inundations.

Further studies could then explore the potential of these adaptations in the process of attenuation of these phenomena and could also quantify how future urban growth, population growth, and climate-changing scenarios, as well as the effects of the increasing anthropogenic heat emissions from traffic, industry, and domestic buildings, can affect the SUHIIs and, consequently, the biophysical parameters within tropical cities. To achieve this, machine learning techniques and atmospheric general circulation models (AGCMs) could be used to determine the future scenarios of the defined parameters in this study.

7 REFERENCES

Akbari, H.; D.M. Kurn; S.E. Bretz; J.W. Hanford. Peak Power and Cooling Energy Savings of Shade Trees. Energy and Buildings 25 (2): 139–48. 1997.

Allen, R. G.; Tasumi, M.; Trezza, R. 2002. Satellite-based energy balance for mapping evapotranspiration with internalized calibration (METRIC) - Model. Journal of Irrigation and Drainage Engineering, v.133, n.4, p.380-394, 2007. https://doi.org/10.1061/(ASCE)0733-9437(2007)133:4(380).

Allen, R. G.; Tasumi, M.; Trezza, R. Satellite-based energy balance for mapping evapotranspiration with internalized calibration (METRIC) - Model. Journal of Irrigation and Drainage Engineering, v.133, n.4, p.380-394, 2007.

Althoff, T.D., Menezes, R.S.C., Carvalho, A.L., Pinto, A.S., Santiago, G.A.C.F., Ometto, J. P.H.B., von Randow, C., Sampaio, E.V.S.B., 2016. Climate change impacts on the sustainability of the firewood harvest and vegetation and soil carbon stocks in a tropical forest in Santa Teresinha Municipality, Northeast Brazil. For. Ecol. Manag. 360, 367–375. https://doi.org/10.1016/j.foreco.2015.10.001.

Alvares, C. A.; Stape, J. L.; Sentelhas, P. C.; De Moraes Gonçalves, J. L.; Sparovek, G. 2013. Köppen's classification map for Brazil. Meteorologische Zeitschrift Vol. 22 No. 6 (2013), p. 711 – 728. https://doi.org/10.1127/0941-2948/2013/0507

Amorim, M. C. C. T. Climatologia e Gestão do Espaço Urbano. MERCATOR - Revista de Geografia da UFC. Vol 9, nº 1, Dezembro de 2010, p 71-90.

Arnfield, A. J. (2003). Two decades of urban climate research: a review of turbulence, exchanges of energy and water, and the urban heat island. International Journal of Climatology, 23, 1–26. https://doi.org/10.1002/joc.859.

Arshad, S., Ahmad, S.R., Abbas, S., Asharf, A., Siddiqui, N.A., Islam, Z.U., 2022. Quantifying the contribution of diminishing green spaces and urban sprawl to urban heat island effect in a rapidly urbanizing metropolitan city of Pakistan. Land Use Policy 113, 105874. https://doi.org/10.1016/j.landusepol.2021.105874

Bastiaanssen, W.G.M.; Menenti, M.; Feddes, R.A.; Holtslag, A.A.M. A remote sensing surface energy balance algorithm for land (SEBAL). 1: Formulation. J. Hydrol 212– 213, 98–212. 1998.

Berland, A., Shiflett, S.A., Shuster, W.D., Garmestani, A.S., Goddard, H.C., Herrmann, D.L., Hopton, M.E., 2017. The role of trees in urban stormwater management. Landscape and Urban Planning 162, 167–177. https://doi.org/10.1016/j.landurbplan.2017.02.017

Berreta, E. Ecophysiology and management response of the subtropical grasslands of Southern America. In Proceedings of the XIX International Grassland Congress, Gomide, J.A.,

Mattos, W.R.S., Silva, S.C., Eds.; São Pedro: Piracicaba, Brazil, 11–21 February 2001; pp. 939-946.

Berry, R.; S.J. Livesley; L. Aye. Tree Canopy Shade Impacts on Solar Irradiance Received by Building Walls and Their Surface Temperature. Building and Environment 69, 2013, 91–100. 2013.

Bhattarai, N.; Quackenbush, L.J.; IM, J.; Shaw, S.B. A new optimized algorithm for automating endmember pixel selection in the SEBAL and METRIC models. Remote Sens. Environ. 196, 178–192. 2017.

Bisht, G.; Bras, R. L. Estimation of net radiation from the MODIS data under all sky conditions: Southern Great Plains case study. Remote Sensing of Environment, v.114, p.1522- 1534, 2010.

Bisht, G.; Venturini, V.; Islam, S.; Jiang, L. Estimation of the net radiation using MODIS (Moderate Resolution Imaging Spectroradiometer) data for clear-sky days. Remote Sensing of Environment, v.97, p.52-67, 2005.

Borges, C.K., dos Santos, C.A.C., Carneiro, R.G., da Silva, L.L., de Oliveira, G., Mariano, D., …, de, S., Medeiros, S., 2020. Seasonal variation of surface radiation and energy balances over two contrasting areas of the seasonally dry tropical forest (Caatinga) in the Brazilian semi-arid. Environ. Monit. Assess. 192 (8) https://doi.org/10.1007/s10661-020-08484-y.

Bowler, D.E.; L. Buyung-Ali; T.M. Knight; A.S. Pullin. Urban Greening to Cool Towns and Cities: A Systematic Review of the Empirical Evidence. Landscape and Urban Planning 97 (3): 147–55. 2010.

Brazilian Institute of Geography And Statistics. 2022 Brazilian population census. https://censo2022.ibge.gov.br/

Carlson, T. N., Arthur, S. T. The impact of land use — land cover changes due to urbanization on surface microclimate and hydrology: a satellite perspective, Global and Planetary Change, Volume 25, Issues 1–2, 2000, Pages 49-65. https://doi.org/10.1016/S0921-8181(00)00021-7.

Carrillo-Niquete, G.A., Andrade, J.L., Valdez-Lazalde, J.R., Reyes-García, C., Hernández-Stefanoni, J.L., 2022. Characterizing spatial and temporal deforestation and its effects on surface urban heat islands in a tropical city using Landsat time series. Landscape and Urban Planning 217, 104280. https://doi.org/10.1016/j.landurbplan.2021.104280

Chakraborty, T., Lee, X., 2019. A simplified urban-extent algorithm to characterize surface urban heat islands on a global scale and examine vegetation control on their spatiotemporal variability. International Journal of Applied Earth Observation and Geoinformation 74, 269–280. https://doi.org/10.1016/j.jag.2018.09.015

Chakraborty, T., Sarangi, C. & Tripathi, S.N. Understanding Diurnality and Inter-Seasonality of a Sub-tropical Urban Heat Island. Boundary-Layer Meteorol **163**, 287–309 (2017). https://doi.org/10.1007/s10546-016-0223-0

Charabi, Y., & Bakhit, A. (2011). Assessment of the canopy urban heat island of a coastal arid tropical city: The case of Muscat, Oman. Atmospheric Research, 101(1-2), 215–227. https://doi.org/10.1016/j.atmosres.2011.02.010.

Chen J; K. T. P. U.; Ustin S. L.; Suchanek T. H.; BOND B. J.; BROSOFSKE K. D.; FALK M. Net ecosystem exchanges of carbon, water, and energy in young and old-growth Douglas-Fir forests. Ecosystems v.7, p.534-544, 2004.

Chen, J.; He, T.; Jiang, B.; Liang, S. Estimation of all-sky all-wave daily net radiation at high latitudes from MODIS data, Remote Sensing of Environment, Volume 245, 2020, 111842. https://doi.org/10.1016/j.rse.2020.111842

Chen, Y., Yang, J., Yang, R., Xiao, X., Xia, J. (Cecilia), 2022. Contribution of urban functional zones to the spatial distribution of urban thermal environment. Building and Environment 216, 109000. https://doi.org/10.1016/j.buildenv.2022.109000

Christopherson, Robert W. (2017). Geosystems: an introduction to physical geography. Upper Saddle River, N.J.: Prentice Hall.

Chrysoulakis, N., Grimmond, S., Feigenwinter, C. et al. Urban energy exchanges monitoring from space. Scientific Reports **8**, 11498 (2018). https://doi.org/10.1038/s41598-018-29873-x

Claudino, C. M. de A., Coelho, V. H. R., Patriota, E. G., Bertrand, G. F., Almeida, C. das N. 2024. ESTIMET: a new algorithm for the Evolution and Spatial-Temporal Improvement of MODIS Evapotranspiration at finer spatial resolution and under all sky conditions - Validation over tropical biomes. Preprint, to be submitted in 2024.

Cleugh, H.A., Leuning, R., Mu, Q., Running, S.W., 2007. Regional evaporation estimates from flux tower and MODIS satellite data. Remote Sensing of Environment 106, 285–304. https://doi.org/10.1016/j.rse.2006.07.007

Clinton, N., Gong, P., 2013. MODIS detected surface urban heat islands and sinks: Global locations and controls. Remote Sensing of Environment 134, 294–304. https://doi.org/10.1016/j.rse.2013.03.008

Correia Filho, W.L.F., Santiago, D.D.B., Oliveira-Júnior, J.F.D., Silva Junior, C.A.D., 2019. Impact of urban decadal advance on land use and land cover and surface temperature in the city of Maceió, Brazil. Land Use Policy 87, 104026. https://doi.org/10.1016/j.landusepol.2019.104026

De Souza E Silva, R., Da Silva, R.M., De Freitas, A.F., Dos Santos, J.S., Santos, C.A.G., De Lima, E.R.V., 2022. Thermal comfort conditions at microclimate scale and surface urban

heat island in a tropical city: A study on João Pessoa city, Brazil. Int J Biometeorol 66, 1079–1093. https://doi.org/10.1007/s00484-022-02260-y.

Dewan, A., Kiselev, G., Botje, D., Mahmud, G.I., Bhuian, Md.H., Hassan, Q.K., 2021. Surface urban heat island intensity in five major cities of Bangladesh: Patterns, drivers and trends. Sustainable Cities and Society 71, 102926. https://doi.org/10.1016/j.scs.2021.102926

Di Bernardino, A., Iannarelli, A.M., Casadio, S., Mevi, G., Campanelli, M., Casasanta, G., Cede, A., Tiefengraber, M., Siani, A.M., Spinei, E., Cacciani, M., 2021. On the effect of sea breeze regime on aerosols and gases properties in the urban area of Rome, Italy. Urban Climate 37, 100842. https://doi.org/10.1016/j.uclim.2021.100842

Du, Hongyu; Wang, Duoduo; Wang, Yuanyuan; Zhao, Xiaolei; Qin, Fei; Jiang, Hong; Cai, Yongli. Influences of land cover types, meteorological conditions, anthropogenic heat, and urban area on surface urban heat island in the Yangtze River Delta Urban Agglomeration. Science of the Total Environment. 2016. 461-470. http://dx.doi.org/10.1016/j.scitotenv.2016.07.012

Duarte, H.F.; Dias, N.L.; Maggiotto, S.R. Assessing daytime downwelling longwave radiation estimates for clear and cloudy skies in Southern Brazil. Agric. For. Meteorol. 139, 171–181. 2006.

Dubreuil, V., Funatsu, B. M., Michot, V. Local rainfall trends and their perceptions by Amazonian communities. Climatic Change, v. 1, p. 1-12, 2017. https://doi.org/10.1007/s10584-017-2006-0.

Dugord, P. A., Lauf, S., Schuster, C., & Kleinschmit, B. (2014). Land use patterns, temperature distribution, and potential heat stress risk - The case study Berlin, Germany. Computers, Environment and Urban Systems, 48, 86–98. http://dx.doi.org/10.1016/j.compenvurbsys.2014.07.005

Evelyn, J. Fumifugium or the inconvenience of the air and smoak of London dissipated. Rota, 1976. 1661.

Fath, B., ed. 2018. Encyclopedia of Ecology. 2nd ed. Amsterdam: Elsevier.

Ferrari, A.; Kubilay, A.; Derome, D.; Carmeliet. The use of permeable and reflective pavements as a potential strategy for urban heat island mitigation, Urban Climate, Volume 31, 2020, 100534. https://doi.org/10.1016/j.uclim.2019.100534.

Ferreira, T. R., Silva, B. B. D., Moura, M. S. B. D., Verhoef, A., & Nóbrega, R. L. B. (2020). The use of remote sensing for reliable estimation of net radiation and its components: a case study for contrasting land covers in an agricultural hotspot of the Brazilian semiarid region. Agricultural and Forest Meteorology. https://doi.org/10.1016/j.agrformet.2020.108052

Flores R., J.L., Pereira Filho, A.J., Karam, H.A., 2016. Estimation of long term low resolution surface urban heat island intensities for tropical cities using MODIS remote sensing data. Urban Climate 17, 32–66. https://doi.org/10.1016/j.uclim.2016.04.002

Furley, P. A. The nature and diversity of neotropical savanna vegetation with particular reference to the Brazilian cerrados. Glob. Ecol. Biogeogr., 8 (1999), pp. 223-241 https://doi.org/https://doi.org/10.1046/j.1466-822X.1999.00142.x.

Gallo, G.P., A. L. McNab, T. R. Karl, J. F. Brown, J. J. Hood & J. D. Tarpley. The use of a vegetation index for assessment of the urban heat island effect, International Journal of Remote Sensing, 14:11, 2223-2230. 1993.

Gao, Y., Zhao, J., Han, L., 2022. Exploring the spatial heterogeneity of urban heat island effect and its relationship to block morphology with the geographically weighted regression model. Sustainable Cities and Society 76, 103431. https://doi.org/10.1016/j.scs.2021.103431

Giulietti, A. M., Bocage neta, A. L., castro, A. A. J. F., Gamarra rojas, C. F. L., Sampaio, E. V. S. B., Virgínio, J. F., Queiroz, L. P., figueiredo, M. A., Rodal, M. J. N., Barbosa, M. R. V., Harley, R. M. Diagnóstico da vegetação nativa do bioma Caatinga. In: Silva, J. M. C., Tabarelli, M., Fonseca, M. T., Lins, L. V. (Orgs.). Biodiversidade da Caatinga: áreas e ações prioritárias para a conservação. Brasília, Ministério do Meio Ambiente, 2004, p.47-90.

Gong, P., Li, X., Wang, J., Bai, Y., Chen, B., Hu, T., Liu, X., Xu, B., Yang, J., Zhang, W., Zhou, Y., 2020. Annual maps of global artificial impervious area (GAIA) between 1985 and 2018. Remote Sensing of Environment 236, 111510. https://doi.org/10.1016/j.rse.2019.111510

Grimm, N.B., Faeth, S.H., Golubiewski, N.E., Redman, C.L., Wu, J., Bai, X., Briggs, J.M., 2008. Global Change and the Ecology of Cities. Science 319, 756–760. https://doi.org/10.1126/science.1150195

Grimmond, C. S. B. (1992). The suburban energy balance: methodological considerations and results for a midlatitude west coast city under winter and spring conditions. Int. J. Climatol. 12, 481–497. https://doi.org/10.1002/joc.3370120506

Groleau, D.; Mestayer, P.G. Urban Morphology Influence on Urban Albedo: A Revisit with the SOLENE Model. Bound.-Lay. Meteorol. 2013, 147, 301–327.

Gupta, H. V., Kling, Harald, Yilmaz, Koray, Martinez, G. F. Decomposition of the mean squared error and NSE performance criteria: Implications for improving hydrological modelling. Journal of Hydrology, v. 377, n. 1–2, p. 80–91, out. 2009. http://dx.doi.org/10.1016/j.jhydrol.2009.08.003.

Halder, Dyutisree; Garg, Rahul Dev; Fedotov, Alexander. Latitudinal Trend Analysis of Land Surface Temperature to Identify Urban Heat Pockets in Global Coastal Megacities. Remote Sensing. 2023, 15(5), 1355. https://doi.org/10.3390/rs15051355.

He, S., Zhang, C., Meng, F., Bourque, C. P. A., Huang, Z., Li, X., Han, Y., Feng, S., Miao, L., Liu, C. Vegetation-cover control of between-site soil temperature evolution in a sandy desertland, Science of The Total Environment, Volume 908, 2024, 168372, https://doi.org/10.1016/j.scitotenv.2023.168372.

Herath, P., Thatcher, M., Jin, H., & Bai, X. (2021). Effectiveness of urban surface characteristics as mitigation strategies for the excessive summer heat in cities. Sustainable Cities and Society, 72, Article 103072. https://doi.org/10.1016/j.scs.2021.103072.

Hosseini, A., Pourahmad, A., & Pajoohan, M. (2016). Assessment of Institutions in Sustainable Urban-Management Effects on Sustainable Development of Tehran: Learning from a Developing Country. In Journal of Urban Planning and Development. https://doi.org/10.1061/(ASCE)UP.1943-5444.0000301

Howard, L. The climate of London. IAUC edition available. 2007. 1993. https://www.urbanclimate.org/documents/LukeHoward_Climate-of-London-V1.pdf.

Howard, L. The climate of London. IAUC edition available. 2007. 1993. Disponível em: https://www.urbanclimate.org/documents/LukeHoward_Climate-of-London-V1.pdf.

Hu, X.-M., Xue, M., Klein, P.M., Illston, B.G., Chen, S., 2016. Analysis of Urban Effects in Oklahoma City using a Dense Surface Observing Network. Journal of Applied Meteorology and Climatology 55, 723–741. https://doi.org/10.1175/JAMC-D-15-0206.1

Huete, A.R., 1988. A soil-adjusted vegetation index (SAVI). Remote Sensing of Environment 25, 295–309. https://doi.org/10.1016/0034-4257(88)90106-X

Hung, T.; Uchihama, D.; Ochi, S.; Yasuoka, Y. Assessment with satellite data of the urban heat island effects in Asian mega cities. Int. J. Appl. Earth Obs. Geoinf. 2006, 8, 34–48. https://doi.org/10.1016/j.jag.2005.05.003

Jiang, Z., Huete, A., Didan, K., Miura, T., 2008. Development of a two-band enhanced vegetation index without a blue band. Remote Sensing of Environment 112, 3833–3845. https://doi.org/10.1016/j.rse.2008.06.006

Kalnay, E., Cai, M. Impact of urbanization and land-use change on climate. Nature 423, 528–531 (2003). https://doi.org/10.1038/nature01675

Kalnay, E.; CAI, M. Impact of urbanization and land-use change on climate. Nature, 423(6939), 528–531. 2003.

Kato, S.; Yamaguchi, Y. Analysis of urban heat-island effect using ASTER and ETM+ Data: Separation of anthropogenic heat discharge and natural heat radiation from sensible heat flux. Remote Sensing of Environment, Volume 99, Issues 1–2, 2005, Pages 44-54. https://doi.org/10.1016/j.rse.2005.04.026.

Kendall, M. G. (1948). Rank correlation methods. Michigan: C. Griffin.

Khamchiangta, D., Dhakal, S. Time series analysis of land use and land cover changes related to urban heat island intensity: Case of Bangkok Metropolitan Area in Thailand. 2020. Journal of Urban Management. 2020 (9). 383-395. https://doi.org/10.1016/j.jum.2020.09.001.

Khosa, F. V.; Feig, G. T.; Van Der Merwe, M. R.; Mateyisi, M. J.; Mudau, A. E.; Savage, M. J. Evaluation of modeled actual evapotranspiration estimates from a land surface, empirical and satellite-based models using in situ observations from a South African semi-arid savanna ecosystem. Agricultural and Forest Meteorology, 279, 107706. 2019.

Kim, Yu, S., Li, D., Gatson, S. N., & Brown, R. D (2022). Linking landscape spatial heterogeneity to urban heat island and outdoor human thermal comfort in Tokyo: Application of the outdoor thermal comfort index. Sustainable Cities and Society, 87, Article 104262. https://doi.org/10.1016/j.scs.2022.104262.

Kruk, N.S.; Vendrame, I.F.; Rocha, H.R; Chou, S.C.; Cabral, O. Downwelling longwave radiation estimates for clear and all-sky conditions in the Sertãozinho region of São Paulo, Brazil. Theor. Appl. Climatol 99, 115–123. 2010.

Lai, J., Zhan, W., Quan, J., Bechtel, B., Wang, K., Zhou, J., Huang, F., Chakraborty, T., Liu, Z., Lee, X., 2021. Statistical estimation of next-day nighttime surface urban heat islands. ISPRS Journal of Photogrammetry and Remote Sensing 176, 182–195. https://doi.org/10.1016/j.isprsjprs.2021.04.009

Laipelt, L; Kayser, R. H. B.; Fleischmann, A. S.; Ruhoff, A.; Bastiaanssen, W.; Erickson, T. A.; Melton, F. Long-term monitoring of evapotranspiration using the SEBAL algorithm and Google Earth Engine cloud computing, ISPRS Journal of Photogrammetry and Remote Sensing, Volume 178, 2021, Pages 81-96. https://doi.org/10.1016/j.isprsjprs.2021.05.018.

Landsberg, H. E. The urban climate. New York: Academic press. 1981.

Li, H., Zhou, Y., Jia, G., Zhao, K., Dong, J., 2022. Quantifying the response of surface urban heat island to urbanization using the annual temperature cycle model. Geoscience Frontiers 13, 101141. https://doi.org/10.1016/j.gsf.2021.101141

Li, L., Zha, Y., & Zhang, J. (2020). Spatial and dynamic perspectives on surface urban heat island and their relationships with vegetation activity in Beijing, China, based on Moderate Resolution Imaging Spectroradiometer data. International Journal of Remote Sensing, 41(3), 882–896. https://doi.org/10.1080/01431161.2019.1650985

Li, L., Zha, Y., 2019. Satellite-Based Spatiotemporal Trends of Canopy Urban Heat Islands and Associated Drivers in China's 32 Major Cities. Remote Sensing 11, 102. https://doi.org/10.3390/rs11010102

Li, L., Zhan, W., Hu, L., Chakraborty, T. C., Wang, Z., Fu, P., Wang, D., Liao, W., Huang, F., Fu, H., Li, J., Liu, Z., Du, H., Wang, S. 2023. Divergent urbanisation-induced impacts on

global surface urban heat island trends since 1980s. Remote Sensing of Environment, Volume 295, 2023, 113650. https://doi.org/10.1016/j.rse.2023.113650

Lima, C.E.S.de, Costa, V.S.de O., Galvíncio, J.D., Silva, R.M.da, Santos, C.A.G, 2021. Assessment of automated evapotranspiration estimates obtained using the GP-SEBAL algorithm for dry forest vegetation (Caatinga) and agricultural areas in the Brazilian semiarid region. Agric. Water Manage. 250, 106863 https://doi.org/10.1016/j.agwat.2021.106863.

Liu, William Tse Horng. Remote sensing applications. Editora UNIDERP, 908p. Campo Grande, 2015.

Maimaitiyiming, M., Ghulam, A., Tiyip, T., Pla, F., Latorre-Carmona, P., Halik, Ü., Sawut, M., Caetano, M., 2014. Effects of green space spatial pattern on land surface temperature: Implications for sustainable urban planning and climate change adaptation. ISPRS Journal of Photogrammetry and Remote Sensing 89, 59–66. https://doi.org/10.1016/j.isprsjprs.2013.12.010.

Mäkiranta, A.; Hiltunen, E. Utilizing Asphalt Heat Energy in Finnish Climate Conditions. 2019. Energies, 12, 2101.

Mann, H.B. (1945) Non-Parametric Test against Trend. Econometrica, 13, 245-259. http://dx.doi.org/10.2307/1907187.

McDonald, R.I., Conservation for cities: How to plan & build natural infrastructure. 2015, Washington, D.C.: Island Press.

Miles, Victoria; Esau, Igor. Seasonal and Spatial Characteristics of Urban Heat Islands (UHIs) in Northern West Siberian Cities. Remote Sensing. 2017, 9 (10), 989. https://doi.org/10.3390/rs9100989

Miller, J.B. A formula for average foliage density. Australian Journal of Botany, v.15, p.141-144, 1967. DOI: https://doi.org/10.1071/BT9670141.

Moazzam, M.F.U., Doh, Y.H., Lee, B.G., 2022. Impact of urbanization on land surface temperature and surface urban heat Island using optical remote sensing data: A case study of Jeju Island, Republic of Korea. Building and Environment 222, 109368. https://doi.org/10.1016/j.buildenv.2022.109368

Mohajerani, A.; J. Bakaric; T. Jeffrey-Bailey. The Urban Heat Island Effect, Its Causes, and Mitigation, with Reference to the Thermal Properties of Asphalt Concrete. Journal of Environmental Management 197 (July): 522–38. 2017.

Monteiro, F.F., Gonçalves, W.A., Andrade, L.D.M.B., Villavicencio, L.M.M., Dos Santos Silva, C.M., 2021. Assessment of Urban Heat Islands in Brazil based on MODIS remote sensing data. Urban Climate 35, 100726. https://doi.org/10.1016/j.uclim.2020.100726

Monteith, J.L., 1965. Evaporation and Environment, in: Symposium of the Society for Experimental Biology. pp. 205–234.

Morakinyo, T.E.; A.A. Balogun; O.B. Adegun. Comparing the Effect of Trees on Thermal Conditions of Two Typical Urban Buildings. Urban Climate 3, 2013, 76–93. 2013.

Morini, E.; Castellani, B.; Presciutti, A.; Anderini, E.; Filipponi, M.; Nicolini, A.; Rossi, F. Experimental Analysis of the Effect of Geometry and Facade Materials on Urban District's Equivalent Albedo. Sustainability 2017, 9, 1245.

Moro, M.F., Lughadha, E.N., Araújo, F.S., Martins, F.R., 2016. A phytogeographical metaanalysis of the Semiarid Caatinga domain in Brazil. Bot. Rev. 82, 91–148. https://www.doi.org/10.1007/s12229-016-9164-z.

Mu, Q., Heinsch, F.A., Zhao, M., Running, S.W., 2007. Development of a global evapotranspiration algorithm based on MODIS and global meteorology data. Remote Sensing of Environment 111, 519–536. https://doi.org/10.1016/j.rse.2007.04.015

Mu, Q., Zhao, M., Running, S.W., 2011. Improvements to a MODIS global terrestrial evapotranspiration algorithm. Remote Sensing of Environment 115, 1781–1800. https://doi.org/10.1016/j.rse.2011.02.019

Muñoz Sabater, J., (2019): ERA5-Land monthly averaged data from 1981 to present. Copernicus Climate Change Service (C3S) Climate Data Store (CDS). doi:10.24381/cds.68d2bb30

Muñoz-Jiménez, J.C.; Sobrino, J.A.; Gillespie, A.; Sabol, D.; Gustafson, W.T. Improved land surface emissivity over agricultural areas using ASTER NDVI. Remote Sens. Environ. 103, 474–487. 2006.

Myhre, G., D. Shindell, F.-M. Bréon, W. Collins, J. Fuglestvedt, J. Huang, D. Koch, J.-F. Lamarque, D. Lee, B. Mendoza, T. Nakajima, A. Robock, G. Stephens, T. Takemura and H. Zhang, 2013: Anthropogenic and Natural Radiative Forcing. In: Climate Change 2013: The Physical Science Basis. Contribution of Working Group I to the Fifth Assessment Report of the Intergovernmental Panel on Climate Change [Stocker, T.F., D. Qin, G.-K. Plattner, M. Tignor, S.K. Allen, J. Boschung, A. Nauels, Y. Xia, V. Bex and P.M. Midgley (eds.)]. Cambridge University Press, Cambridge, United Kingdom and New York, NY, USA.

Nascimento, A.C.L. do, Galvani, E., Gobo, J.P.A., Wollmann, C.A., 2022. Comparison between Air Temperature and Land Surface Temperature for the City of São Paulo, Brazil. Atmosphere 13, 491. https://doi.org/10.3390/atmos13030491

Nature Based Solutions Handbook, Somarakis, G.; Stagakis, S.; Chrysoulakis, N. Think Nature project funded by the EU Horizon 2020 research and innovation programme. Nature Based Solutions Handbook. https://platform.think-nature.eu/system/files/thinknature_handbook_final_print_0.pdf.

Nowak, D.J.; J.F. Dwyer. Understanding the Benefits and Costs of Urban Forest Ecosystems. In Urban and Community Forestry in the Northeast, edited by J.E. Kuser, 25–46. Dordrecht: Springer Netherlands. 2007.

Nwakaire, C. M.; Onn, C. C.; Yap, S. P.; Yuen, C. W.; Onodagu, P. D. Urban Heat Island Studies with emphasis on urban pavements: A review. Sustainable Cities and Society, 63, Article 102476. 2020. http://dx.doi.org/10.1016/j.scs.2020.102476.

Ojeh, V. N., Balogun, A. A., & Okhimamhe, A. A. (2016). Urban-rural temperature differences in Lagos. Climate, 4(2), 29. https://doi.org/10.3390/cli4020029.

Oke, T. R. (1982). The energetic basis of the urban heat island. Quarterly Journal of the Royal Meteorological Society, 108(455), 1–24. https://doi.org/10.1002/qj.49710845502

Oke, T. R. (1987). Boundary layer climates Routledge. London: Mathuem & CO. https://doi.org/10.4324/9780203407219

Oke, T. R. (1988). The urban energy balance. Prog. Phys. Geog. 12:471–508. https://doi.org/10.1177/030913338801200401

Oke, T. R.; Mills, G.; Christen, A.; Voogt, J. A. Urban climates. Cambridge University Press. 2017.

Ouyang, Xiao; Xu, Jun; Li, Jiayu; Wei, Xiao; Li, Yonghui. Land space optimization of urban-agriculture-ecological functions in the Changsha-Zhuzhou-Xiangtan Urban Agglomeration, China, Land Use Policy, Volume 117, 2022, 106112. https://doi.org/10.1016/j.landusepol.2022.106112.

Peng, J., Ma, J., Liu, Q., Liu, Y., Hu, Y., Li, Y., Yue, Y., 2018. Spatial-temporal change of land surface temperature across 285 cities in China: An urban-rural contrast perspective. Science of The Total Environment 635, 487–497. https://doi.org/10.1016/j.scitotenv.2018.04.105

Peng, S., Piao, S., Ciais, P., Friedlingstein, P., Ottle, C., Bréon, F.-M., Nan, H., Zhou, L., Myneni, R.B., 2012. Surface Urban Heat Island Across 419 Global Big Cities. Environ. Sci. Technol. 46, 696–703. https://doi.org/10.1021/es2030438

Peng, Shijia; Feng, Zhili; Liao, Huixuan; Huang, Bei; Peng, Shaolin; Zhou, Ting. Spatial-temporal pattern of, and driving forces for, urban heat island in China. Ecological Indicators 96. 2019. 127-132. https://doi.org/10.1016/j.ecolind.2018.08.059

Peres, L.D.F., Lucena, A.J.D., Rotunno Filho, O.C., França, J.R.D.A., 2018. The urban heat island in Rio de Janeiro, Brazil, in the last 30 years using remote sensing data. International Journal of Applied Earth Observation and Geoinformation 64, 104–116. https://doi.org/10.1016/j.jag.2017.08.012

Piracha, A., Chaudhary, M.T., 2022. Urban Air Pollution, Urban Heat Island and Human Health: A Review of the Literature. Sustainability 14, 9234. https://doi.org/10.3390/su14159234

Portela, C.I., Massi, K.G., Rodrigues, T., Alcântara, E., 2020. Impact of urban and industrial features on land surface temperature: Evidences from satellite thermal indices. Sustainable Cities and Society 56, 102100. https://doi.org/10.1016/j.scs.2020.102100

Prata, A.J. A new long-wave formula for estimating downwelling clear-sky radiation at the surface. Q. J. R. Meteorol. Soc. 122, 1127–1151. 1996.

Qiao, Z., Tian, G., & Xiao, L. (2013). Diurnal and seasonal impacts of urbanization on the urban thermal environment: a case study of Beijing using MODIS data. ISPRS Journal of Photogrammetry and Remote Sensing, 85, 93–101.

Qihao Weng; Dengsheng Lu; Jacquelyn Schubring. Estimation of land surface temperature-vegetation abundance relationship for urban heat island studies, Remote Sensing of Environment, Volume 89, Issue 4, 2004, Pages 467-483.

Quan, J., Chen, Y., Zhan, W., Wang, J., Voogt, J., Wang, M., 2014. Multi-temporal trajectory of the urban heat island centroid in Beijing, China based on a Gaussian volume model. Remote Sensing of Environment 149, 33–46. https://doi.org/10.1016/j.rse.2014.03.037

Quan, J., Zhan, W., Chen, Y., Wang, M., & Wang, J. (2016). Time series decomposition of remotely sensed land surface temperature and investigation of trends and seasonal variations in surface urban heat islands. Journal of Geophysical Research Atmospheres, 121(6), 2638–2657. 10.1002/2015JD024354. https://doi.org/10.1002/2015JD024354

Queiroz, L.P., Cardoso, D., Fernandes, M.F., Moro, M.F., 2017. Diversity and evolution of flowering plants of the Caatinga domain. In: da Silva, J.M.C., Leal, I.R., Tabarelli, M. (Eds.), Caatinga: The Largest Tropical Dry Forest Region in South America. Springer, Cham, pp. 23–63. https://doi.org/10.1007/978-3-319-68339-3.

Raj S, Paul SK, Chakraborty A, Kuttippurath J. Anthropogenic forcing exacerbating the urban heat islands in India. J Environ Manage. 2020 Mar 1;257:110006. doi: 10.1016/j.jenvman.2019.110006. Epub 2019 Dec 24. PMID: 31989962.

Randow, C., Manzi, A., Kruijt, B. et al. Comparative measurements and seasonal variations in energy and carbon exchange over forest and pasture in South West Amazonia. Theor Appl Climatol 78, 5–26 (2004). https://doi.org/10.1007/s00704-004-0041-z.

Raymond, C., Matthews, T., Horton, R.M., 2020. The emergence of heat and humidity too severe for human tolerance. Sci. Adv. 6, eaaw1838. https://doi.org/10.1126/sciadv.aaw1838

Rocha, A. D., Vulova, S., Meier, F., Forster, M., Kleinschmit, B. 2022. Mapping evapotranspirative and radiative cooling services in an urban environment. Sustainable Cities and Society 85, 104051.

Rodell, M., Houser, P.R., Jambor, U., Gottschalck, J., Mitchell, K., Meng, C.-J., Arsenault, K., Cosgrove, B., Radakovich, J., Bosilovich, M., Entin, J.K., Walker, J.P., Lohmann, D., Toll, D., 2004. The Global Land Data Assimilation System. Bull. Amer. Meteor. Soc. 85, 381–394. https://doi.org/10.1175/BAMS-85-3-381

Roth, M. Review of urban climate research in (sub) tropical regions. International Journal of Climatology: A Journal of the Royal Meteorological Society, 27(14), 1859–1873. 2007.

Rouse, J.W., Haas, R.H., Schell, J.A. and Deering, D.W. (1973) Monitoring Vegetation Systems in the Great Plains with ERTS (Earth Resources Technology Satellite). Proceedings of 3rd Earth Resources Technology Satellite Symposium, Greenbelt, 10-14 December, SP-351, 309-317.

Ryu, Y.; S. Kang; S. Moon; J. Kim. Evaluation of land surface radiation balance derived from moderate resolution imaging spectroradiometer (MODIS) over complex terrain and heterogeneous landscape on clear sky days. Agricultural and Forest Meteorology, v. 148, p. 1538-1552. 2008.

Sabino, M., Silva, J.B.; Costa, R.O.; Duarte, L.G.; Souza, A.P., 2020. Biophysical parameters and extreme air temperature indices in the Cerrado-Amazon transition. Sociedade e Natureza (Online) 32, 513-524. http://dx.doi.org/10.14393/SN-v32-2020.

Saher, Rubab; Stephen, Haroon; Ahmad, Sajjad. Urban evapotranspiration of green spaces in arid regions through two established approaches: a review of key drivers, advancements, limitations, and potential opportunities, Urban Water Journal, 2020.

Sailor, D. J., Georgescu, M., Milne, J. M., and Hart, M. A. (2015). Development of a national anthropogenic heating database with an extrapolation for international cities. Atmos. Environ. 118, 7–18. doi: 10.1016/j.atmosenv.2015.07.016.

Samal, D.R.; Gedam, S.S.; Nagarajan, R. GIS Based Drainage Morphometry and Its Influence on Hydrology in Parts of Western Ghats region, Maharashtra, India. Geocarto International, 30, 755-778. 2015.

Santamouris, M., Ding, L., Fiorito, F., Oldfield, P., Osmond, P., Paolini, R., Prasad, D., Synnefa, A., 2017. Passive and active cooling for the outdoor built environment – Analysis and assessment of the cooling potential of mitigation technologies using performance data from 220 large scale projects. Solar Energy 154, 14–33. https://doi.org/10.1016/j.solener.2016.12.006

Santos e Silva, C. M., Bezerra, B. G., Mendes, K. R., Mutti, P. R., Rodrigues, D. T., Costa, G. B., Oliveira, P. E. S. de, Reis, J., Marques, T. V., Ferreira, R. R., Campos, S., Ramos, T. M., Mariana, M. L., Vieira, A. C. C. F. de O., Silva, C. L. C. da, Silva, A. C., Antonino, A. C. D., Menezes, R. Rainfall and rain pulse role on energy, water vapor and CO2 exchanges in a tropical semiarid environment. Agricultural and Forest Meteorology, Volume 345, 2024, 109829. https://doi.org/10.1016/j.agrformet.2023.109829.

Santos, A.R. dos, De Oliveira, F.S., Da Silva, A.G., Gleriani, J.M., Gonçalves, W., Moreira, G.L., Silva, F.G., Branco, E.R.F., Moura, M.M., Da Silva, R.G., Juvanhol, R.S., De Souza, K.B., Ribeiro, C.A.A.S., De Queiroz, V.T., Costa, A.V., Lorenzon, A.S., Domingues, G.F., Marcatti, G.E., De Castro, N.L.M., Resende, R.T., Gonzales, D.E., De Almeida Telles, L.A., Teixeira, T.R., Dos Santos, G.M.A.D.A., Mota, P.H.S., 2017. Spatial and temporal distribution of urban heat islands. Science of The Total Environment 605–606, 946–956. https://doi.org/10.1016/j.scitotenv.2017.05.275

Santos, C.A.C.; Silva, B.B.; Da, Rao, T.V.R.; Satyamurti, P.; Manzi, A.O. Downwelling longwave radiation estimates for clear-sky conditions over Northeast Brazil. Rev. Bras. Meteorology 26, 443–450. 2011.

Säumel, I., F. Weber, and I. Kowarik. 2016. "Toward Livable and Healthy Urban Streets: Roadside Vegetation Provides Ecosys

Scherer, D.; Fehrenbach, U.; Lakes, T.; Lauf, S.; Meier, F.; Schuster, C. Quantification of heat-Stress related mortality hazard, vulnerability and risk in Berlin, Germany. Die Erde; Zeitschrift der Gesellschaft fur Erdkunde zu Berlin, 144(3–4), 238–259. 2013.

Sen, P. K. (1968). Estimates of the regression coefficient based on Kendall's tau. Journal of the American Statistical Association, 63(324), 1379–1389.

Sfîcă, L., Corocăescu, A.-C., Crețu, C.-Ștefănel, Amihăesei, V.-A., Ichim, P., 2023. Spatiotemporal Features of the Surface Urban Heat Island of Bacău City (Romania) during the Warm Season and Local Trends of LST Imposed by Land Use Changes during the Last 20 Years. Remote Sensing 15, 3385. https://doi.org/10.3390/rs15133385

Shahmohamadi, P.; Che-Ani, A.; Maulud, K.; Tawil, N.; Abdullah, N. The impact of anthropogenic heat on formation of urban heat island and energy consumption balance. Urban Stud. Res. 2011, 497524. https://doi.org/10.1155/2011/497524.

Shen, Pengke; Zhao, Ma, Yongjing; Liu, Shuguang. Urbanization-induced Earth's surface energy alteration and warming: A global spatiotemporal analysis. Remote Sensing of Environment, Volume 284. 2023, 113361. https://doi.org/10.1016/j.rse.2022.113361.

Shojaei, P., Gheysari, M., Myers, B., Eslamian, S., Shafieiyoun, E., & Esmaeili, H. (2017). Effect of different land cover/use types on canopy layer air temperature in an urban area with a dry climate. Building and Environment, 125, 451–463. https://doi.org/10.1016/j.buildenv.2017.09.010.

Shojanoori, Razieh; Shafri, Helmi. Review on the Use of Remote Sensing for Urban Forest Monitoring. Arboriculture & Urban Forestry. 2016. 42. 400-417.

Si, M., Li, Z.-L., Nerry, F., Tang, B.-H., Leng, P., Wu, H., Zhang, X., Shang, G., 2022. Spatiotemporal pattern and long-term trend of global surface urban heat islands characterized by dynamic urban-extent method and MODIS data. ISPRS Journal of Photogrammetry and Remote Sensing 183, 321–335. https://doi.org/10.1016/j.isprsjprs.2021.11.017

Silva, B. B. D.; Braga, A. C.; Braga, C. C. Balanço de radiação no perímetro irrigado São Gonçalo - PB mediante imagens orbitais. Revista Caatinga, v. 24, n. 3, 2011.

Silva, B. B.; Wilcox, B. P.; Silva, V. P. R.; Montenegro, S. M. G. L.; Oliveira, L. M. M. Changes to the energy budget and evapotranspiration following conversion of tropical savannas to agricultural lands in São Paulo State, Brazil. Ecohydrology, v.8, p.1272-1283, 2015.

Silva, J.M.C.D., Prasad, S., Diniz-Filho, J.A.F., 2017. The impact of deforestation, urbanization, public investments, and agriculture on human welfare in the Brazilian Amazonia. Land Use Policy 65, 135–142. https://doi.org/10.1016/j.landusepol.2017.04.003

Silva, J.S., Silva, R.M.D., Santos, C.A.G., 2018. Spatiotemporal impact of land use/land cover changes on urban heat islands: A case study of Paço do Lumiar, Brazil. Building and Environment 136, 279–292. https://doi.org/10.1016/j.buildenv.2018.03.041

Souza, C.M., Z. Shimbo, J., Rosa, M.R., Parente, L.L., A. Alencar, A., Rudorff, B.F.T., Hasenack, H., Matsumoto, M., G. Ferreira, L., Souza-Filho, P.W.M., De Oliveira, S.W., Rocha, W.F., Fonseca, A.V., Marques, C.B., Diniz, C.G., Costa, D., Monteiro, D., Rosa, E.R., Vélez-Martin, E., Weber, E.J., Lenti, F.E.B., Paternost, F.F., Pareyn, F.G.C., Siqueira, J.V., Viera, J.L., Neto, L.C.F., Saraiva, M.M., Sales, M.H., Salgado, M.P.G., Vasconcelos, R., Galano, S., Mesquita, V.V., Azevedo, T., 2020. Reconstructing Three Decades of Land Use and Land Cover Changes in Brazilian Biomes with Landsat Archive and Earth Engine. Remote Sensing 12, 2735. https://doi.org/10.3390/rs12172735

Stenka Vulova, Alby Duarte Rocha, Fred Meier, Hamideh Nouri, Christian Schulz, Chris Soulsby, Doerthe Tetzlaff, Birgit Kleinschmit. City-wide, high-resolution mapping of evapotranspiration to guide climate-resilient planning, Remote Sensing of Environment, Volume 287, 2023, 113487. https://doi.org/10.1016/j.rse.2023.113487.

Stone, B., & Rodgers, M. O. (2001). Urban form and thermal efficiency: How the design of cities influences the Urban Heat Island effect. Journal of the American Planning Association, 67(2), 186–198. https://doi.org/10.1080/01944360108976228.

Sugita, M., Brutsaert, W.H. Cloud effect in the estimation of instantaneous downwelling longwave radiation. Water Resour. Res. 29, 599–605. 1993.

Suomi, J., Hjort, J., Käyhkö, J., 2012. Effects of scale on modelling the urban heat island in Turku, SW Finland. Clim. Res. 55, 105–118. https://doi.org/10.3354/cr01123

Taha, H. Meso-urban meteorological and photochemical modeling of heat island mitigation. Atmospheric Environment. Volume 42, Issue 38, 2008, Pages 8795-8809. https://doi.org/10.1016/j.atmosenv.2008.06.036

Taha, H. Modeling the Impacts of Large-Scale Albedo Changes on Ozone Air Quality in the South Coast Air Basin. Atmos. Environ. 1997, 31, 1667–1676.

Tang, B.; LI, Z.L. Estimation of instantaneous net surface longwave radiation from MODIS cloud-free data. Remote Sens. Environ. 112, 3482–3492. 2008.

Tasumi, M. Progress in Operational Estimation of Regional Evapotranspiration Using Satellite Imagery. Ph.D. dissertation. University of Idaho, Moscow, ID. 2003.

Tavares-Damasceno, J.P., Silveira, J.L.G.S., Camara, ˆ T., Stedile, P.C., Macario, P., ToledoLima, G.S., Pichorim, M., 2017. Effect of drought on demography of Pileated Finch (Coryphospingus pileatus: thraupidae) in northeastern Brazil. J. Arid Environ. 147, 63–70. https://doi.org/10.1016/j.jaridenv.2017.09.006

Teixeira, A. de C., Scherer-Warren, M., Hernandez, F., Andrade, R., Leivas, J., 2013. Large-Scale Water Productivity Assessments with MODIS Images in a Changing Semi-Arid Environment: A Brazilian Case Study. Remote Sensing 5, 5783–5804. https://doi.org/10.3390/rs5115783

Teixeira, A. H. C., Bastiaanssen, W.G.M., Ahmad, M.D., Bos, M.G. Reviewing SEBAL input parameters for assessing evapotranspiration and water productivity for the Low-Middle São Francisco River basin, Brazil: Part A: Calibration and validation, Agricultural and Forest Meteorology, Volume 149, Issues 3–4, 2009, Pages 462-476, ISSN 0168-1923, https://doi.org/10.1016/j.agrformet.2008.09.016.

Teixeira, A.H. de C., Victoria, D.C., Andrade, R.G., Leivas, J.F., Bolfe, E.L., Cruz, C.R., 2014. Coupling MODIS images and agrometeorological data for agricultural water productivity analyses in the Mato Grosso State, Brazil, in: Neale, C.M.U., Maltese, A. (Eds.), . Presented at the SPIE Remote Sensing, Amsterdam, Netherlands, p. 92390W. https://doi.org/10.1117/12.2065967

Teixeira, H. M.; Cardoso, I. M.; Bianchi, F. J. J. A.; Silva, A. da C.; Jamme, D.; Peña-Claros, M. Linking vegetation and soil functions during secondary forest succession in the Atlantic Forest, Forest Ecology and Management, Volume 457, 2020, 117696. https://doi.org/10.1016/j.foreco.2019.117696.

Tian, P., Li, J., Cao, L., Pu, R., Wang, Z., Zhang, H., Chen, H., Gong, H., 2021. Assessing spatiotemporal characteristics of urban heat islands from the perspective of an urban expansion and green infrastructure. Sustainable Cities and Society 74, 103208. https://doi.org/10.1016/j.scs.2021.103208

Tong, X.; Zhang, J.; Meng, P.; LI, J.; Zheng, N. Environmental controls of evapotranspiration in a mixed plantation in North China. International Journal of Biometeorology, 61(2), 227–238. 2017.

Tran, H.; Uchihama, D.; Ochi, S.; Yasuoka, Y. Assessment with satellite data of the urban heat island effects in Asian mega cities. International Journal of Applied Earth Observation and Geoinformation 8 (2006) 34–48. doi:10.1016/j.jag.2005.05.003.

Trenberth, K. E.; Fasullo, J. T. Climate extremes and climate change: The Russian heat wave and other climate extremes of 2010. Journal of Geophysical Research Atmospheres, 117(17), 1–12. 2012.

United Nations, Department Of Economic And Social Affairs. Statistical Annex: Global and regional data for Sustainable Development Goal indicators. New York: United Nations, 2018.

Vahmani, P.; Hogue, T.S. High-resolution land surface modeling utilizing remote sensing parameters and the Noah UCM: A case study in the Los Angeles Basin. Hydrol. Earth Syst. Sci. 2014, 18, 4791–4806.

Valle Júnior, L. C. G.; Ventura, T. M.; Gomes, R. S. R.; DE Nogueira, J.; DE A. Lobo, Vourlitis; G. L., & Rodrigues, T. R. Comparative assessment of modelled and empirical reference evapotranspiration methods for a brazilian savanna. Agricultural Water Management, 232, 106040. 2020.

Venter, Z.S., Chakraborty, T., Lee, X., 2021. Crowdsourced air temperatures contrast satellite measures of the urban heat island and its mechanisms. Sci. Adv. 7, eabb9569. https://doi.org/10.1126/sciadv.abb9569

Voogt, J. A., & Oke, T. R. (2003). Thermal remote sensing of urban climates. Remote Sensing of Environment, 86, 370–384. https://doi.org/10.1016/S0034-4257(03)00079-8.

Vujovic S, Haddad B, Karaky H, Sebaibi N, Boutouil M. Urban Heat Island: Causes, Consequences, and Mitigation Measures with Emphasis on Reflective and Permeable Pavements. CivilEng. 2021; 2(2):459-484. https://doi.org/10.3390/civileng2020026

Wan, W., Liu, Z., Li, K., Wang, G., Wu, H., Wang, Q., 2021. Drought monitoring of the maize planting areas in Northeast and North China Plain. Agricultural Water Management 245, 106636. https://doi.org/10.1016/j.agwat.2020.106636

Wang, C.; Yang, J.; Myint, S.W; Wang, Z.H.; Tong, B. Empirical modeling, and spatio-temporal patterns of urban evapotranspiration for the Phoenix metropolitan area, Arizona. GIScience Remote Sens. 53 (6), 778–792. 2016.

Wang, C.; Yang, J.; Myint, S.W; Wang, Z.H.; Tong, B. Empirical modeling, and spatio-temporal patterns of urban evapotranspiration for the Phoenix metropolitan area, Arizona. GIScience Remote Sens. 53 (6), 778–792. 2016.

Wang, J., Xiao, X., Basara, J., Wu, X., Bajgain, R., Qin, Y., Doughty, R.B., Moore III, B., 2021. Impacts of juniper woody plant encroachment into grasslands on local climate. Agric. For. Meteorol. 307, 108508 https://doi.org/10.1016/j.agrformet.2021.108508.

Wang, K.; Wang, J.; Wang, P.; Sparrow, M.; Yang, J.; Chen, H. Influences of urbanization on surface characteristics as derived from the Moderate-Resolution Imaging Spectroradiometer: A case study for the Beijing metropolitan area. Journal of Geophysical Research Atmospheres, 112(D22). 2007.

Wang, X.; Huo, Z.; Shukla, M. K.; Wang, X.; Guo, P.; Xu, X.; Huang, G. Energy fluxes and evapotranspiration over irrigated maize field in an arid area with shallow groundwater. Agricultural Water Management, 228, 105922. 2020.

Wang, Y.; F. Bakker; R. DE Groot; H. Wörtche. 2014. Effect of Ecosystem Services Provided by Urban Green Infrastructure on Indoor Environment: A Literature Review. Building and Environment 77 (July): 88–100. 2014.

West, T. A. P., Börner, J., Fearnside, P. M. Climatic benefits from the 2006–2017 avoided deforestation in Amazonian Brazil. Frontiers in Forests and Global Change, v. 2, n. 52, 2019. https://doi.org/10.3389/ffgc.2019.00052.

Wienert, U.; Kuttler, W. The dependence of the urban heat island intensity on latitude—A statistical approach. Meteorol. Z. 2005, 14, 677–686.

Wolf, K.L.; S.T. Lam; J.K. Mckeen; G.R.A. Richardson; M. Van Den Bosch; A.C. Bardekjian. Urban Trees and Human Health: A Scoping Review. International Journal of Environmental Research and Public Health 17 (12): 4371. 2020.

Xian, G., Shi, H., Auch, R., Gallo, K., Zhou, Q., Wu, Z., Kolian, M., 2021. The effects of urban land cover dynamics on urban heat Island intensity and temporal trends. GIScience & Remote Sensing 58, 501–515. https://doi.org/10.1080/15481603.2021.1903282

Xiao, H., Weng, Q., 2007. The impact of land use and land cover changes on land surface temperature in a karst area of China. Journal of Environmental Management 85, 245–257. https://doi.org/10.1016/j.jenvman.2006.07.016

Xu, Di; Chen, Ruishan. Comparison of urban heat island and urban reflection in Nanjing City of China. Sustainable Cities and Society. 2017. Volume 31. 26-36. https://doi.org/10.1016/j.scs.2017.01.017

Yang, C.; Li, Q.; Zhao, T.; Liu, H.; Gao, W.; Shi, T.; Guan, M.; Wu, G. Detecting Spatiotemporal Features and Rationalities of Urban Expansions within the Guangdong–Hong Kong–Macau Greater Bay Area of China from 1987 to 2017 Using Time-Series Landsat Images and Socioeconomic Data. Remote Sens. 2019, 11, 2215.

Yang, J. C., Wang, Z. H., Chen, F., Miao, S. G., Tewari, M., Voogt, J. A., et al. (2015). Enhancing hydrologic modelling in the coupled weather research and forecasting–urban modelling system. Bound. Layer Meteorol. 155, 87–109. doi:10.1007/s10546-014-9991-6.

Yang, W., Luan, Y., Liu, X., Yu, X., Miao, L., and Cui, X. (2017). A new global anthropogenic heat estimation based on high-resolution nighttime light data. Sci. Data. 4:170116. doi: 10.1038/sdata.2017.116

Yang, X.; LI, Y. The Impact of Building Density and Building Height Heterogeneity on Average Urban Albedo and Street Surface Temperature. Build. Environ. 2015, 90, 146–156.

Yao, R., Wang, L., Huang, X., Niu, Y., Chen, Y., & Niu, Z. (2018). The influence of different data and method on estimating the surface urban heat island intensity. Ecological Indicators, 89, 45–55.

Yuan, J.; Farnham, C.; Emura, K. Development of a Retro-Reflective Material as Building Coating and Evaluation on Albedo of Urban Canyons and Building Heat Loads. Energy Build. 2015, 103, 107–117.

Zha, Y., Gao, J., Ni, S., 2003. Use of normalized difference built-up index in automatically mapping urban areas from TM imagery. International Journal of Remote Sensing 24, 583–594. https://doi.org/10.1080/01431160304987

Zhang, L., Yang, L., Zohner, C.M., Crowther, T.W., Li, M., Shen, F., Guo, M., Qin, J., Yao, L., Zhou, C., 2022. Direct and indirect impacts of urbanization on vegetation growth across the world's cities. Sci. Adv. 8, eabo0095. https://doi.org/10.1126/sciadv.abo0095

Zhang, X., 2015. Reconstruction of a complete global time series of daily vegetation index trajectory from long-term AVHRR data. Remote Sensing of Environment 156, 457–472. https://doi.org/10.1016/j.rse.2014.10.012

Zhang, Y.; LI, L.; Chen, L.; Liao, Z.; Wang, Y.; Wang, B.; Yang, X. A Modified Multi-Source Parallel Model for Estimating Urban Surface Evapotranspiration Based on ASTER Thermal Infrared Data. Remote Sens. 2017, 9, 1029.

Zhang, Y.; Li, L.; Qin, K.; Wang, Y.; Chen, L.; Yang, X. Remote sensing estimation of urban surface evapotranspiration based on a modified Penman–Monteith model. J. Appl. Remote Sens. 2018, 12, 1.

Zhao L, Lee X, Smith RB, Oleson K. Strong contributions of local background climate to urban heat islands. Nature. 2014 Jul 10;511(7508):216-9. doi: 10.1038/nature13462. PMID: 25008529.

Zhou, D., Zhao, S., Liu, S., Zhang, L., Zhu, C., 2014. Surface urban heat island in China's 32 major cities: Spatial patterns and drivers. Remote Sensing of Environment 152, 51–61. https://doi.org/10.1016/j.rse.2014.05.017

Zhou, T., Liu, H., Gou, P., Xu, N. Conflict or Coordination? measuring the relationships between urbanization and vegetation cover in China, Ecological Indicators, Volume 147, 2023, 109993, https://doi.org/10.1016/j.ecolind.2023.109993.

Zhou, X., Okaze, T., Ren, C., Cai, M., Ishida, Y., Watanabe, H., Mochida, A., 2020. Evaluation of urban heat islands using local climate zones and the influence of sea-land breeze. Sustainable Cities and Society 55, 102060. https://doi.org/10.1016/j.scs.2020.102060

Zillman, J. W. A study of some aspects of the radiation and heat budgets of the southern hemisphere oceans. Meteorological Study, n.26, Meteorology Canberra, Australia Dept. of the Inter, 1972.

8 APPENDIXES

8.1 Table S1: Population and population density of the 21 Metropolitan Regions

Table S1. Population and population density of the 21 Metropolitan Regions

Metropolitan Region	Population density (hab/km^2)	Total population (hab)
SP	2,610.29	20,743,587
RJ	1,751.71	13,191,031
BH	541.32	5,127,694
DF	50.85	4,808,484
PA	417.31	4,317,508
FO	548.09	4,077,811
SA	910.71	3,984,479
CU	234.51	3,731,769
RE	1,349.00	3,726,442
CAM	881.54	3,342,707
BE	549.02	2,677,089
GO	357.27	2,613,491
MA	19.89	2,532,226
VI	872.18	2,033,067
SAN	784.13	1,897,551
SL	175.89	1,656,503
NA	4,488.03	1,647,414
FLO	181.53	1,356,861
JP	476.77	1,331,885
MAC	409,320.31	1,330,291
TE	113.85	1,249,822

8.2 Figure S1 to S21: Annual (5-year-period) spatial distributions of Built-up index (BU, 250-m spatial resolution)

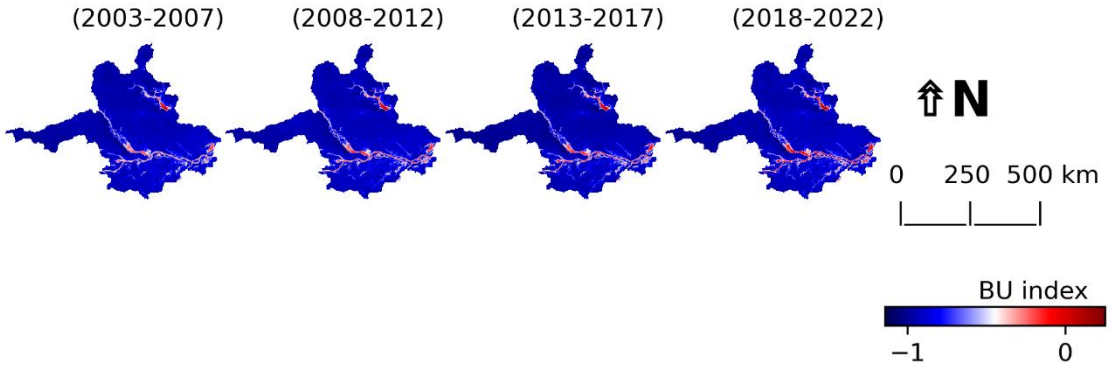

Fig. S1. Annual (5-year-period) spatial distributions of Built-up index for Manaus (MA).

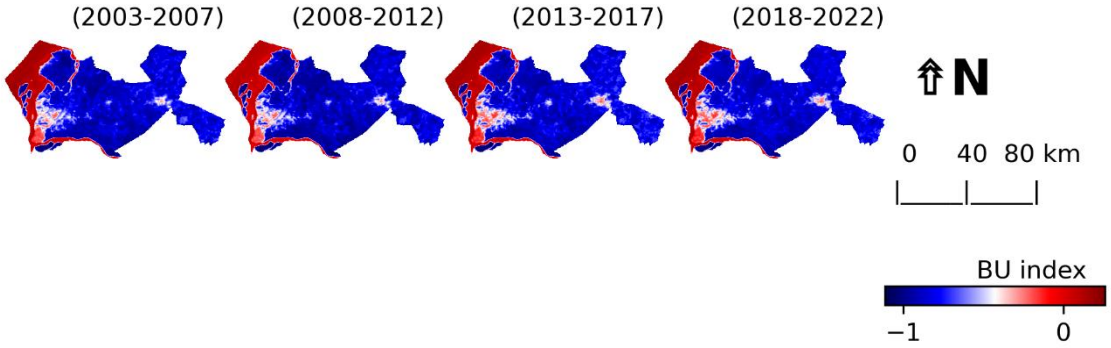

Fig. S2. Annual (5-year-period) spatial distributions of Built-up index for Belém (BE).

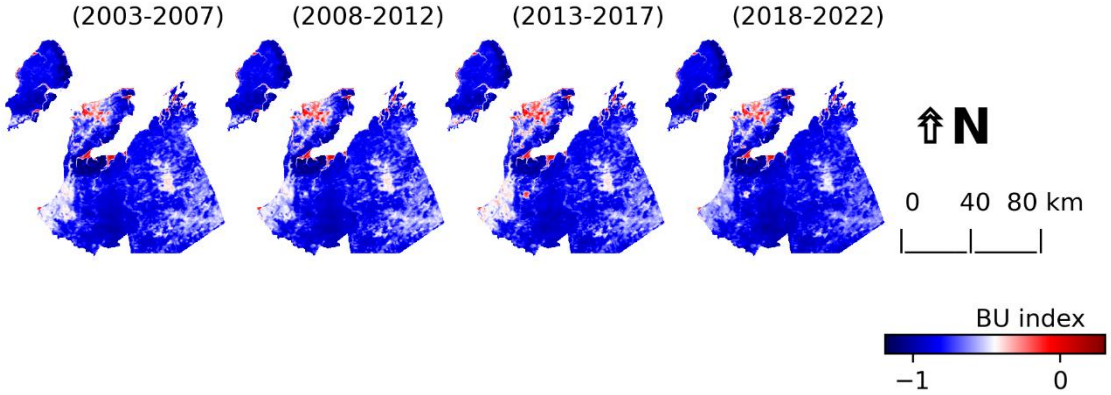

Fig. S3. Annual (5-year-period) spatial distributions of Built-up index for São Luís (SL).

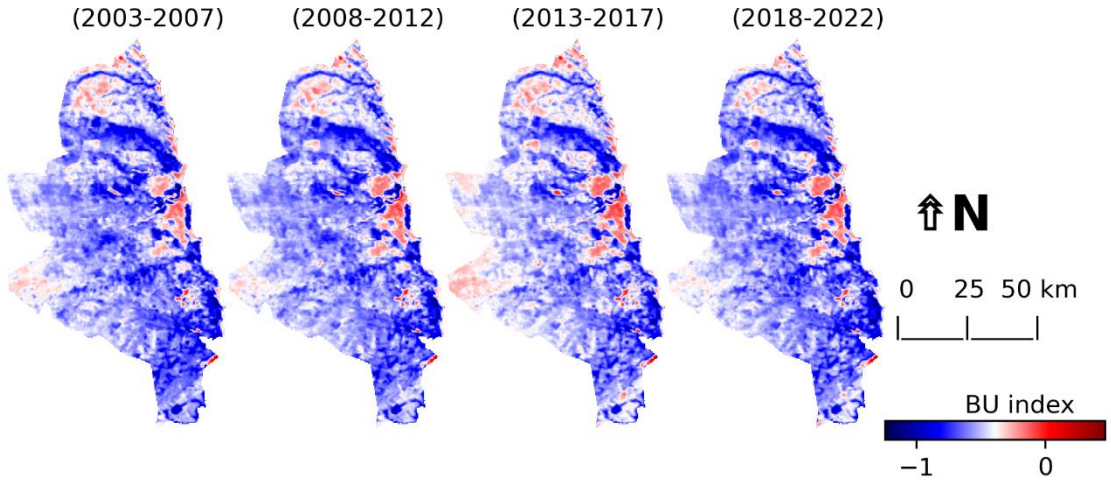

Fig. S4. Annual (5-year-period) spatial distributions of Built-up index for Natal (NA).

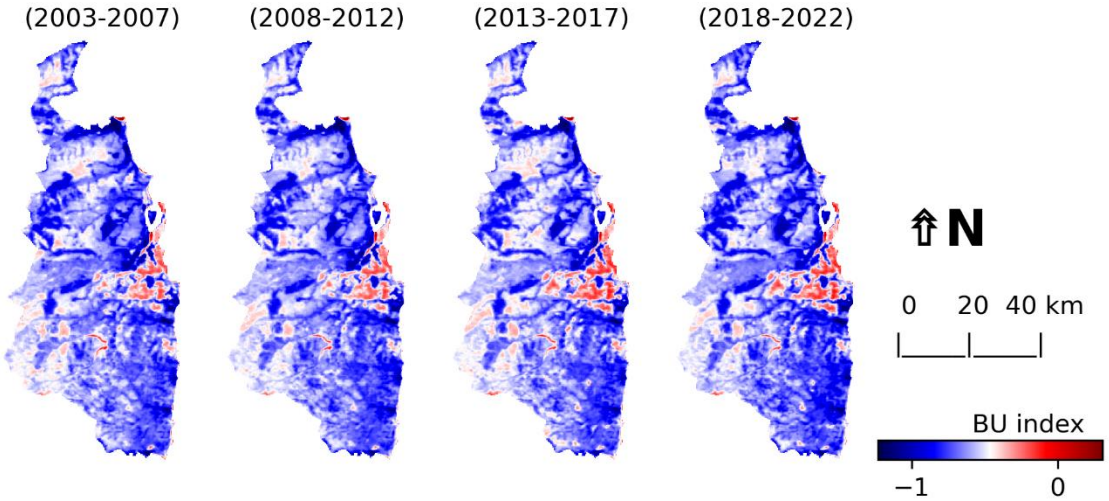

Fig. S5. Annual (5-year-period) spatial distributions of Built-up index for João Pessoa (JP).

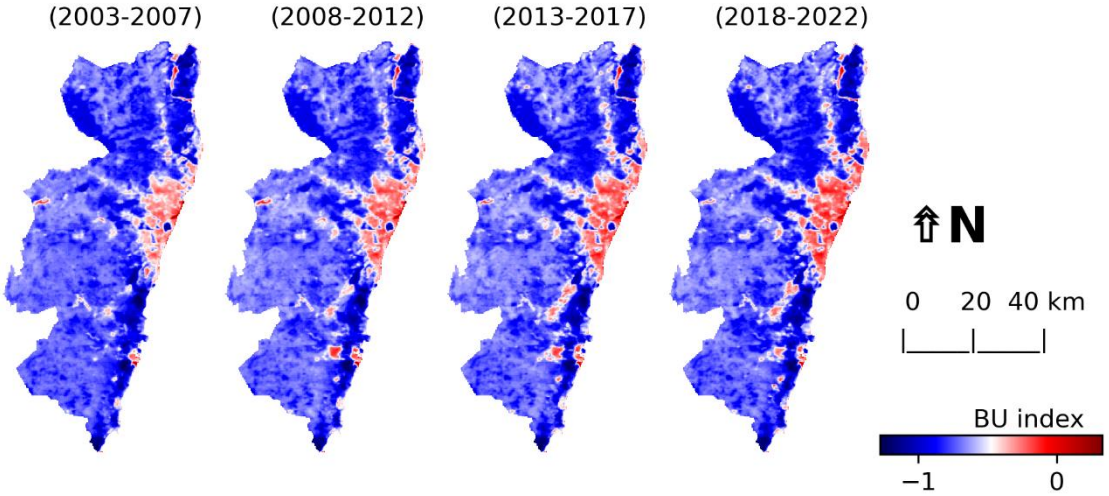

Fig. S6. Annual (5-year-period) spatial distributions of Built-up index for Recife (RE).

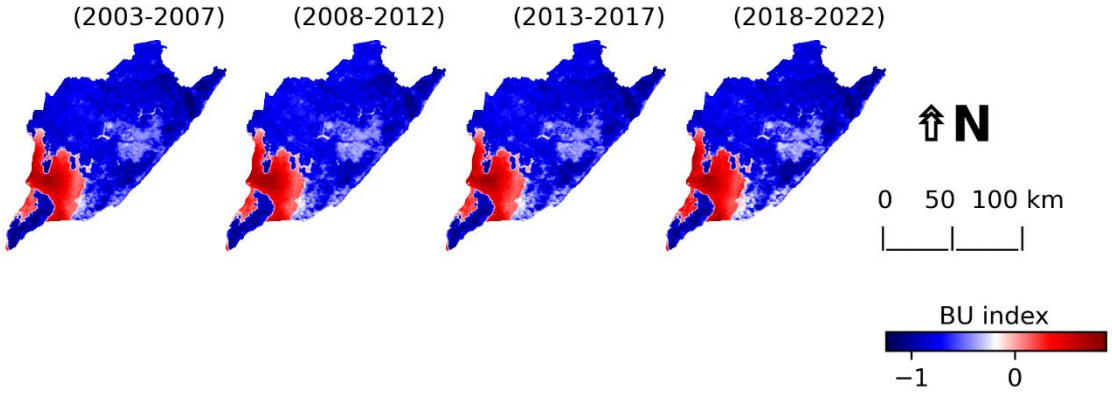

Fig. S7. Annual (5-year-period) spatial distributions of Built-up index for Salvador (SA).

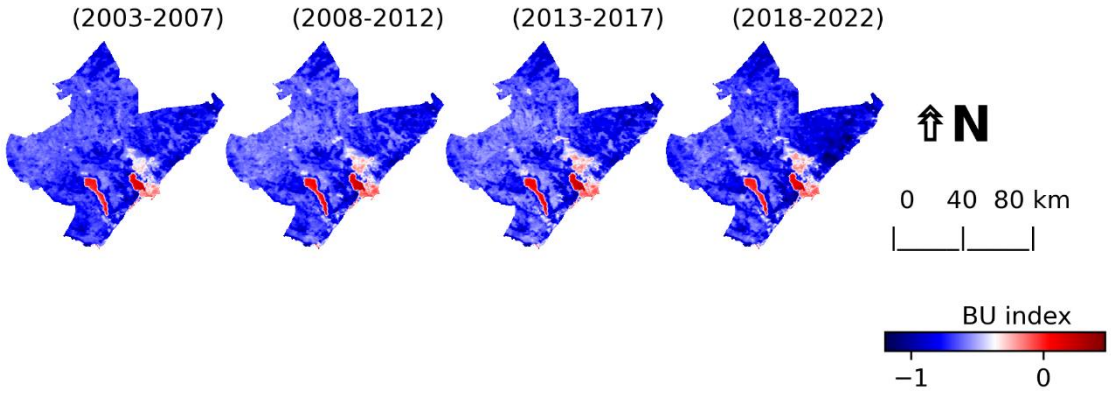

Fig. S8. Annual (5-year-period) spatial distributions of Built-up index for Maceió (MAC).

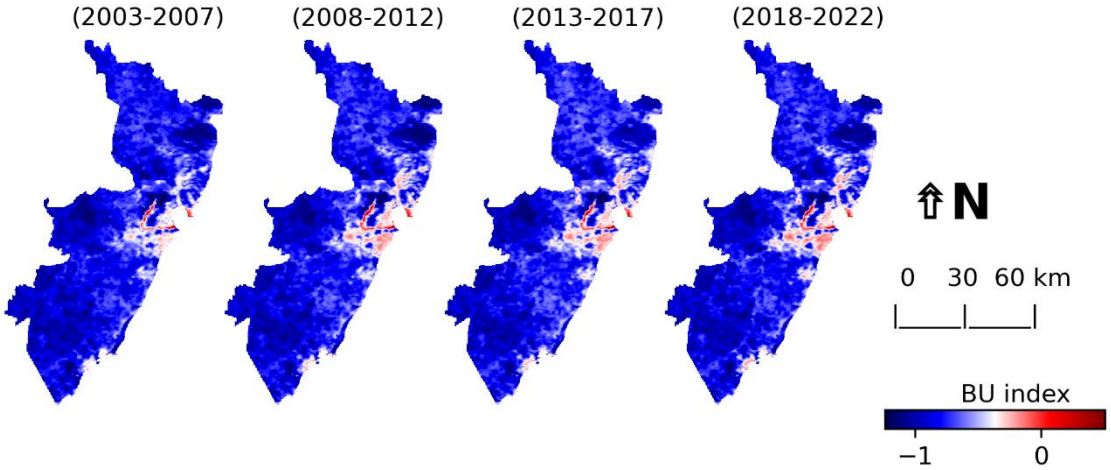

Fig. S9. Annual (5-year-period) spatial distributions of Built-up index for Vitória (VI).

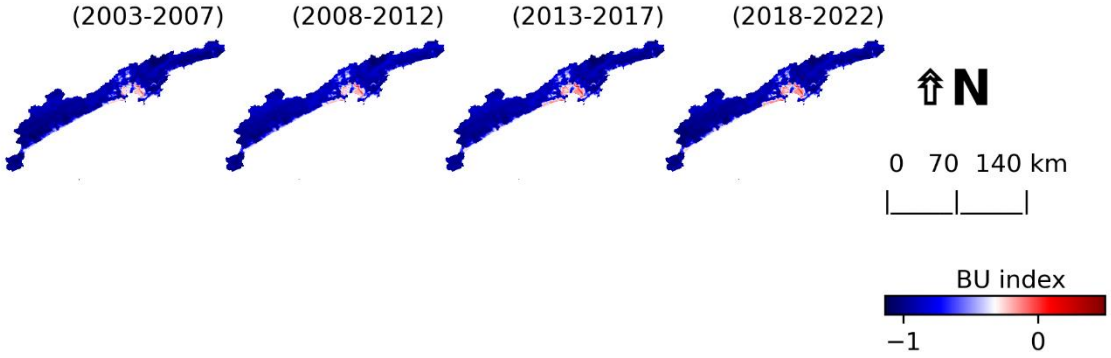

Fig. S10. Annual (5-year-period) spatial distributions of Built-up index for Santos (SAN).

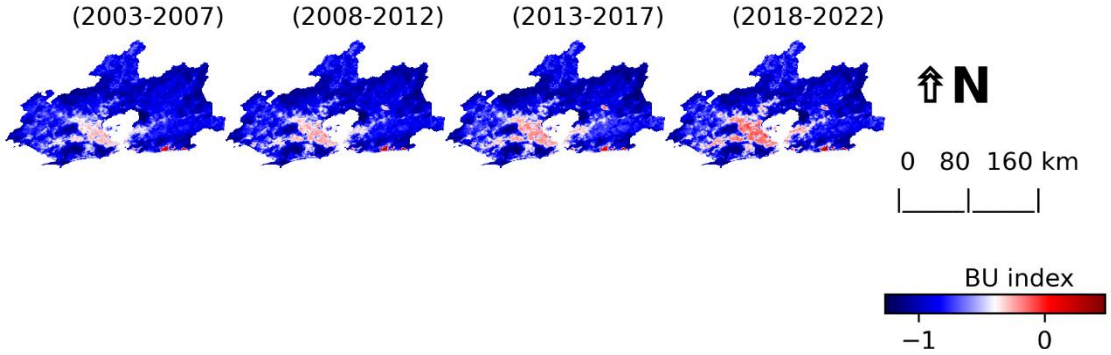

Fig. S11. Annual (5-year-period) spatial distributions of Built-up index for Rio de Janeiro (RJ).

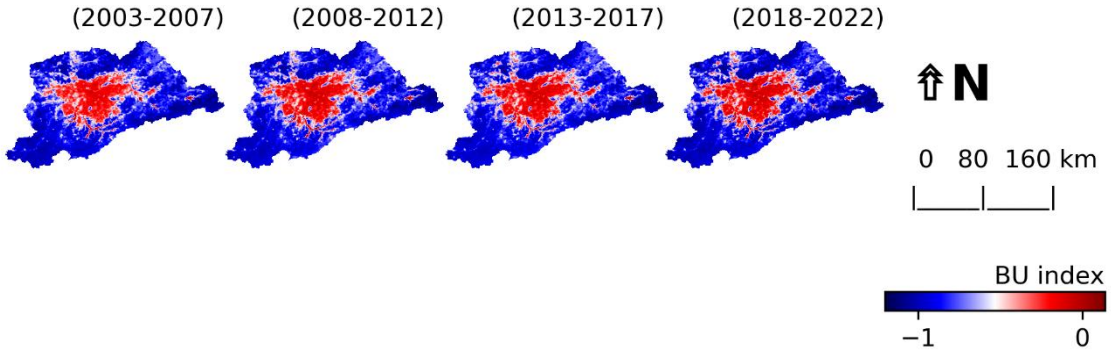

Fig. S12. Annual (5-year-period) spatial distributions of Built-up index for São Paulo (SP).

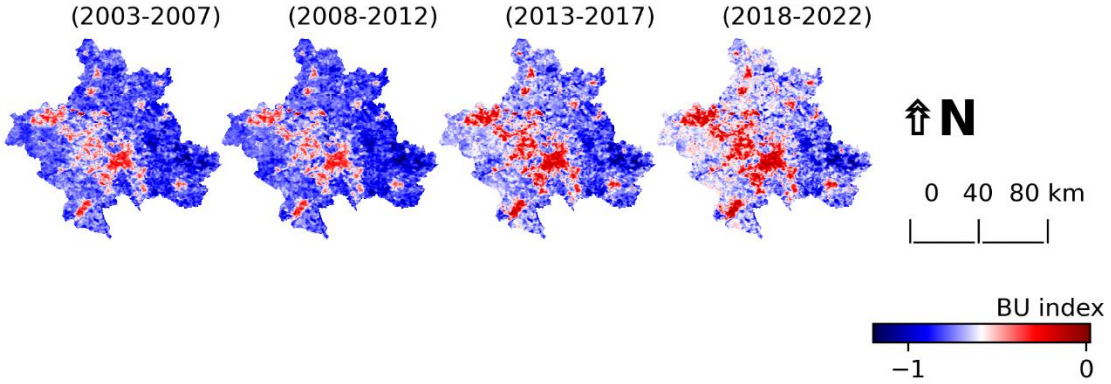

Fig. S13. Annual (5-year-period) spatial distributions of Built-up index for Campinas (CAM).

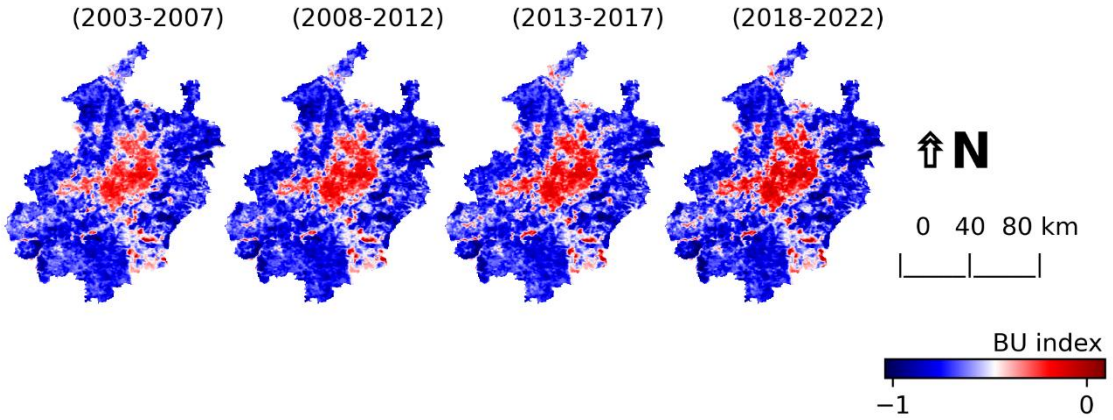

Fig. S14. Annual (5-year-period) spatial distributions of Built-up index for Belo Horizonte (BH).

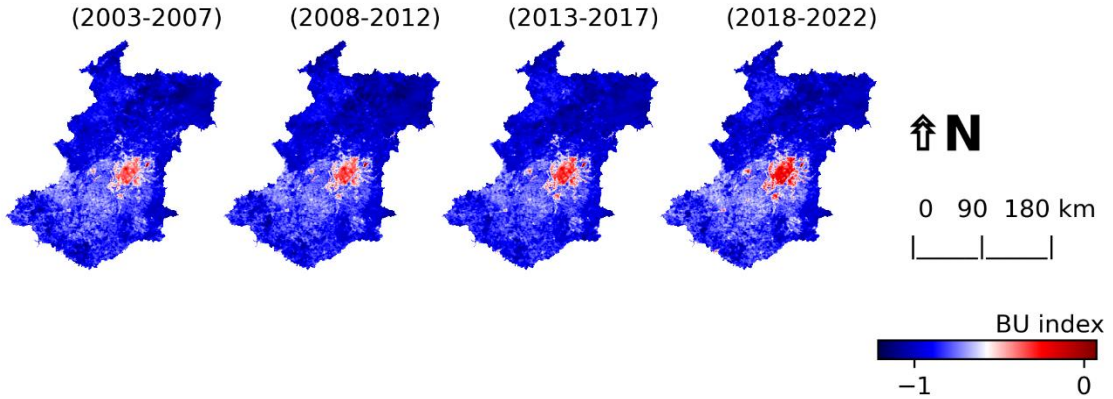

Fig. S15. Annual (5-year-period) spatial distributions of Built-up index for Curitiba (CU).

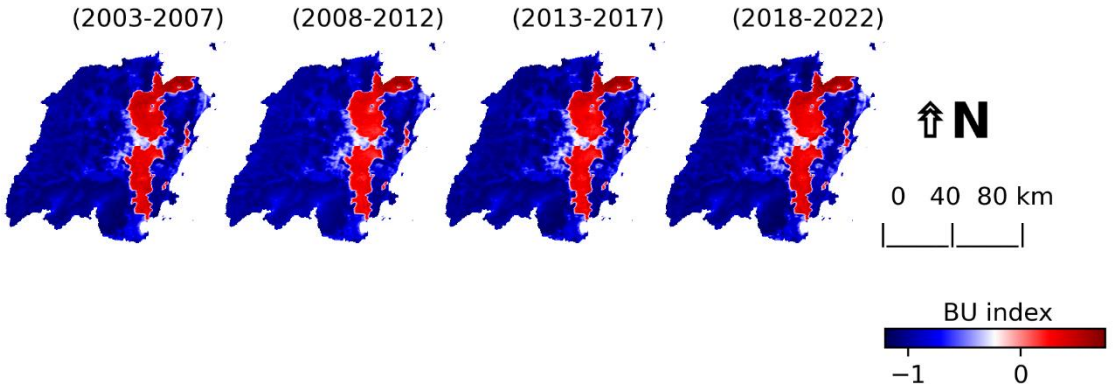

Fig. S16. Annual (5-year-period) spatial distributions of Built-up index for Florianópolis (FLO).

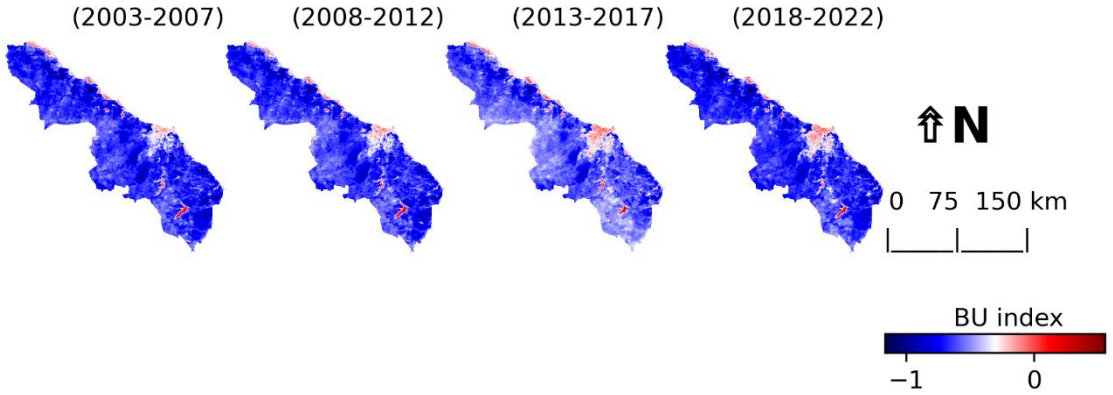

Fig. S17. Annual (5-year-period) spatial distributions of Built-up index for Fortaleza (FO).

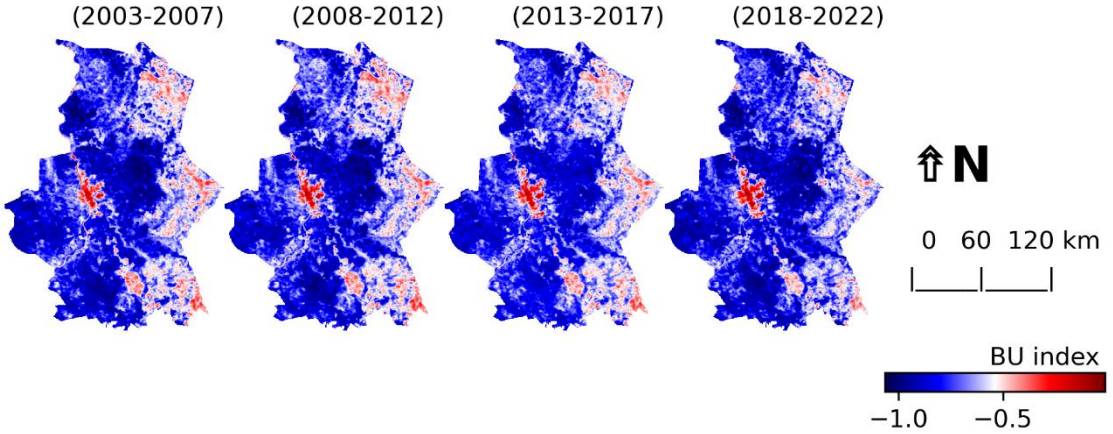

Fig. S18. Annual (5-year-period) spatial distributions of Built-up index for Teresina (TE).

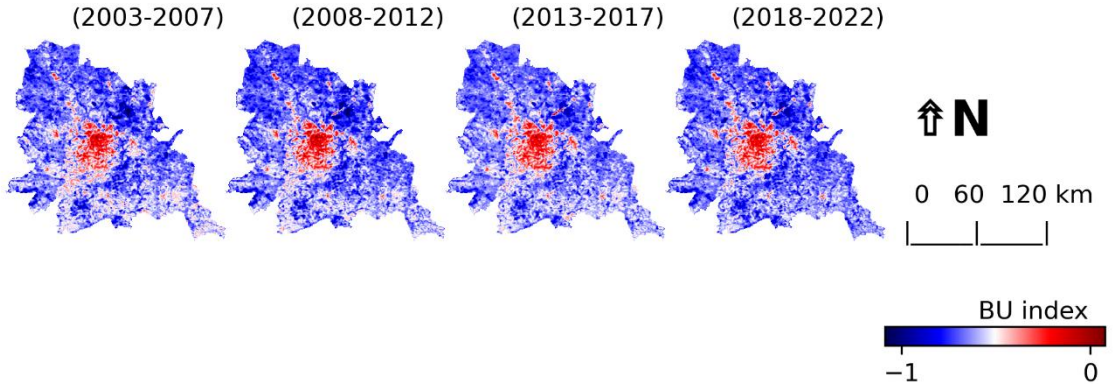

Fig. S19. Annual (5-year-period) spatial distributions of Built-up index for Goiânia (GO).

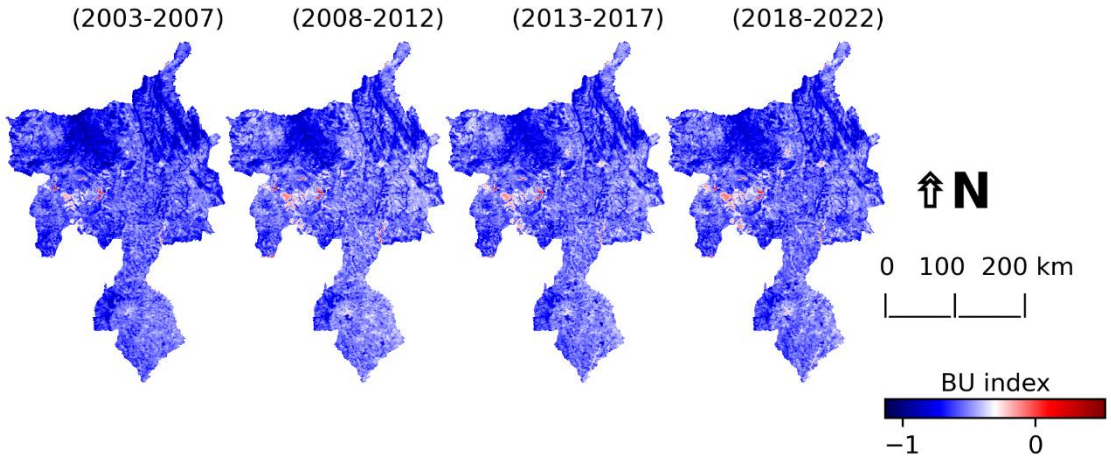

Fig. S20. Annual (5-year-period) spatial distributions of Built-up index for Distrito Federal (DF).

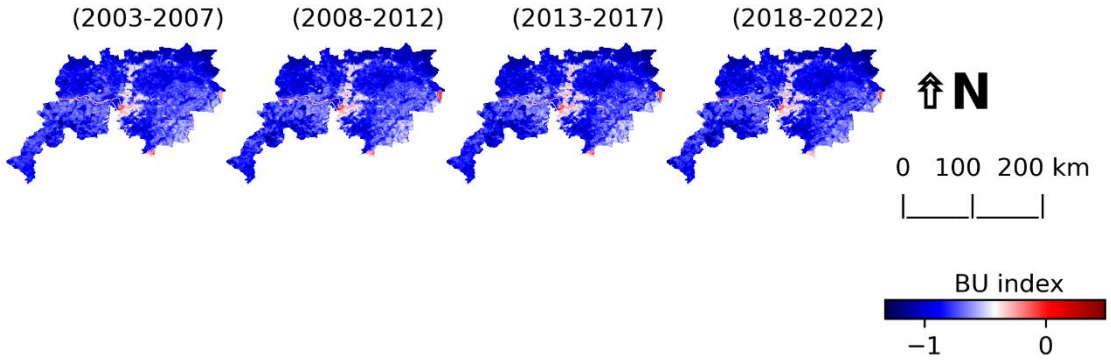

Fig. S21. Annual (5 year-period) Built-up index of Porto Alegre (PA)

8.3 Tables S2 to S5: Associations between the variables

Tables S2. Associations between urban LST and urban areas (UAs)

MR	day LST x UA			night LST x UA		
	r	R2	KGE	r	R2	KGE
MA	0,72	0,51	0,13	0,55	0,30	0,11
BE	0,46	0,21	0,09	0,58	0,34	0,12
SL	0,73	0,53	0,13	0,49	0,24	0,10
NA	0,58	0,34	0,12	0,07	0,01	0,00
JP	0,44	0,20	0,08	0,44	0,20	0,08
RE	0,63	0,40	0,13	0,46	0,21	0,09
MAC	0,74	0,55	0,13	0,39	0,15	0,07
SA	0,74	0,55	0,13	0,30	0,09	0,04
VI	0,81	0,66	0,12	0,34	0,12	0,05
BH	0,52	0,27	0,10	0,02	0,00	0,00
CAM	0,76	0,58	0,13	0,03	0,00	0,00
SAN	0,40	0,16	0,07	0,20	0,04	0,02
RJ	0,76	0,57	0,13	0,63	0,40	0,13
SP	-0,19	0,04	0,02	-0,42	0,18	0,08
FLO	0,38	0,14	0,06	-0,20	0,04	0,02
CU	-0,14	0,02	0,01	-0,25	0,06	0,03
FO	0,84	0,71	0,11	0,53	0,28	0,11
TE	0,88	0,77	0,09	0,73	0,53	0,13
GO	0,74	0,55	0,13	0,68	0,46	0,13
DF	0,25	0,06	0,03	-0,38	0,14	0,06
PA	0,22	0,05	0,02	0,09	0,01	0,00

Tab. S3. Associations between daytime and nighttime Rn, and ET with urban areas (UA).

MR	day Rn x UA			night Rn x UA			ET x UA		
	r	R^2	KGE	r	R^2	KGE	r	R^2	KGE
MA	-0,36	0,13	0,06	0,75	0,56	0,13	-0,64	0,42	0,13
BE	-0,44	0,19	0,08	0,77	0,59	0,13	0,00	0,00	0,00
SL	0,33	0,11	0,05	0,71	0,51	0,13	0,05	0,00	0,00
NA	0,26	0,07	0,03	0,23	0,05	0,03	-0,57	0,33	0,12
JP	0,78	0,61	0,13	0,62	0,38	0,13	0,00	0,00	0,00
RE	0,76	0,57	0,13	0,65	0,42	0,13	0,28	0,08	0,04
MAC	0,47	0,22	0,09	0,35	0,13	0,06	-0,18	0,03	0,02
SA	0,35	0,12	0,06	0,58	0,34	0,12	-0,04	0,00	0,00
VI	0,36	0,13	0,06	0,64	0,41	0,13	-0,71	0,50	0,13
BH	0,41	0,17	0,07	0,32	0,10	0,05	-0,57	0,33	0,12
CAM	0,41	0,17	0,07	0,37	0,13	0,06	0,70	0,49	0,13
SAN	-0,14	0,02	0,01	0,33	0,11	0,05	0,27	0,07	0,03
RJ	0,30	0,09	0,04	0,66	0,43	0,13	-0,84	0,70	0,11
SP	0,00	0,00	0,00	-0,17	0,03	0,01	0,09	0,01	0,00
FLO	0,52	0,27	0,10	0,62	0,38	0,13	0,10	0,01	0,01
CU	-0,20	0,04	0,02	0,32	0,11	0,05	0,21	0,04	0,02
FO	0,48	0,23	0,09	0,70	0,49	0,13	-0,48	0,23	0,09
TE	-0,05	0,00	0,00	0,79	0,62	0,13	-0,47	0,22	0,09
GO	0,16	0,03	0,01	-0,19	0,43	0,13	-0,81	0,66	0,12
DF	0,48	0,23	0,09	0,66	0,04	0,02	-0,21	0,04	0,02
PA	0,11	0,01	0,01	0,16	0,03	0,01	-0,44	0,19	0,08

Tab. S4. Associations between daytime and nighttime LST with EVI2 and α.

MR	day LST x EVI2			night LST x EVI2			day LST x α			night LST x α		
	r	R^2	KGE	r	R^2	KGE	r	R^2	KGE	r	R^2	KGE
MA	-0,53	0,28	0,11	-0,36	0,13	0,06	-0,49	0,24	0,10	-0,28	0,08	0,04
BE	-0,37	0,14	0,06	-0,53	0,28	0,11	-0,52	0,27	0,10	-0,58	0,33	0,12
SL	-0,66	0,44	0,13	-0,52	0,27	0,10	-0,59	0,35	0,12	-0,45	0,20	0,08
NA	-0,32	0,10	0,05	-0,28	0,08	0,04	-0,33	0,11	0,05	-0,26	0,07	0,03
JP	-0,24	0,06	0,03	-0,39	0,15	0,07	-0,26	0,07	0,03	-0,33	0,11	0,05
RE	-0,50	0,25	0,10	-0,37	0,14	0,06	-0,55	0,30	0,11	-0,35	0,12	0,06
MAC	-0,65	0,42	0,13	-0,45	0,20	0,08	-0,57	0,32	0,12	-0,34	0,12	0,05
SA	-0,48	0,23	0,09	-0,17	0,03	0,01	-0,45	0,20	0,08	-0,04	0,00	0,00
VI	-0,72	0,52	0,13	-0,25	0,06	0,03	-0,73	0,54	0,13	-0,28	0,08	0,04
BH	-0,50	0,25	0,10	-0,10	0,01	0,01	-0,73	0,53	0,13	-0,46	0,21	0,09
CAM	-0,65	0,42	0,13	-0,05	0,00	0,00	-0,36	0,13	0,06	0,23	0,05	0,03
SAN	0,14	0,02	0,01	-0,03	0,00	0,00	-0,03	0,00	0,00	-0,31	0,10	0,04
RJ	-0,61	0,37	0,12	-0,53	0,28	0,11	-0,57	0,32	0,12	-0,61	0,38	0,13
SP	0,49	0,24	0,10	0,42	0,18	0,08	0,29	0,06	0,03	0,44	0,19	0,08
FLO	-0,24	0,06	0,03	0,25	0,06	0,03	-0,25	0,06	0,03	0,22	0,05	0,02
CU	0,38	0,14	0,06	0,21	0,04	0,02	0,46	0,21	0,09	0,33	0,11	0,05
FO	-0,67	0,45	0,13	-0,39	0,16	0,07	-0,54	0,29	0,11	-0,41	0,17	0,07
TE	-0,82	0,67	0,12	-0,64	0,40	0,13	-0,77	0,59	0,13	-0,64	0,41	0,13
GO	-0,65	0,42	0,13	-0,68	0,46	0,13	-0,62	0,38	0,13	-0,49	0,24	0,10
DF	-0,11	0,01	0,01	0,50	0,25	0,10	-0,14	0,02	0,01	0,40	0,16	0,07
PA	0,02	0,00	0,00	0,26	0,07	0,03	-0,03	0,00	0,00	0,06	0,00	0,00

Tab. S5. Associations between land surface temperature (LST) and the surface biophysical parameters.

MR	day LST x day Rn			night LST x night Rn			day LST x ET			night LST x ET		
	r	R^2	KGE	r	R^2	KGE	r	R^2	KGE	r	R^2	KGE
MA	0,12	0,02	0,01	0,75	0,57	0,13	-0,70	0,49	0,13	-0,63	0,39	0,13
BE	-0,27	0,07	0,03	0,78	0,61	0,13	-0,08	0,01	0,00	-0,33	0,11	0,05
SL	0,32	0,10	0,05	0,69	0,47	0,13	0,00	0,00	0,00	0,27	0,07	0,04
NA	0,31	0,10	0,04	0,82	0,67	0,12	-0,34	0,11	0,05	0,21	0,04	0,02
JP	0,27	0,07	0,03	0,76	0,58	0,13	-0,34	0,12	0,05	0,14	0,02	0,01
RE	0,44	0,19	0,08	0,70	0,49	0,13	-0,24	0,06	0,03	0,02	0,00	0,00
MAC	0,53	0,29	0,11	0,78	0,62	0,13	-0,11	0,01	0,01	0,07	0,00	0,00
SA	0,53	0,28	0,11	0,62	0,39	0,13	-0,20	0,04	0,02	0,00	0,00	0,00
VI	0,56	0,31	0,11	0,79	0,62	0,13	-0,56	0,31	0,11	-0,14	0,02	0,01
BH	0,75	0,57	0,13	0,76	0,58	0,13	-0,82	0,67	0,12	-0,58	0,34	0,12
CAM	0,45	0,20	0,08	0,80	0,64	0,12	-0,93	0,86	0,06	-0,55	0,31	0,11
SAN	0,17	0,03	0,01	0,77	0,59	0,13	-0,08	0,01	0,00	-0,12	0,01	0,01
RJ	0,55	0,30	0,11	0,89	0,80	0,08	-0,67	0,45	0,13	-0,49	0,24	0,10
SP	0,40	0,16	0,07	0,79	0,62	0,13	-0,53	0,29	0,11	-0,40	0,16	0,07
FLO	0,35	0,12	0,05	0,27	0,07	0,03	-0,12	0,01	0,01	-0,40	0,16	0,07
CU	-0,11	0,01	0,01	0,63	0,39	0,13	-0,84	0,71	0,11	-0,59	0,34	0,12
FO	0,39	0,15	0,07	0,65	0,42	0,13	-0,42	0,17	0,07	-0,29	0,08	0,04
TE	0,07	0,01	0,00	0,80	0,63	0,12	-0,66	0,44	0,13	-0,68	0,46	0,13
GO	0,36	0,13	0,06	0,88	0,77	0,09	-0,77	0,63	0,13	-0,60	0,36	0,12
DF	0,41	0,16	0,07	0,86	0,73	0,10	-0,80	0,64	0,12	-0,69	0,48	0,13
PA	0,42	0,18	0,08	0,42	0,18	0,08	-0,51	0,26	0,10	-0,19	0,03	0,02

8.4 Figures S22 to S151: Annual spatial distribution (5-year-period) of Land surface temperature (LST, 1-km spatial resolution), Enhanced Vegetation Index 2 (EVI2, 250-m spatial resolution), surface albedo (α, 250-m spatial resolution), surface net radiation (Rn, 250-m spatial resolution), and actual evapotranspiration (ET, 250-m spatial resolution).

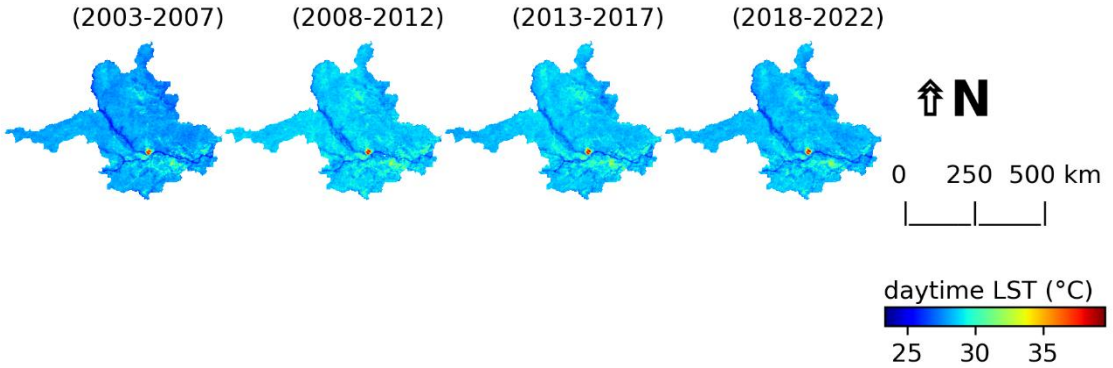

Fig. S22. Annual (5-year-period) daytime LST for Manaus (MA).

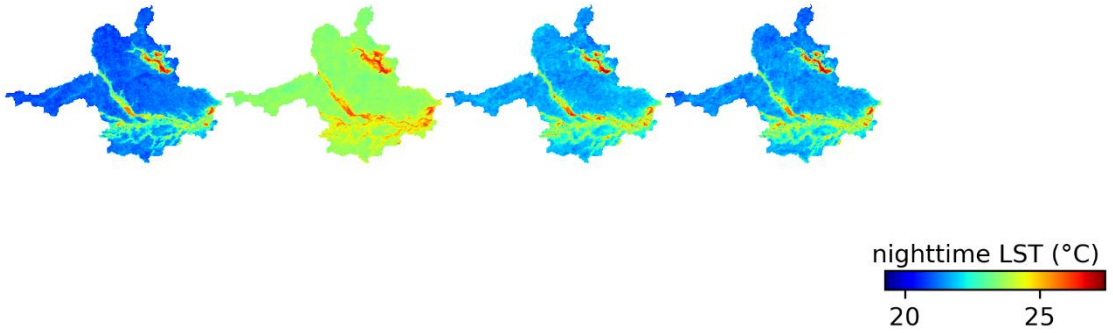

Fig. S22. Annual (5-year-period) nighttime LST for Manaus (MA).

Fig. S23. Annual (5-year-period) EVI2 for Manaus (MA).

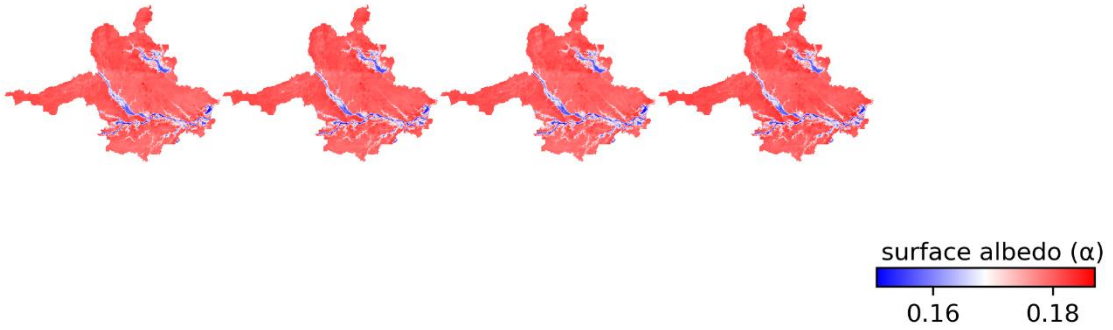

Fig. S24. Annual (5-year-period) α for Manaus (MA).

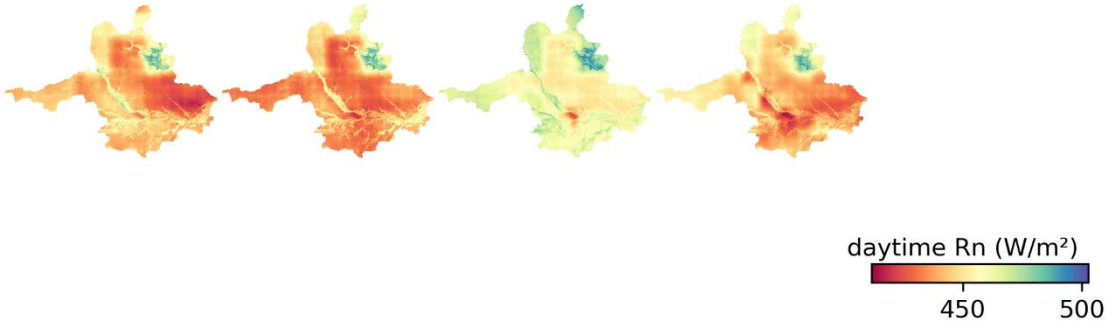

Fig. S25. Annual (5-year-period) daytime Rn for Manaus (MA).

Fig. S26. Annual (5-year-period) nighttime Rn for Manaus (MA).

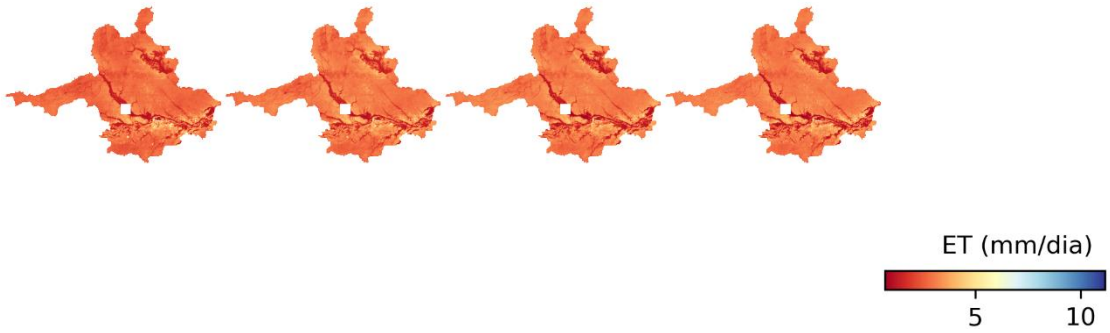

Fig. S27. Annual (5-year-period) ET for Manaus (MA).

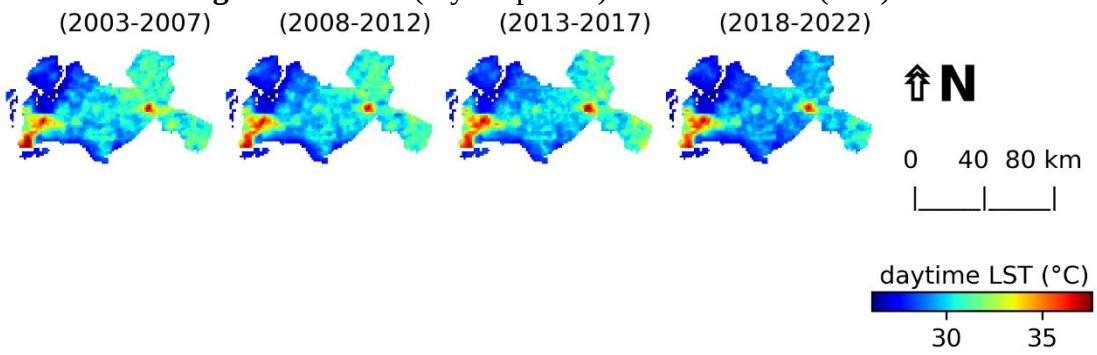

Fig. S28. Annual (5-year-period) daytime LST for Belém (BE).

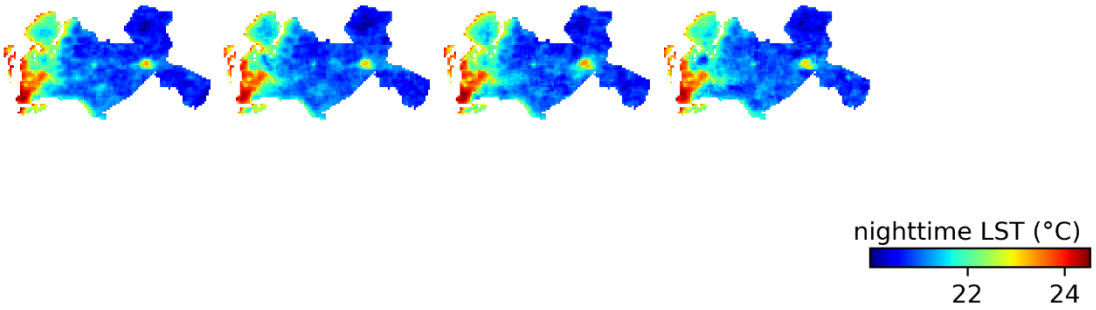

Fig. S29. Annual (5-year-period) nighttime LST for Belém (BE).

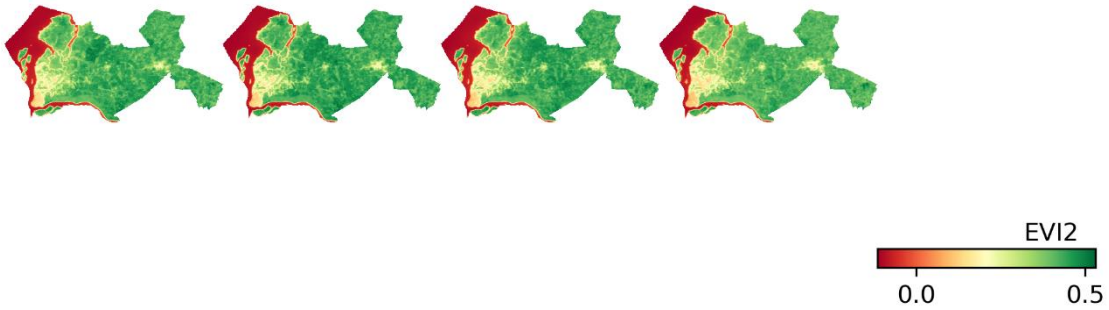

Fig. S30. Annual (5-year-period) EVI2 for Belém (BE).

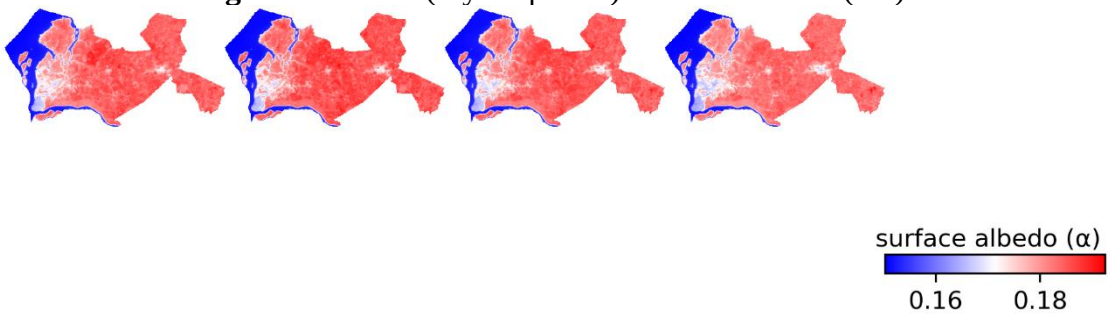

Fig. S31. Annual (5-year-period) α for Belém (BE).

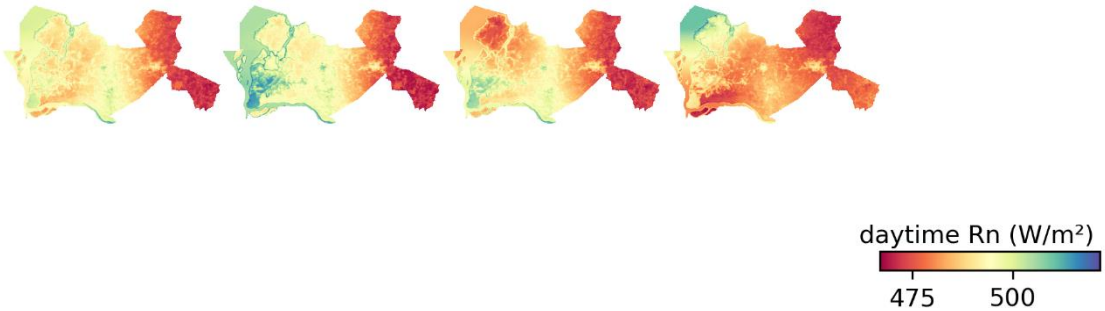

Fig. S32. Annual (5-year-period) daytime Rn for Belém (BE).

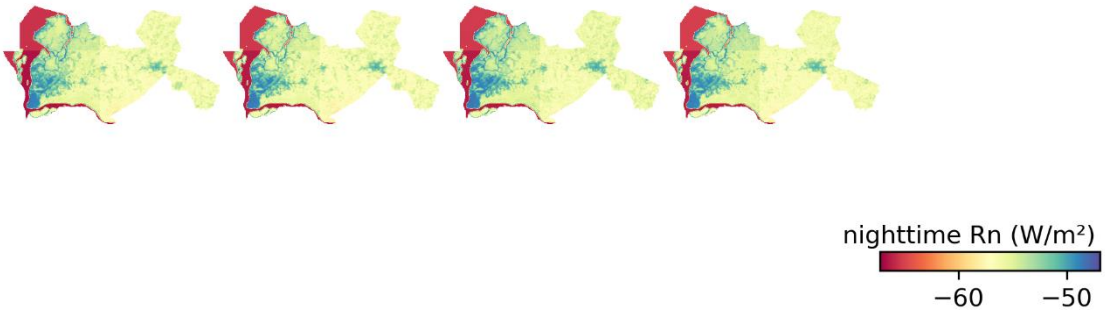

Fig. S33. Annual (5-year-period) nighttime Rn for Belém (BE).

Fig. S34. Annual (5-year-period) ET for Belém (BE).

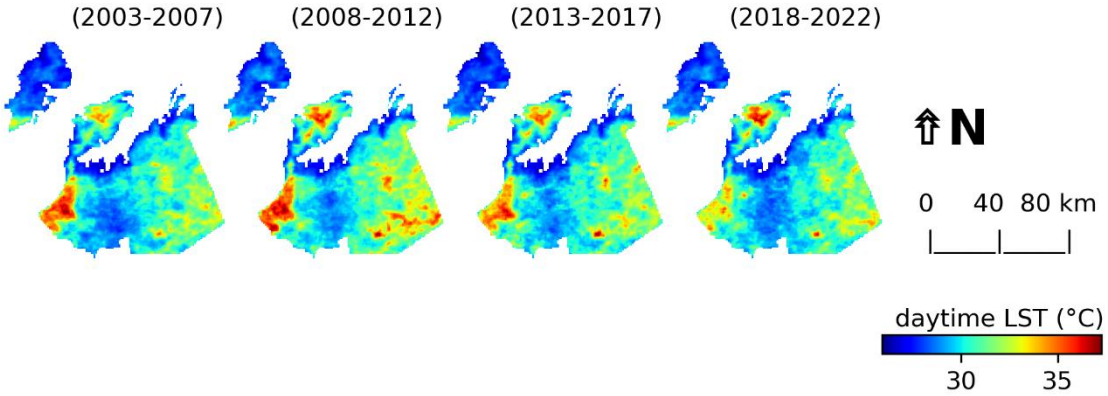

Fig. S35. Annual (5-year-period) daytime LST for São Luís (SL).

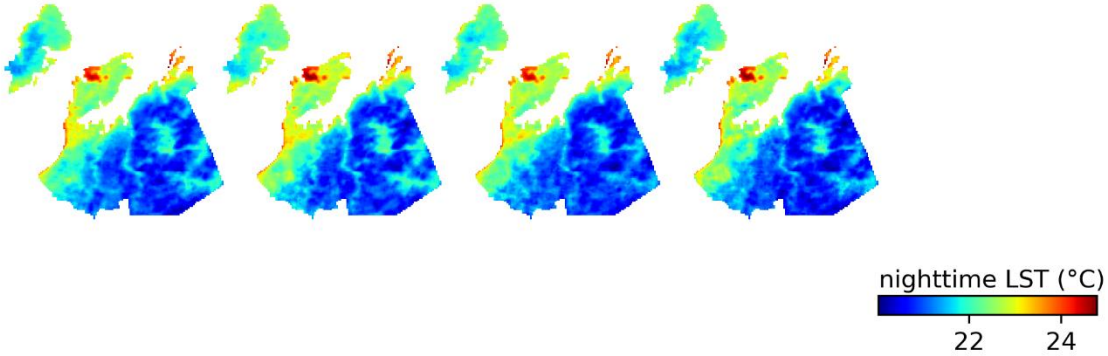

Fig. S36. Annual (5-year-period) nighttime LST for São Luís (SL).

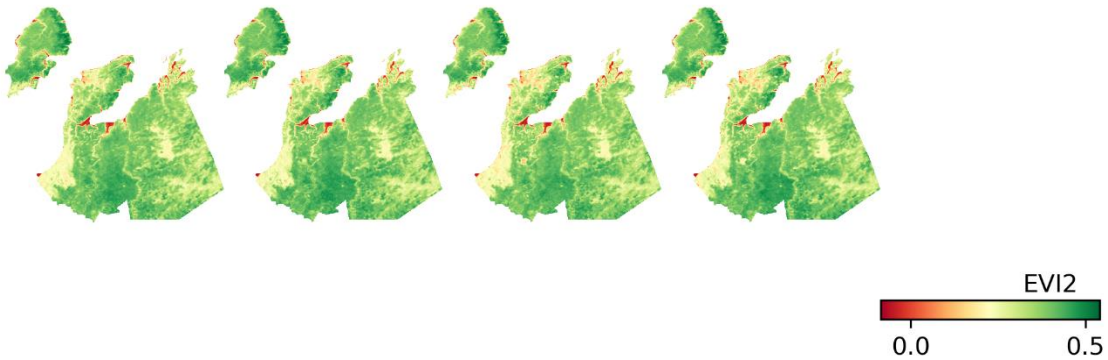

Fig. S37. Annual (5-year-period) EVI2 for São Luís (SL).

Fig. S38. Annual (5-year-period) α for São Luís (SL).

Fig. S39. Annual (5-year-period) daytime Rn for São Luís (SL).

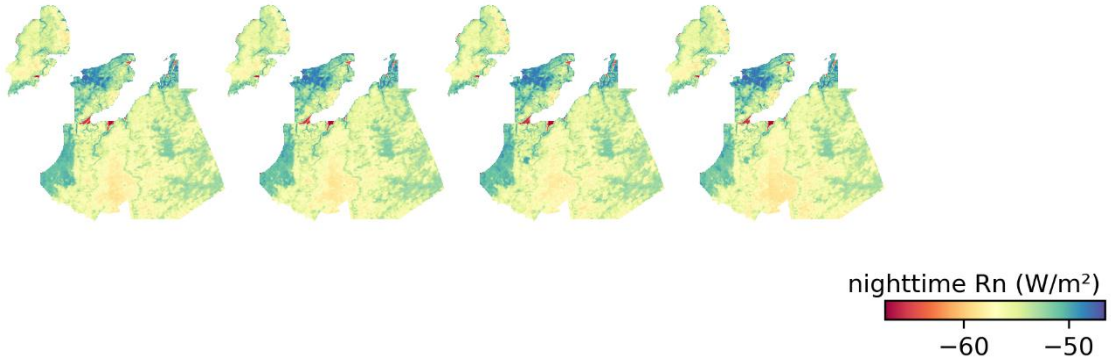

Fig. S40. Annual (5-year-period) nighttime Rn for São Luís (SL).

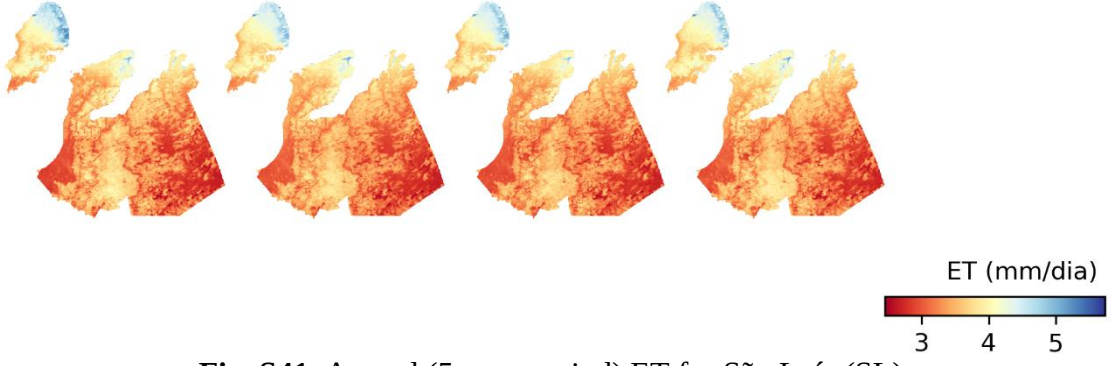

Fig. S41. Annual (5-year-period) ET for São Luís (SL).

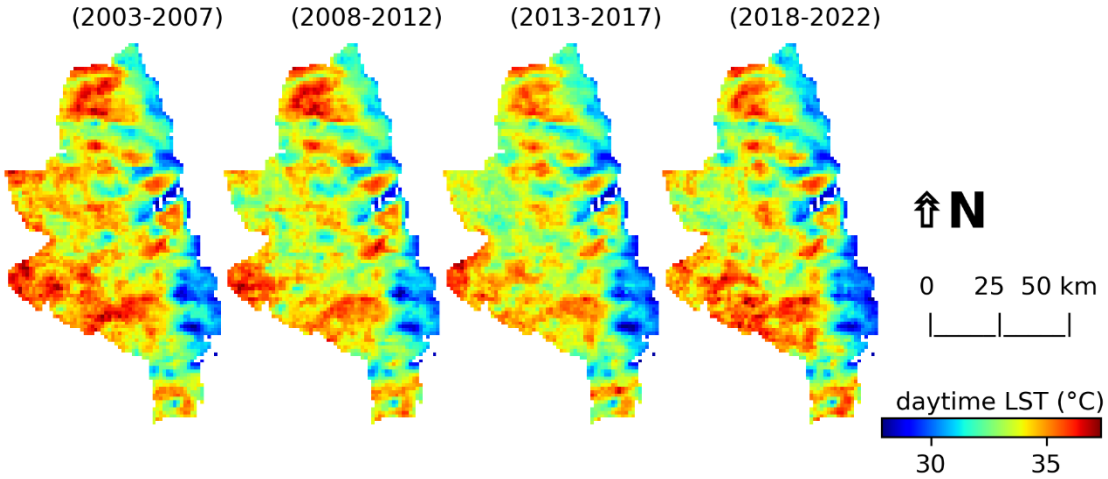

Fig. S42. Annual (5-year-period) daytime LST for Natal (NA).

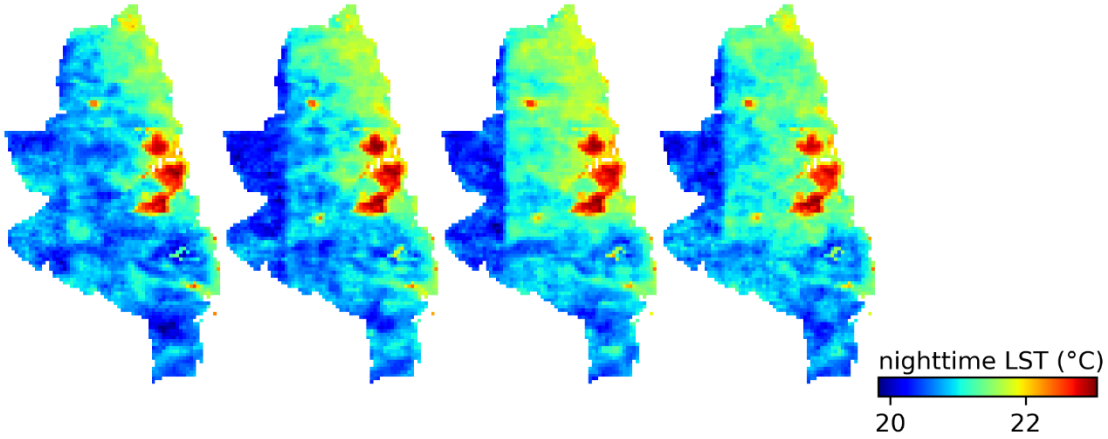

Fig. S43. Annual (5-year-period) nighttime LST for Natal (NA).

Fig. S44. Annual (5-year-period) EVI2 for Natal (NA).

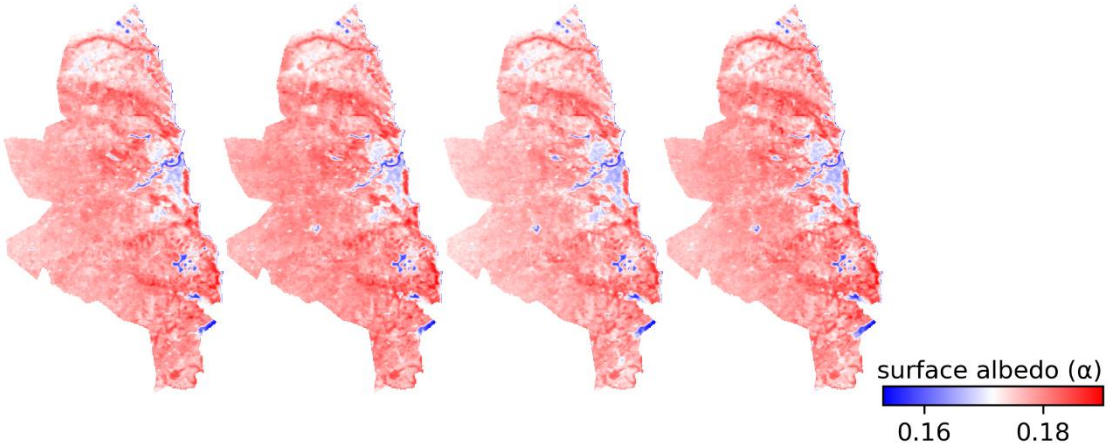

Fig. S45. Annual (5-year-period) α for Natal (NA).

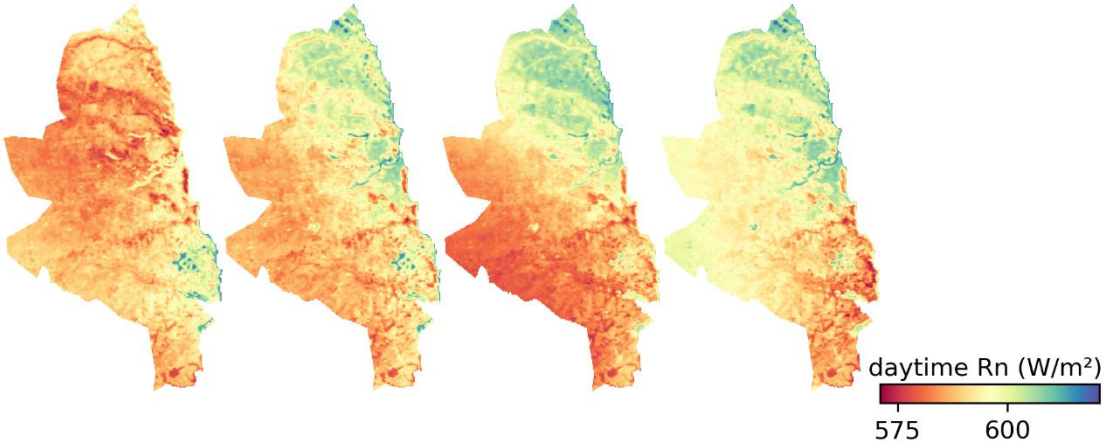

Fig. S46. Annual (5-year-period) daytime Rn for Natal (NA).

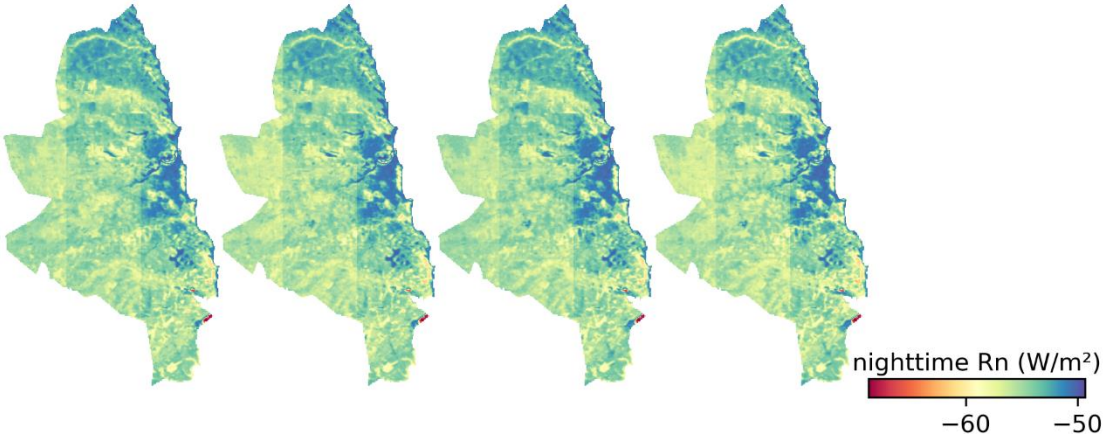

Fig. S47. Annual (5 year-period) nighttime Rn of Natal (NA).

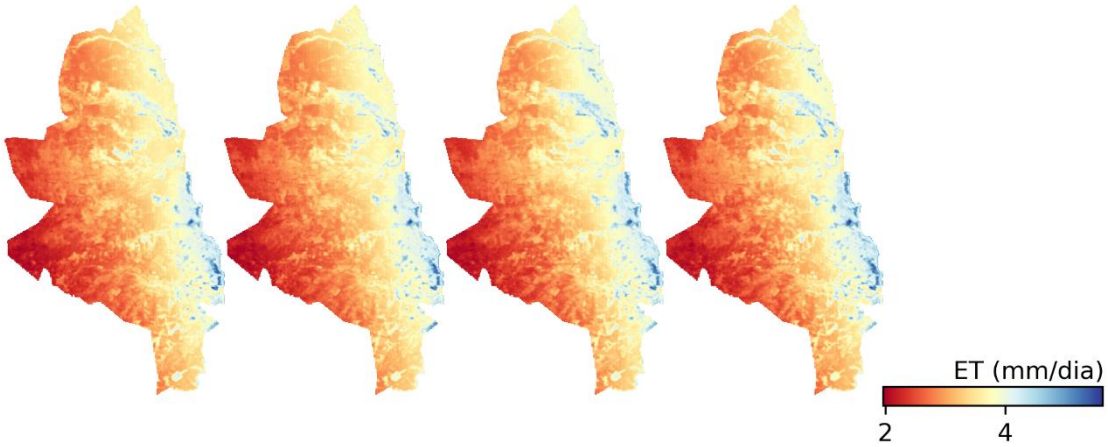

Fig. S48. Annual (5 year-period) ET of Natal (NA).

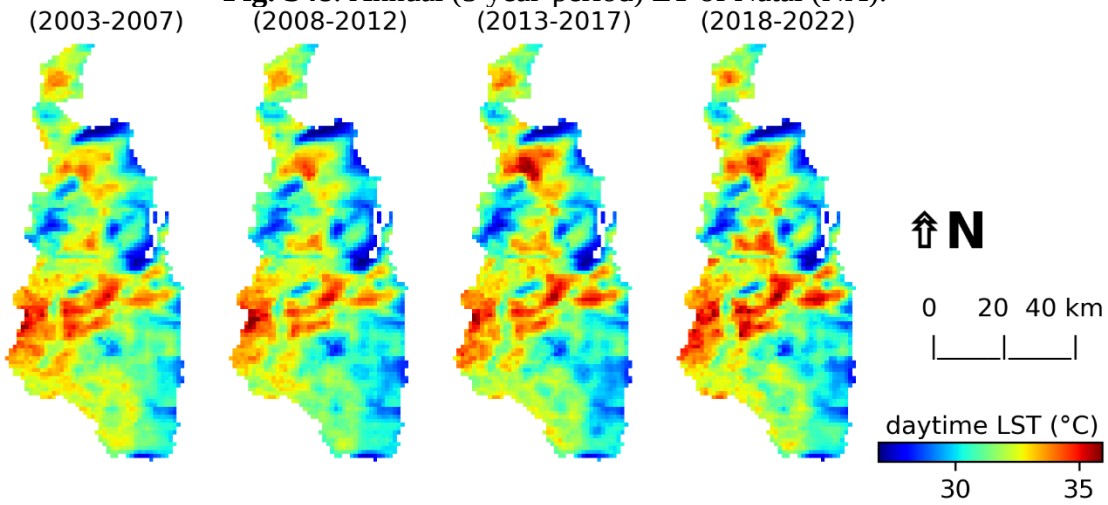

Fig. S49. Annual (5 year-period) daytime LST of João Pessoa (JP).

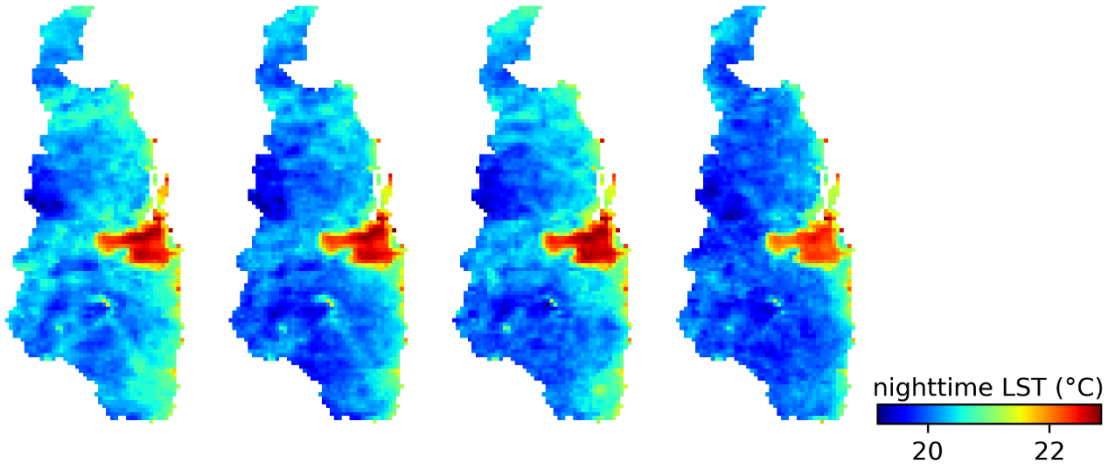

Fig. S50. Annual (5 year-period) nighttime LST of João Pessoa (JP).

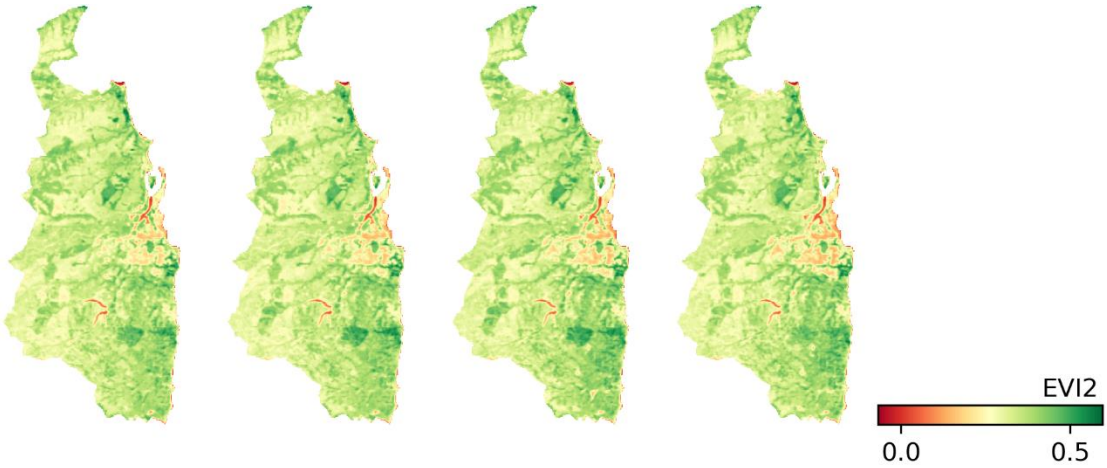

Fig. S51. Annual (5 year-period) EVI2 of João Pessoa (JP).

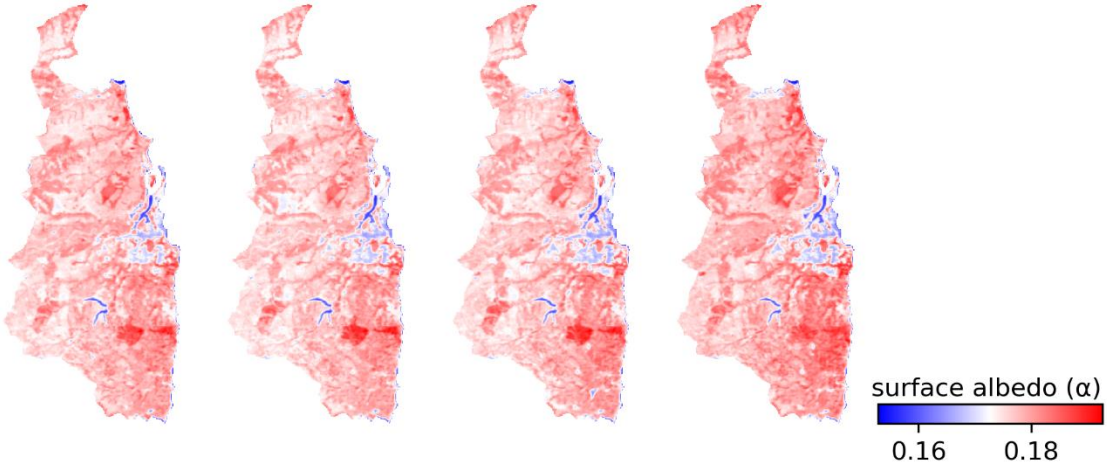

Fig. S52. Annual (5 year-period) α of João Pessoa (JP).

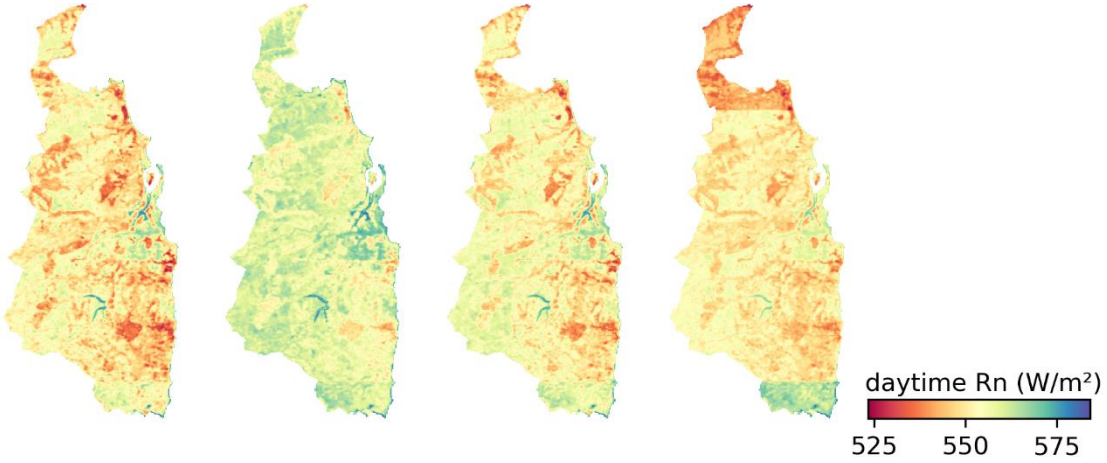

Fig. S53. Annual (5 year-period) daytime Rn of João Pessoa (JP).

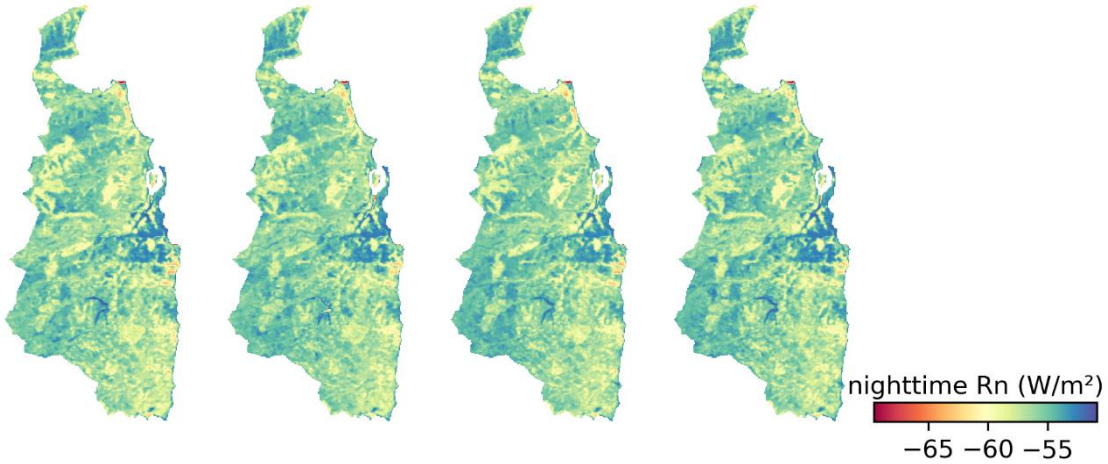

Fig. S54. Annual (5 year-period) nighttime Rn of João Pessoa (JP).

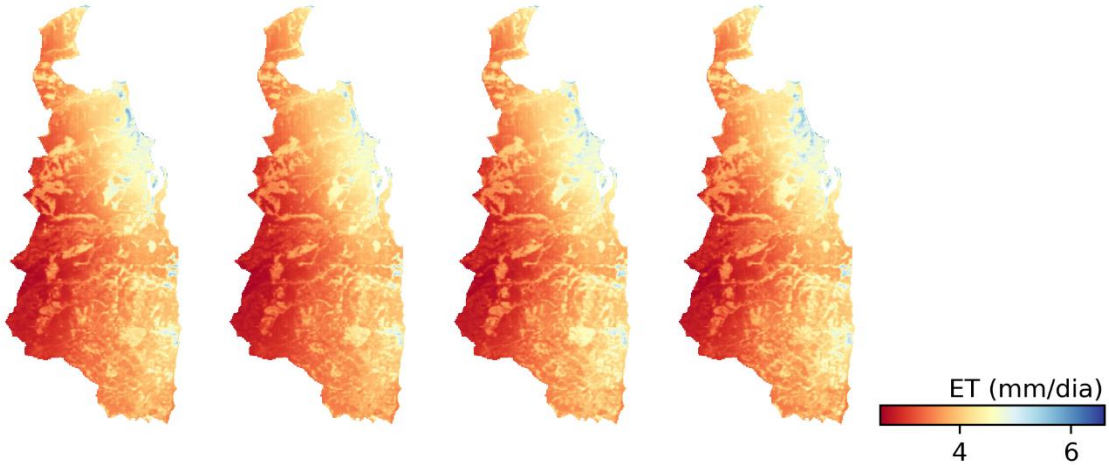

Fig. S55. Annual (5 year-period) ET of João Pessoa (JP).

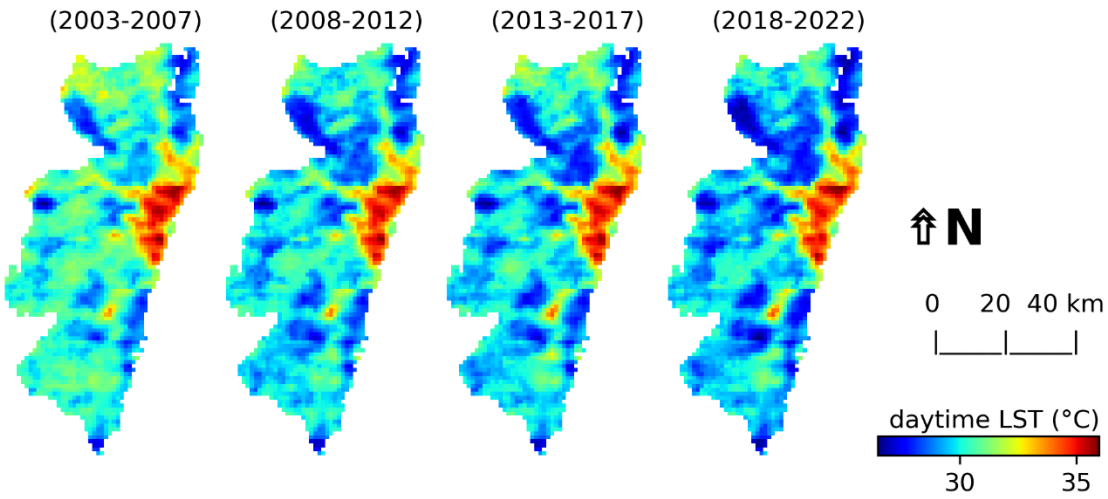

Fig. S56. Annual (5 year-period) daytime LST of Recife (RE).

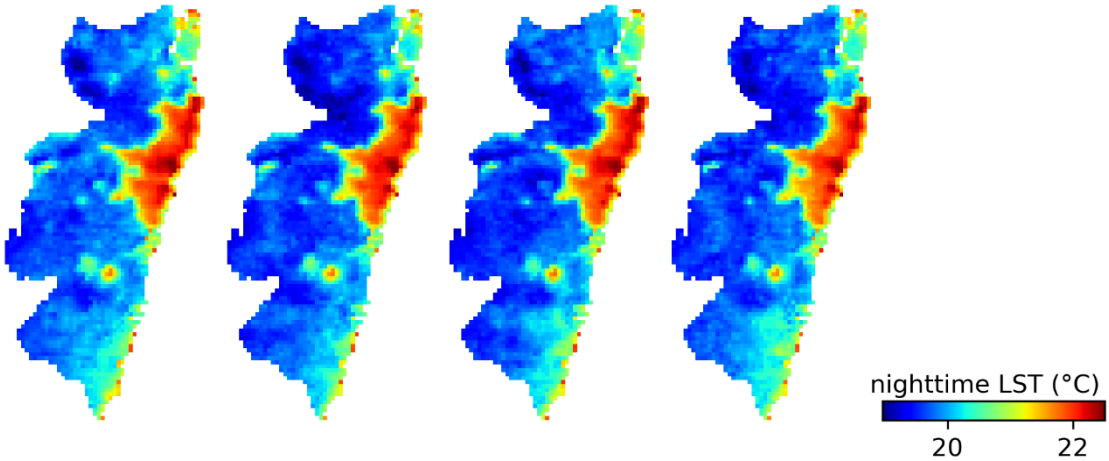

Fig. S57. Annual (5 year-period) nighttime LST of Recife (RE).

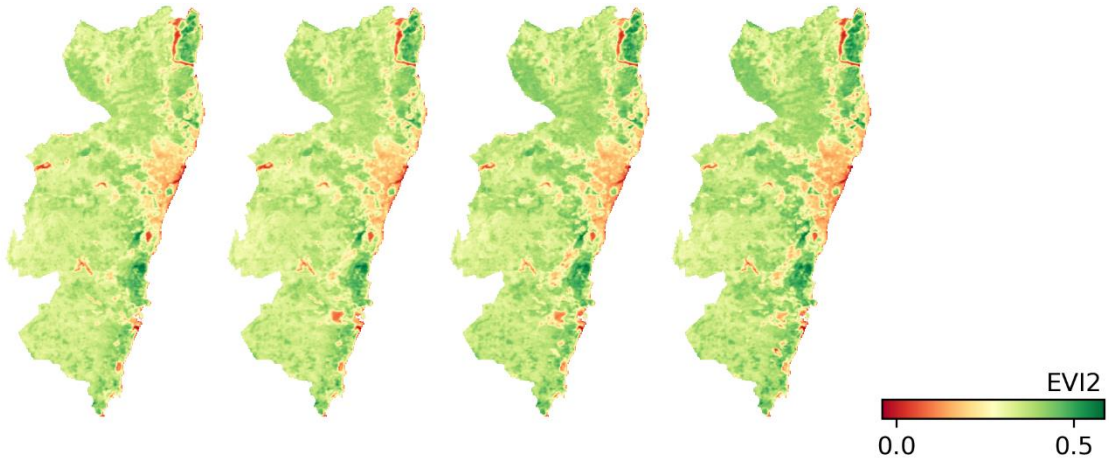

Fig. S58. Annual (5 year-period) EVI2 of Recife (RE).

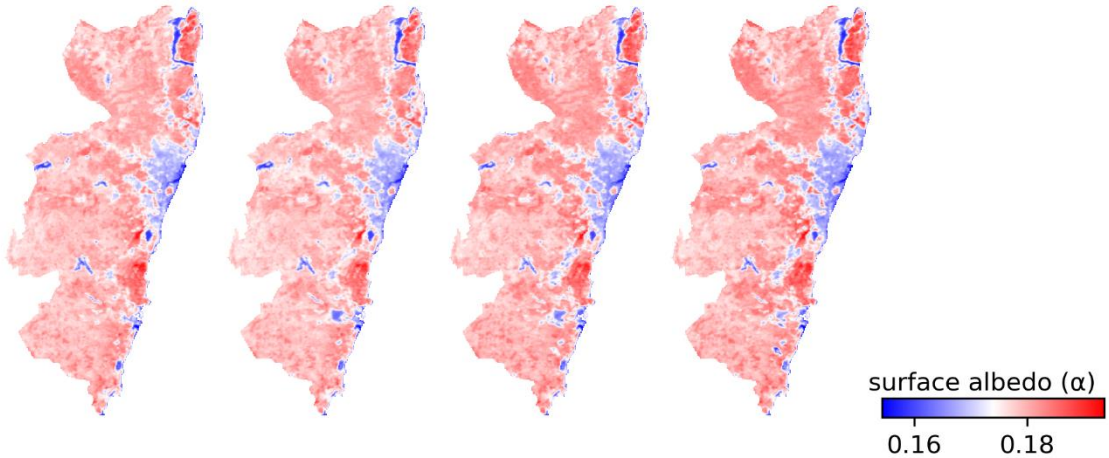

Fig. S59. Annual (5 year-period) α of Recife (RE).

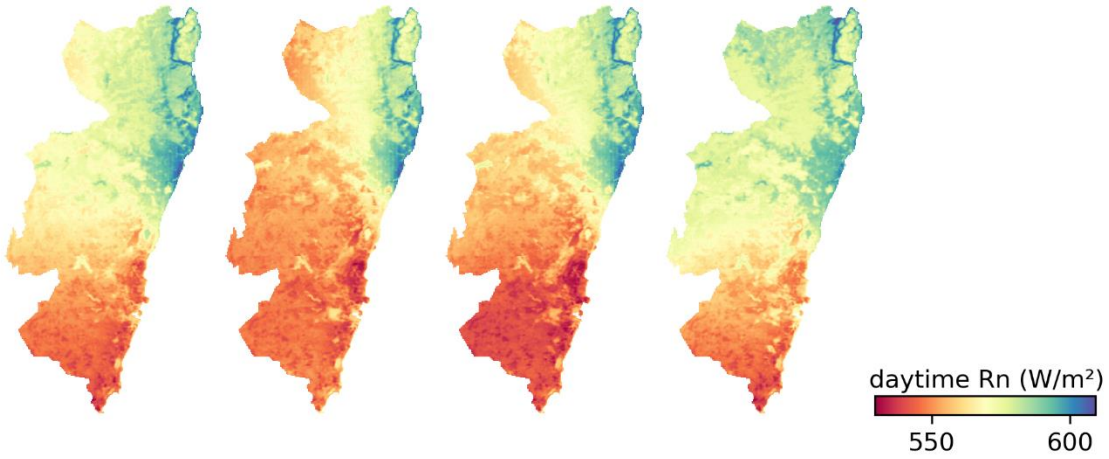

Fig. S60. Annual (5 year-period) daytime Rn of Recife (RE).

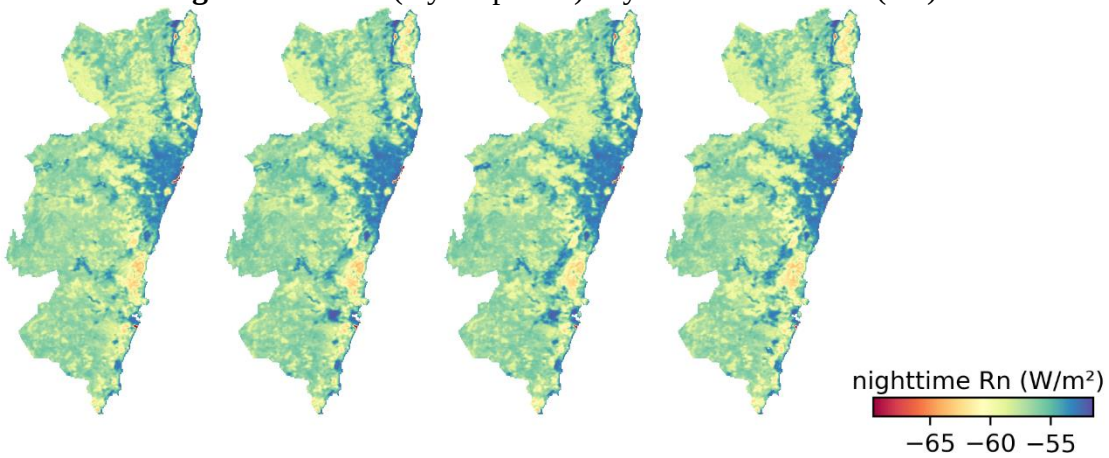

Fig. S61. Annual (5 year-period) nighttime Rn of Recife (RE).

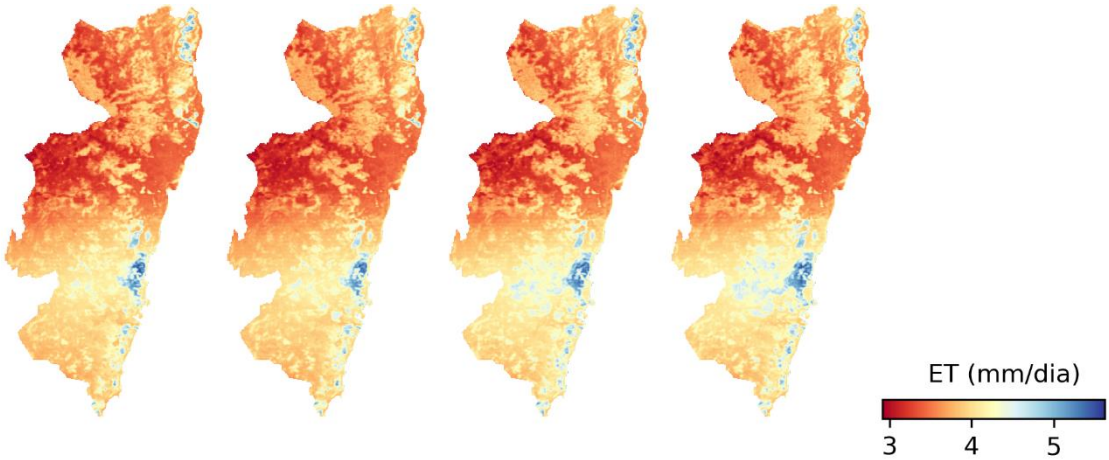

Fig. S62. Annual (5 year-period) ET of Recife (RE).

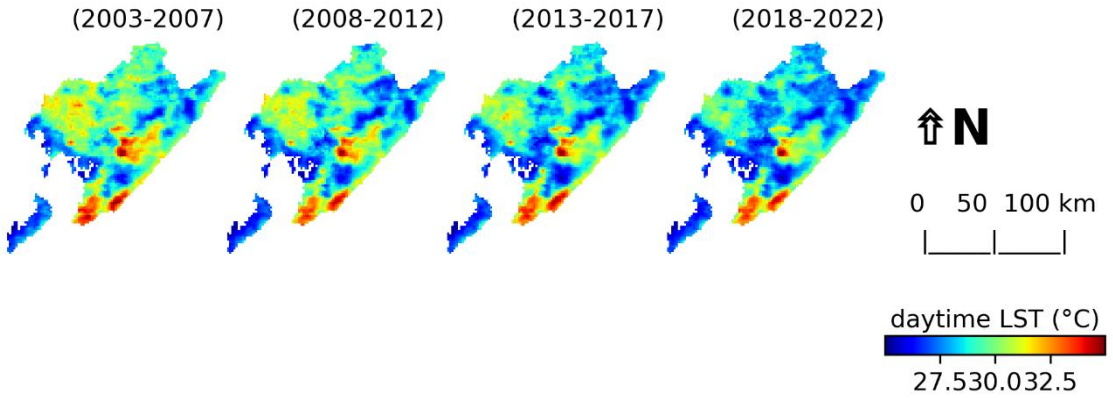

Fig. S63. Annual (5 year-period) daytime LST of Salvador (SA).

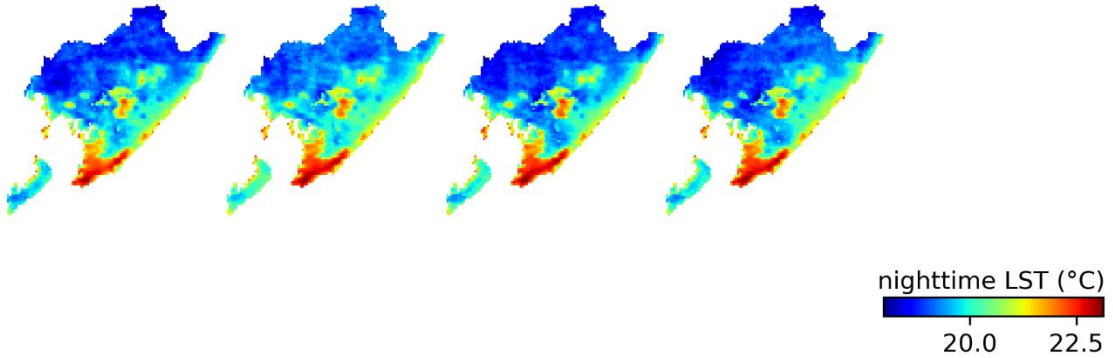

Fig. S64. Annual (5 year-period) nighttime LST of Salvador (SA).

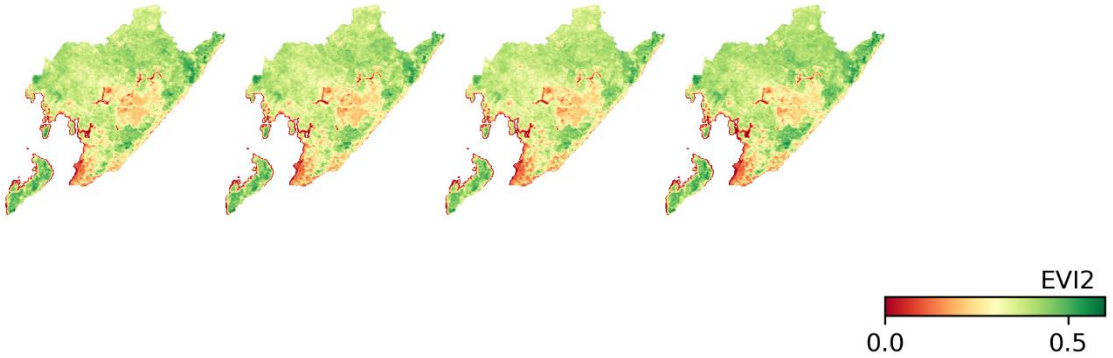

Fig. S65. Annual (5 year-period) EVI2 of Salvador (SA).

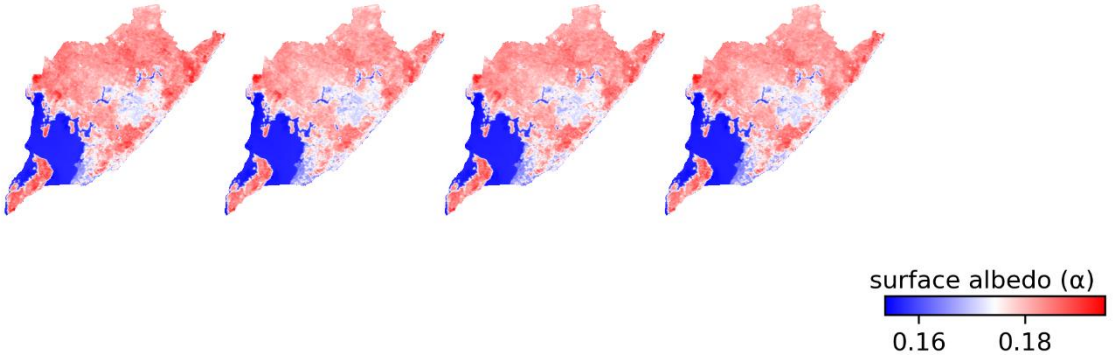

Fig. S66. Annual (5 year-period) α of Salvador (SA).

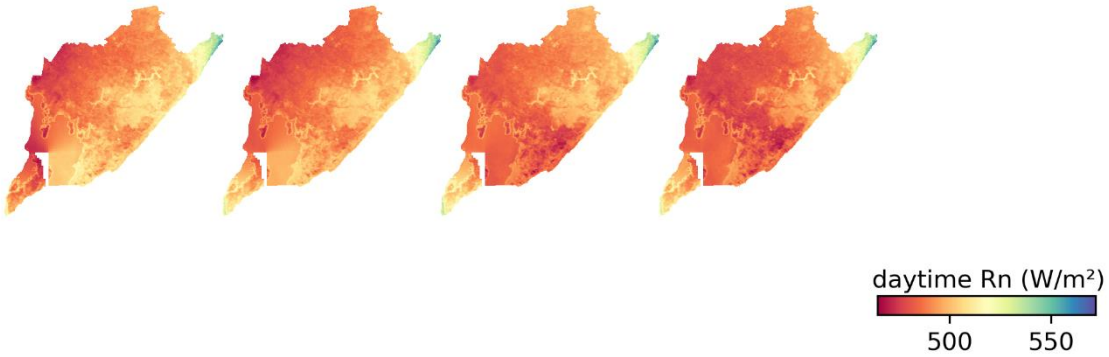

Fig. S67. Annual (5 year-period) daytime Rn of Salvador (SA).

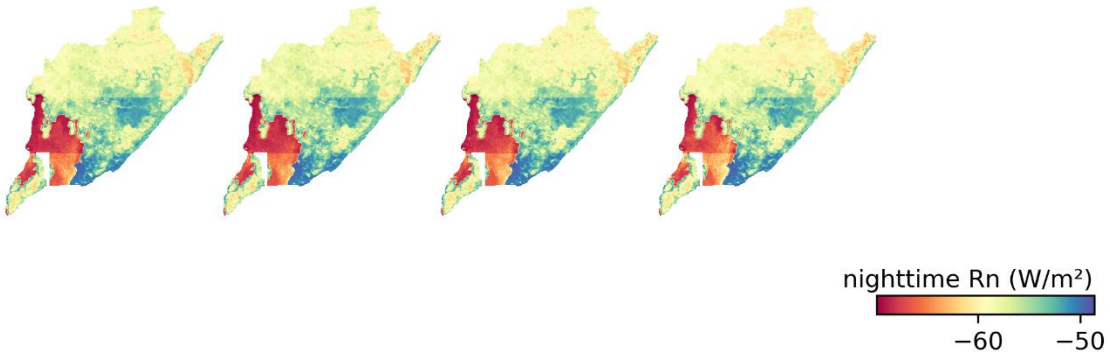

Fig. S68. Annual (5 year-period) nighttime Rn of Salvador (SA).

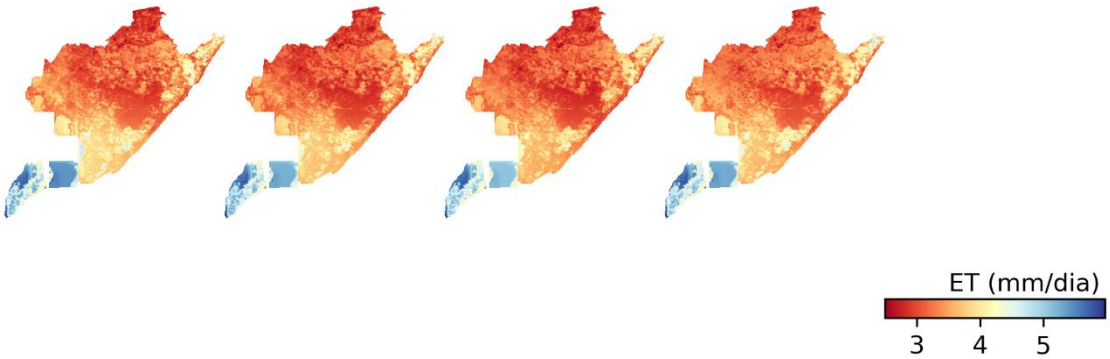

Fig. S69. Annual (5 year-period) ET of Salvador (SA).

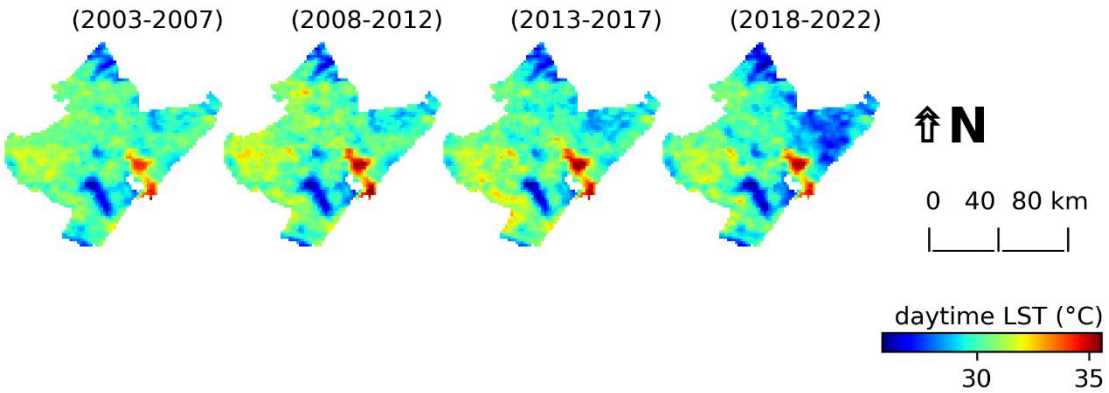

Fig. S70. Annual (5 year-period) daytime LST of Maceió (MAC).

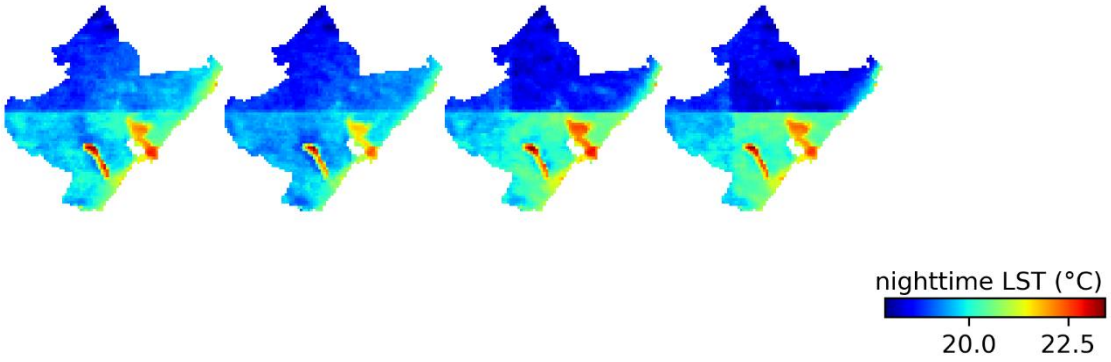

Fig. S71. Annual (5 year-period) nighttime LST of Maceió (MAC).

Fig. S72. Annual (5 year-period) EVI2 of Maceió (MAC).

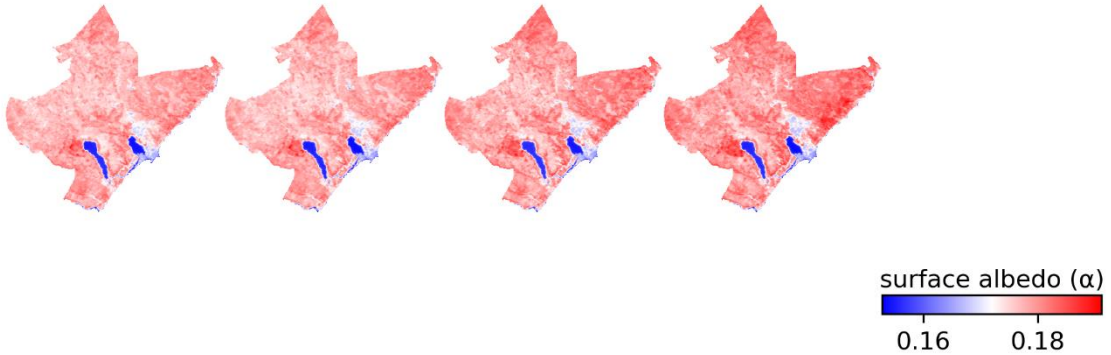

Fig. S73. Annual (5 year-period) α of Maceió (MAC).

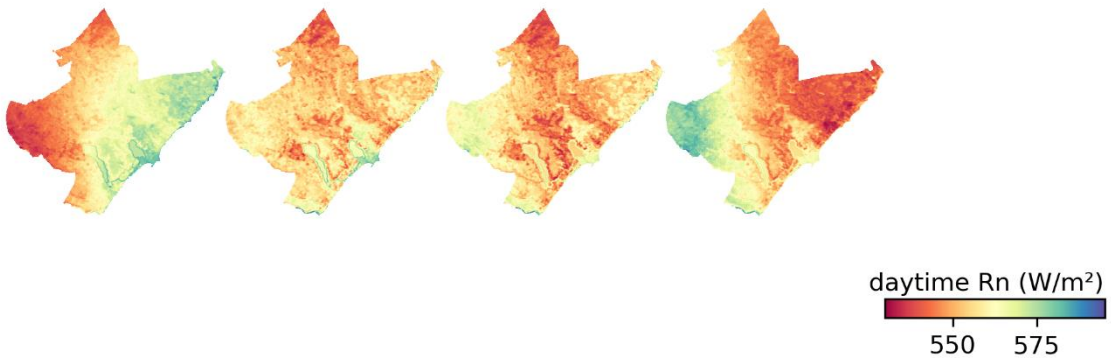

Fig. S74. Annual (5 year-period) daytime Rn of Maceió (MAC).

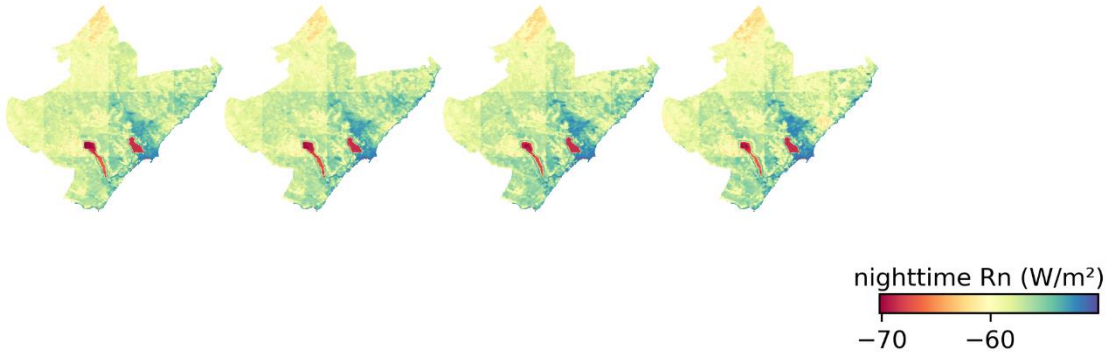

Fig. S74. Annual (5 year-period) nighttime Rn of Maceió (MAC).

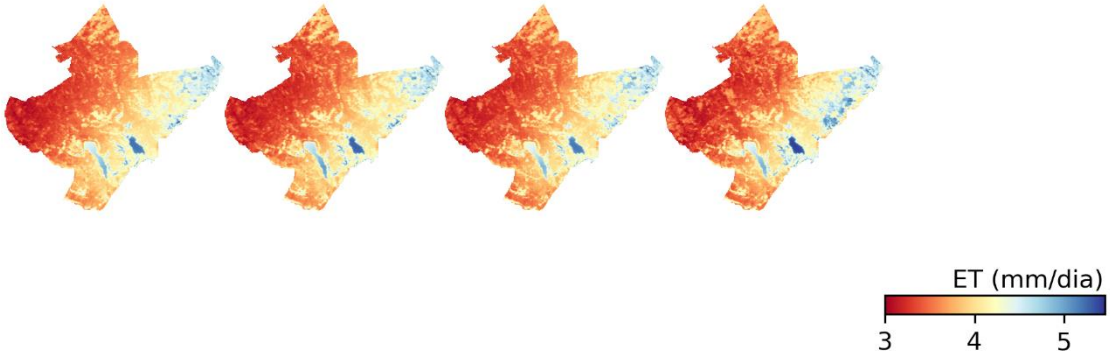

Fig. S74. Annual (5 year-period) ET of Maceió (MAC).

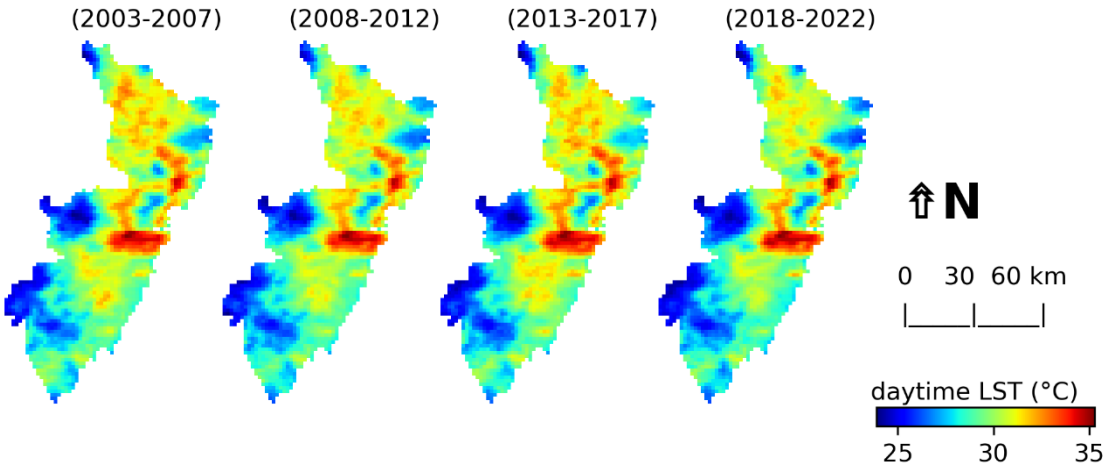

Fig. S75. Annual (5 year-period) daytime LST of Vitória (VI).

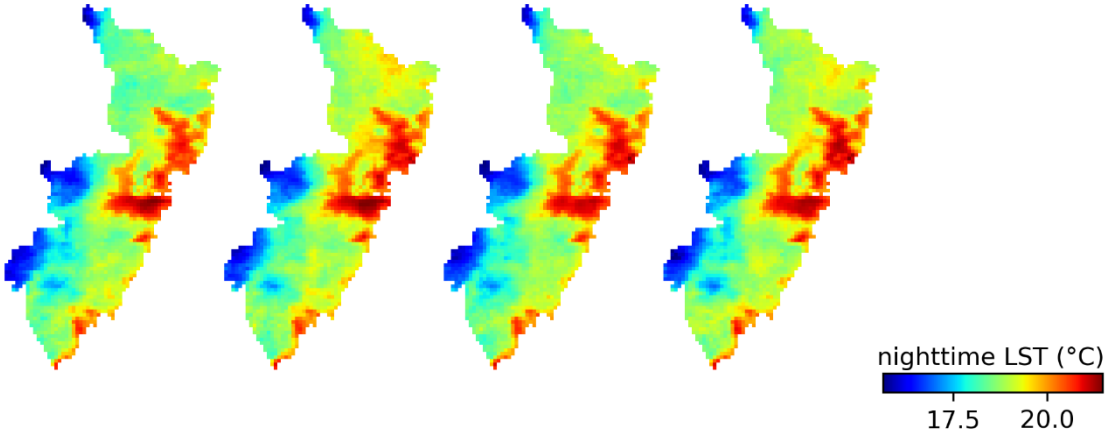

Fig. S76. Annual (5 year-period) nighttime LST of Vitória (VI).

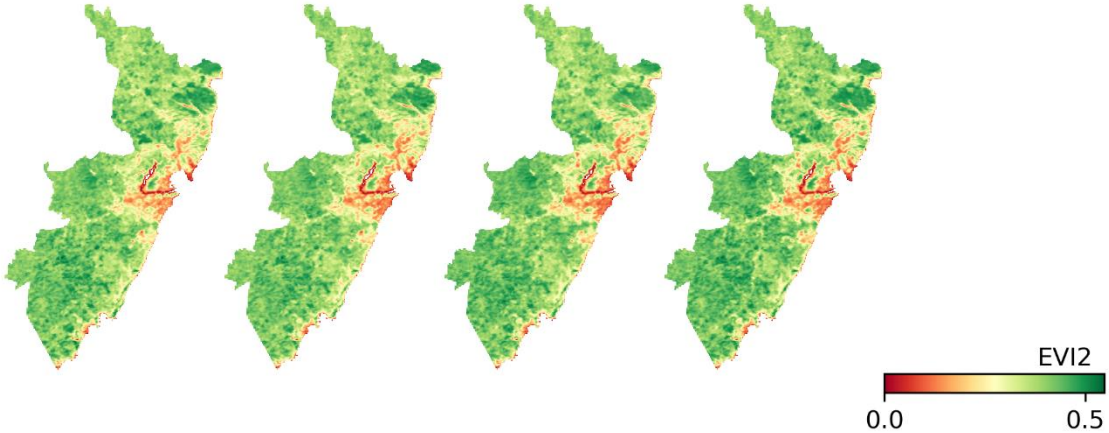

Fig. S77. Annual (5 year-period) EVI2 of Vitória (VI).

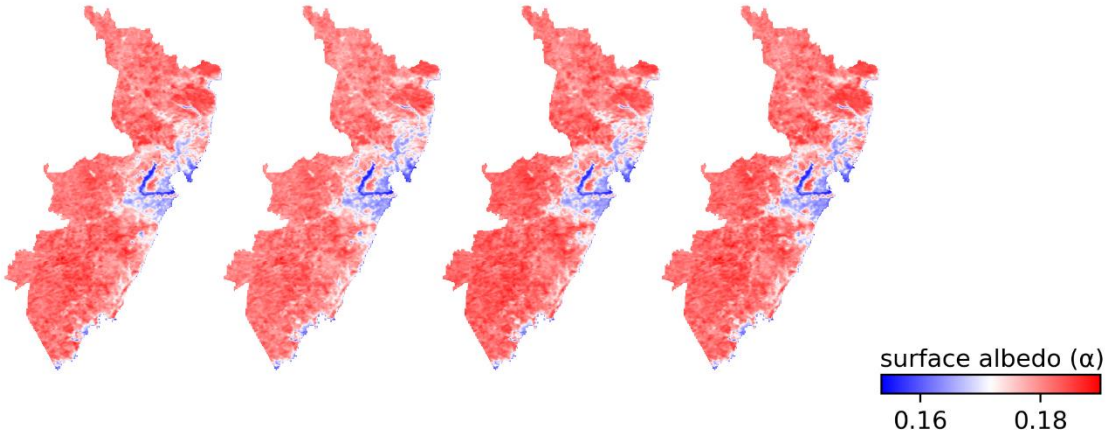

Fig. S78. Annual (5 year-period) α of Vitória (VI).

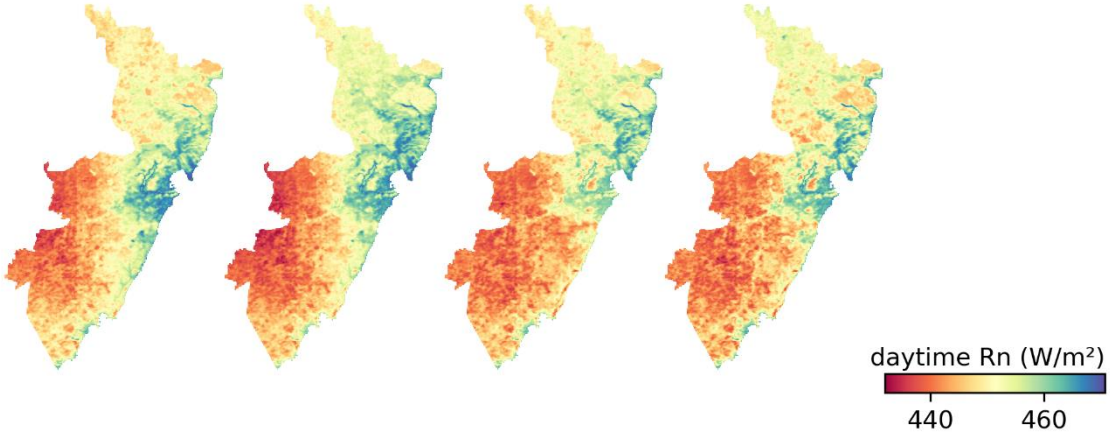

Fig. S79. Annual (5 year-period) daytime Rn of Vitória (VI).

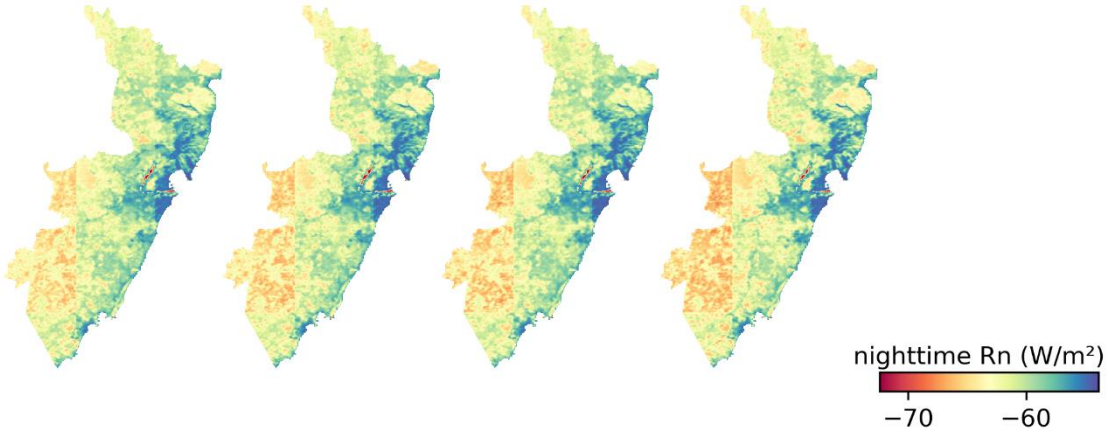

Fig. S80. Annual (5 year-period) nighttime Rn of Vitória (VI).

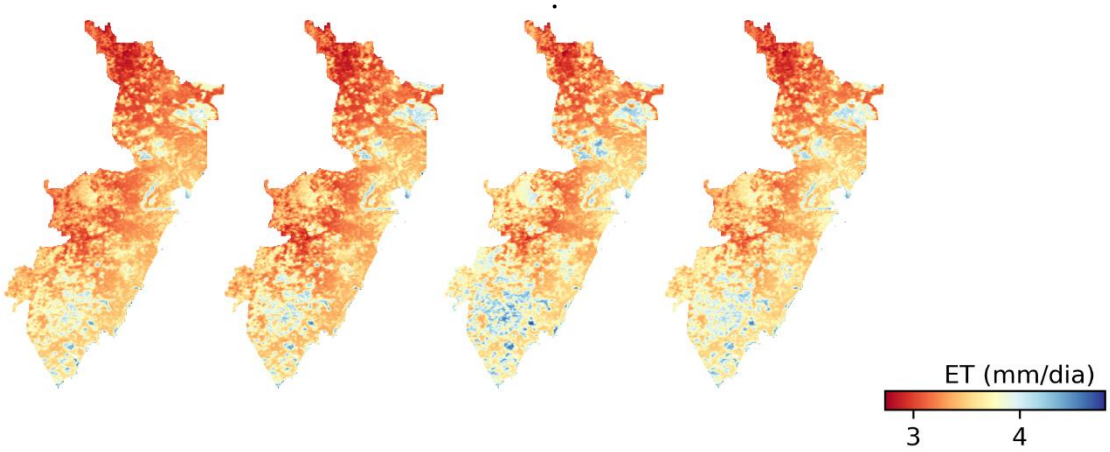

Fig. S81. Annual (5 year-period) ET of Vitória (VI).

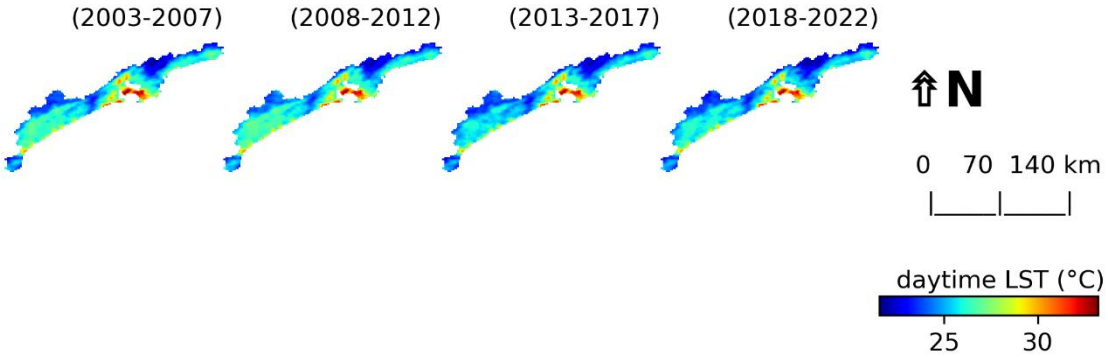

Fig. S75. Annual (5 year-period) daytime LST of Santos (SAN).

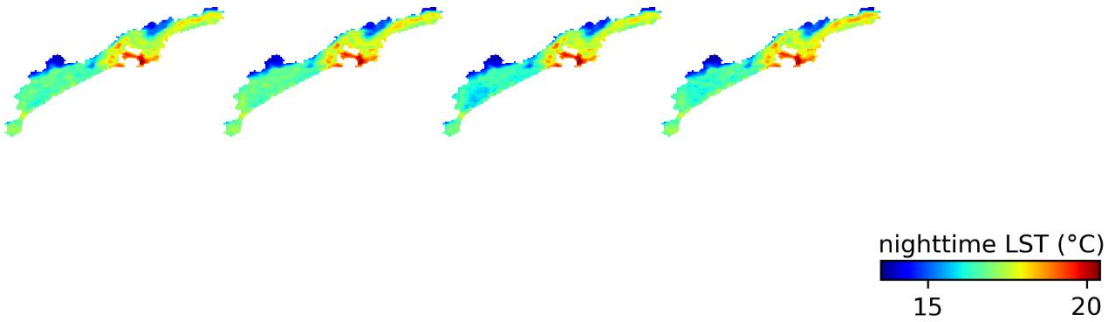

Fig. S76. Annual (5 year-period) nighttime LST of Santos (SAN).

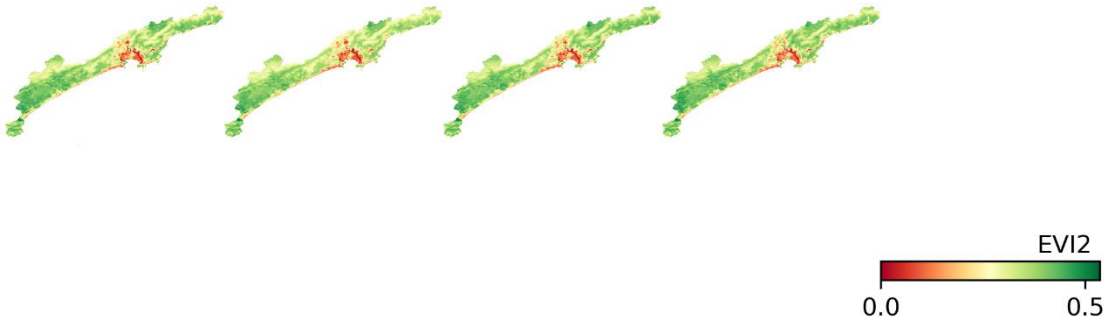

Fig. S77. Annual (5 year-period) EVI2 of Santos (SAN).

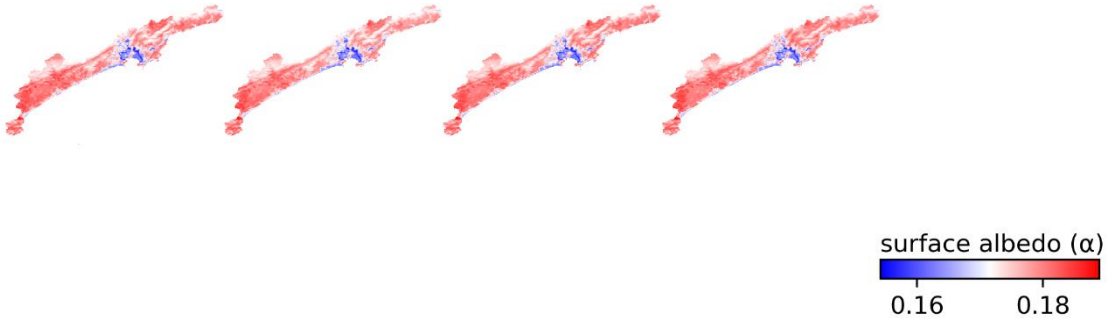

Fig. S78. Annual (5 year-period) α of Santos (SAN).

Fig. S79. Annual (5 year-period) daytime Rn of Santos (SAN).

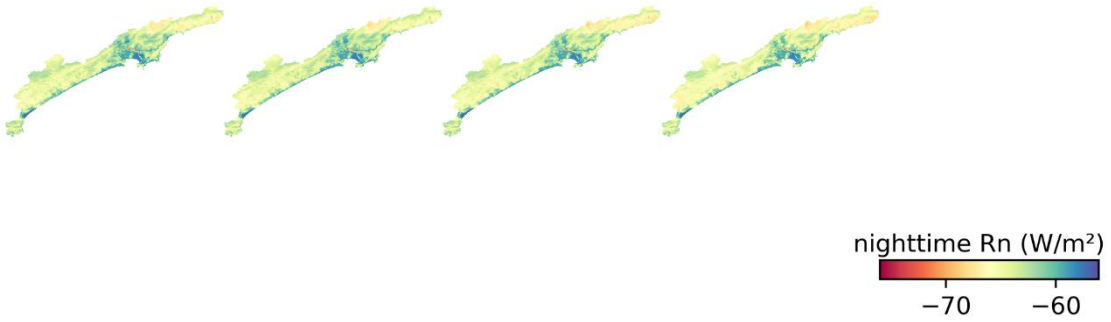

Fig. S80. Annual (5 year-period) nighttime Rn of Santos (SAN).

Fig. S81. Annual (5 year-period) ET of Santos (SAN).

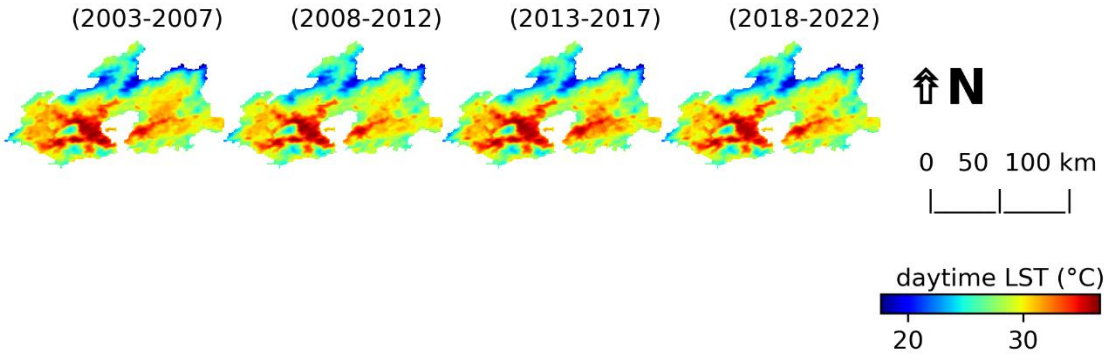

Fig. S82. Annual (5 year-period) daytime LST of Rio de Janeiro (RJ).

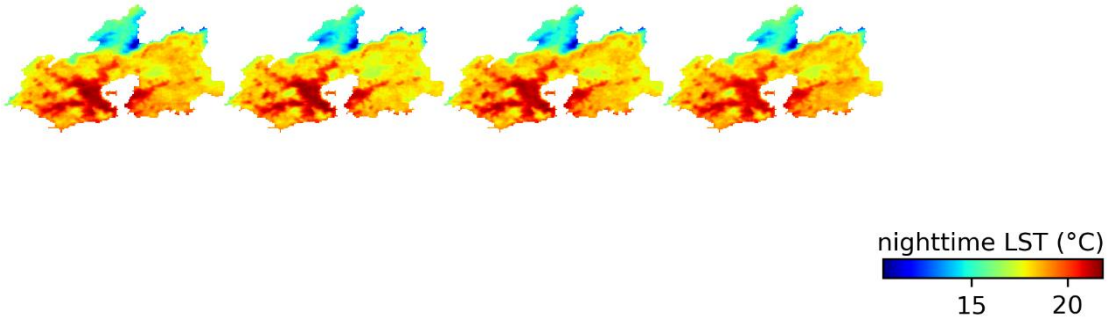

Fig. S83. Annual (5 year-period) nighttime LST of Rio de Janeiro (RJ).

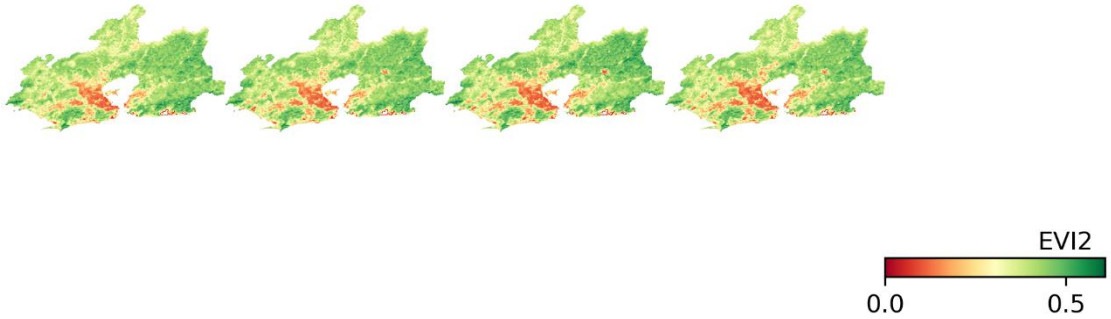

Fig. S84. Annual (5 year-period) EVI2 of Rio de Janeiro (RJ).

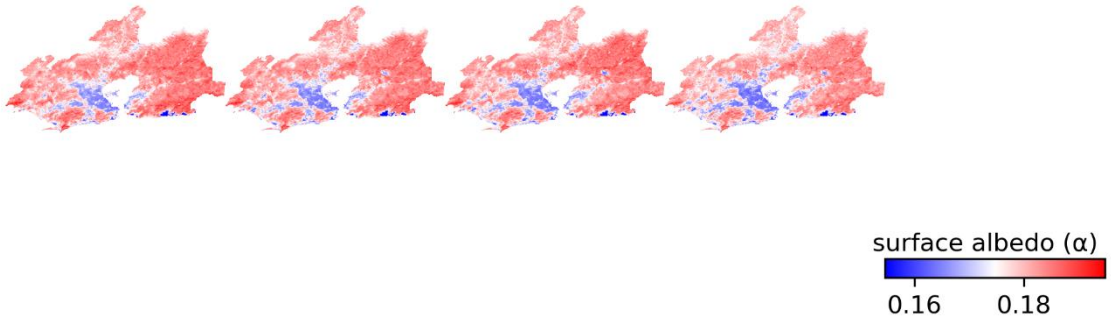

Fig. S85. Annual (5 year-period) α of Rio de Janeiro (RJ).

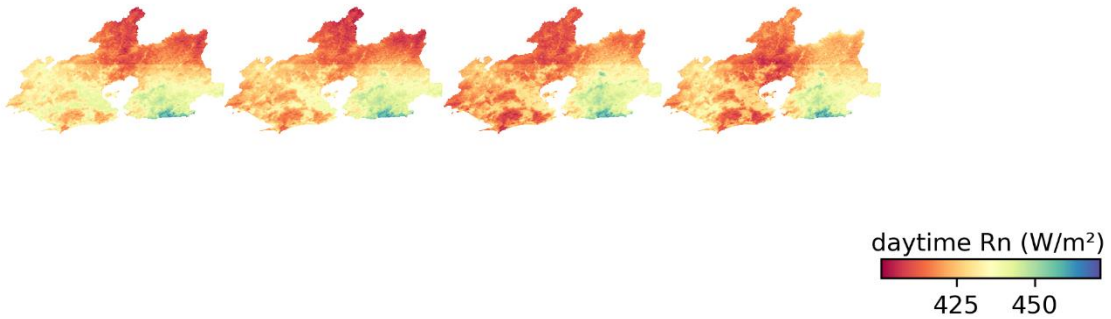

Fig. S86. Annual (5 year-period) daytime Rn of Rio de Janeiro (RJ).

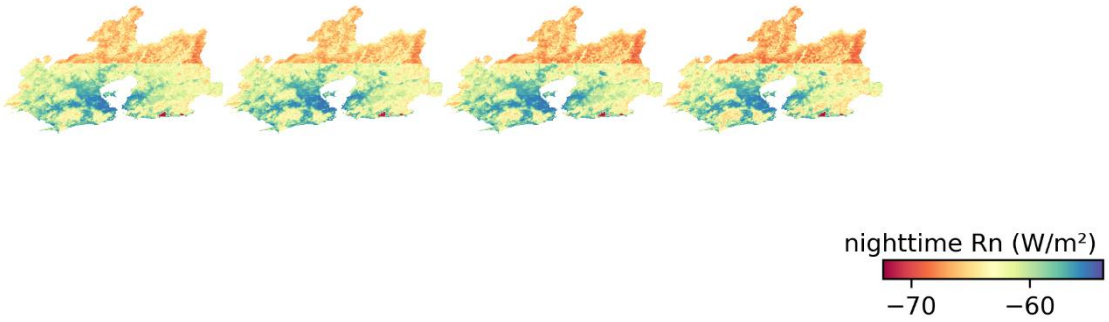

Fig. S87. Annual (5 year-period) nighttime Rn of Rio de Janeiro (RJ).

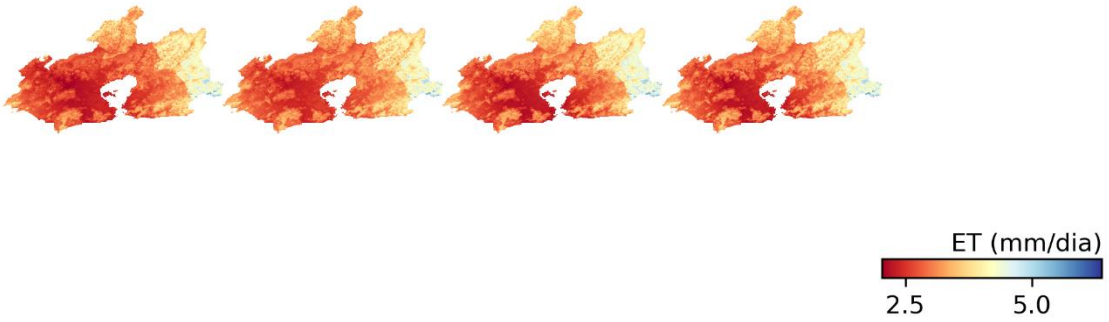

Fig. S88. Annual (5 year-period) ET of Rio de Janeiro (RJ).

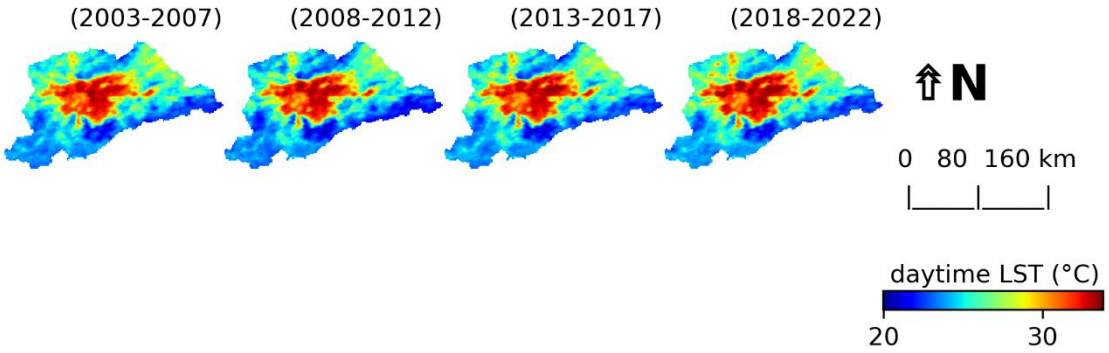

Fig. S89. Annual (5 year-period) daytime LST of São Paulo (SP).

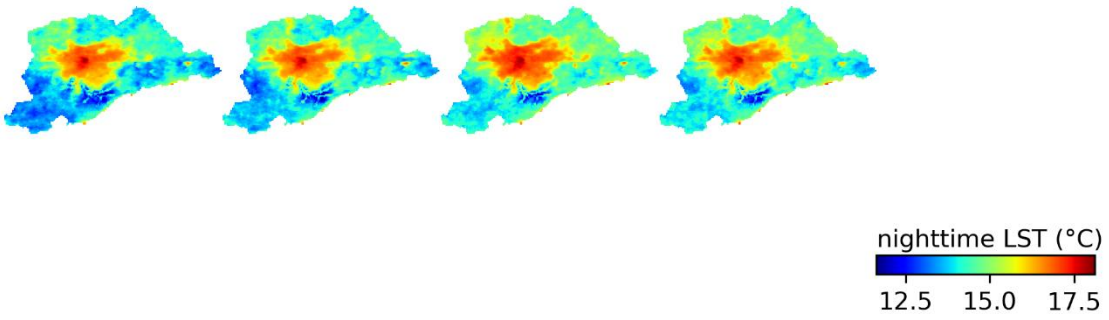

Fig. S90. Annual (5 year-period) nighttime LST of São Paulo (SP).

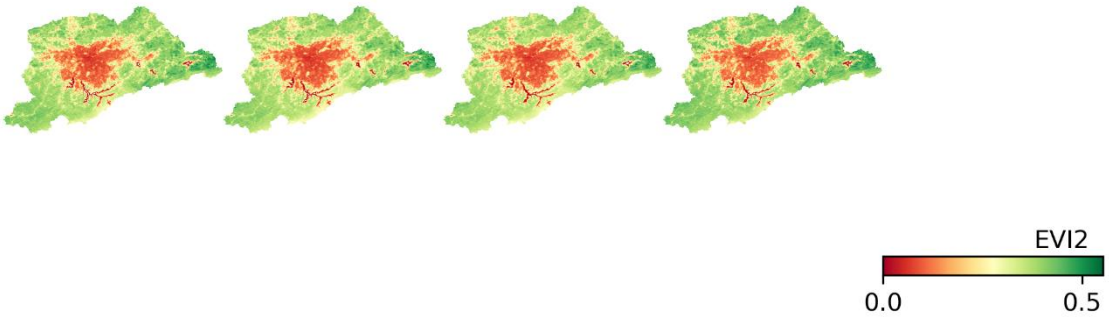

Fig. S91. Annual (5 year-period) EVI2 of São Paulo (SP).

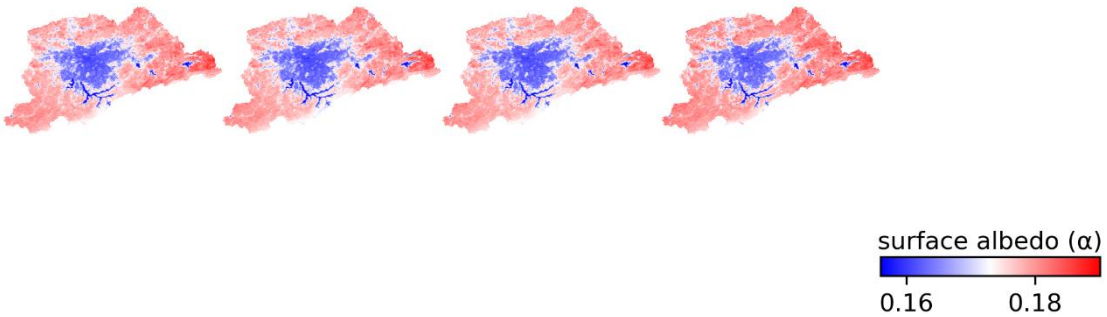

Fig. S92. Annual (5 year-period) α of São Paulo (SP).

Fig. S93. Annual (5 year-period) daytime Rn of São Paulo (SP).

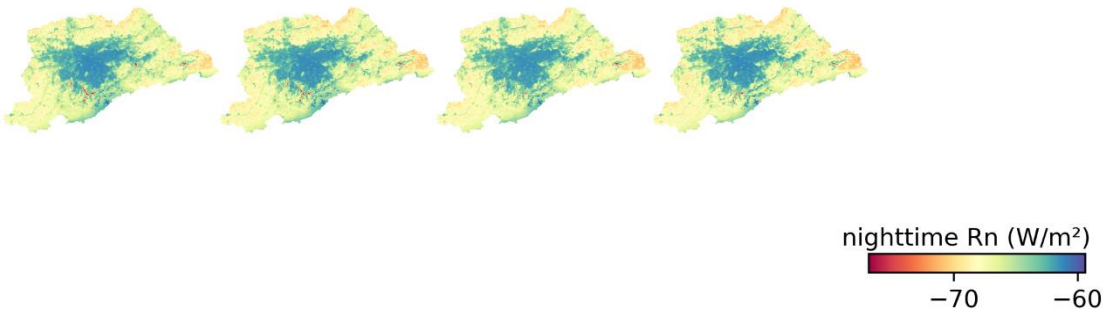

Fig. S94. Annual (5 year-period) nighttime Rn of São Paulo (SP).

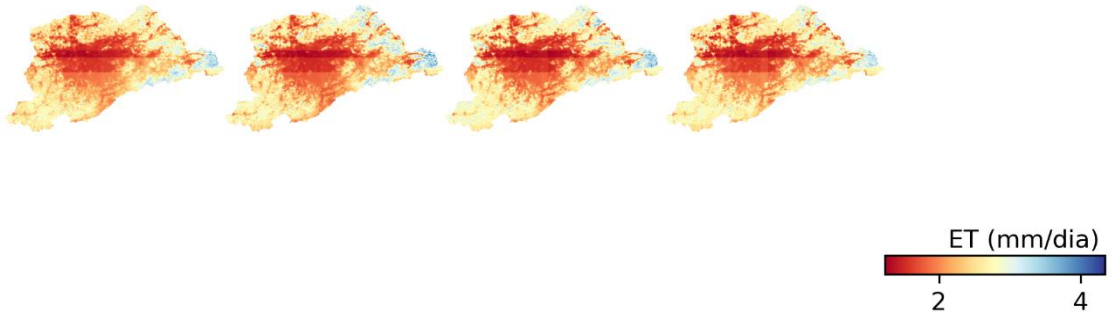

Fig. S95. Annual (5 year-period) ET of São Paulo (SP).

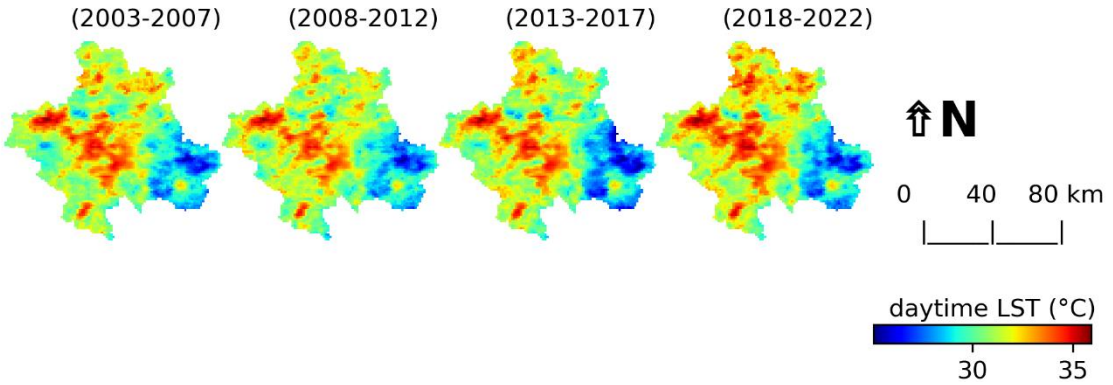

Fig. S96. Annual (5 year-period) daytime LST of Campinas (CAM).

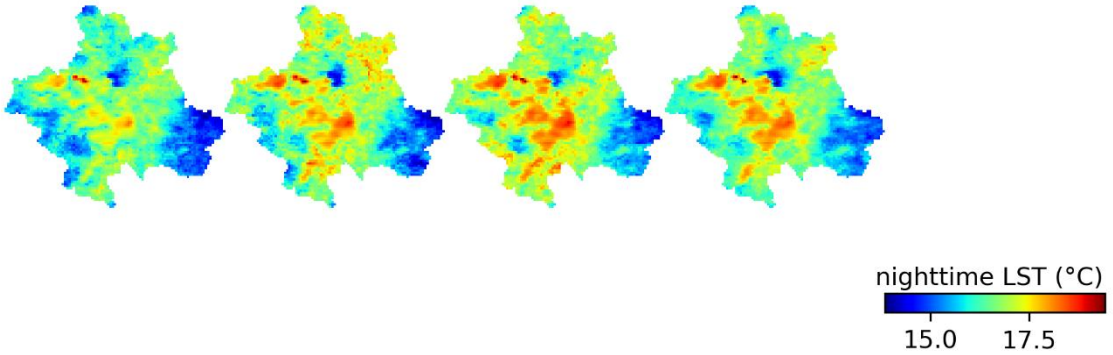

Fig. S97. Annual (5 year-period) nighttime LST of Campinas (CAM).

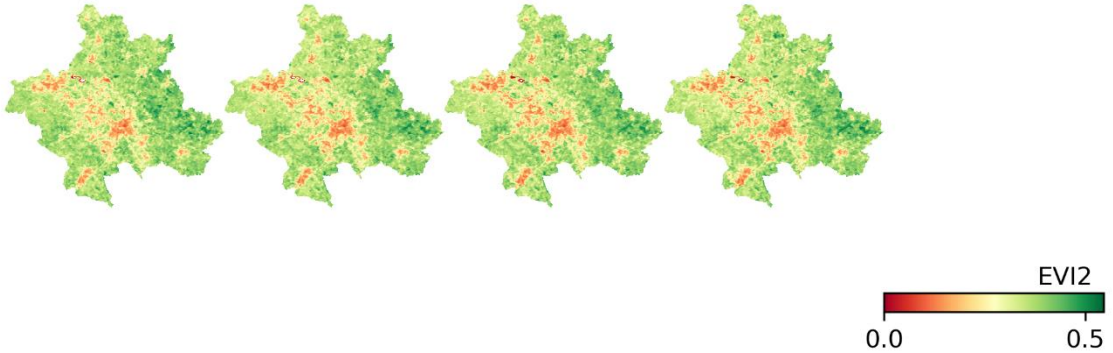

Fig. S98. Annual (5 year-period) EVI2 of Campinas (CAM).

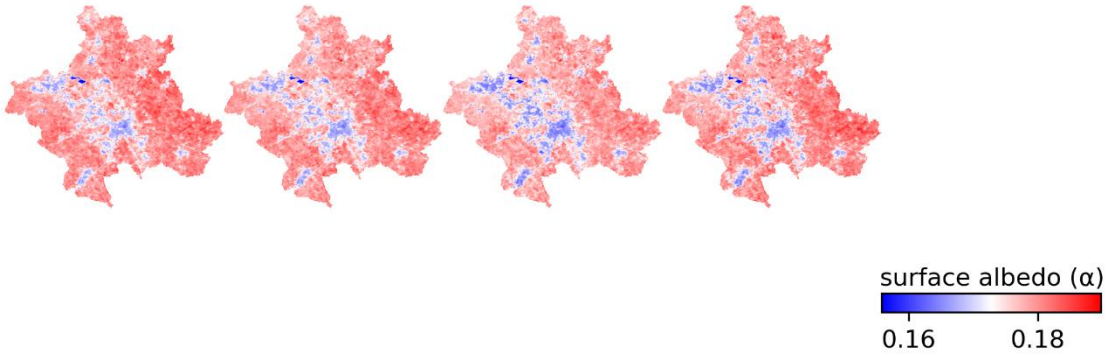

Fig. S99. Annual (5 year-period) α of Campinas (CAM).

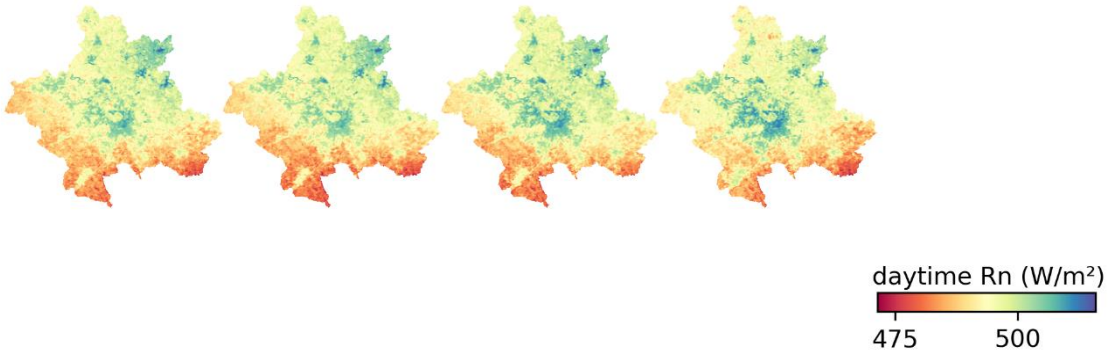

Fig. S100. Annual (5 year-period) daytime Rn of Campinas (CAM).

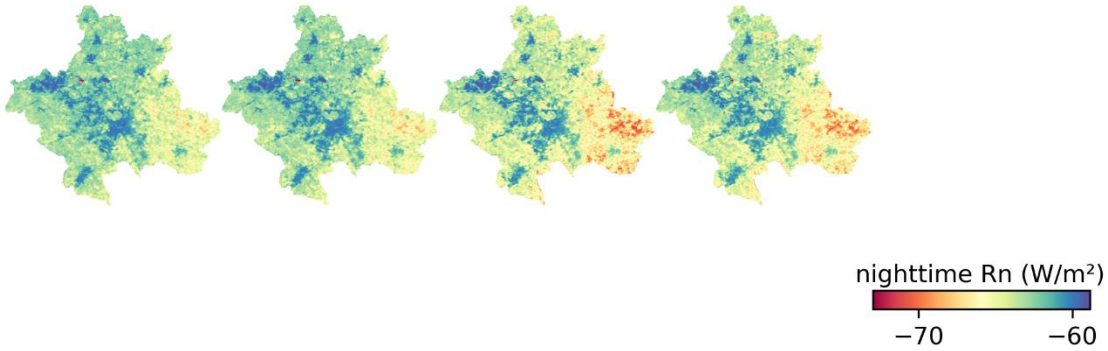

Fig. S101. Annual (5 year-period) nighttime Rn of Campinas (CAM).

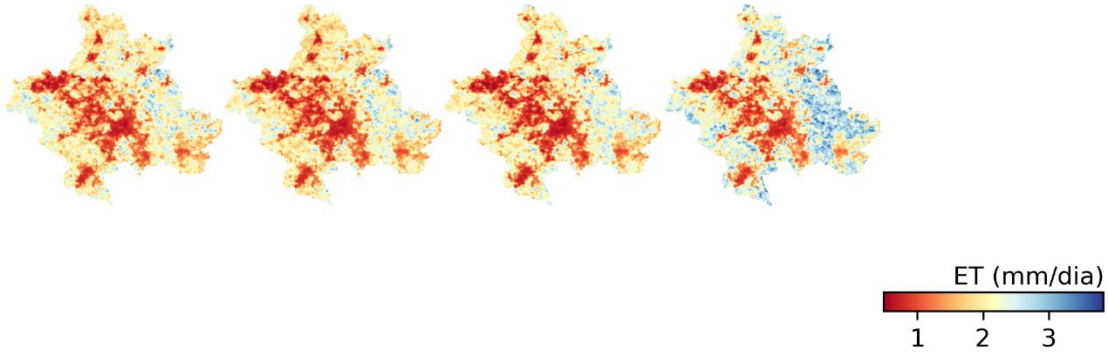

Fig. S102. Annual (5 year-period) ET of Campinas (CAM).

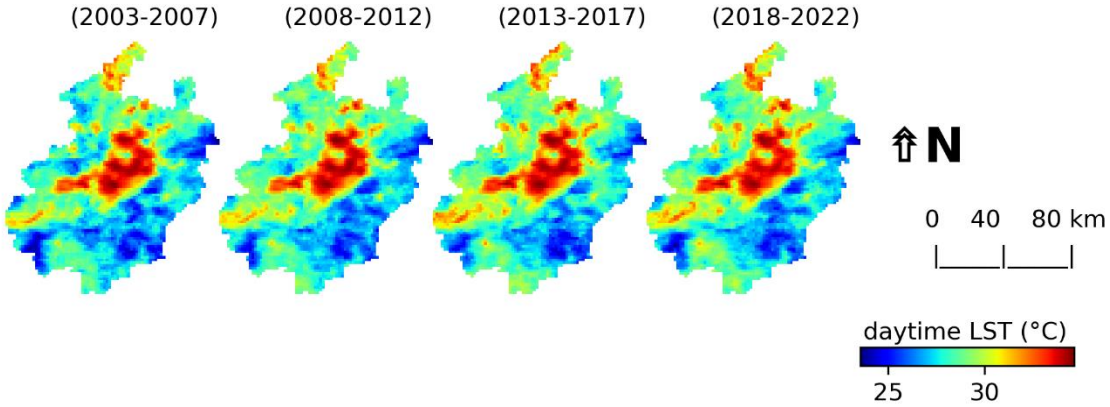

Fig. S103. Annual (5 year-period) daytime LST of Belo Horizonte (BH).

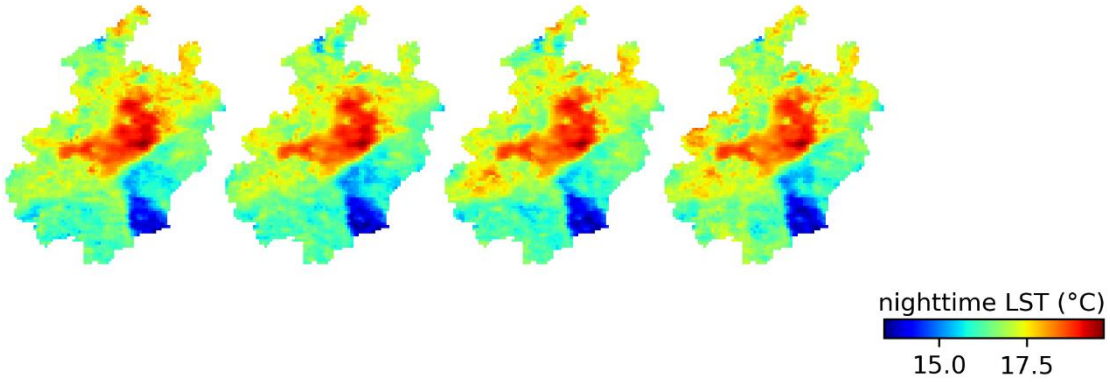

Fig. S104. Annual (5 year-period) nighttime LST of Belo Horizonte (BH).

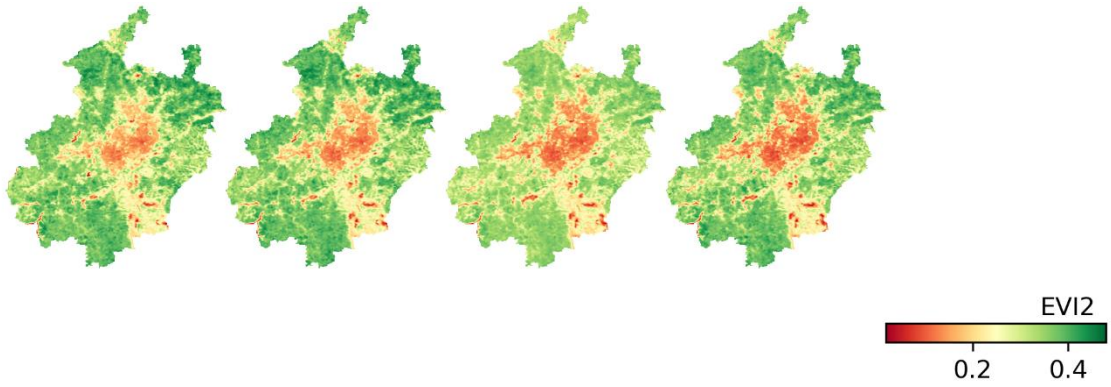

Fig. S105. Annual (5 year-period) EVI2 of Belo Horizonte (BH).

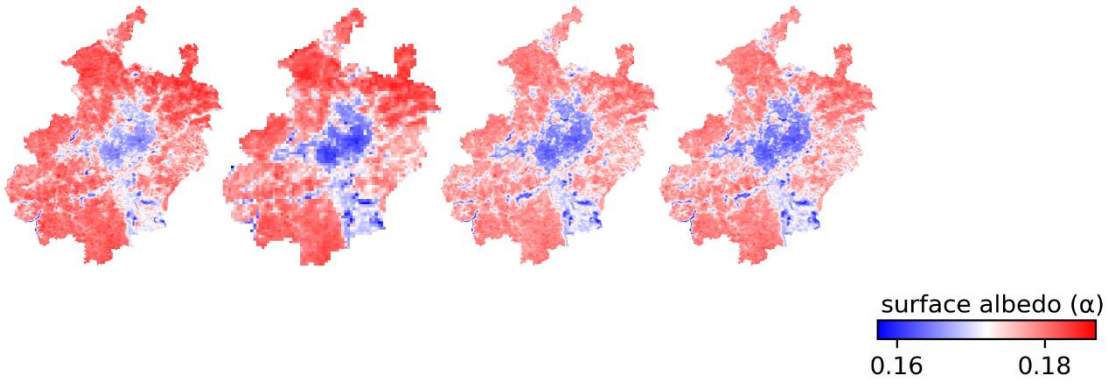

Fig. S106. Annual (5 year-period) α of Belo Horizonte (BH).

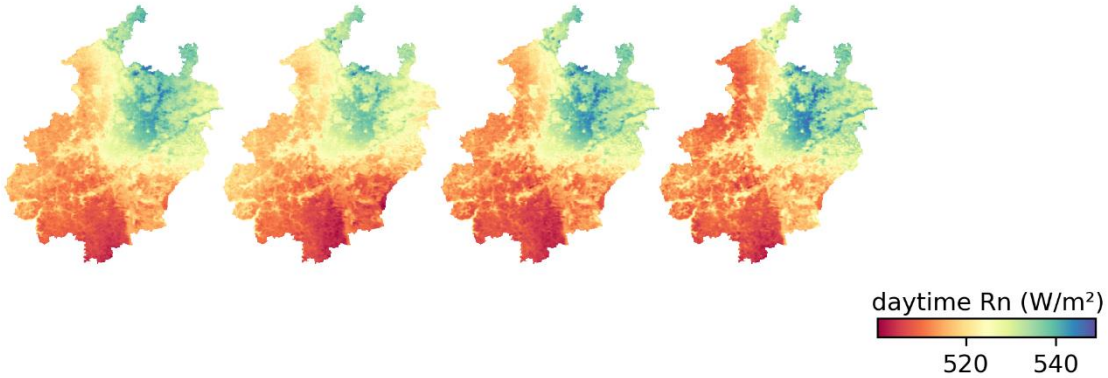

Fig. S107. Annual (5 year-period) daytime Rn of Belo Horizonte (BH).

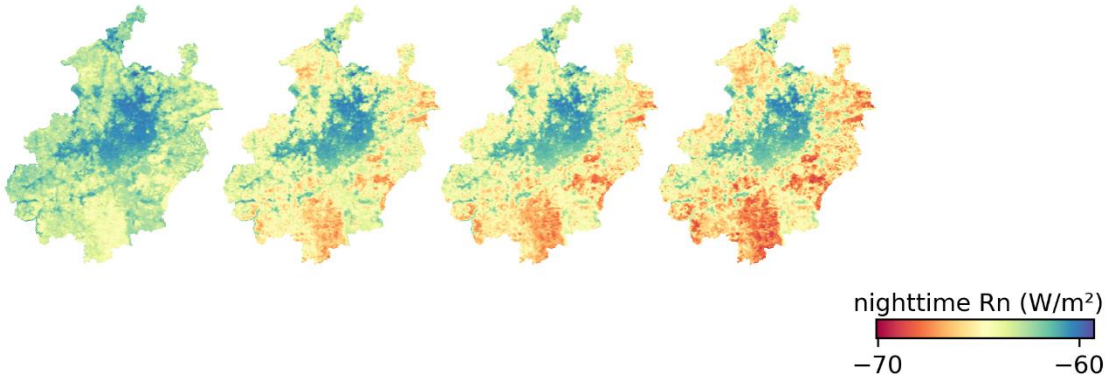

Fig. S108. Annual (5 year-period) nighttime Rn of Belo Horizonte (BH).

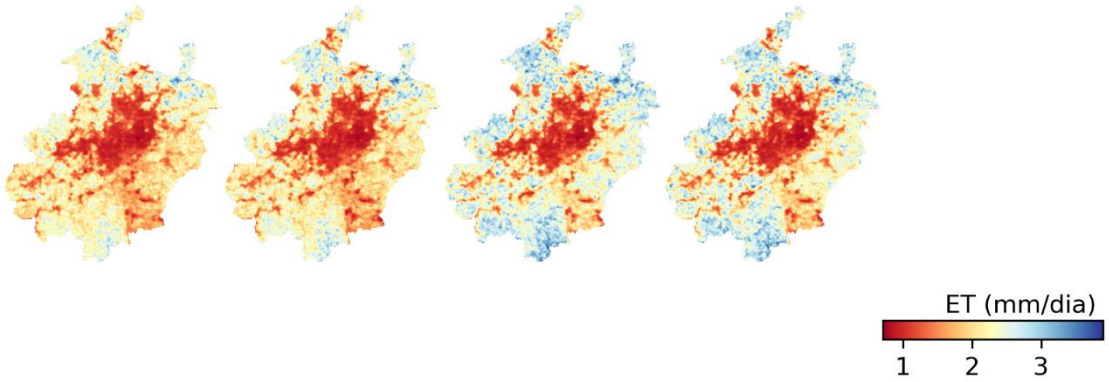

Fig. S109. Annual (5 year-period) ET of Belo Horizonte (BH).

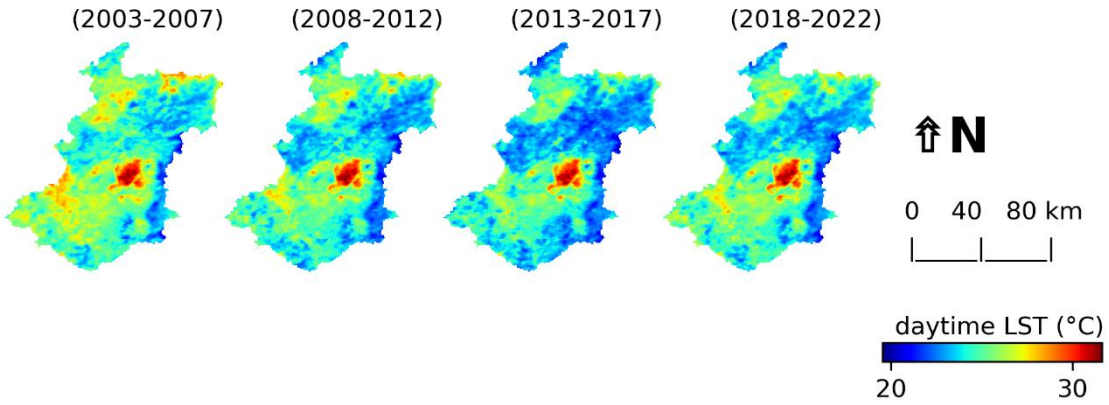

Fig. S110. Annual (5 year-period) daytime LST of Curitiba (CU).

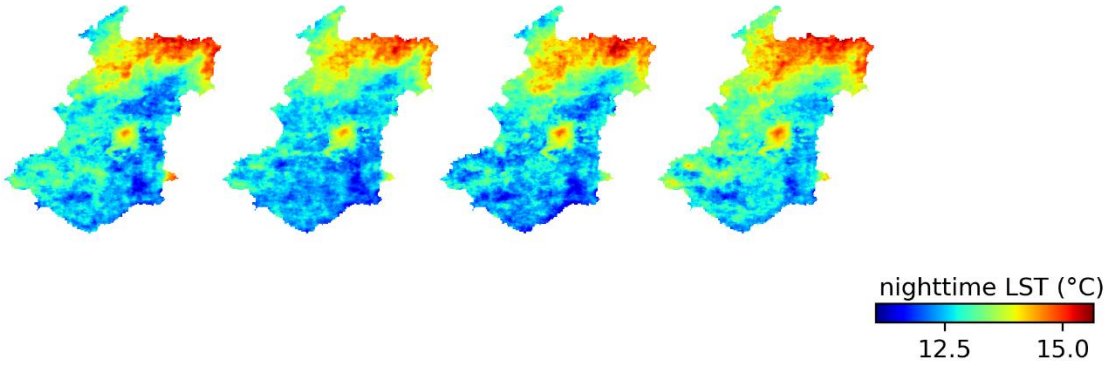

Fig. S111. Annual (5 year-period) nighttime LST of Curitiba (CU).

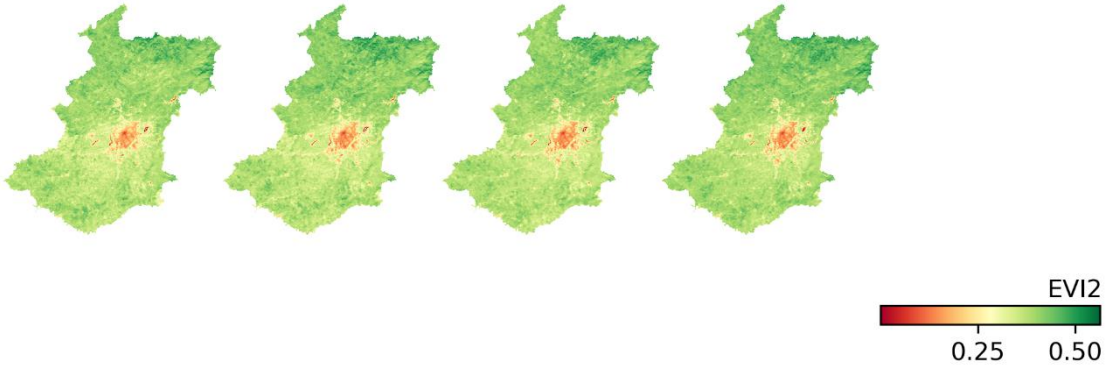

Fig. S112. Annual (5 year-period) EVI2 of Curitiba (CU).

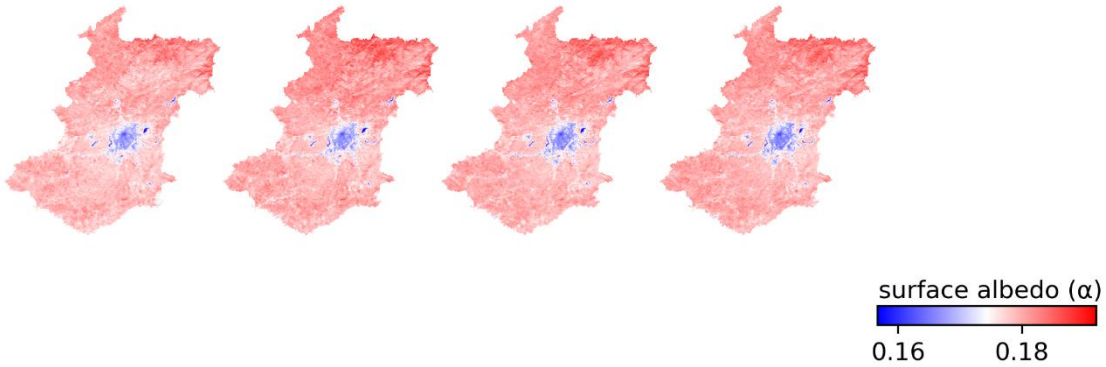

Fig. S113. Annual (5 year-period) α of Curitiba (CU).

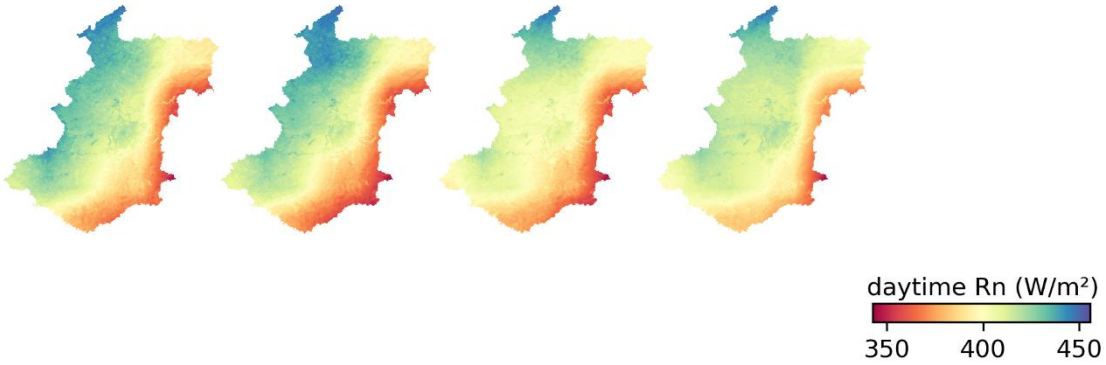

Fig. S114. Annual (5 year-period) daytime Rn of Curitiba (CU).

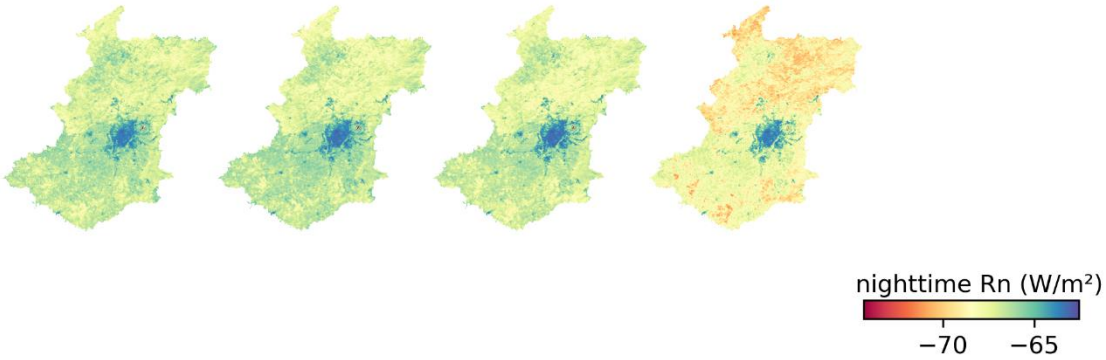

Fig. S115. Annual (5 year-period) nighttime Rn of Curitiba (CU).

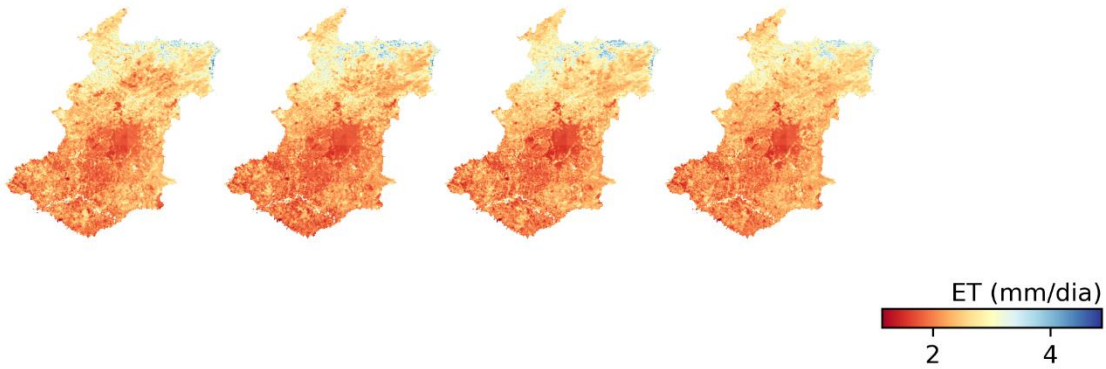

Fig. S116. Annual (5 year-period) ET of Curitiba (CU).

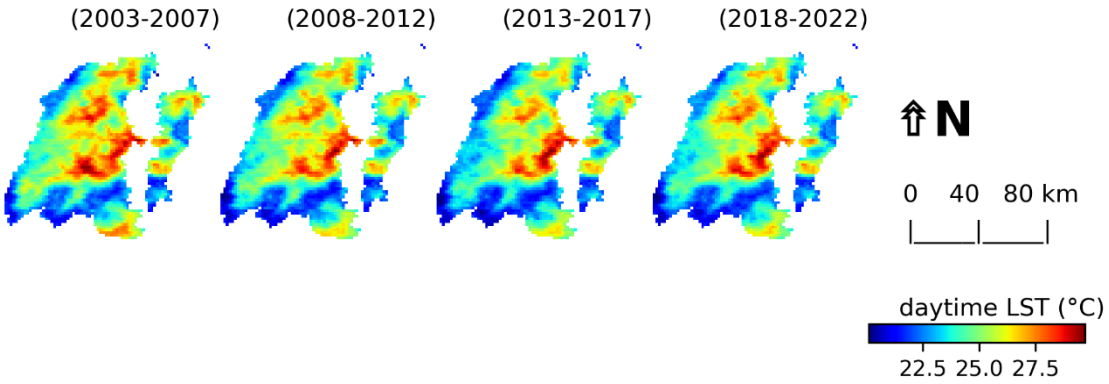

Fig. S117. Annual (5 year-period) daytime LST of Florianópolis (FLO).

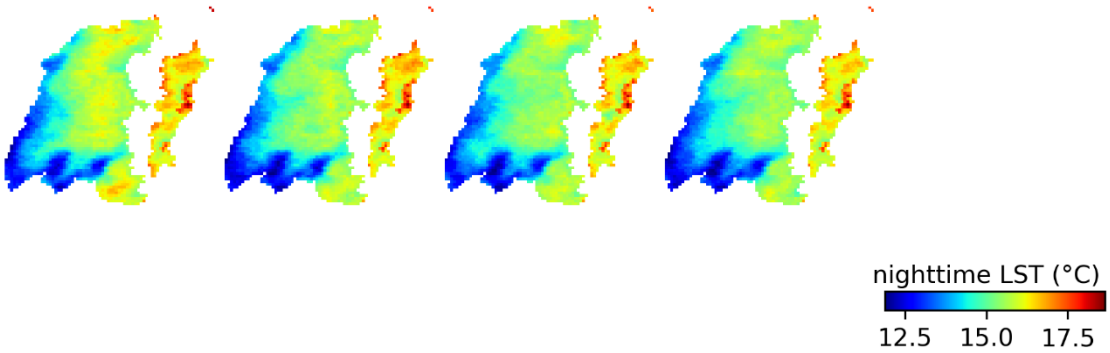

Fig. S118. Annual (5 year-period) nighttime LST of Florianópolis (FLO).

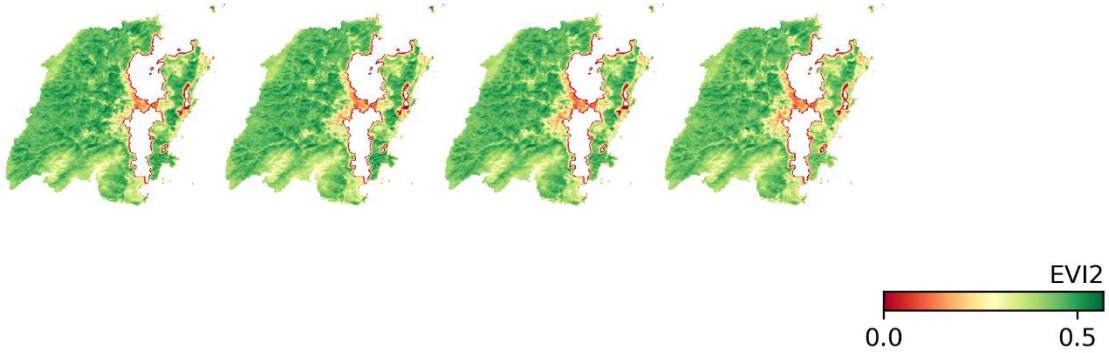

Fig. S119. Annual (5 year-period) EVI2 of Florianópolis (FLO).

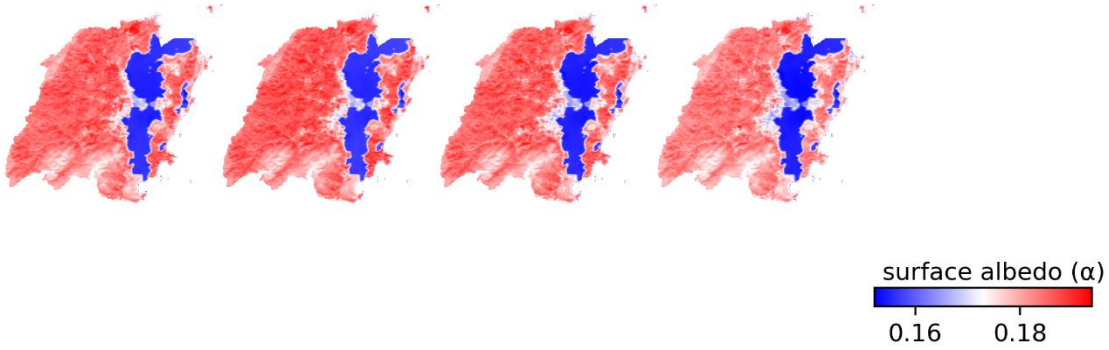

Fig. S120. Annual (5 year-period) α of Florianópolis (FLO).

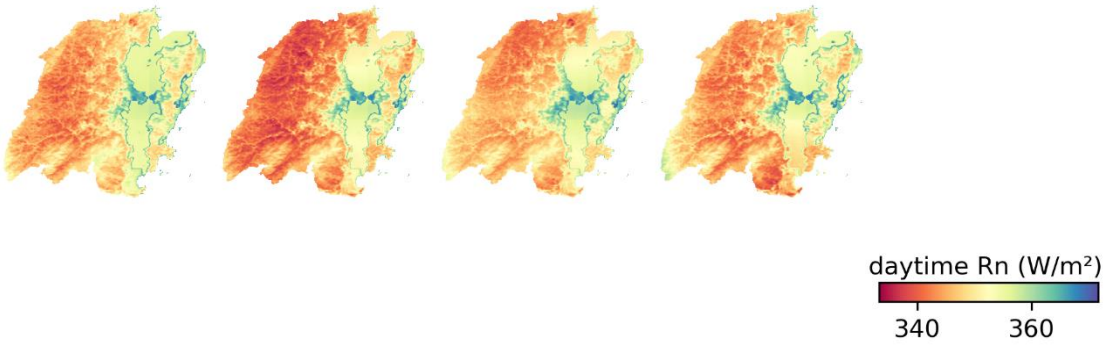

Fig. S121. Annual (5 year-period) daytime Rn of Florianópolis (FLO).

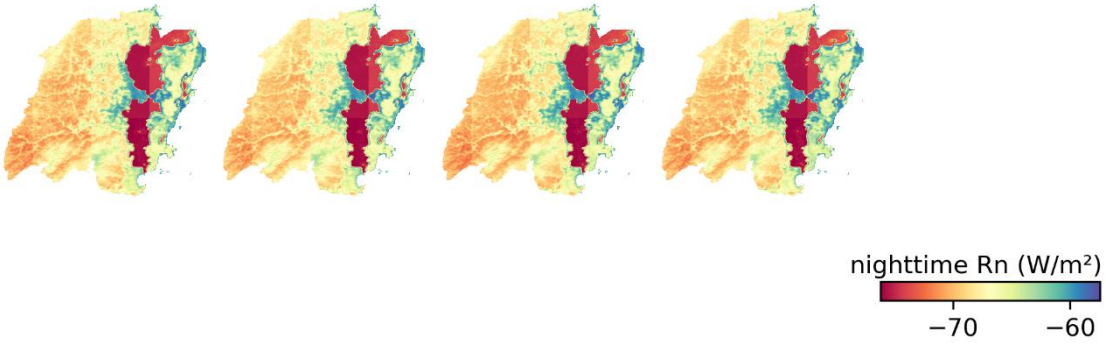

Fig. S122. Annual (5 year-period) nighttime Rn of Florianópolis (FLO).

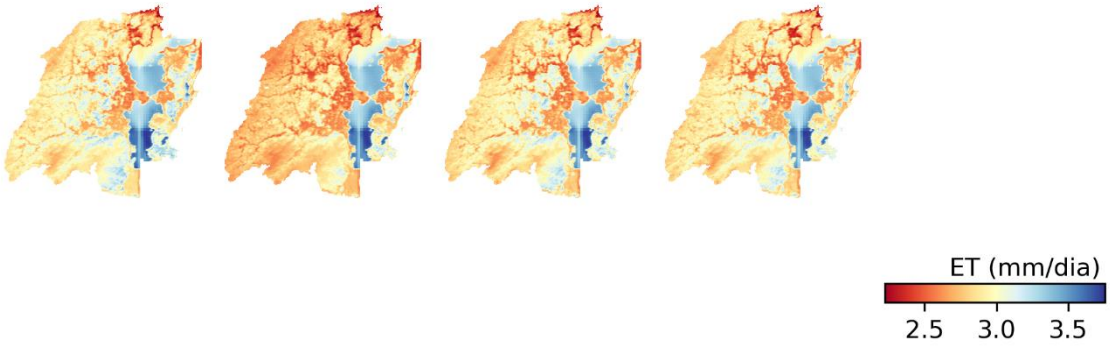

Fig. S123. Annual (5 year-period) ET of Florianópolis (FLO).

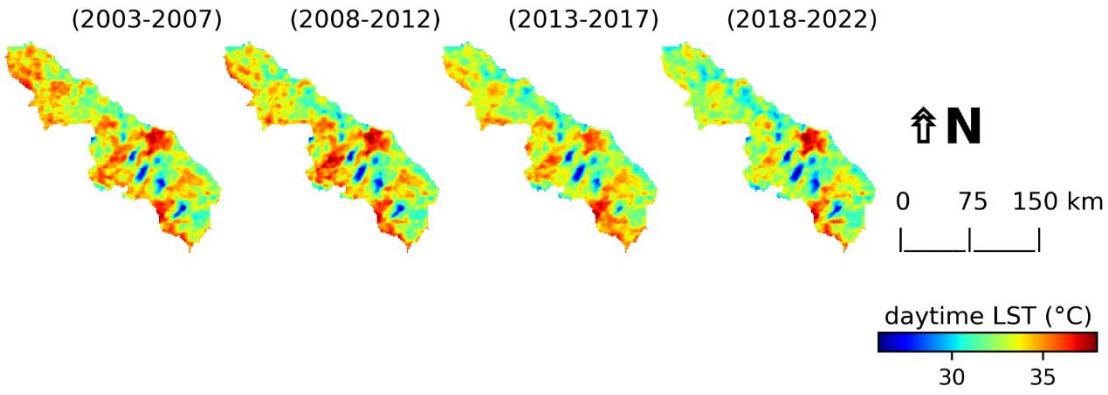

Fig. S124. Annual (5 year-period) daytime LST of Fortaleza (FO).

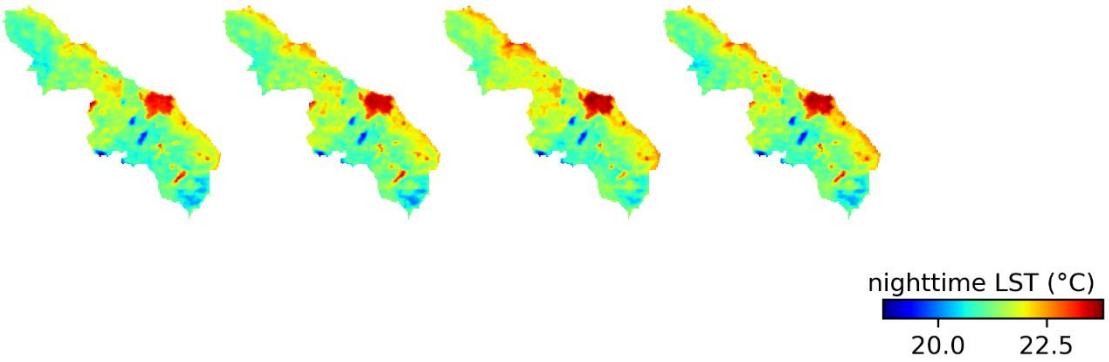

Fig. S125. Annual (5 year-period) nighttime LST of Fortaleza (FO).

Fig. S126. Annual (5 year-period) EVI2 of Fortaleza (FO).

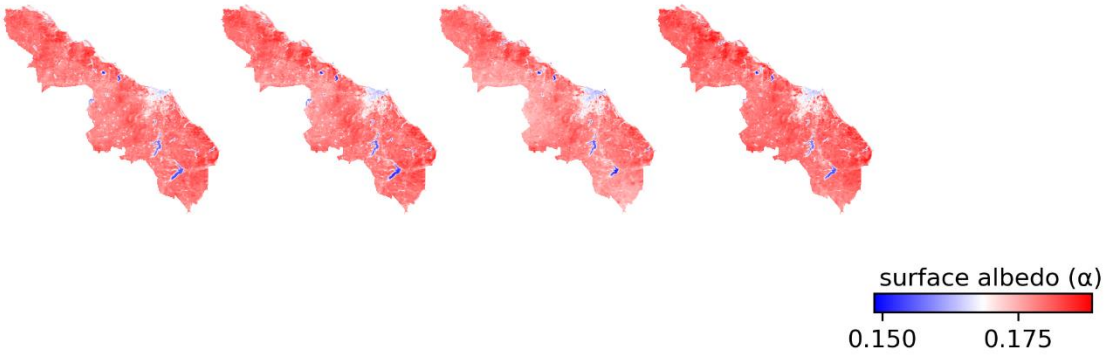

Fig. S127. Annual (5 year-period) α of Fortaleza (FO).

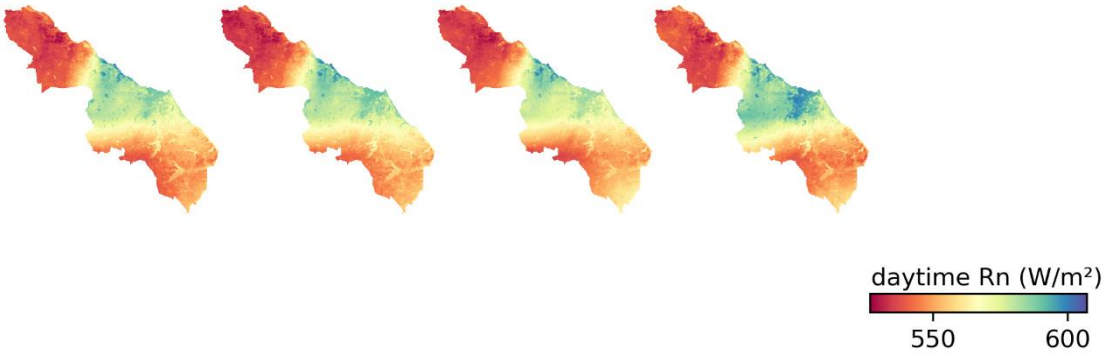

Fig. S128. Annual (5 year-period) daytime Rn of Fortaleza (FO).

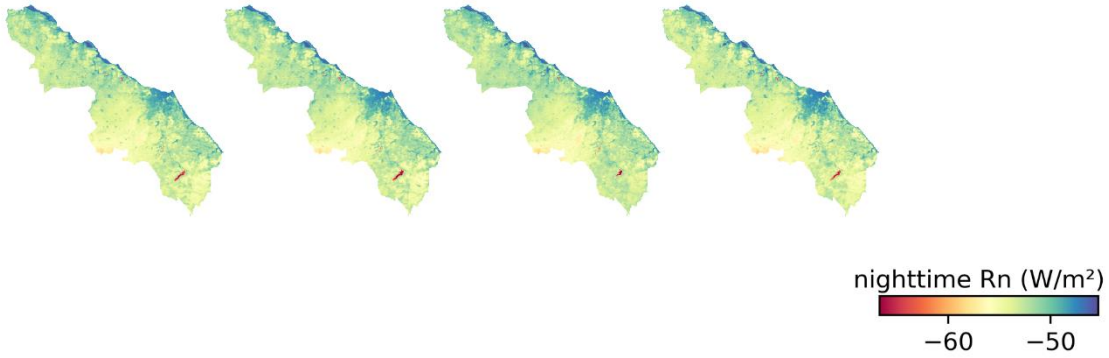

Fig. S129. Annual (5 year-period) nighttime Rn of Fortaleza (FO).

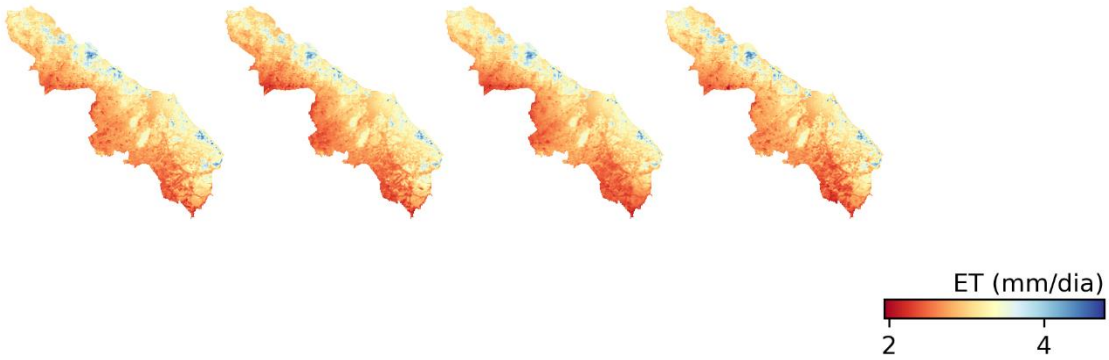

Fig. S130. Annual (5 year-period) ET of Fortaleza (FO).

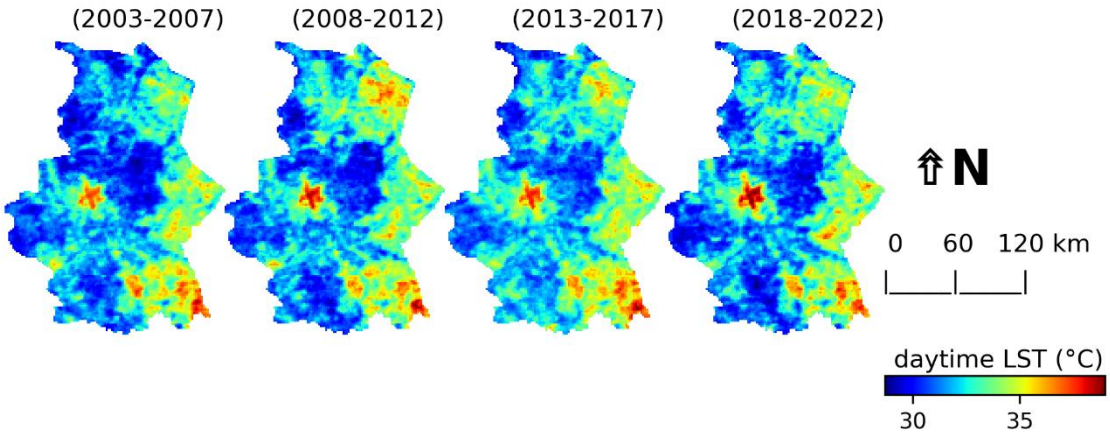

Fig. S131. Annual (5 year-period) daytime LST of Teresina (TE).

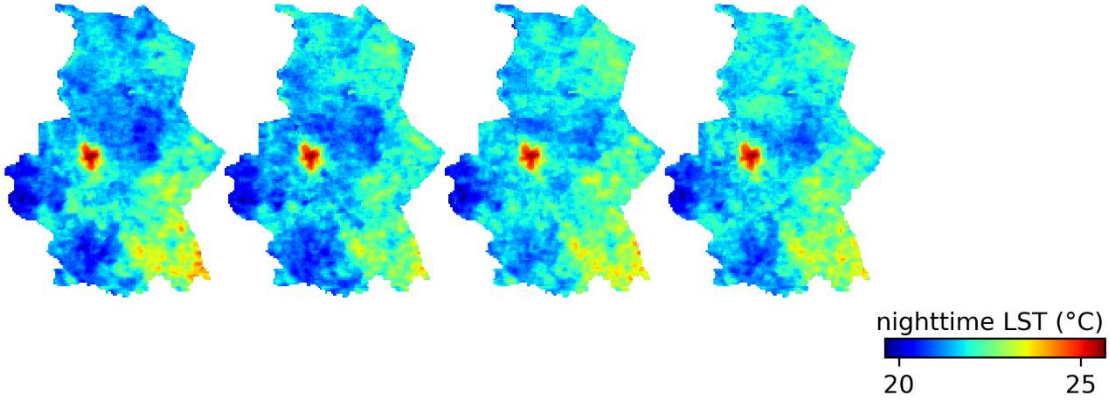

Fig. S132. Annual (5 year-period) nighttime LST of Teresina (TE).

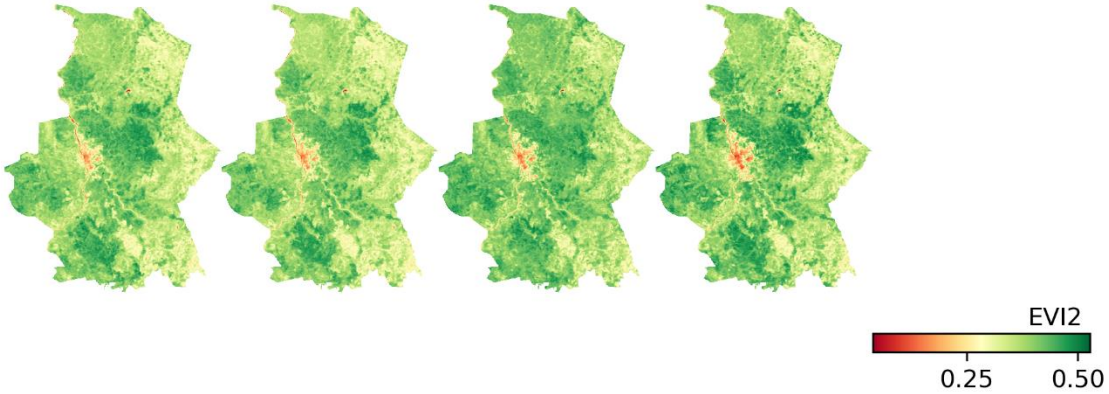

Fig. S133. Annual (5 year-period) EVI2 of F Teresina (TE).

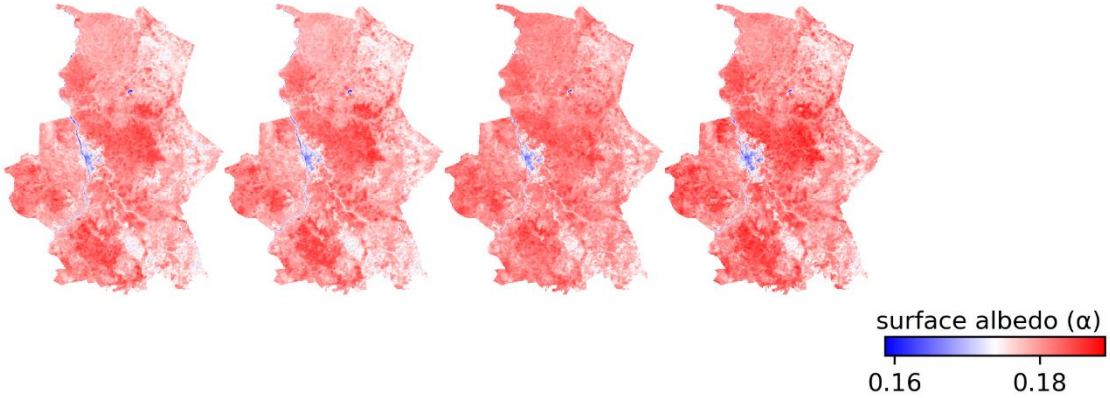

Fig. S134. Annual (5 year-period) α of Teresina (TE).

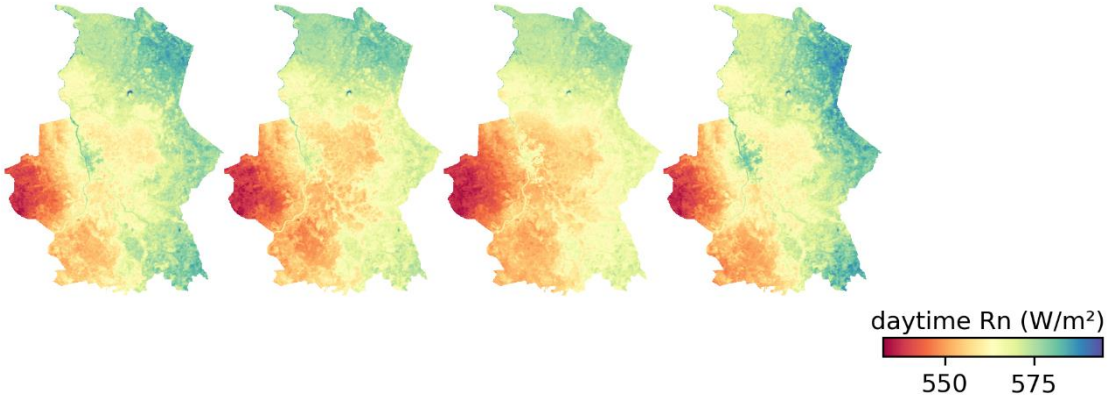

Fig. S135. Annual (5 year-period) daytime Rn of Teresina (TE).

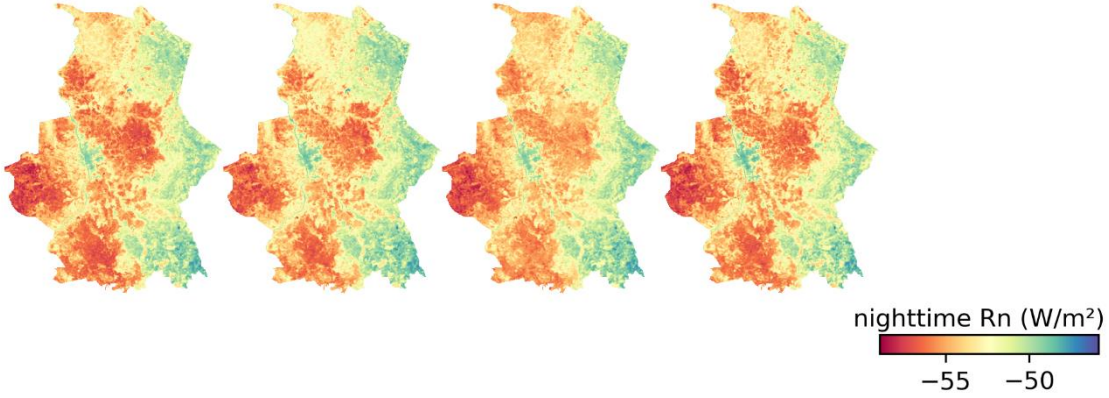

Fig. S136. Annual (5 year-period) nighttime Rn of Teresina (TE).

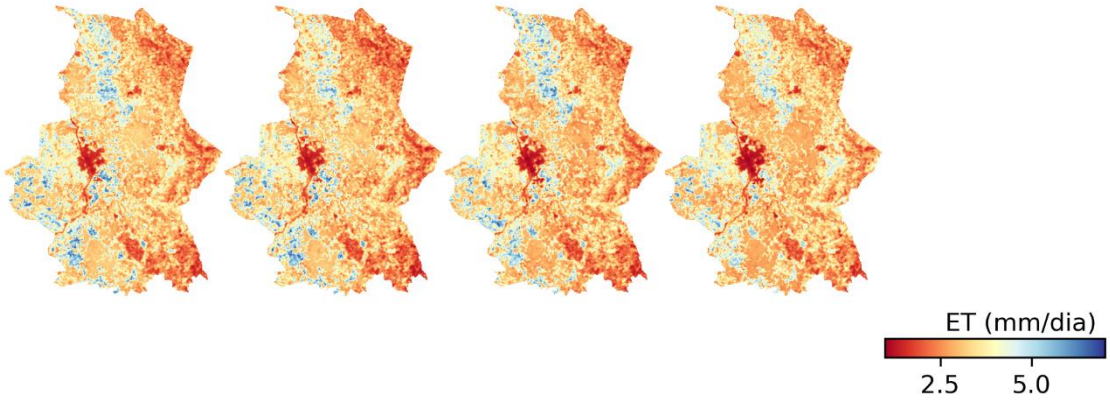

Fig. S137. Annual (5 year-period) ET of Teresina (TE).

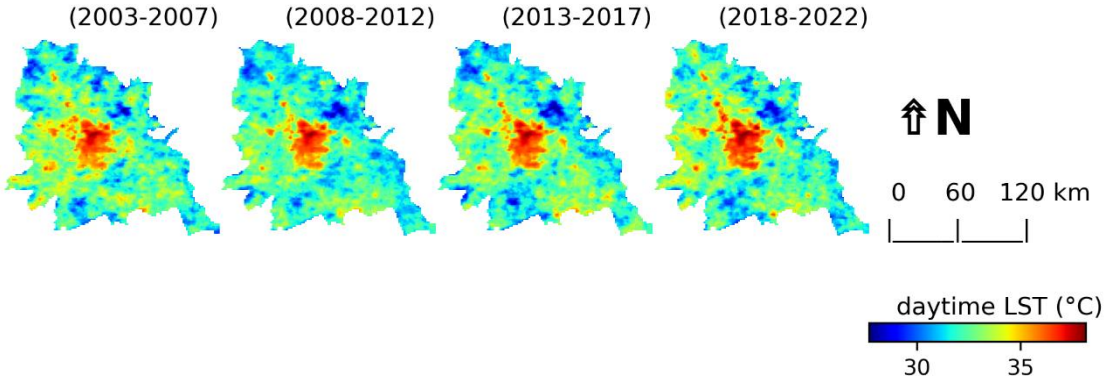

Fig. S131. Annual (5 year-period) daytime LST of Goiânia (GO).

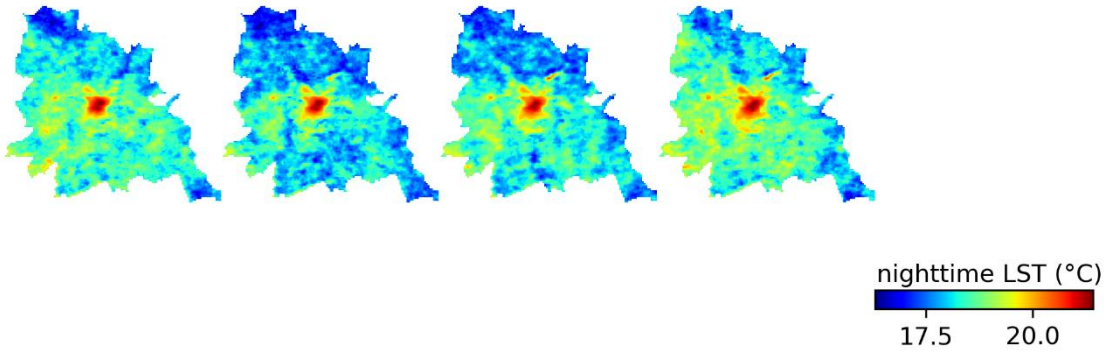

Fig. S132. Annual (5 year-period) nighttime LST of Goiânia (GO).

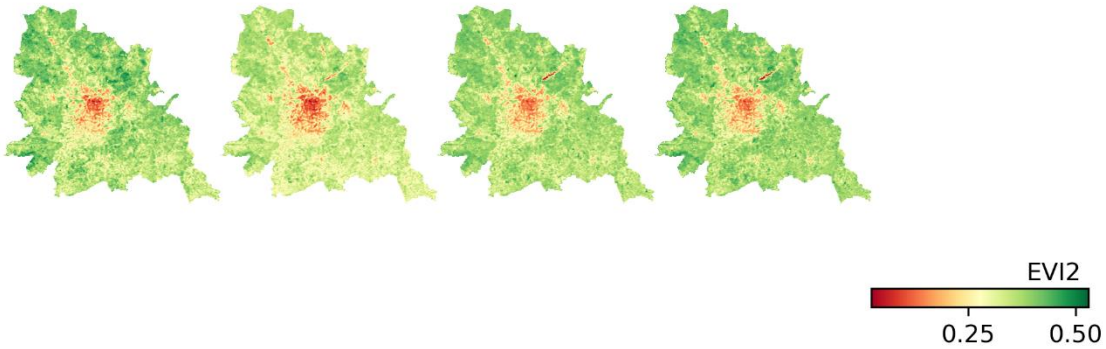

Fig. S133. Annual (5 year-period) EVI2 of F Goiânia (GO).

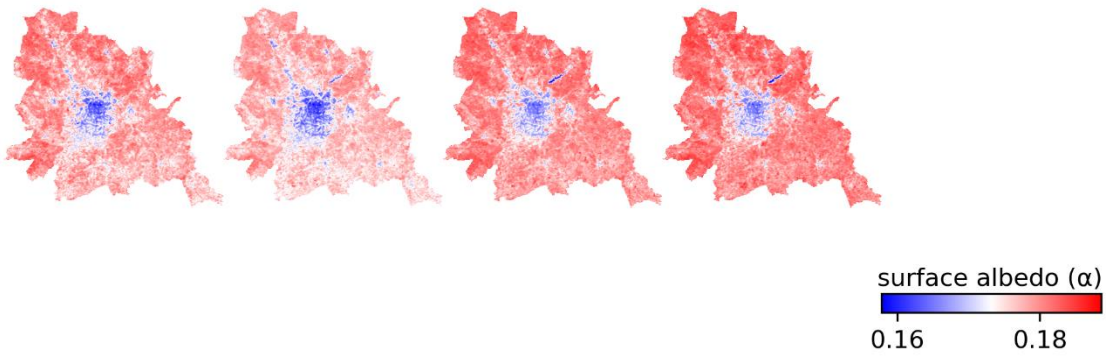

Fig. S134. Annual (5 year-period) α of Goiânia (GO).

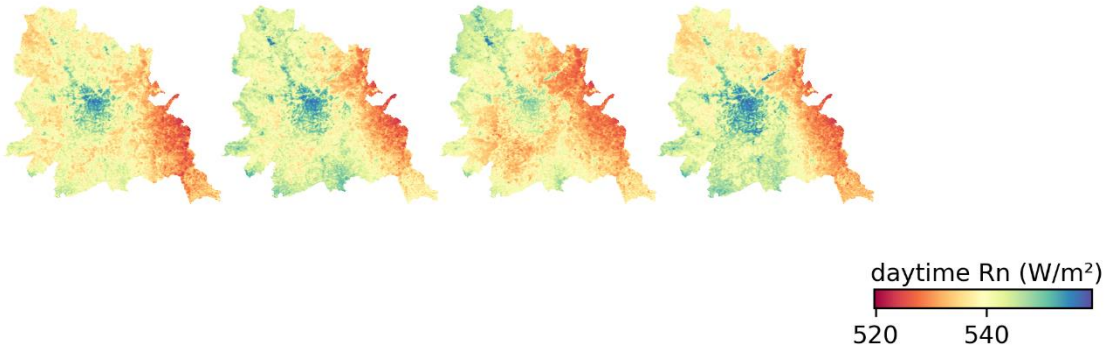

Fig. S135. Annual (5 year-period) daytime Rn of Goiânia (GO).

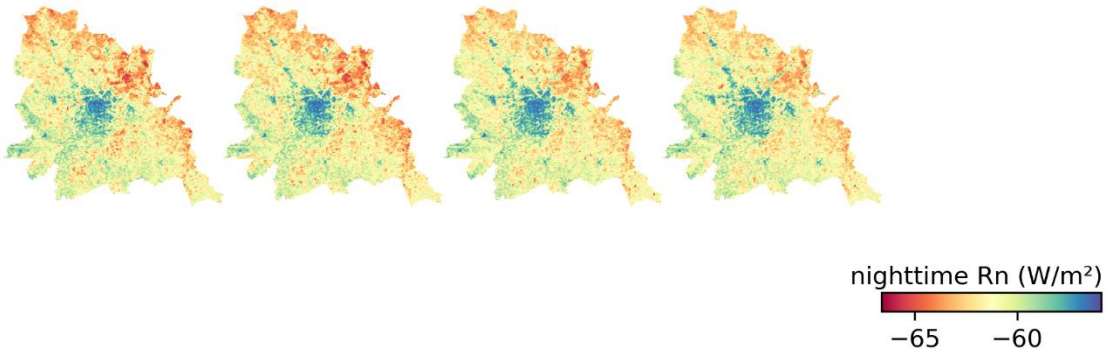

Fig. S136. Annual (5 year-period) nighttime Rn of Goiânia (GO).

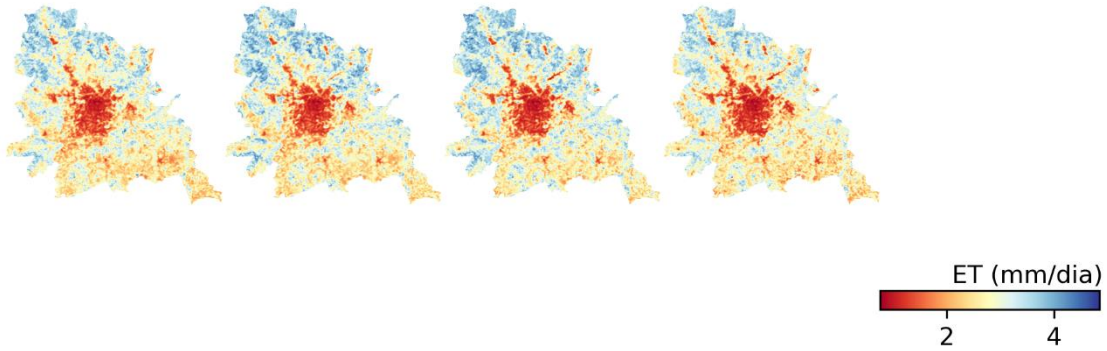

Fig. S137. Annual (5 year-period) ET of Goiânia (GO).

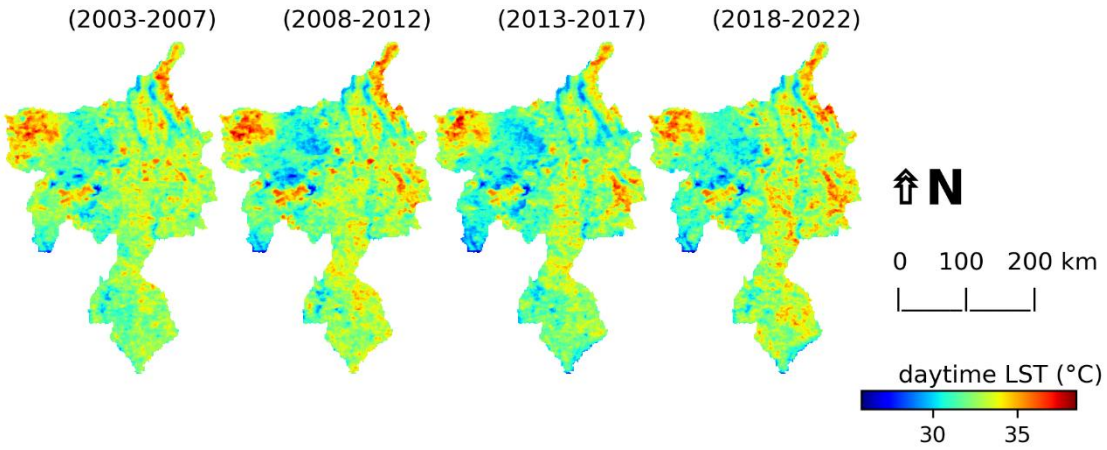

Fig. S138. Annual (5 year-period) daytime LST of Distrito Federal (DF).

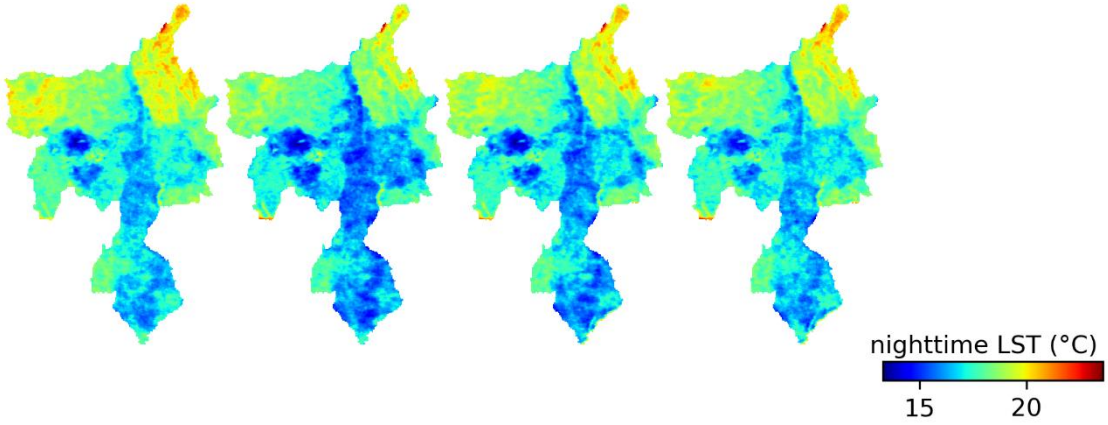

Fig. S139. Annual (5 year-period) nighttime LST of Distrito Federal (DF).

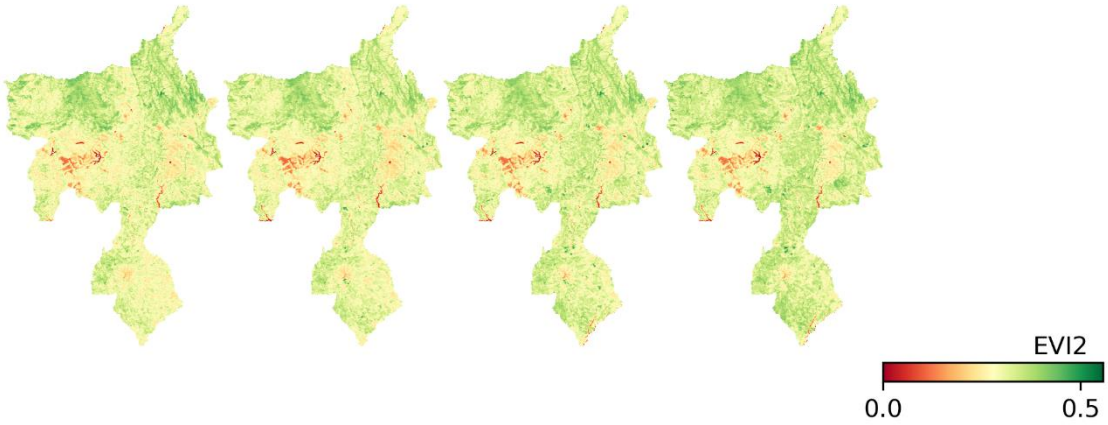

Fig. S140. Annual (5 year-period) EVI2 of Distrito Federal (DF).

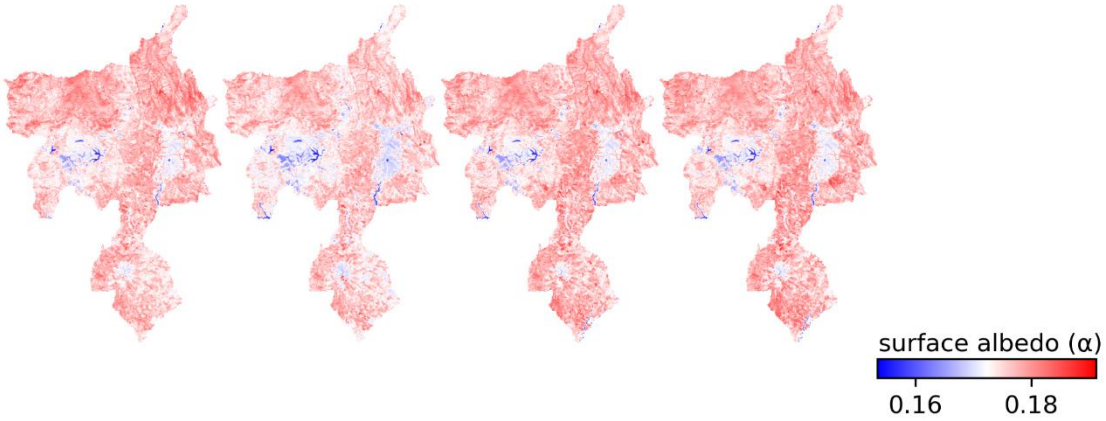

Fig. S141. Annual (5 year-period) α of Distrito Federal (DF).

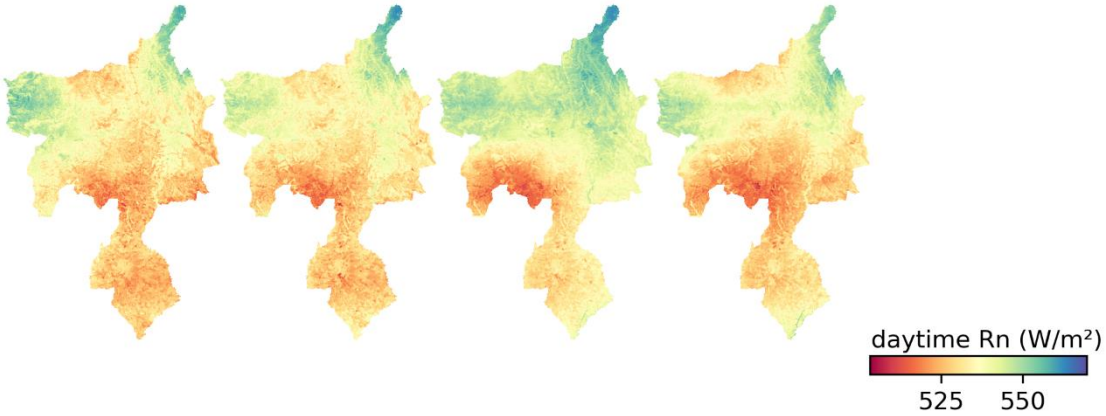

Fig. S142. Annual (5 year-period) daytime Rn of Distrito Federal (DF).

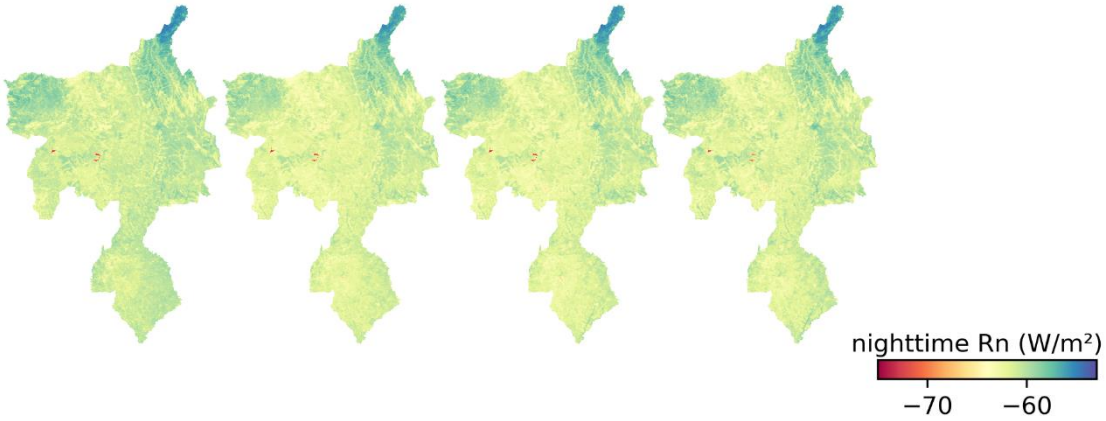

Fig. S143. Annual (5 year-period) nighttime Rn of Distrito Federal (DF).

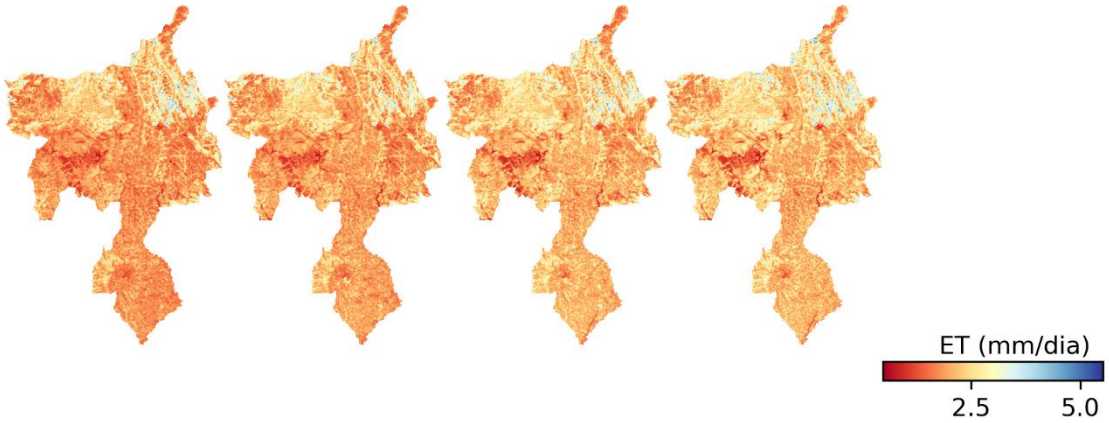

Fig. S144. Annual (5 year-period) ET of Distrito Federal (DF).

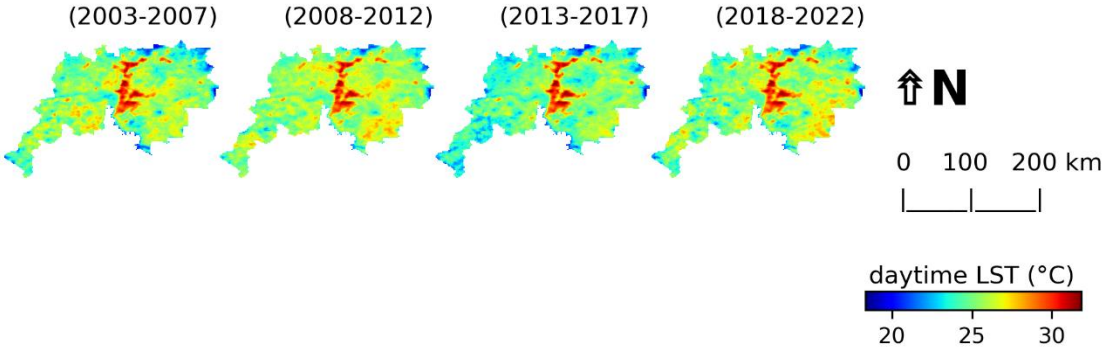

Fig. S145. Annual (5 year-period) daytime LST of Porto Alegre (PA).

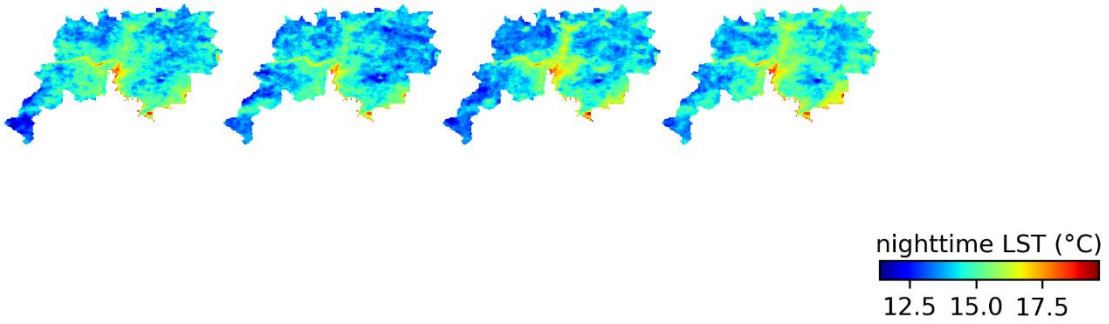

Fig. S146. Annual (5 year-period) nighttime LST of Porto Alegre (PA).

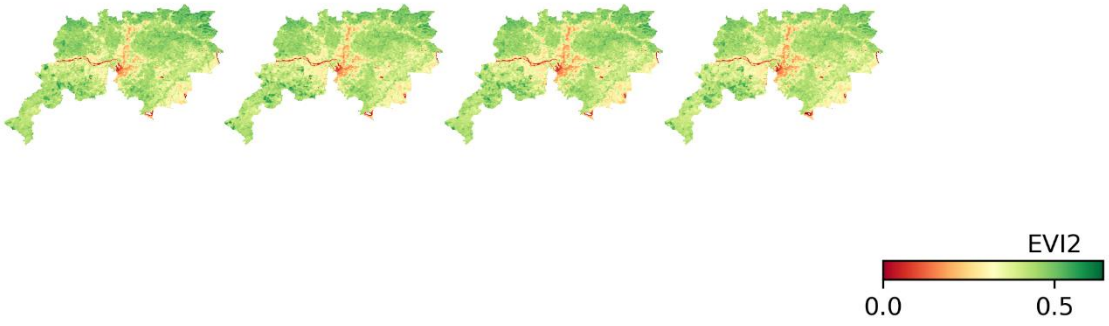

Fig. S147. Annual (5 year-period) EVI2 of Porto Alegre (PA).

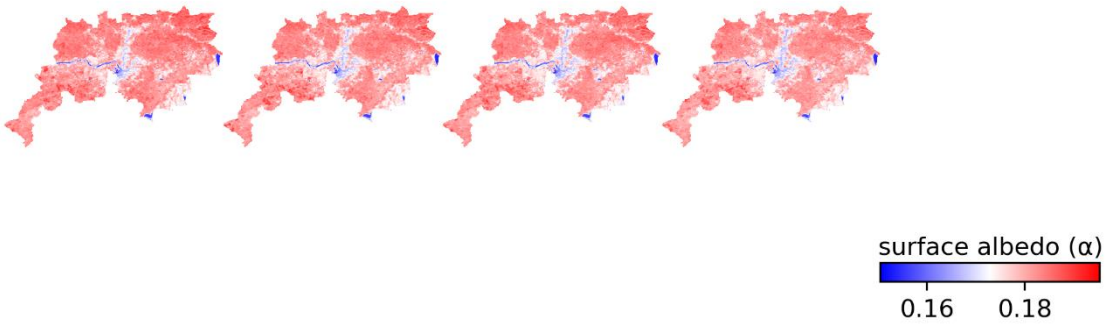

Fig. S148. Annual (5 year-period) α of Porto Alegre (PA).

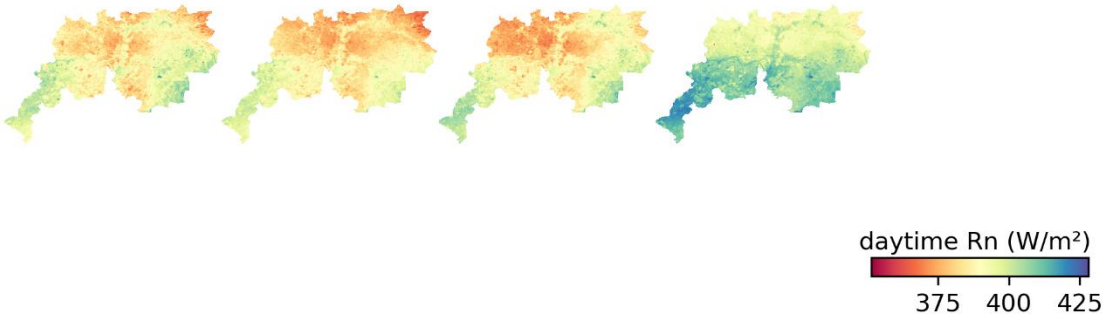

Fig. S149. Annual (5 year-period) daytime Rn of Porto Alegre (PA).

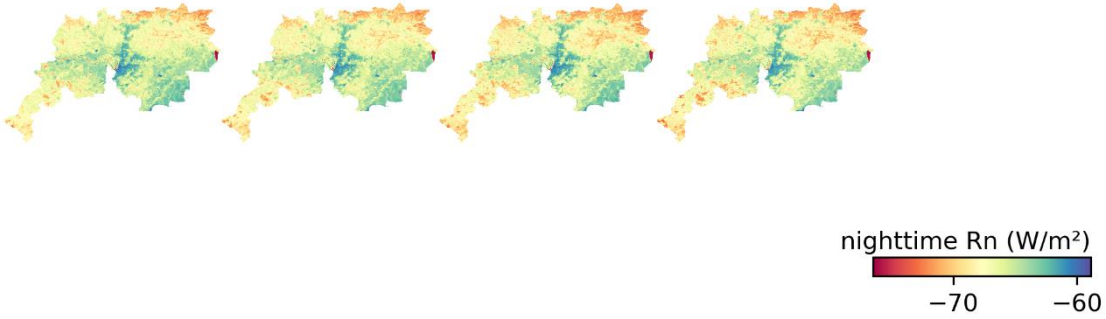

Fig. S150. Annual (5 year-period) nighttime Rn of Porto Alegre (PA).

Fig. S151. Annual (5 year-period) ET of Porto Alegre (PA).

8.5 Figures S152 to S172: Monthly variability (2003-2022) of daytime and nighttime urban LST, daytime and nighttime SUHII, Enhanced Vegetation Index 2 (EVI2), surface albedo (α), surface net radiation (Rn), and actual evapotranspiration (ET).

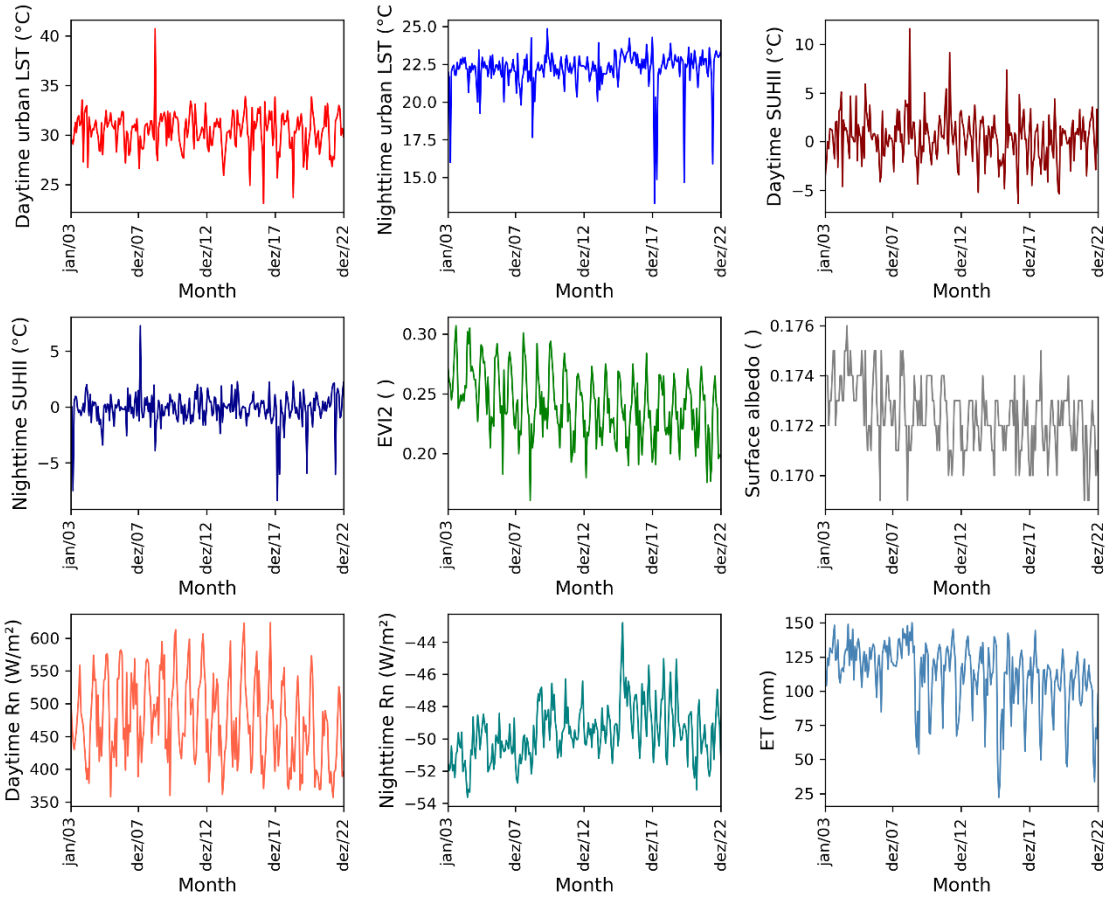

Fig. S152. Monthly variability of daytime and nighttime urban LST (ºC), daytime and nighttime SUHII (ºC), Enhanced Vegetation Index 2 (EVI2), surface albedo (α), surface net radiation (Rn, W/m^2), and actual evapotranspiration (ET, mm) of Manaus (MA).

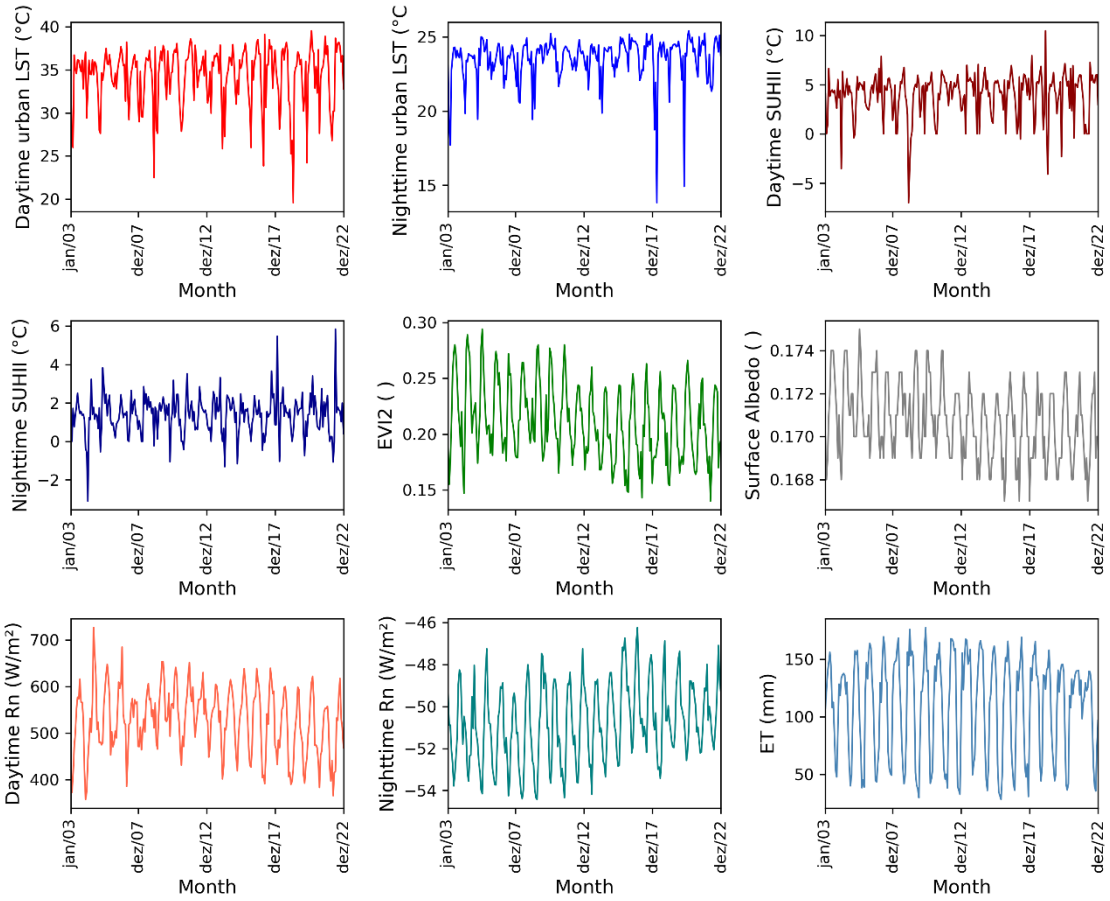

Fig. S153. Monthly variability of daytime and nighttime urban LST (ºC), daytime and nighttime SUHII (ºC), Enhanced Vegetation Index 2 (EVI2), surface albedo (α), surface net radiation (Rn, W/m^2), and actual evapotranspiration (ET, mm) of Belém (BE).

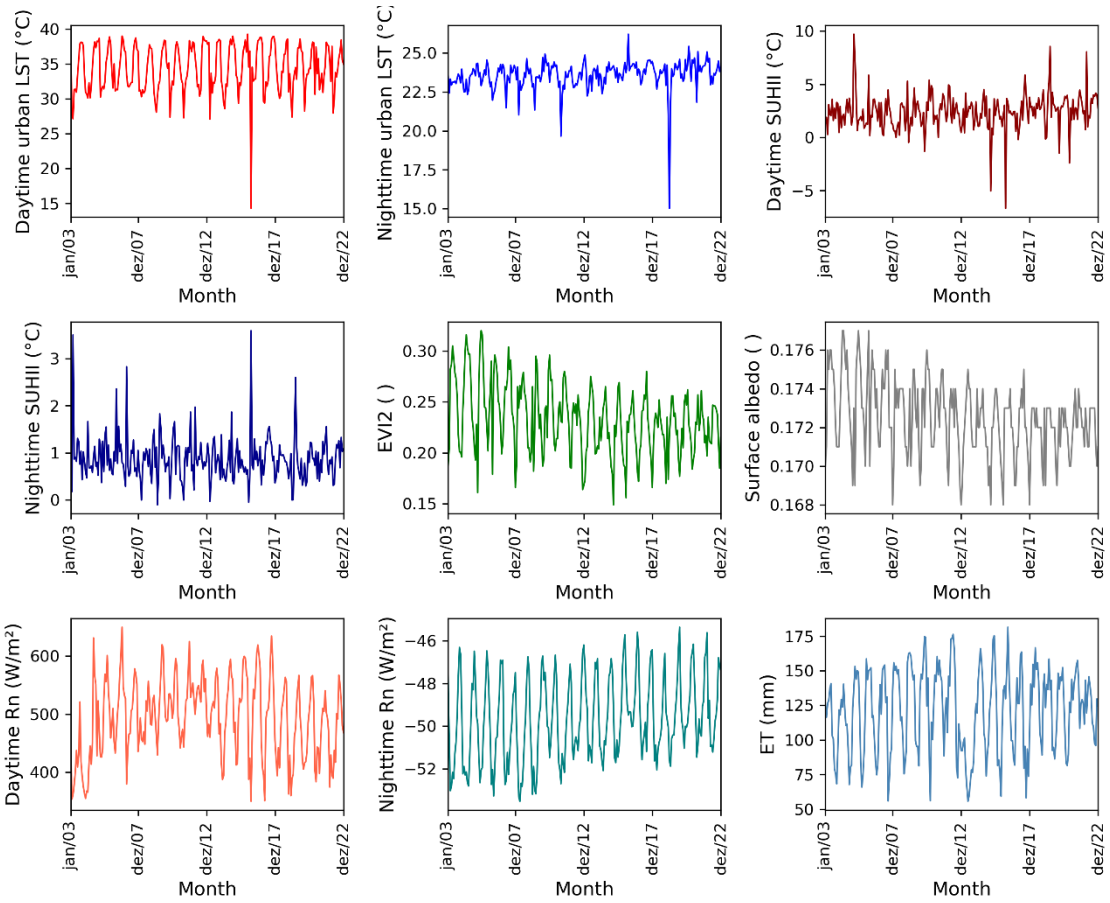

Fig. S154. Monthly variability of daytime and nighttime urban LST (ºC), daytime and nighttime SUHII (ºC), Enhanced Vegetation Index 2 (EVI2), surface albedo (α), surface net radiation (Rn, W/m^2), and actual evapotranspiration (ET, mm) of São Luís (SL).

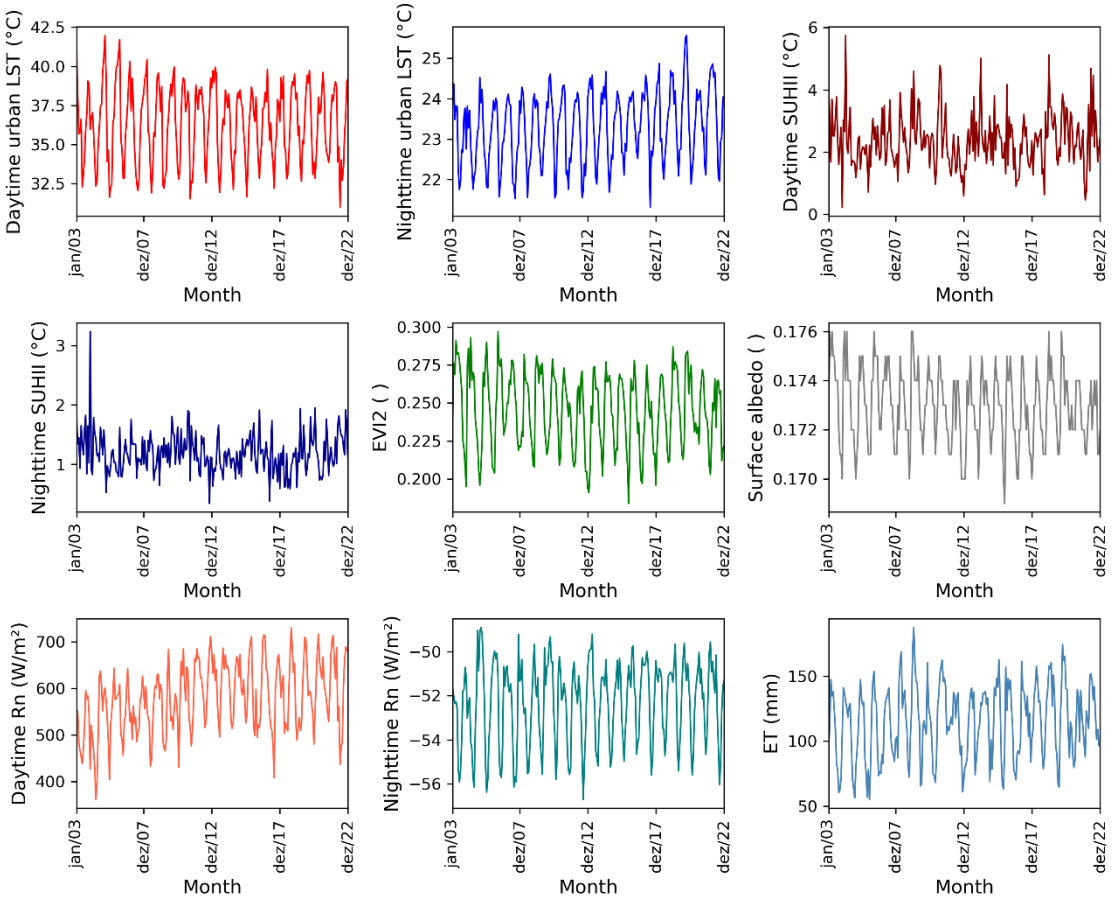

Fig. S155. Monthly variability of daytime and nighttime urban LST (ºC), daytime and nighttime SUHII (ºC), Enhanced Vegetation Index 2 (EVI2), surface albedo (α), surface net radiation (Rn, W/m^2), and actual evapotranspiration (ET, mm) of Natal (NA).

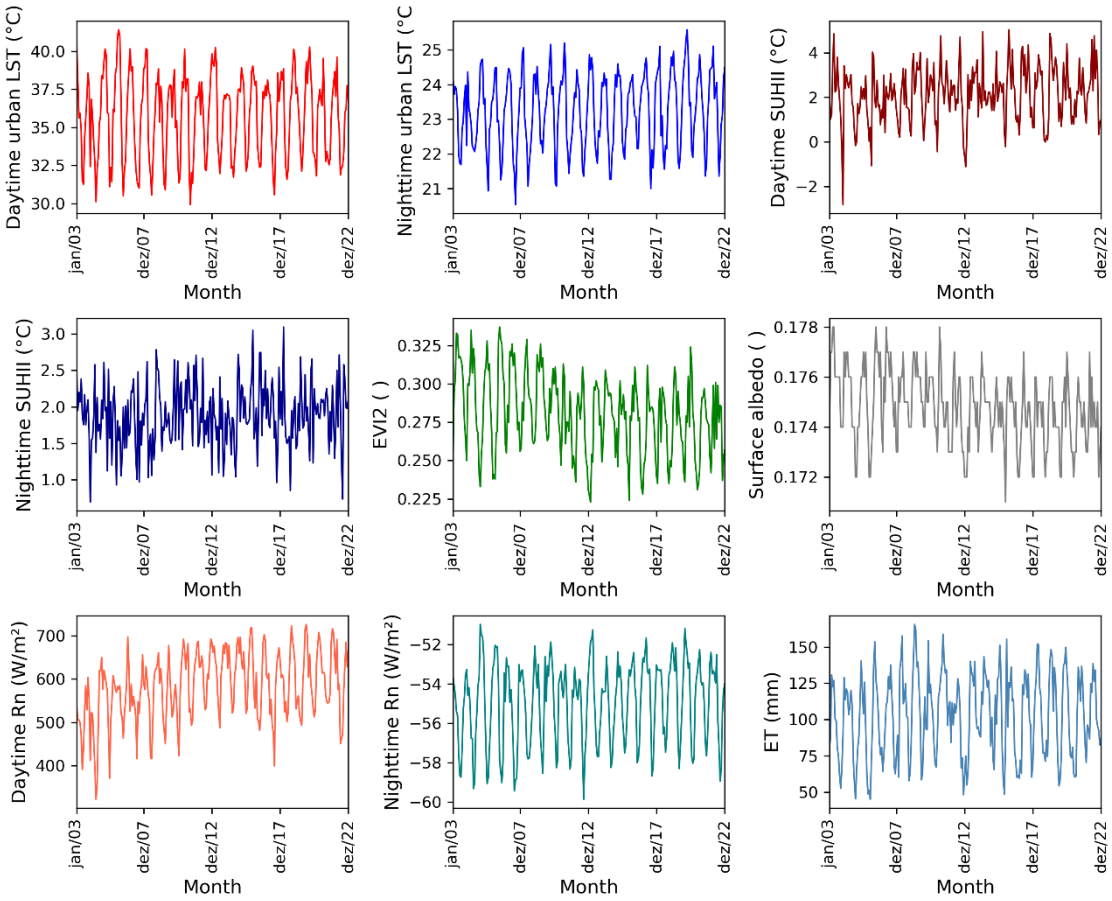

Fig. S156. Monthly variability of daytime and nighttime urban LST (ºC), daytime and nighttime SUHII (ºC), Enhanced Vegetation Index 2 (EVI2), surface albedo (α), surface net radiation (Rn, W/m^2), and actual evapotranspiration (ET, mm) of João Pessoa (JP).

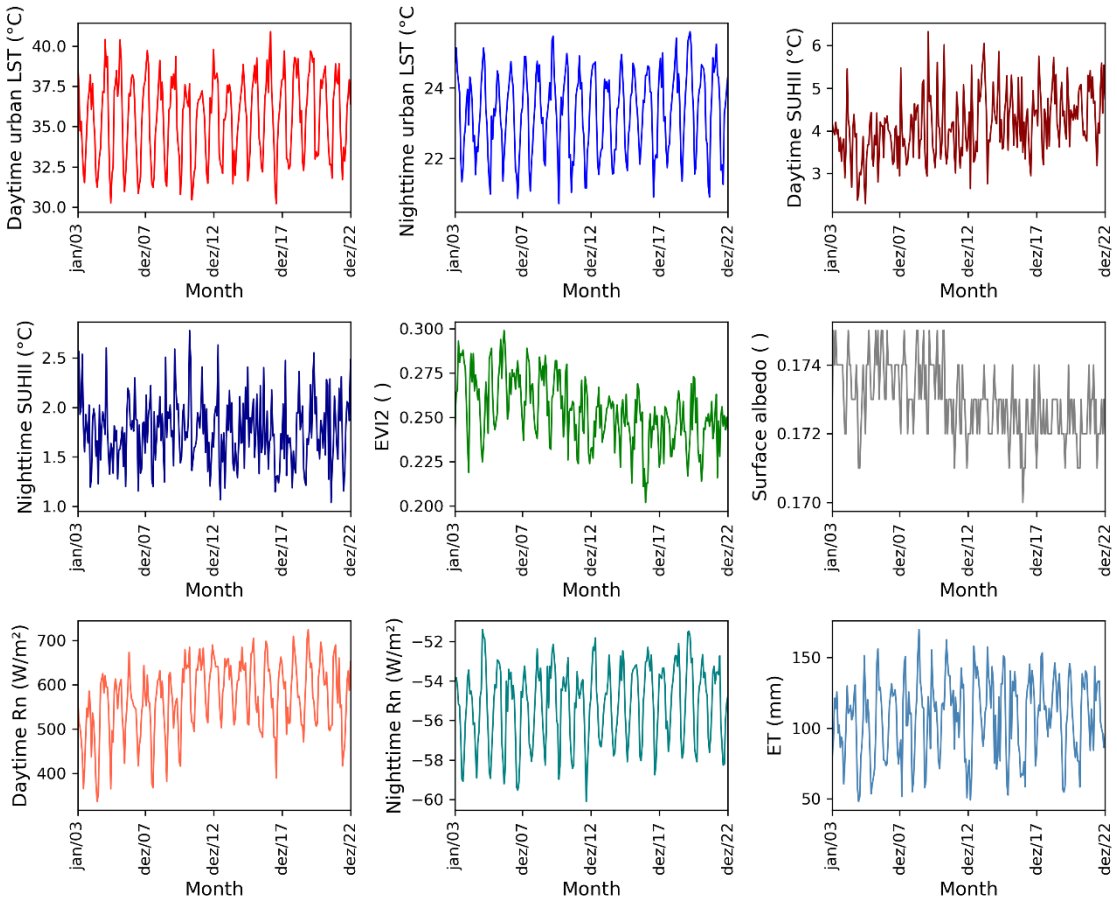

Fig. S157. Monthly variability of daytime and nighttime urban LST (ºC), daytime and nighttime SUHII (ºC), Enhanced Vegetation Index 2 (EVI2), surface albedo (α), surface net radiation (Rn, W/m^2), and actual evapotranspiration (ET, mm) of Recife (RE).

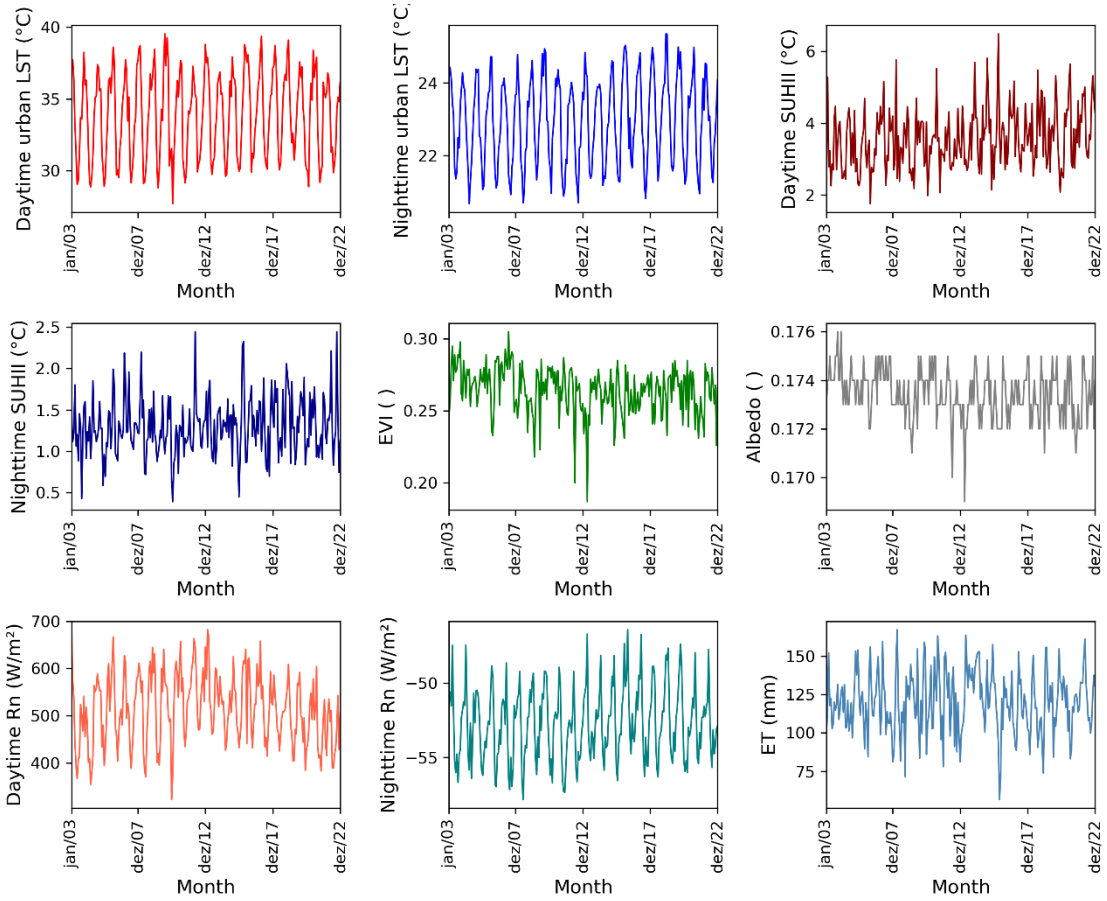

Fig. S158. Monthly variability of daytime and nighttime urban LST (ºC), daytime and nighttime SUHII (ºC), Enhanced Vegetation Index 2 (EVI2), surface albedo (α), surface net radiation (Rn, W/m^2), and actual evapotranspiration (ET, mm) of Salvador (SA).

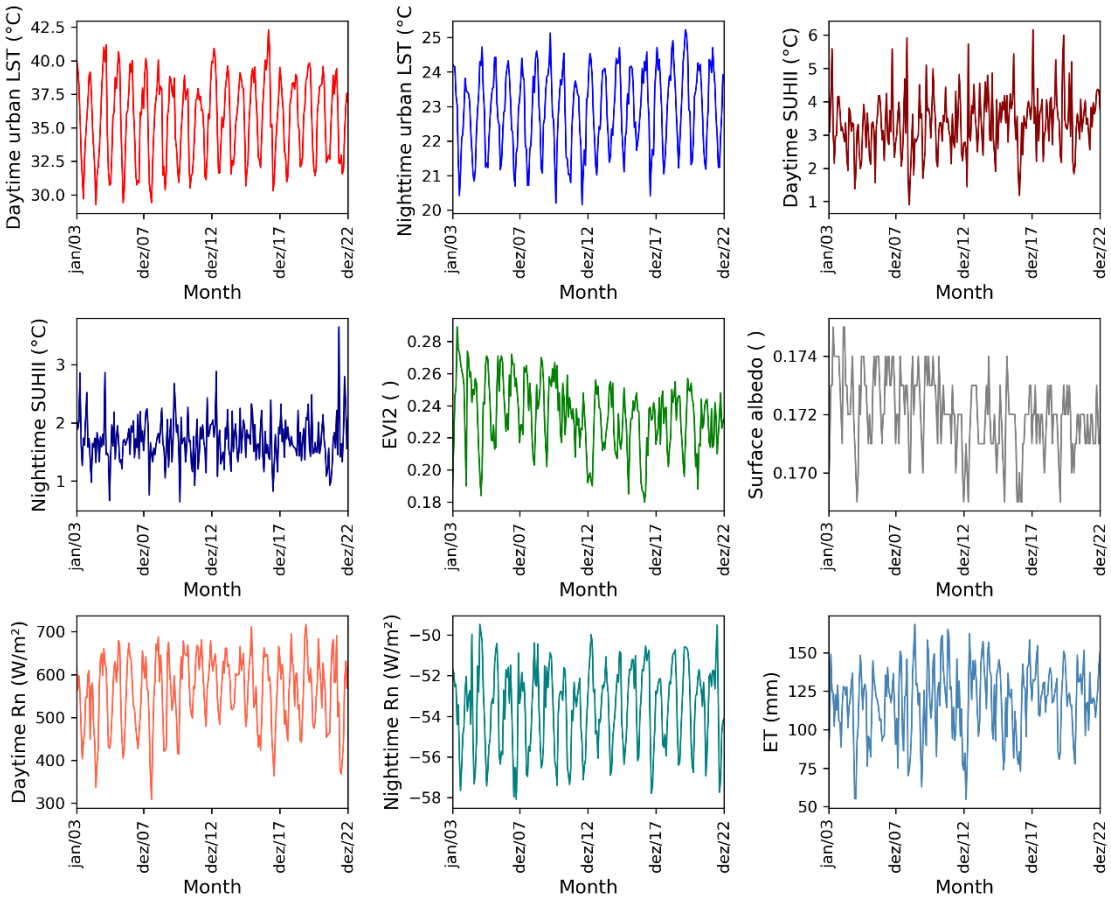

Fig. S159. Monthly variability of daytime and nighttime urban LST (ºC), daytime and nighttime SUHII (ºC), Enhanced Vegetation Index 2 (EVI2), surface albedo (α), surface net radiation (Rn, W/m^2), and actual evapotranspiration (ET, mm) of Maceió (MAC).

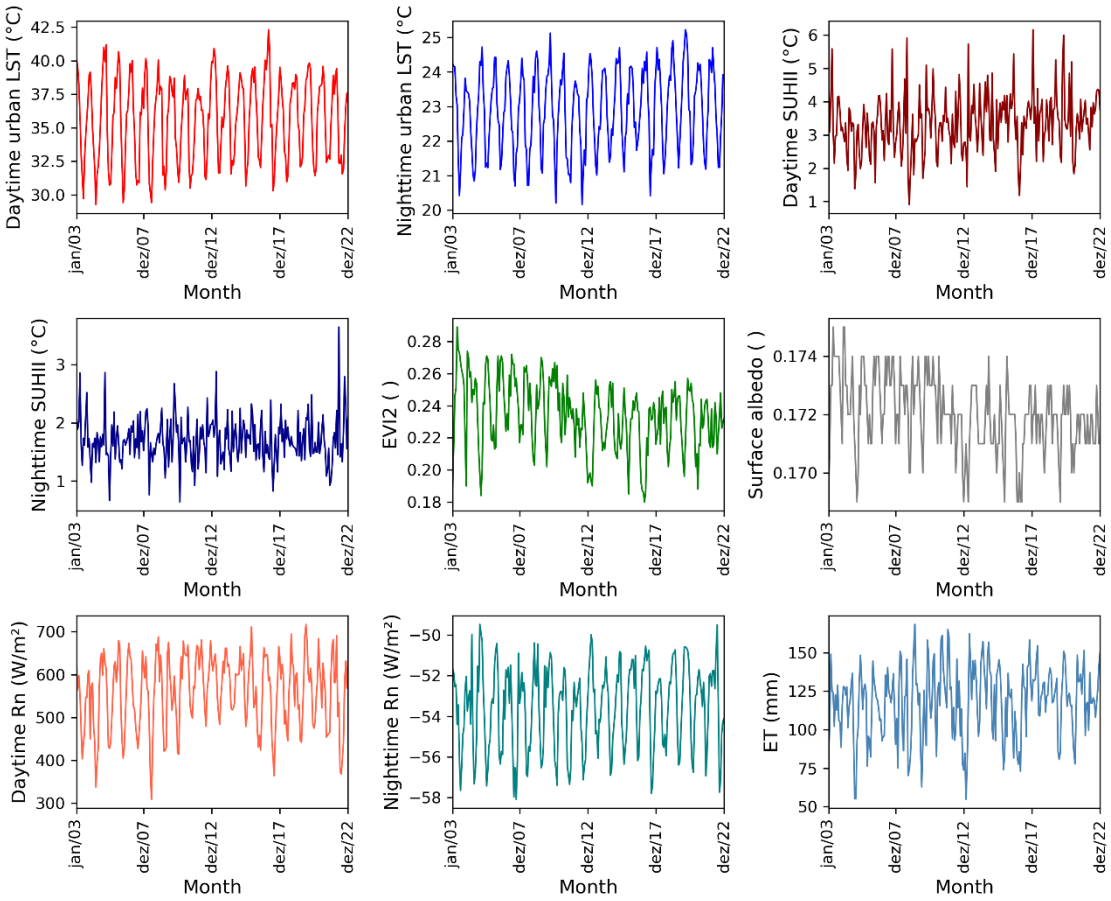

Fig. S160. Monthly variability of daytime and nighttime urban LST (ºC), daytime and nighttime SUHII (ºC), Enhanced Vegetation Index 2 (EVI2), surface albedo (α), surface net radiation (Rn, W/m^2), and actual evapotranspiration (ET, mm) of Vitória (VI).

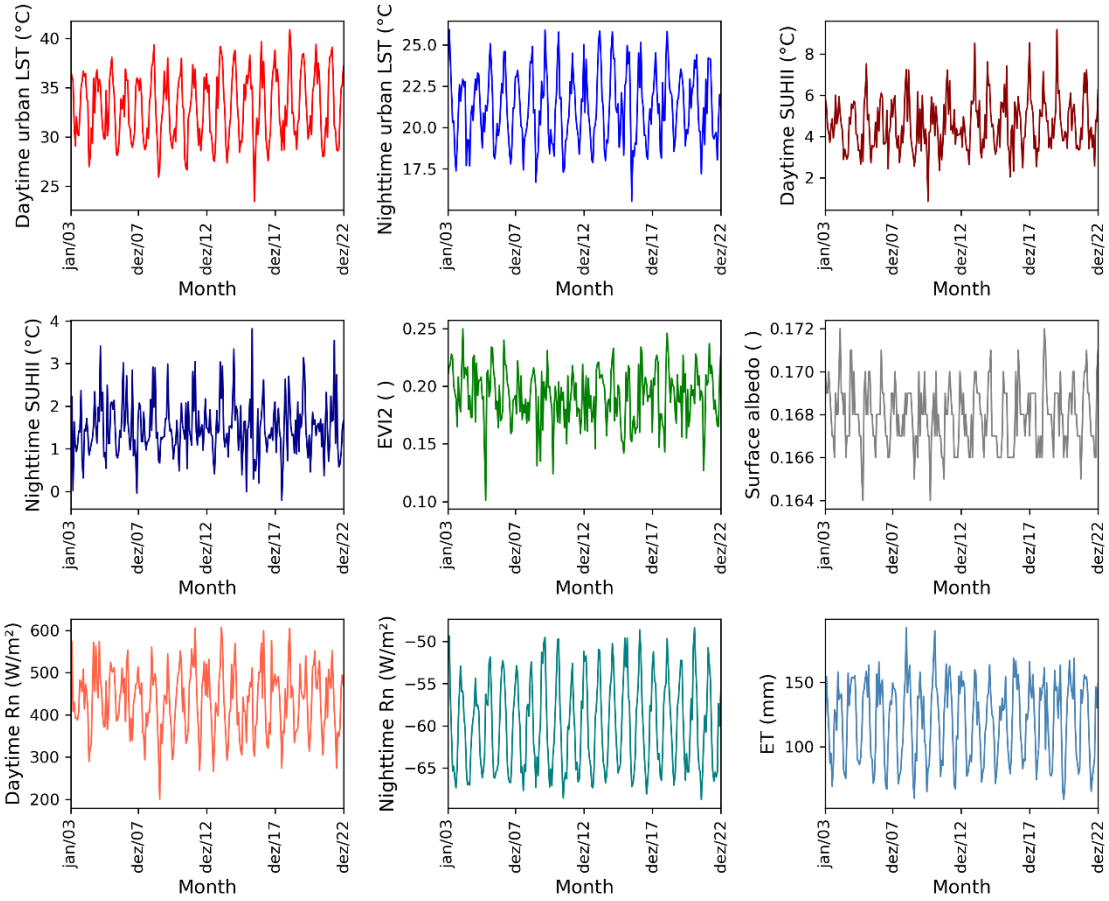

Fig. S161. Monthly variability of daytime and nighttime urban LST (ºC), daytime and nighttime SUHII (ºC), Enhanced Vegetation Index 2 (EVI2), surface albedo (α), surface net radiation (Rn, W/m^2), and actual evapotranspiration (ET, mm) of Santos (SAN).

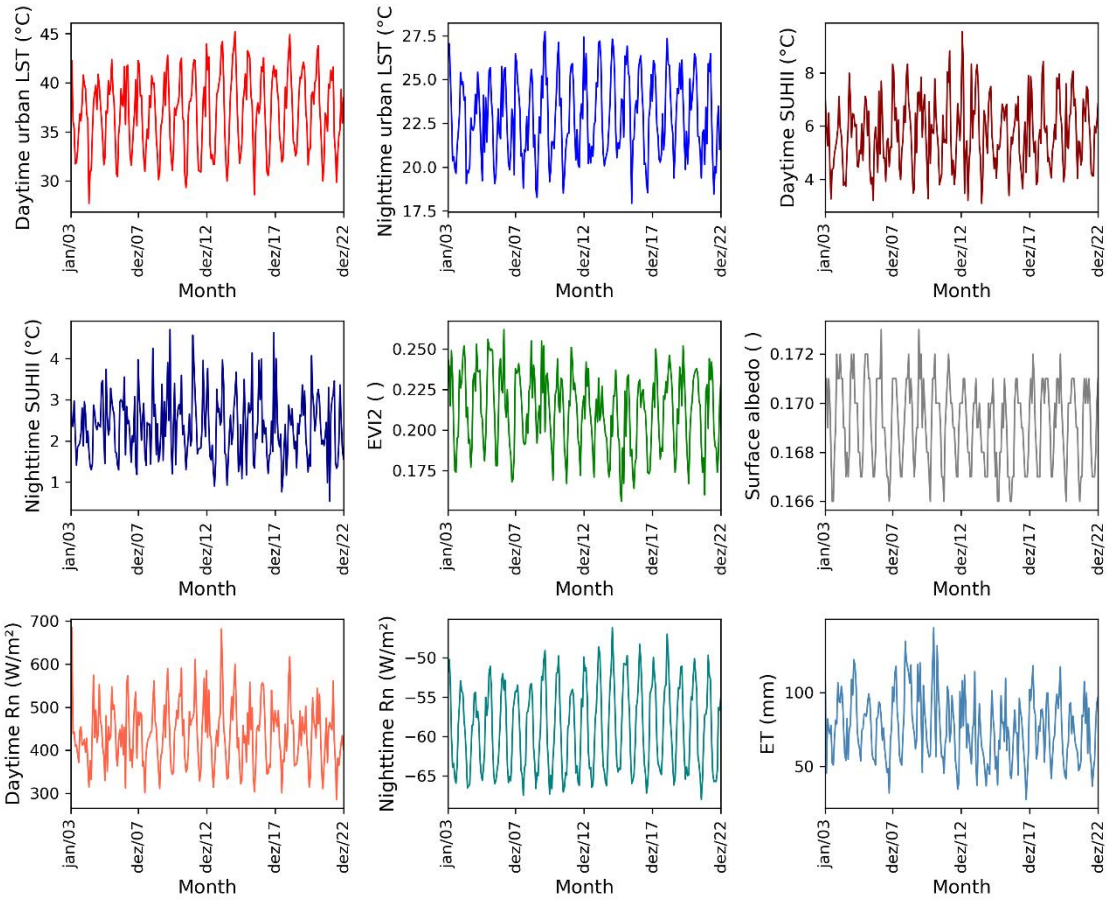

Fig. S162. Monthly variability of daytime and nighttime urban LST (ºC), daytime and nighttime SUHII (ºC), Enhanced Vegetation Index 2 (EVI2), surface albedo (α), surface net radiation (Rn, W/m^2), and actual evapotranspiration (ET, mm) of Rio de Janeiro (RJ).

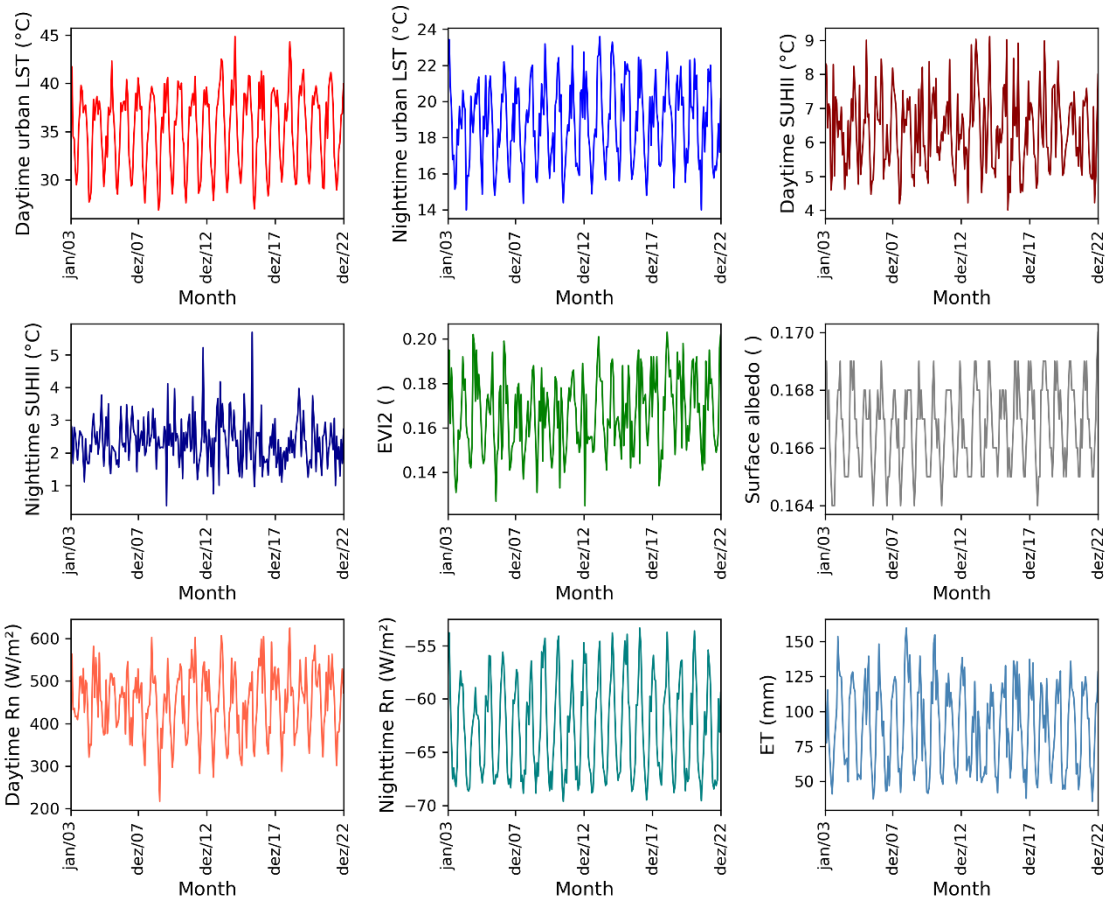

Fig. S163. Monthly variability of daytime and nighttime urban LST (ºC), daytime and nighttime SUHII (ºC), Enhanced Vegetation Index 2 (EVI2), surface albedo (α), surface net radiation (Rn, W/m^2), and actual evapotranspiration (ET, mm) of São Paulo (SP).

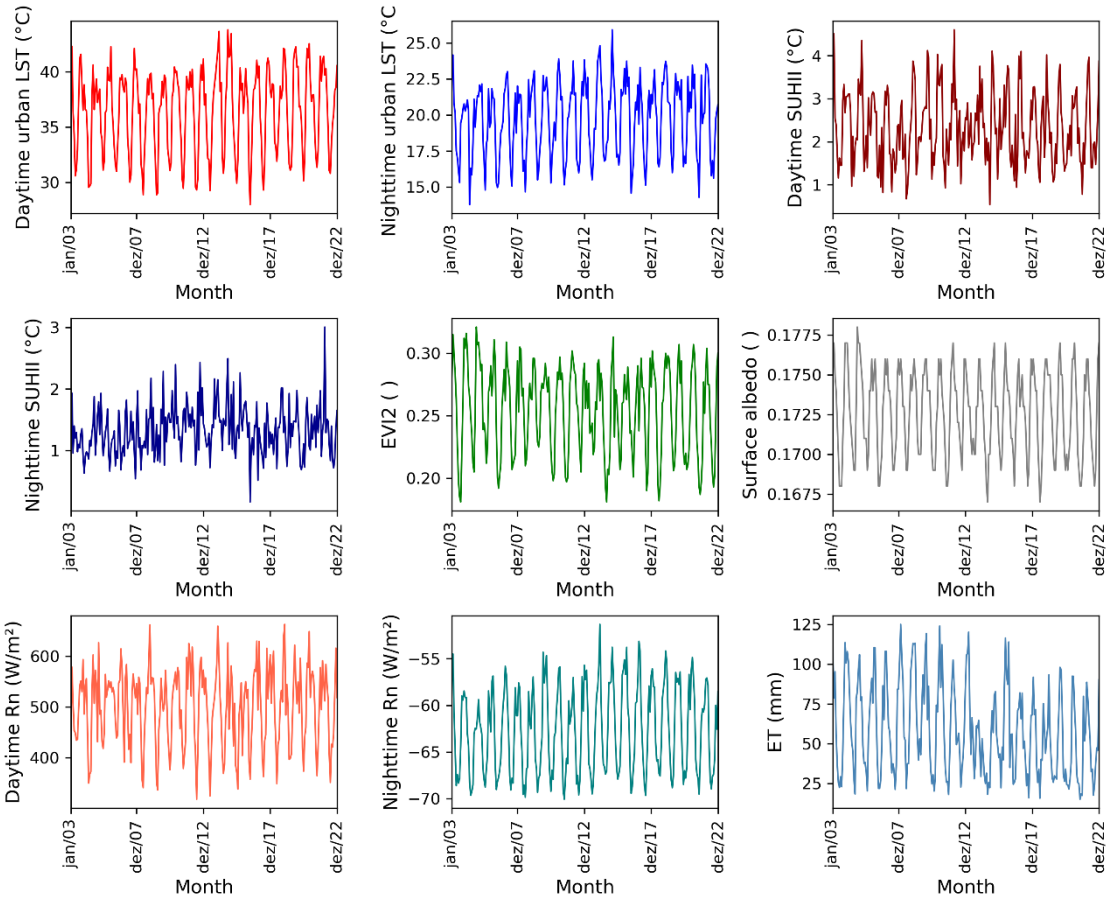

Fig. S164. Monthly variability of daytime and nighttime urban LST (ºC), daytime and nighttime SUHII (ºC), Enhanced Vegetation Index 2 (EVI2), surface albedo (α), surface net radiation (Rn, W/m^2), and actual evapotranspiration (ET, mm) of Campinas (CAM).

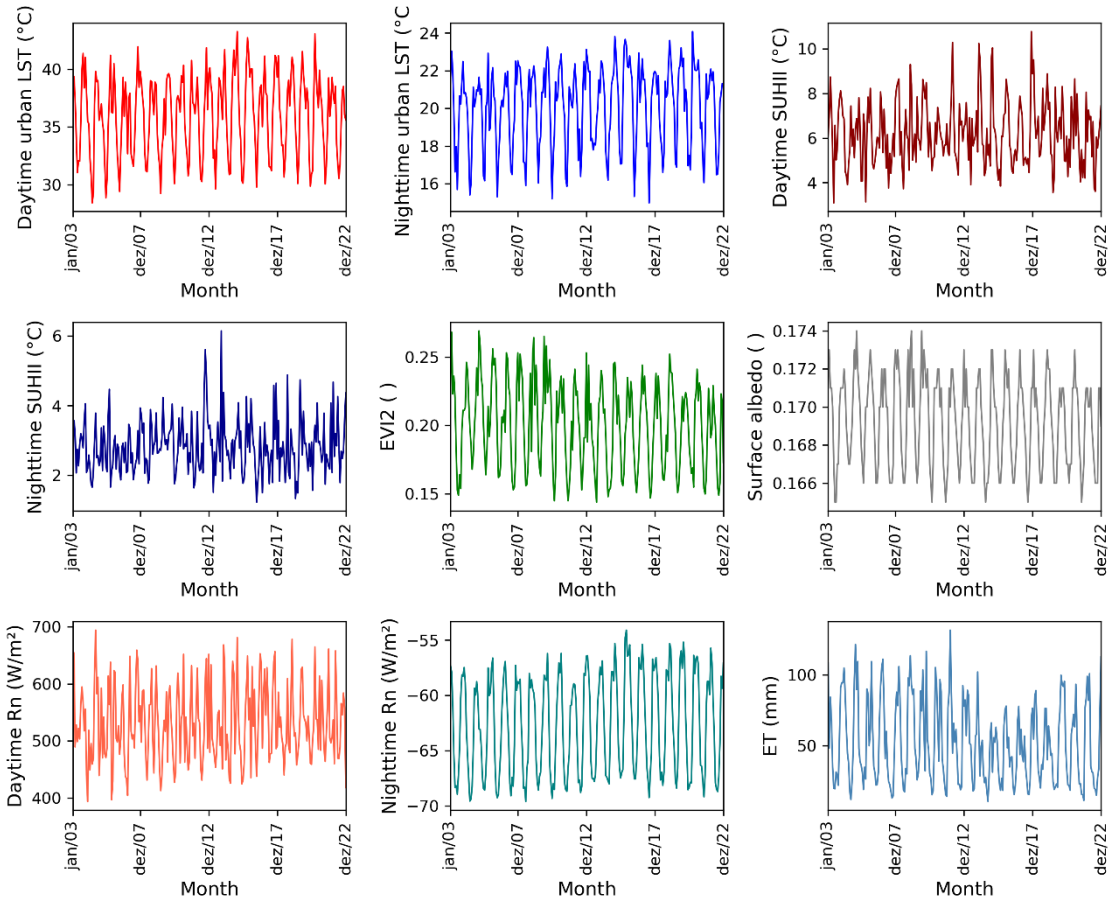

Fig. S165. Monthly variability of daytime and nighttime urban LST (ºC), daytime and nighttime SUHII (ºC), Enhanced Vegetation Index 2 (EVI2), surface albedo (α), surface net radiation (Rn, W/m^2), and actual evapotranspiration (ET, mm) of Belo Horizonte (BH).

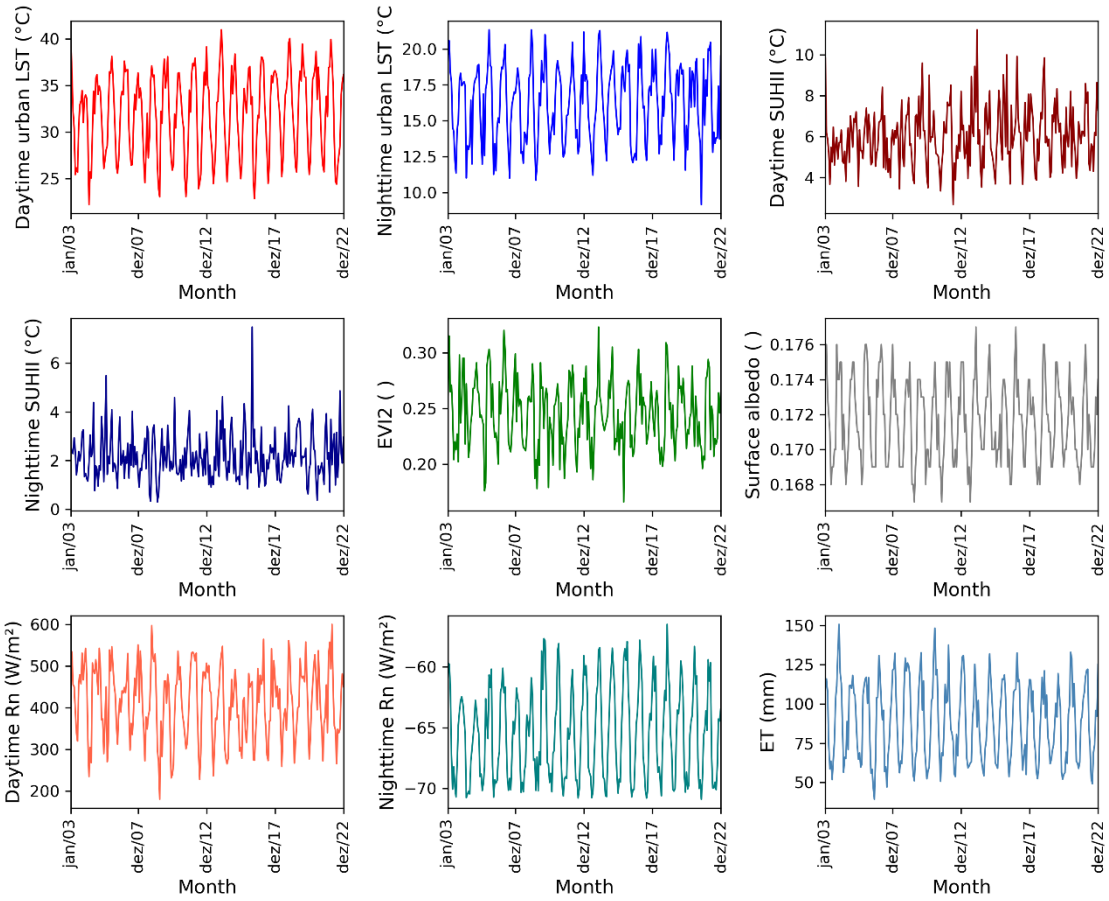

Fig. S166. Monthly variability of daytime and nighttime urban LST (ºC), daytime and nighttime SUHII (ºC), Enhanced Vegetation Index 2 (EVI2), surface albedo (α), surface net radiation (Rn, W/m^2), and actual evapotranspiration (ET, mm) of Curitiba (CU).

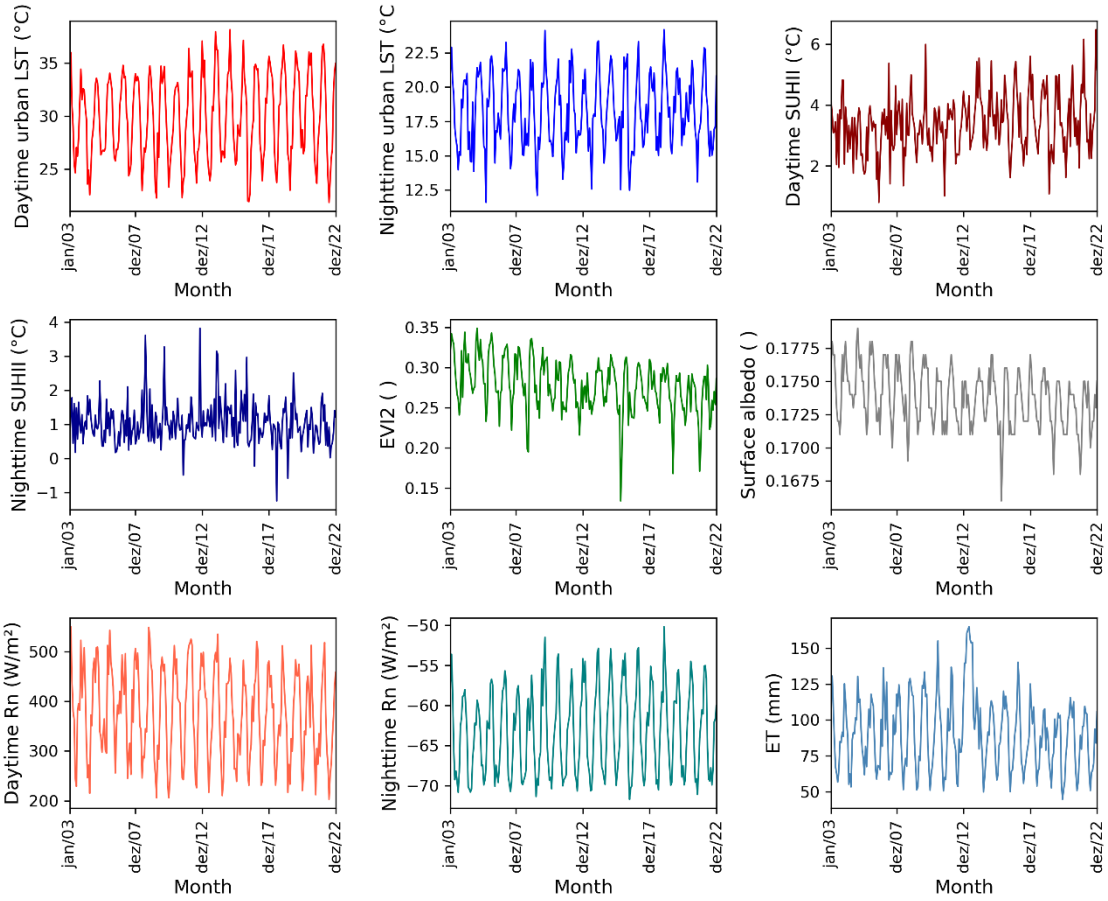

Fig. S167. Monthly variability of daytime and nighttime urban LST (ºC), daytime and nighttime SUHII (ºC), Enhanced Vegetation Index 2 (EVI2), surface albedo (α), surface net radiation (Rn, W/m^2), and actual evapotranspiration (ET, mm) of Florianópolis (FLO).

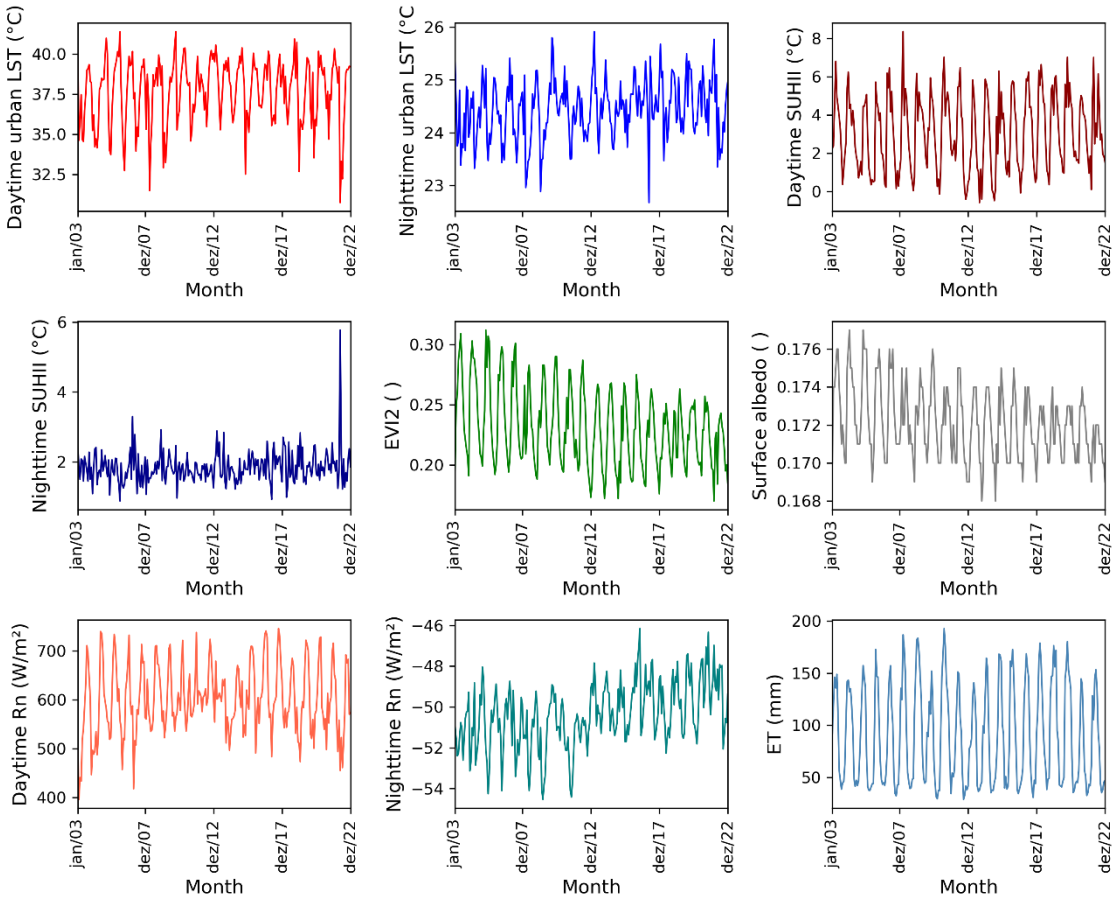

Fig. S168. Monthly variability of daytime and nighttime urban LST (ºC), daytime and nighttime SUHII (ºC), Enhanced Vegetation Index 2 (EVI2), surface albedo (α), surface net radiation (Rn, W/m^2), and actual evapotranspiration (ET, mm) of Fortaleza (FO).

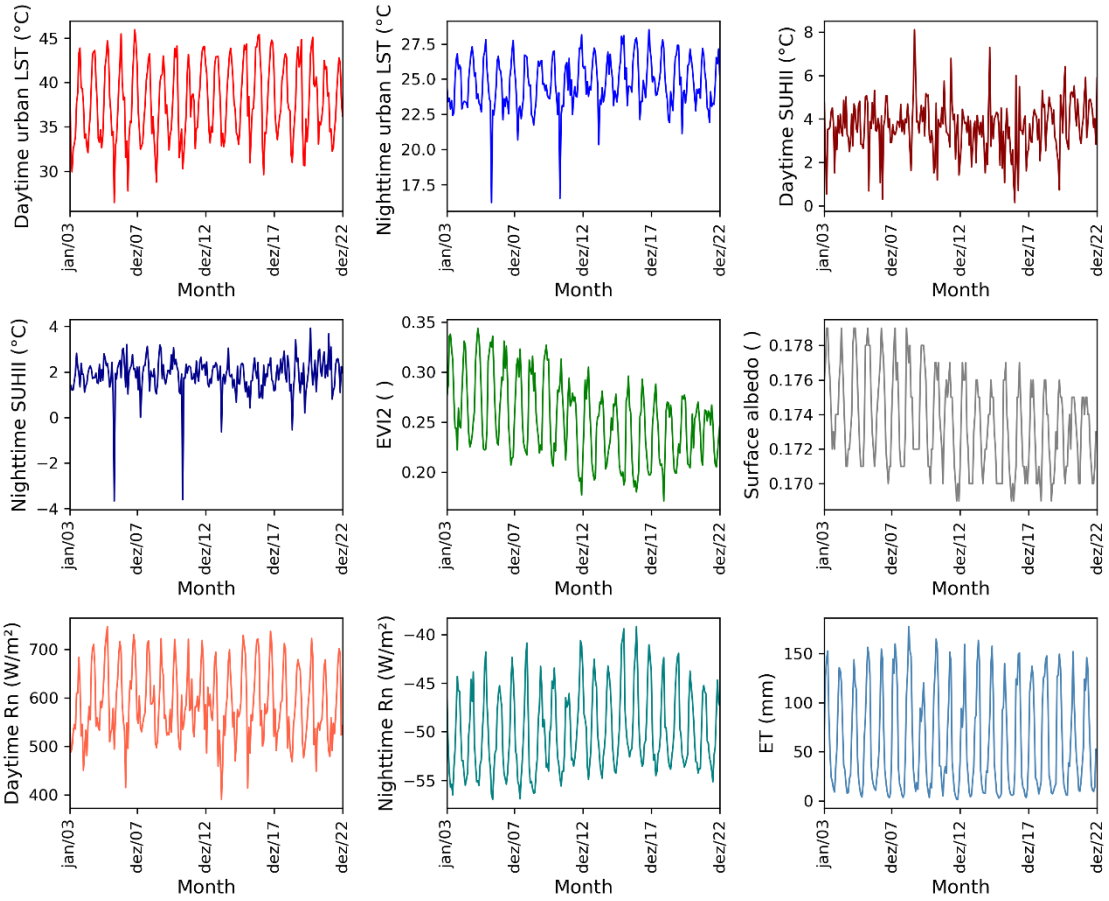

Fig. S169. Monthly variability of daytime and nighttime urban LST (ºC), daytime and nighttime SUHII (ºC), Enhanced Vegetation Index 2 (EVI2), surface albedo (α), surface net radiation (Rn, W/m^2), and actual evapotranspiration (ET, mm) of Teresina (TE).

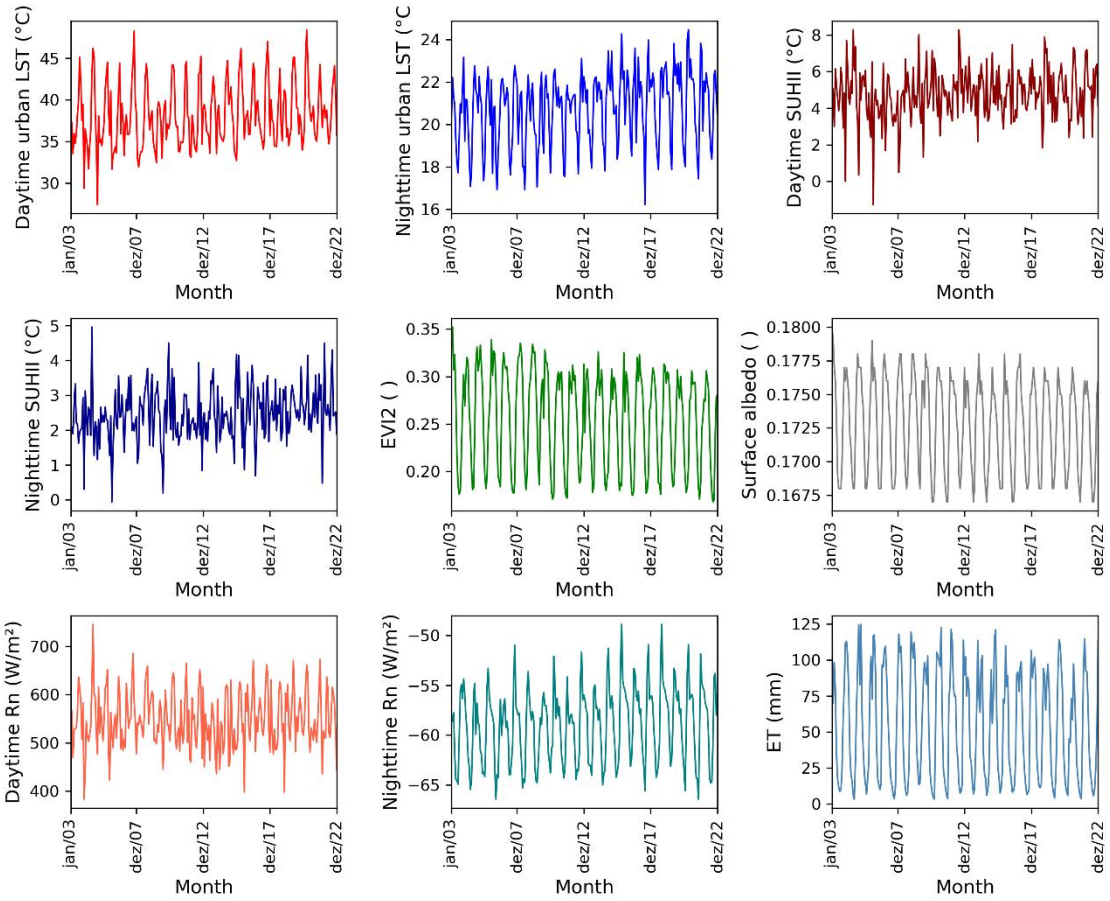

Fig. S170. Monthly variability of daytime and nighttime urban LST (ºC), daytime and nighttime SUHII (ºC), Enhanced Vegetation Index 2 (EVI2), surface albedo (α), surface net radiation (Rn, W/m^2), and actual evapotranspiration (ET, mm) of Goiânia (GO).

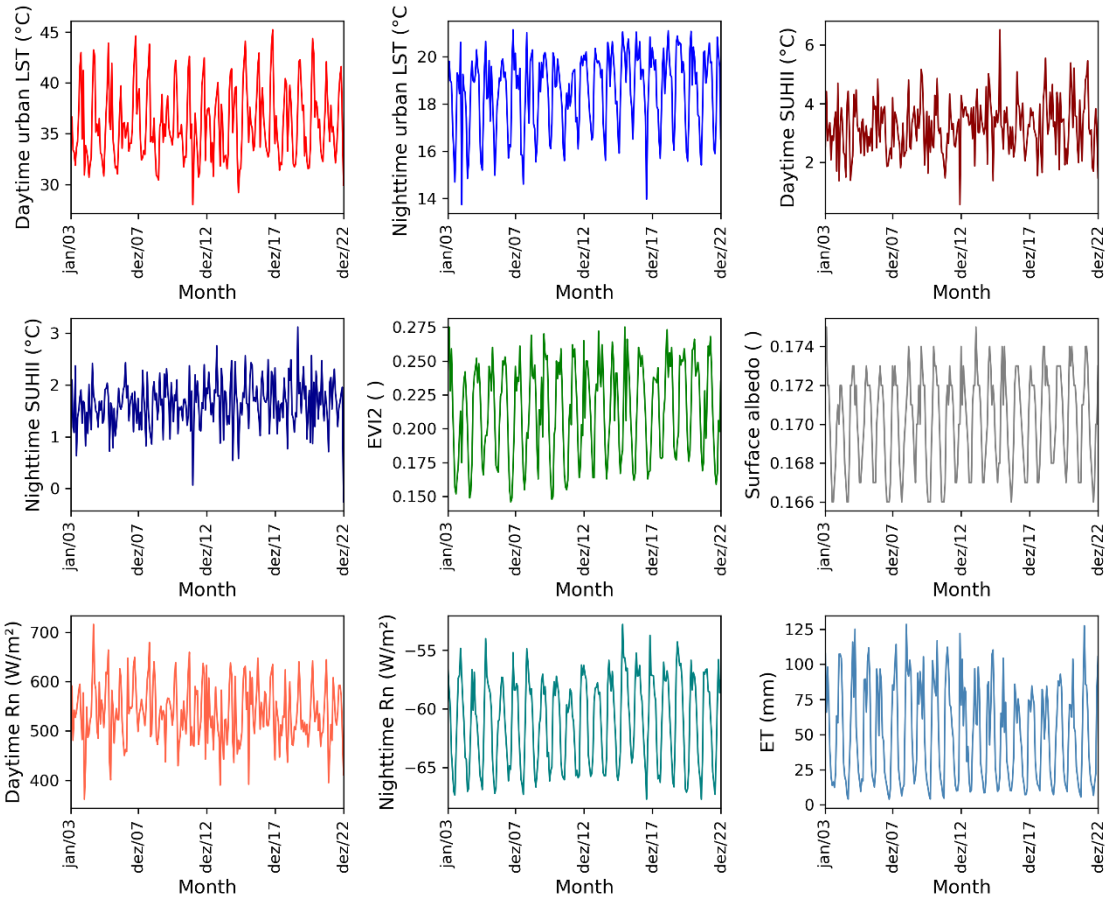

Fig. S171. Monthly variability of daytime and nighttime urban LST (ºC), daytime and nighttime SUHII (ºC), Enhanced Vegetation Index 2 (EVI2), surface albedo (α), surface net radiation (Rn, W/m^2), and actual evapotranspiration (ET, mm) of Distrito Federal (DF).

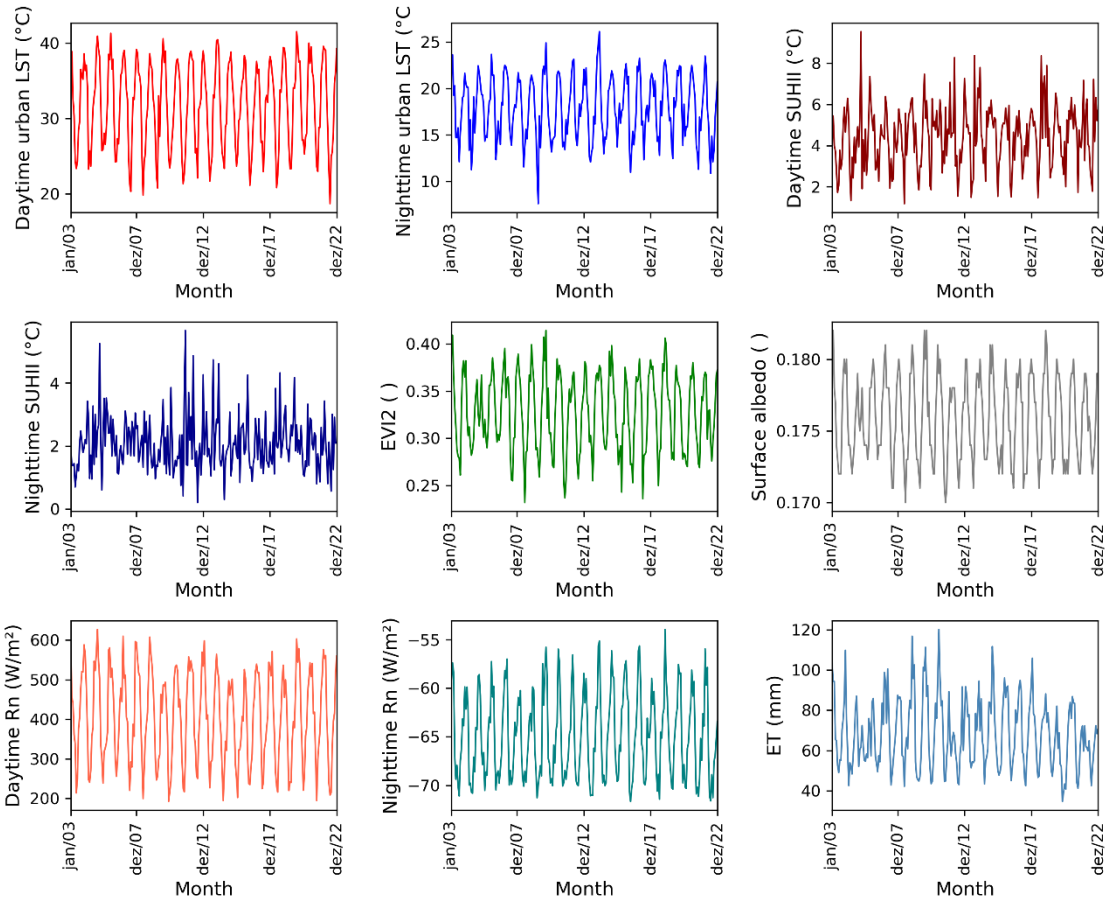

Fig. S172. Monthly variability of daytime and nighttime urban LST (ºC), daytime and nighttime SUHII (ºC), Enhanced Vegetation Index 2 (EVI2), surface albedo (α), surface net radiation (Rn, W/m^2), and actual evapotranspiration (ET, mm) of Porto Alegre (PA).